THE UNIVERSITY *of* EDINBURGH

High Spectral Resolution Mass Spectrometry Imaging of Three-Dimensional Cell Culture

Lulu H. Tucker

PhD Chemistry

The University of Edinburgh

2019

Declaration

I declare that this thesis has been composed solely by myself and that it has not been submitted, in whole or in part, in any previous application for a degree. Except where states otherwise by reference or acknowledgment, the work presented is entirely my own.

Lulu H. Tucker

Abstract

Three-dimensional (3D) cell culture combines the simplicity of two-dimensional (2D) cell culture systems with the complex interplay of factors resembling the multifaceted physiology of tissues *in vivo.* These microscale spherical cell clusters – known as multicellular tumour spheroids (MTS) – replicate the oxygen, nutrient, and waste gradients observed within tumours, and provide useful model systems to improve our understanding of cancer biology.

Matrix-assisted laser desorption/ionisation (MALDI) mass spectrometry imaging (MSI) is an analytical technique that permits broad spectral and label-free analysis to observe the distribution of compounds without requiring any significant prior knowledge. MALDI-MSI can be used as a global untargeted approach to elucidate the various microenvironments within MTS at high spatial resolution.

Here, method development for MALDI-MSI of MTS will be reported. Breast cancer (MCF-7) and prostate cancer (PC3) spheroids were grown to diameters of approximately 500 μm using the hanging drop method. For MALDI imaging, the spheroids were embedded in gelatin, cryosectioned, and coated with a matrix. Using the optimised protocol, up to eight spheroids were embedded in a gelatin block, and up to 100 spheroid sections were mounted onto a slide.

To discern the ionisable metabolome of an MCF-7 spheroid, MALDI mass spectrometry (MS) analysis was employed to compile a list of tentative metabolite identifications. Using various matrices in both polarities, over 760 tentative formulae were assigned at sub-ppm errors.

A targeted MALDI-MSI approach suggested that adenosine triphosphate (**ATP**), adenosine diphosphate (**ADP**), and glutathione can be used as metabolite markers to indicate regions of increased oxidative stress and hypoxia. **ATP** was found to be primarily localised to the outer region, whereas **ADP** was more uniformly distributed, suggesting there is a decreasing oxygen gradient through the spheroid.

Subsequently, an untargeted approach of discriminatory analysis tentatively identified the metabolites that colocalised to these areas. The assignments were used to investigate the regional flux through specific metabolic branch pathways. The hexosamine biosynthetic pathway (HBP) was found to be upregulated in the

regions of the spheroid with greater access to oxygen, whereas there was greater glycolytic flux within the regions limited by hypoxia.

MALDI-MSI is useful for elucidating the absorption, distribution, metabolism, and excretion (ADME) of drugs within MTS. Therefore, the developed protocol was employed to observe the time-dependent distribution of the hypoxia marker pimonidazole within PC3 spheroids. Due to the low signal-to-noise (S/N) of pimonidazole and its metabolites, continual accumulation of ions (CASI) was used to effectively lower the limit of detection and increase the signal intensities. Over 24 hours, pimonidazole was distributed throughout the spheroid and underwent reduction. Furthermore, its reduction derivatives showed a central localisation throughout the time course, suggestive of a hypoxic core.

Finally, a 3D printer and other parts commonly found in an analytical chemistry lab were employed as a low-cost alternative to commercial sprayers for matrix deposition. Using printed rhodamine B microarrays and fluorescence imaging, matrix application conditions were optimised to effectively reduce delocalisation from 403% to 9.4%. Subsequently, MALDI-MSI of MTS was used to compare the optimised conditions of the home-built sprayer to a commercially available matrix application platform. Using this system, robust and reproducible distributions of endogenous metabolite distributions with a high spatial resolution were observed.

Lay Summary

Oxygen is required to produce the energy that drives many processes within every cell in our bodies. Sometimes, cells can divide uncontrollably and cause cancer. These cancer cells grow and divide so quickly that the tumour is unable to obtain sufficient oxygen. Whilst this would cause our ‘healthy’ cells to run out of energy and die, cancer cells have found methods enabling them to adapt, survive, and continue to divide.

Many anti-cancer drugs are developed to specifically target these adaptations. Initially, during drug development, a potential drug is tested on cells that are grown on a flat surface. However, these carefully controlled conditions are unable to accurately mimic the complicated environments within our body. This over-simplification within the drug discovery pipeline necessitates the development of alternative, more representative models. Three-dimensional (3D) cell cultures involve growing cells in the absence of a surface, causing the cells to attach to each other and produce spherical structures up to 1 mm in diameter.

The work presented here focuses on a specific 3D cell culture known as multicellular tumour spheroids (MTS). As a result of their size, these clusters of cancer cells experience the same environments that are observed in a tumour within the body. By using spheroids as models of tumours, we can improve our understanding of how cancer cells adapt and survive under otherwise lethal conditions. Furthermore, by treating the spheroids with drugs, we are able to better understand how the drug will affect a tumour, thus reducing the need for animal models during drug discovery.

This work employs a technique called mass spectrometry imaging (MSI) to elucidate the structures of these spheroids. In a single experiment, MSI is able to detect a variety of important biological molecules without the requirement for additional labels. Furthermore, as an imaging technique, MSI enables us to observe the distributions of these molecules and drugs, contributing towards improving our understanding of how drugs interact with a tumour.

Acknowledgements

Thank you to Dave, Colin, Logan and Richard for your supervision; Faye, Alan and the SIRCAMS facility for the use of the instruments; and to Greg at AstraZeneca for all your help. Thank you to to Sam, Katie, Jenn, Kelly and the rest of the Clarke and Campbell groups for your (life) advice and expertise.

Thank you to everyone at Ronde CC and Ronde \ Works Racing for making Edinburgh my home for the last four years.

Thank you to my incredible friends, who are always there despite being so many miles away.

Thank you to my awesome family, I'm very lucky to have you.

And to Jez, you're a good egg.

This thesis is for Nick Wells, whose passion for knowledge never faltered, even when mine did.

List of figures

List of tables

Abbreviations

ACN acetonitrile

ADME absorption, distribution, metabolism, and excretion

ADP adenosine diphosphate

AMP adenosine monophosphate

ATP adenosine triphosphate

AUC area under the ROC curve

CASI continual accumulation of selected ions

cCMP cytidine-2’3’- cyclic phosphate

CEM chain ejection model

CDP cytidine diphosphate

CDP-Etn cytidine diphosphate ethanolamine

CHCA α-cyano-4-hydroxycinnamic acid

CMC carboxymethylcellulose

CMP cytidine monophosphate

CRM confocal Raman microscopy

CRM charge residue model

CTO colorectal tumour organoids

CTP cytidine triphosphate

DDTC diethyldithiocarbamate

DESI desorption electrospray ionisation

DHAP dihydroxyacetone phosphate

DHB 2,5-dihydroxybenzoic acid

DMEM Dulbecco modified eagle's medium

DMSO dimethyl sulfoxide

ECM extracellular matrix

eIF2 eukaryotic initiation factor 2

ESI electrospray ionisation

FBS fetal bovine serum

FFPE formalin fixation and paraffin embedding

FT-ICR Fourier-transform ion cyclotron resonance

F-6-P fructose-6-phosphate

GlcNAc-1-P N-acetyl glucosamine-1-phosphate

GSH reduced glutathione

GSSG oxidised glutathione

G-6-P glucose-6-phosphate

HBP hexosamine biosynthetic pathway

HMDB human metabolome database

H&E haematoxylin eosin

IEM ion evaporation model

IFS isotopic fine structure

ITO indium-tin oxide

iTRAQ isobaric tag for relative and absolute quantitation

LC liquid chromatography

LDA linear discriminant analysis

LESA liquid extraction surface analysis

MALDI matrix-assisted laser desorption/ionisation

ManNAc N-acetylmannosamine

ManNAc -6-P N-acetylmannosamine-6-phosphate

MS mass spectrometry

MSI mass spectrometry imaging

MS/MS tandem mass spectrometry

MTS multicellular tumour spheroids

m/z mass-to-charge

NeuNAc N-acetylneuraminic acid

Neu9NAc-9-P N-acetylneuraminic acid-9-phosphate

OCT optimal cutting temperature

PA phosphatidic acid

PBS phosphate buffered saline

PCA principal component analysis

PLA polylactic acid

PLS partial least-squares

RF radio frequency

ROC receiver operating characteristic

ROI region of interest

ROS reactive oxygen species

RPMI Roswell park memorial institute medium

SA sinapinic acid

SEM scanning electron microscopy

SILAC stable isotope labelling of amino acids in cell culture

SIMS secondary ion mass spectrometry

S/N signal-to-noise

TEC tissue extinction coefficient

TFA trifluoroacetic acid

TIC total ion count

TLC thin layer chromatography

ToF time-of-flight

UDP uridine diphosphate

UDP-GlcNAc uridine diphosphate N-acetylglucosamine

UMP uridine monophosphate

UTP uridine triphosphate

2D two-dimensional

2D-PAGE 2D polyacrylamide gel electrophoresis

3D three-dimensional

9AA 9-aminoacridine

Contents

Chapter 1.

Introduction

1.1 Mass spectrometry

Mass Spectrometry (MS) is a key contributor to the 'omics' era; an analytical method that enables the comprehensive profiling of small molecules (metabolomics) and proteins (proteomics).[1,2] It is advantageous for global untargeted analysis as a result of its speed, sensitivity, and wide dynamic range.[3] The fundamental principle of MS involves three stages: ionisation of the sample into the gas phase, separation of the ions based on their mass-to-charge ratios (*m/z*), and subsequent detection of the ions.

1.1.1 Ionisation

The principal aim of ionisation is to introduce the analytes of interest to into the gas-phase and impart a fixed charge. Soft ionisation methods such as electrospray ionisation (ESI) and matrix-assisted laser desorption/ionisation (MALDI) produce gas-phase ions without fragmentation, enabling the formation of intact molecular ions. In 2002, Koichi Tanaka and John Fenn were awarded the Nobel prize in Chemistry for their work on MALDI[4] and ESI[5] and their applications to biological MS. Whilst ESI is primarily used for solution-phase samples, MALDI uses a laser to analyse a sample's surface. Alternative surface ionisation methods include secondary ion mass spectrometry (SIMS),[6] desorption electrospray ionisation (DESI),[7] and liquid extraction surface analysis (LESA).[8]

1.1.1.1 Matrix-assisted laser desorption/ionisation (MALDI)

MALDI ionises molecules across a wide mass range in a single polarity by laser ablation of a matrix-coated sample. Initially, the sample is co-crystallised with a matrix compound. These matrices are commonly small, aromatic, volatile acids that have a strong optical absorption at the wavelength of the laser.[9] The most common matrices for low molecular weight analyses are α-cyano-4-hydroxycinnamic acid (CHCA) and 2,5-dihydroxybenzoic acid (DHB) for positive mode MS, 9-aminoacridine (9AA) and DHB for negative mode MS, and sinapinic acid (SA) is commonly used for larger proteins (figure 1.1).[9,10] Typically, matrices are applied in a saturated solution consisting of a mixture of water and an organic solvent, and the combination of matrix and matrix solvent can be optimised for the ionisation of specific analytes of interest.[11]

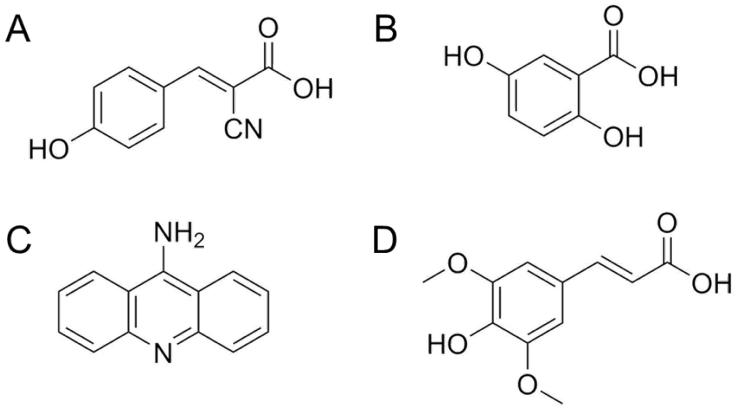

Figure 1.1. Structures of common MALDI matrices. (A) α-cyano-4-hydroxycinnamic acid, (B) 2,5-dihydroxybenzoic acid (C) 9-aminoacridine and (D) sinapinic acid.

MALDI works by pulsing a laser at a distinct location on the matrix-coated sample. The matrix absorbs this energy, causing rapid volatilisation of the crystal with its associated compounds.[2,12] The detailed mechanism of MALDI is still debated.[13,14] However, evidence suggests that the matrix acts as a proton donor to the analyte, producing $[M+H]^+$ ions, or accepts a proton to produce $[M-H]^-$ ions; where M is the mass of the analyte (figure 1.2).[15,16] Subsequent desolvation of the charged analyte occurs as gas phase ions are accelerated by an electrostatic field towards the mass analyser.[11]

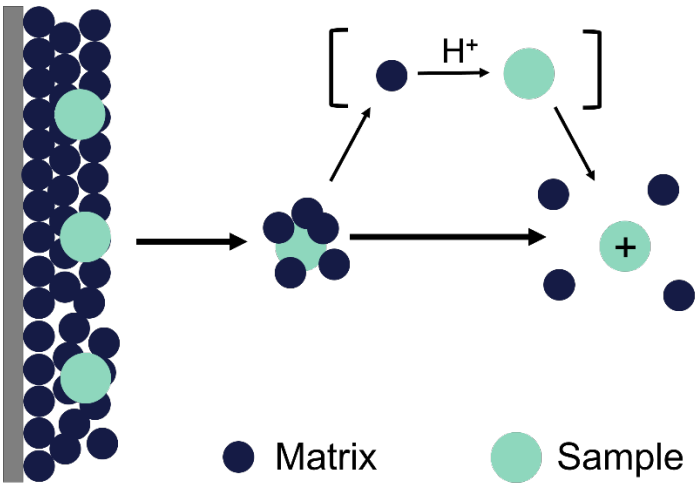

Figure 1.2. Schematic of MALDI. The sample is co-crystallised with a small photoactive matrix which absorbs energy at a wavelength similar to the laser. Ionisation of the matrix and analyte leads to proton transfer from the matrix to the analyte, producing singly charged ions.

A primary limitation of MALDI is the requirement of a matrix, as the presence of matrix peaks in the spectrum can suppress low abundance analytes.[17,18] Additionally, native tissue samples often have high concentrations of sodium and potassium ions, which can cluster with matrix ions and produce numerous peaks for each molecular species.[17]

1.1.1.2 Secondary ion mass spectrometry (SIMS)

SIMS utilises a primary ion beam to analyse the composition of solid surfaces.[19] Under ultra-high vacuum conditions, a high-energy primary beam of ions is focused onto a sample surface to initiate a collision cascade. The interaction of the ion beam with the sample provides sufficient collisional energy to overcome the surface binding energy and ejects ionic and neutral atoms, molecular fragments, and intact molecules (figure 1.3).[20] More than 90% of the emitted particles are neutral, and only the ionised particles – known as secondary ions – are used for analysis. Ionisation is suggested to occur by the bond-breaking model, whereby the heterolytic cleavage of a bond in the target emits an ion from the surface of the sample.[20] Alternatively, after emission, sputtered particles can release an Auger electron and ionise.[20] The composition of the ion beam determines the polarity of the secondary ions produced. Primary beams of positively charged ions favour the production of negative secondary ions, whereas negatively charged primary beams enhance the generation of positively charged secondary ions. The yield of secondary ions is strongly influenced by the components of the sample and the nature of the local chemical environment of the material being analysed.[19]

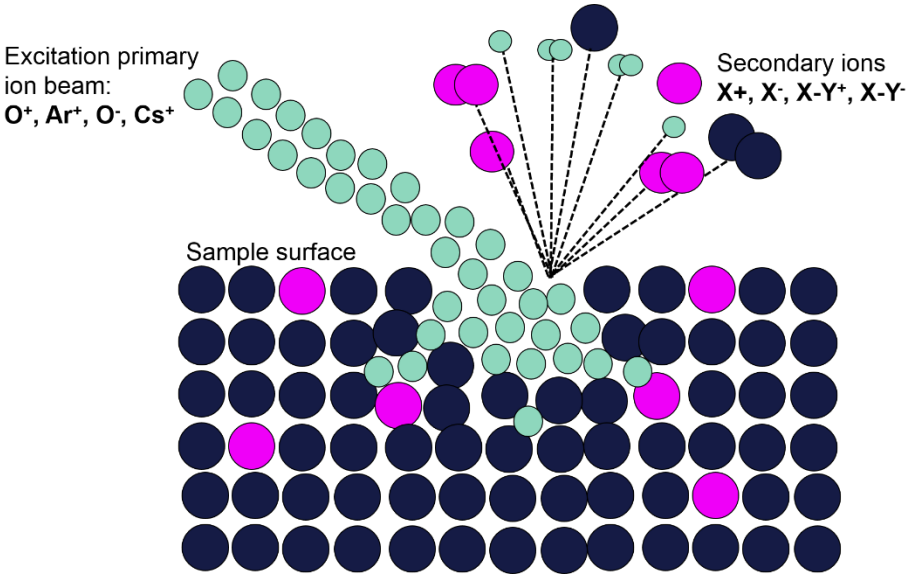

Figure 1.3. Schematic of SIMS. A primary ion beam is focused onto the surface of a sample, initiating a collision cascade leading to the emission of secondary ions.

More specifically, static SIMS employs a low energy primary ion beam to analyse the top atomic monolayer of a sample, whereas dynamic SIMS uses a much higher energy primary ion beam to erode the sample surface (figure 1.4). The secondary ions generated can be used to characterise the composition of the surface to a depth of 1 to 2 nm.[6]

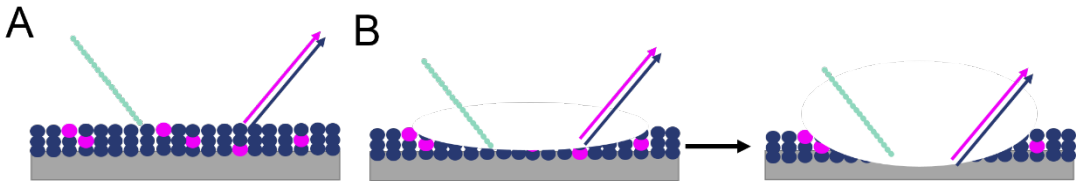

Figure 1.4. Schematic of (A) static SIMS and (B) dynamic SIMS. Static SIMS utilises a low energy primary ion beam to analyse the top atomic layer of a sample. Dynamic SIMS produces a depth profile of the sample through serial ablation of layers with the primary ion beam.

1.1.1.3 Electrospray ionisation (ESI)

ESI directly samples an analyte from solution and provides a sensitive tool for studying micro-litre sample volumes of non-volatile molecules that are not amenable to analysis by other conventional techniques.[21] After aspiration of the solution

containing the analyte into a capillary, charged droplets are formed at the tip which is held at a high potential. The presence of an electric field causes a partial separation of charges in the solution in the capillary tip, and the charges are attracted to the oppositely charged electrode, forming a Taylor cone.[22] Small droplets containing the charged particles break off the Taylor cone, producing a fine spray of charged droplets. A heated counter flow or drying gas causes the evaporation of the solvent in the charged droplet, increasing the density of the charged ions. At the Rayleigh limit of charge density, the Coulombic repulsion between these charges overcomes the surface tension holding the droplet together. Coulomb fissions occurs forming successively smaller droplets until the analyte is ionised, producing multiply-charged gas-phase ions (figure 1.5).[21]

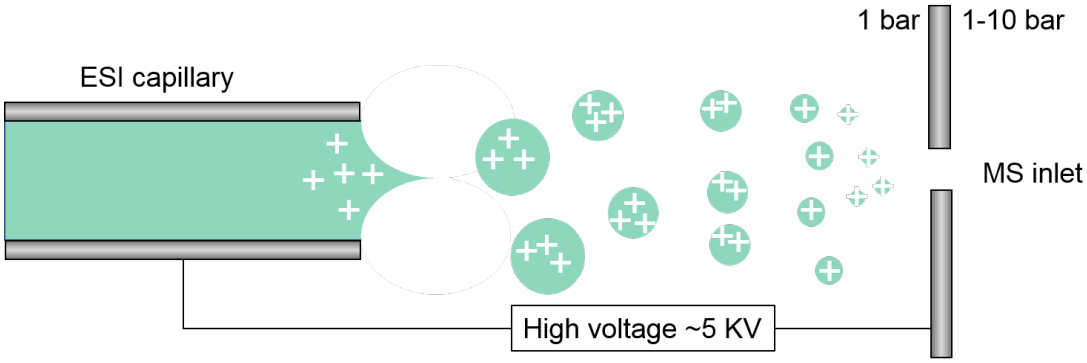

Figure 1.5. Schematic of ESI. The high potential difference between the capillary and the inlet causes the analyte solution to undergo charge separation to produce a Taylor cone. Charged droplets are ejected and reduce in size through solvent evaporation.

Two ionisation models for the production of multiply charged gas-phase ions have been proposed (figure 1.6). The ion evaporation model (IEM) suggests that droplets reduce in size through evaporation.[23] Once a droplet reaches a certain radius, the surface field strength becomes sufficient that solvated ions are expelled from the droplet.[23] Alternatively, the charge residue model (CRM) suggests that the droplets undergo successive evaporation and fission, eventually producing droplets containing one analyte or less. Gas-phase ions are produced after the remaining solvent evaporates, leaving the analyte carrying the charges that were initially in the droplet. Evidence suggests that small molecules utilise the IEM, whereas larger ions such as proteins employ CRM.[24,25] A third model – known as the chain ejection model (CEM) – has been proposed to account for protein ESI behaviour under non-

native conditions.[26] This model suggests that hydrophobic interactions and electrostatic factors drive unfolded or disordered proteins to the droplet surface, where they are ejected and the droplets carry extended protein tails.

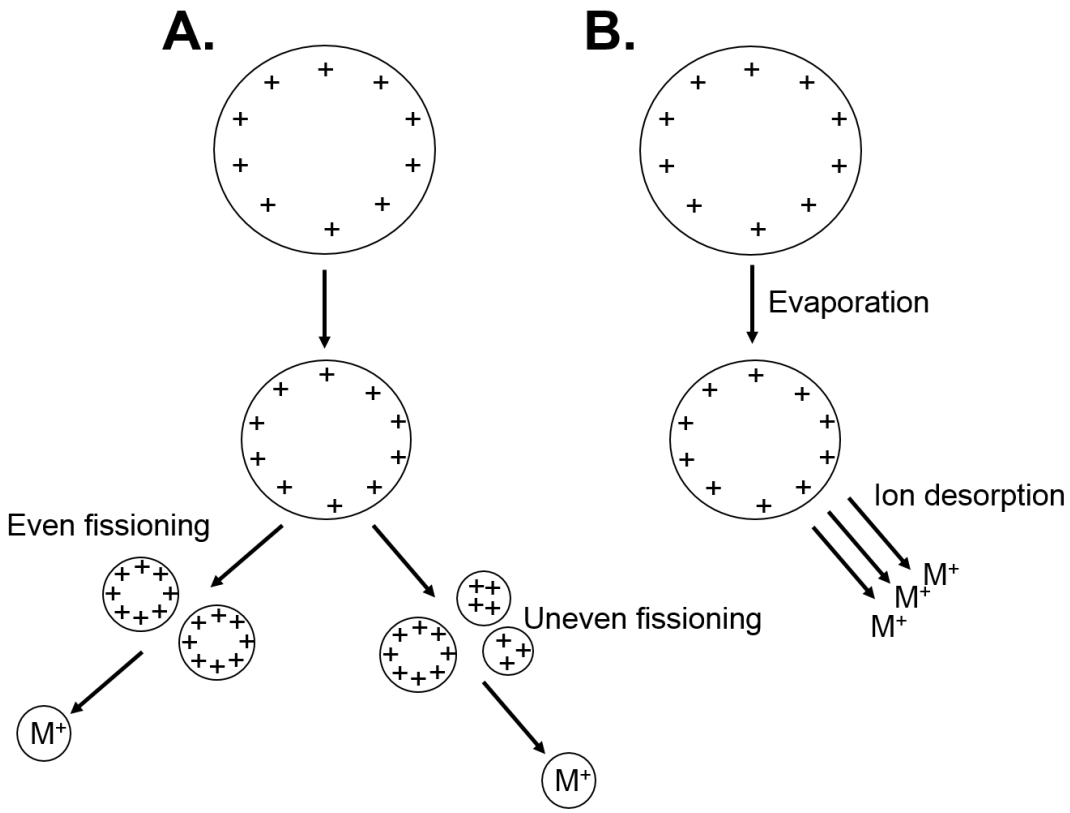

Figure 1.6. Ionisation theories for ESI. (A) Charge residue model uses even or uneven fissioning to produce analytes that carry the solvent charge. (B) Ion evaporation model expels the charged analyte as a result of evaporation and desorption.

1.1.1.4 Liquid extraction surface analysis (LESA) ionisation

Initially developed to extract small molecules from thin layer chromatography (TLC) plates for MS analysis,[27] LESA employs liquid micro junction sampling and nanoESI to analyse the composition of discrete locations on a sample's surface.[8] A robotic pipette aspirates a single droplet (a few µL) from a solvent reservoir, and dispenses the droplet onto the surface of a sample. The droplet is held in contact between the pipette and the surface to produce a wall-less liquid micro junction. As a result, soluble analytes are extracted and diffuse into the solvent via passive diffusion.

After a few seconds, the sample droplet is re-aspirated and the analyte-solvent mixture is directly injected into the mass spectrometer (figure 1.7).[8] Ionisation utilises the principles of ESI previously discussed.[8]

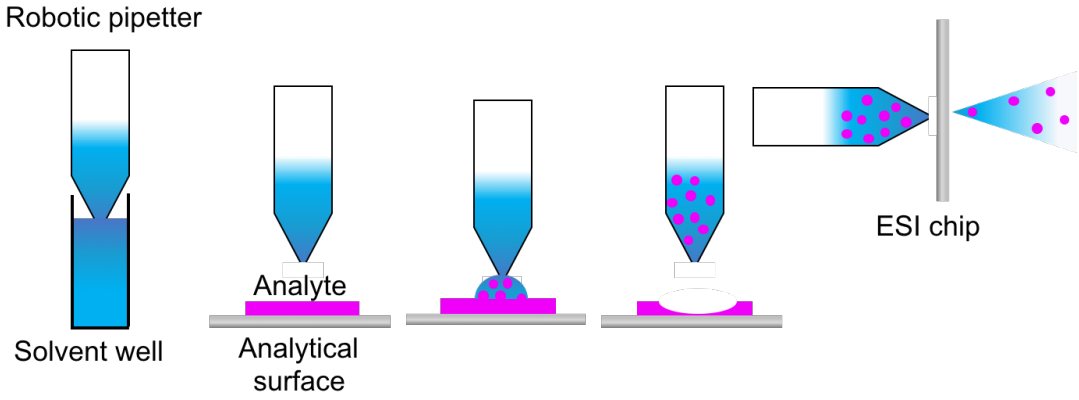

Figure 1.7. Schematic of LESA ionisation. A solvent is taken up into a robotic spotter. It is then placed onto the sample, whereby the analyte dissolves into the solvent via a wall-less liquid micro junction. The spotter is removed, and the solvent-analyte mixture is put through an electrospray chip for inlet into the mass analyser.

1.1.1.5 Desorption electrospray ionisation (DESI)

DESI is a direct probe exposure method based on ESI that can be used on samples under ambient conditions.[7] A charged solvent stream produced by an ESI source sprays charged droplets and solvent ions onto the sample surface. The exact mechanism of ionisation is not yet established, but it is suggested that the collision of the primary droplets with the surface forms a thin film into which the analyte is dissolved.[28] Subsequent droplet collisions result in momentum transfer and take-off of secondary droplets containing the material extracted from the surface (figure 1.8).[29] Gas phase ions are believed to be produced through similar mechanisms to ESI, producing multiply charged species.[30] Unlike MALDI, DESI does not require application of a matrix, making it useful for investigating samples in their native environment, and as a complementary platform for compounds that are not ionised by MALDI.[31] As desorption relies on localised microextraction, DESI sensitivity is strongly dependent upon the optimisation of the solvent content to maximise the solubility of the analyte.[32]

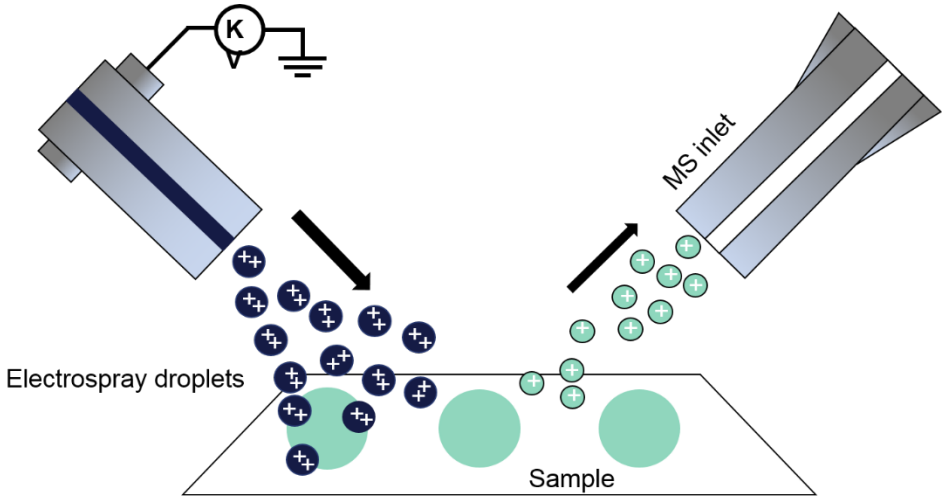

Figure 1.8. Schematic of DESI. A fast-flowing solvent is directed at the sample surface, causing the ionisation of analytes in the liquid-interface. The production of gas phase ions utilises the same mechanism as ESI. The ions produced are subsequently taken into the MS inlet for separation.

1.1.2 Separation and detection

Separation of ions can be done using any of the common mass analysers based on the desired spectral quality and resolution; including time-of-flight (ToF), Orbitrap, or Fourier-transform ion cyclotron resonance (FT-ICR).[16] Mass analysers are chosen based on the reproducibility of data, efficiency of ion separation, and their mass accuracy and range.[2] Separation by ToF and FT-ICR will be discussed in this section.

1.1.2.1 Time-of-flight (ToF)

ToF mass analysers separate ions based on the time taken for different species to travel to a detector through a drift zone, or field free region.[33] Ions are expelled from the source in pulses and accelerated towards the flight tube by a difference of potential applied between an electrode and the extraction grid, giving the ions equal kinetic energies. The ions then enter into a field-free drift region where they are separated according to their velocities before reaching the detector at the opposite end of the flight tube (figure 1.9).

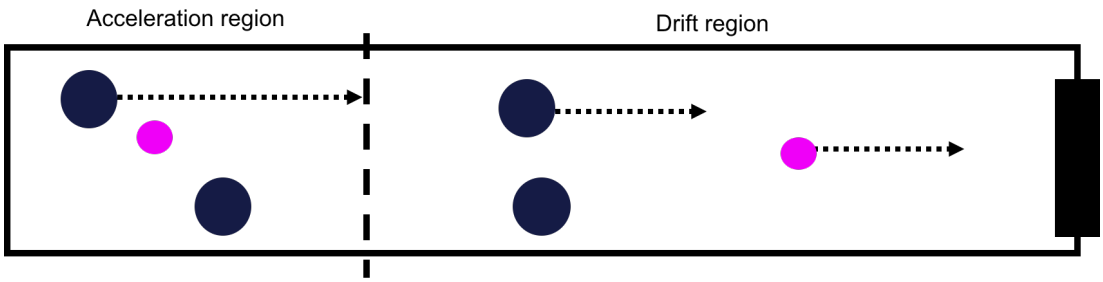

Figure 1.9. A schematic linear ToF mass analyser. Ions are given equal kinetic energy in the acceleration region, before being separated by their m/z in the drift zone. The ion with a smaller m/z (pink) arrives at the detector before the ion with a higher m/z (blue) because of its greater velocity.

The *m/z* of analytes are determined by measuring the time that ions take to move through the field-free region between the source and the detector. Before it enters this region, an ion with mass (m) and total charge ($q = ze$) is accelerated by potential (V_s) to give the kinetic energy (E_k)

$$E_k = \frac{mv^2}{2} = qV_s = zeV_s$$

Equation 1.1

The velocity of the ion leaving the source is given by rearranging equation 1.1 into

$$v = (2zeV_s/m)^{1/2}$$

Equation 1.2

After the initial acceleration, the ion travels in a straight line at a constant velocity towards the detector. The time (t) needed to cover the distance (L) before reaching the detector is given by

$$t = \frac{L}{v}$$

Equation 1.3

Replacing v with its value in equation 1.2 gives

$$t^2 = \frac{m}{z}\left(\frac{L^2}{2eV_s}\right)$$

Equation 1.4

Showing that *m/z* can be calculated from a measurement of t^2 and that the lower the mass of the ion, the faster it will reach the detector.

The major limitation of the linear ToF is its poor mass resolution. Factors such as the length of the ion formation pulse and the variation of initial kinetic energy produce a distribution of flight times for ions with the same *m/z* ratio.[11] The heterogeneous initial energies of the ions prior to acceleration results in ions with the same *m/z* travelling through the field-free drift region at different velocities and arriving at the detector at different times. Reflectrons can be added into the drift regions of ToF instruments to improve the mass resolution (figure 1.10). The reflectron increases the length of the drift region and reverses the direction of ion velocities, correcting for variations in the kinetic energies. Ions with greater initial kinetic energy penetrate further into the reflectron and therefore take longer to be reflected.[11]

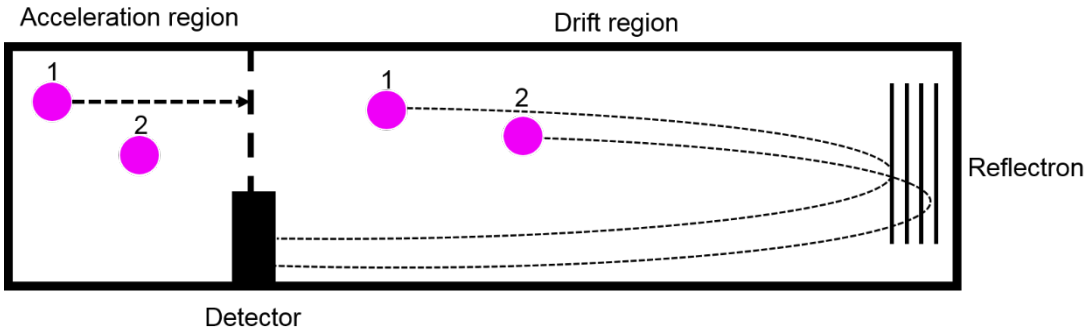

Figure 1.10. Schematic of a reflectron ToF mass analyser. Ions with a greater initial kinetic energy (2) penetrate further into the reflectron, whilst ions with less kinetic energy (1) are reflected faster. This improves the mass resolution obtained.

ToF-MS systems provide high sensitivity and relative fast acquisition of MS data. Modern ToF instruments typically have a mass resolving power of up to ~50,000 and mass accuracies of 1–5 ppm after external calibration.[34]

1.1.2.2 Fourier-transform ion cyclotron resonance (FT-ICR)

FT-ICR determines the *m/z* of ions based on the ICR frequency within a fixed magnetic field under ultra-high vacuum, producing a higher mass resolution and accuracy than any other available mass spectrometer.[35,36] A set of trapping plates hold the ions inside the analyser cell which is composed of two sets of opposed electrodes: the excitation plates and the detection plates (figure 1.11).[35]

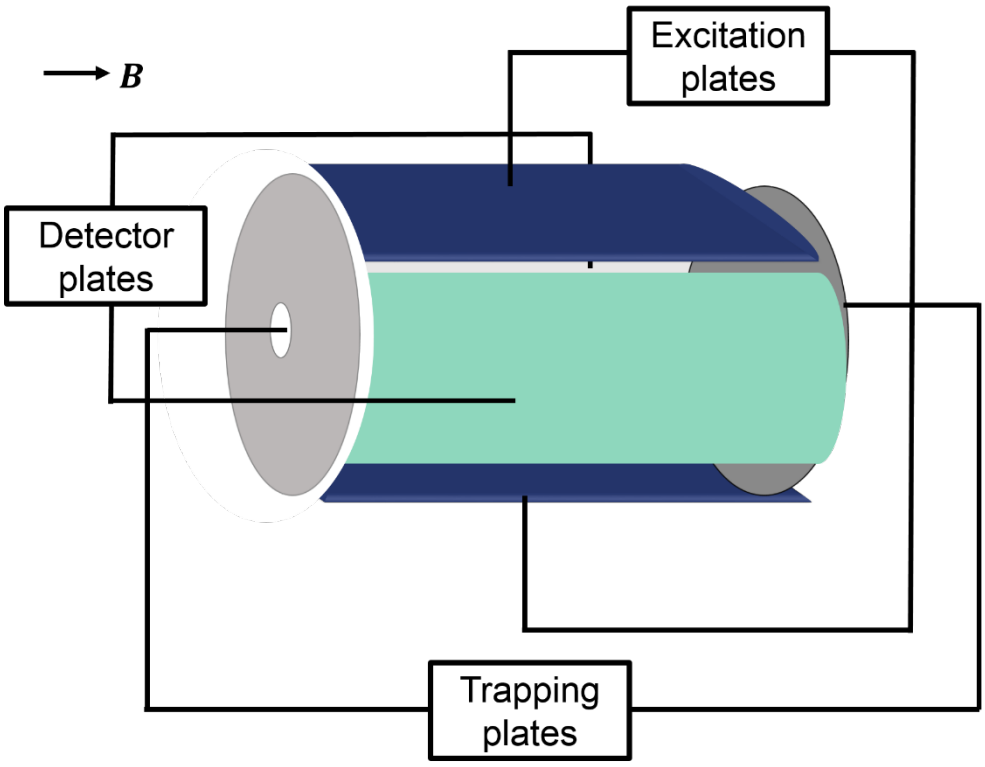

Figure 1.11. Schematic of a FT-ICR mass analyser. Two sets of opposed plates form the excitation and detection functions of the cell. Ions enter through an inlet, where they are kept in place by front and back trapping plates. $\boldsymbol{B}$ *shows the direction of the magnetic field*

An ion moving in the presence of a spatially uniform magnetic field ($\boldsymbol{B}$) is subject to a force, known as the Lorentz force (equation 1.5).

$$Force = mass \times acceleration = m\frac{dv}{dt} = qv\boldsymbol{B}$$

Equation 1.5

Where mass, velocity and charge are given by m, v and q respectively. If the ion is moving in the presence of a directional magnetic field ($\boldsymbol{B}$), the Lorentz force acts at an angle perpendicular to the plane determined by v and $\boldsymbol{B}$. Therefore, at a constant speed in the absence of collisions, the magnetic field bends the ions path into a radius of a circle (r) (figure 1.12).

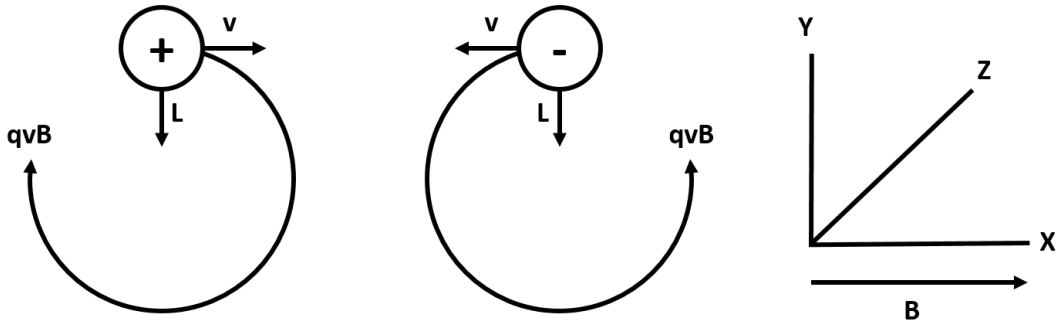

Figure 1.12. Schematic showing that with a velocity of $\boldsymbol{v}$, and the acting Lorentz force at an angle perpendicular to that of the magnetic field $\boldsymbol{B}$, an ion moves in a curve.

By considering the following, that the velocity in the xy plane (perpendicular to $\boldsymbol{B}$)

$$v_{xy} = \sqrt{v_x^2 + v_y^2}$$

Equation 1.6

And that the angular acceleration is equivalent by

$$\frac{dv}{dt} = \frac{{v^2}_{xy}}{r}$$

Equation 1.7

Substitution into the equation above shows that

$$\frac{m{v^2}_{xy}}{r} = q v_{xy} \boldsymbol{B}_0$$

Equation 1.8

However, the angular velocity (ω) about the x axis is defined by

$$\omega = \frac{v_{xy}}{r}$$

Equation 1.9

Making equation 1.8

$$Force = m\omega^2 r = q\boldsymbol{B}_0\omega r$$

Equation 1.10

Or simplified and cancelled to give the ion cyclotron equation

$$\omega = \frac{q\boldsymbol{B}_0}{m}$$

Equation 1.11

Showing that all ions of a given *m/q* have the same ICR frequency independent of their velocity. Therefore, by holding the magnetic field ($\boldsymbol{B}_0$) constant, the *m/z* of the ions can be determined by calculating the cyclotron frequency.

In the absence of a radio frequency (RF), the ions are localised to the centre of the cell and their cyclotron orbit is small. The ions are excited by applying a uniform electric field oscillating at or near the cyclotron frequency corresponding to a particular *m/z*, accelerating these ions to a larger and detectable radius. A rapid frequency sweep is applied across the excitation plates to simultaneously excite all the ions within the cell to a higher orbital radius. Ions with similar *m/z* values move into groups of the same radius.[16] As these ions approach a detection plate, they attract or repel electrons and induce an alternating current as they pass each of the detection plates. The ICR signal produced is measured using the voltage difference between the two plates as a function of time, and the Fourier-transform of this difference produces a frequency spectrum that can be converted to a mass spectrum (figure 1.13).

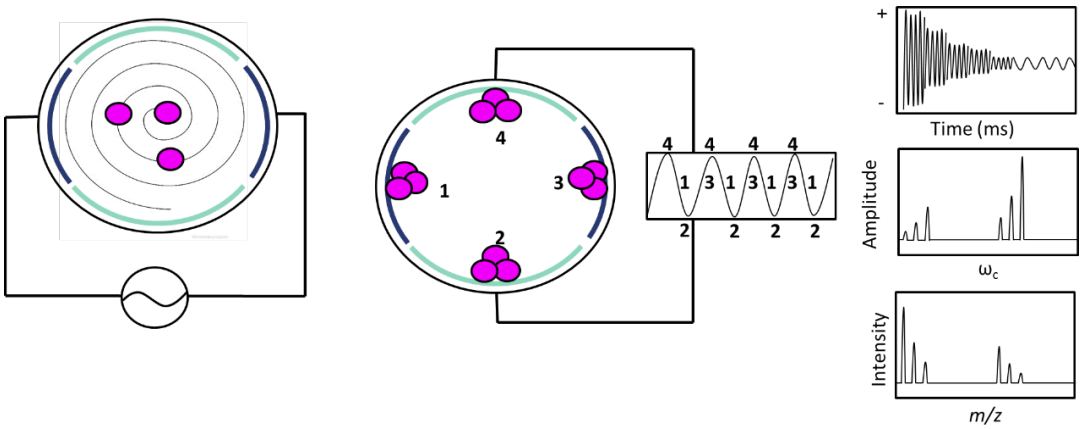

Figure 1.13. A schematic of an FT-ICR cell. An electric field is applied across the voltage plates (navy), exciting ions into a greater cyclotron resonance. As ions approach the detection plates (green), they induce an alternating current and an oscillating spectrum of charge as a function of time. By calculating the Fourier-transform of this difference, a frequency spectrum and subsequent mass spectrum can be produced.

The high mass measurement accuracy obtained with FT-ICR MS is a result of inherently accurate frequency measurements. The cyclotron frequency of an ion is independent of its kinetic energy. Therefore, unlike ToF analysers, resolution is not limited by the spread in the kinetic energy distribution of the ions. This insensitivity of cyclotron frequency to kinetic energy is one of the principle reasons why FT-ICR MS is able to achieve ultra-high resolution. Increasing the magnetic field increases the resolving power by increasing the cyclotron frequency of an ion, thus enabling more measurements to be taken within a given timeframe. The difference between two cyclotron frequencies is also increased, corresponding to greater resolving power.[36]

1.1.2.3 Quadrupoles

MS approaches can be either ‘target mode’ when the *m/z* of interest is known, or ‘discovery mode’ when no previous knowledge of the sample is required.[15] This is especially useful when using MS as a global approach to understand the metabolism of a drug in development. This is because an untargeted analysis aims to maximise the range of masses investigated; however this can compromise the sensitivity and specificity for any particular analyte.[37] For targeted analysis where

the *m/z* of the ion of interest is known, a narrow mass region can be isolated using quadrupoles to provide an improved signal-to-noise ratio (S/N) and mass resolution.

A quadrupole consists of four parallel circular rods which act as two opposing pairs of electrodes with a voltage of both a direct and alternating current applied (figure 1.14).[35] Ions are attracted towards the oppositely charged electrodes, but as the electrodes switch potential, this results in the ions constantly moving. As ions travel through the quadrupole, ions of a certain *m/z* will have a stable trajectory to facilitate transmission through the quadrupole for any given voltages. Ions that don't possess the specific voltages will have unstable trajectories and will collide with the rods, thus isolating ions with specific *m/z* values to be selected from complex mixtures of ions.[35]

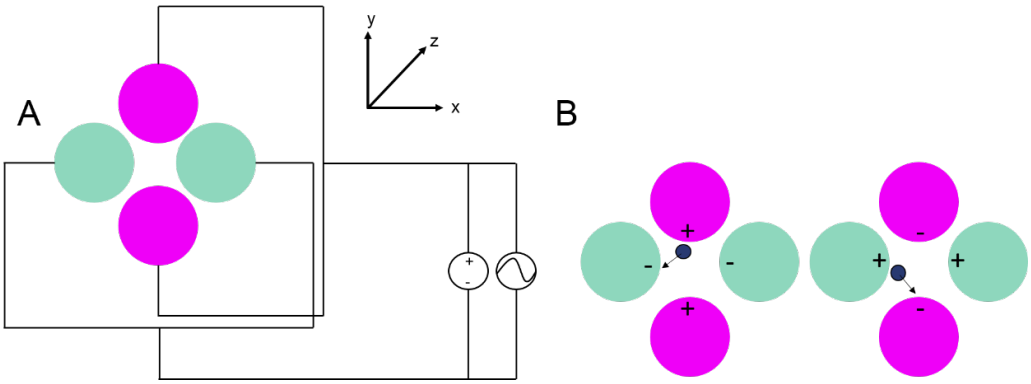

Figure 1.14. Schematic of quadrupole set-up in the z plane. (A) Two opposed pair of electrodes possess an alternating and direct current. (B) Ions are attracted to the oppositely charged electrode, but as the potential switches in these electrodes the ions continually move in the xy plane.

1.2 Mass spectrometry imaging (MSI)

The primary limitation of conventional MS is its inability to identify heterogeneity within a sample.[38] This is especially important for elucidating the time-dependent spatial distribution of a drug and its metabolites within tissue samples.[39] MSI combines the principles of MS with spatial information, permitting broad spectral and label-free analysis to observe the distribution of compounds without any significant prior knowledge.[15,40,41] MSI employs the process of ionisation, separation and detection at a discrete location on a sample – referred to as a 'pixel' – to produce a

mass spectrum. This process is repeated across the sample. The spectra within the pixels are compiled to produce a profile spectrum from which the distributions of each *m/z* value can be observed using ion density maps (figure 1.15).[42] The spectrum from each pixel can also be exported from the ion density maps and individually analysed.

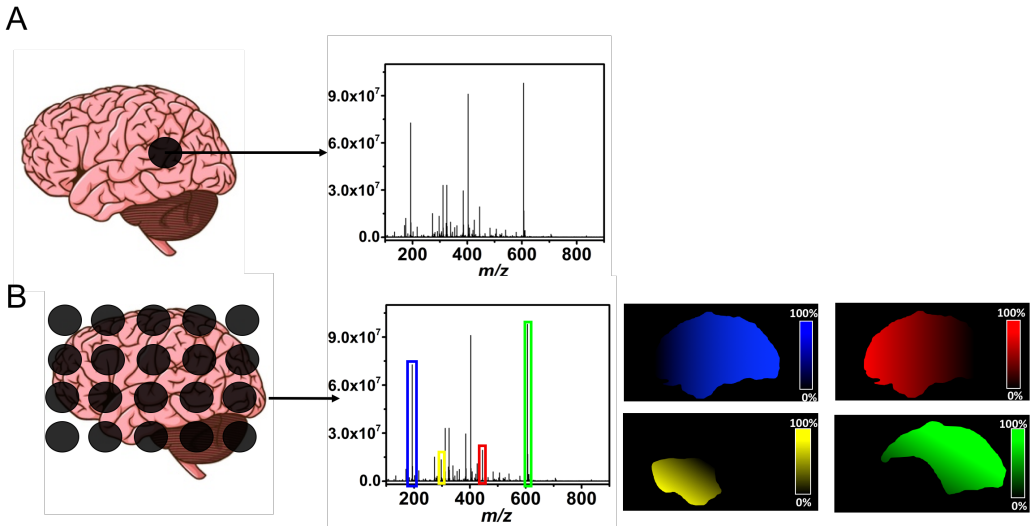

Figure 1.15. Schematic of MSI. (A) In conventional MS, ionisation, separation and detection at an individual 'pixel' on the sample produces a mass spectrum. (B) In MSI, this process is repeated at regular intervals across the sample to produce a profile spectrum, from which the distributions of various m/z values can be displayed using an ion density map.

The first publication of applying MS to understand the spatial arrangement of elements on the surfaces of biological samples employed SIMS.[43] SIMS is especially useful for MSI, as dynamic SIMS is capable of producing a three-dimensional (3D) map of the sample at high spatial resolution.[44] Alternative ionisation processes have also been applied to MSI, including DESI,[45] LESA,[46,47] and MALDI.[48] Each of the ionisation methods has unique advantages and limitations which are summarised in table 1.1.

Table 1.1. Summary table of the current MSI approaches employed within the field.

Ionisation technique	Spatial resolution	Mass range (Da)	Sample preparation	Advantages	Limitations
SIMS	50–100 nm	0–10000	N/A	High spatial resolution, minimal sample preparation	Low sensitivity, vacuum conditions, limited mass range
DESI	35–50 μm	100–250000	N/A	Ambient conditions, minimal sample preparation	Low spatial resolution, ionisation efficiency of analytes
LESA	500 μm–1 mm	500–800000	N/A	Ambient conditions, solution-based	Low spatial resolution, analyte delocalisation
MALDI	10–50 μm	100–250000	Matrix application	Increased ionization efficiency, high spatial resolution	Interference of matrix ions in spectrum, delocalisation of analytes

Whilst the spatial resolution of SIMS is the highest of all MSI techniques, the small primary beam diameter used at high resolution reduces the amount of material produced during ionisation, thus compromising its sensitivity.[49] Conversely, LESA is limited by its spatial resolution, as the diameter of the liquid micro junction determines the minimum pixel size, but its solvent-based extraction is useful for molecules with poor volatility.[50] Similarly, the solvent jet in DESI also limits its spatial resolution.[51] The primary advantage of DESI is its ambient ionisation conditions and minimal sample preparation, making it useful for application in clinical settings.[52] The requirement of a matrix in MALDI involves additional sample preparation, the application of which can cause delocalisation of soluble analytes, thus compromising the biological validity of the information obtained.[40] However, the addition of a matrix increases the number of analytes ionised, and alternative solvent-free matrix application methods have been developed to reduce this phenomenon.[53,54] Combining these MSI approaches can produce complementary spatial information for molecules covering a range of masses from *m/z* 20 to 50,000.[6] MALDI-MSI was utilised in the work presented here, so the next section will focus on the development of this technique.

1.2.1 MALDI-MSI

MALDI-MSI was first developed in 1997 to observe the distribution of peptides and small proteins across tissue samples.[55] Serial ablation of sectioned pancreatic and pituitary samples followed by ToF separation produced an ordered array of complete mass spectra contained in discrete 'pixels.' Individual *m/z* values in each spectrum were assembled to produce images showing the distribution of the proteins observed. By blotting the tissue onto a C-18 resin surface, interfering peaks and salts were removed and over 50 peptides and proteins could be tentatively identified, with on-tissue proteolysis supporting the identifications. However, the acquisition of these images required over one minute per pixel, resulting in a total analysis time of over 15 hours for an image comprising 30^2 pixels. In 1999, Stoeckli developed a new software (Mass Spectrometry Image Tool) enabling the automated acquisition of spectra and presentation of the distributions obtained, reducing the data acquisition to one second per pixel.[56] As a result of improvements in instrumentation and throughput, MALDI-MSI offers a promising tool to obtain global information on the spatial proteomic composition of samples without the requirement of labels and prior information.[57] Initial biological applications of this technique focused on the identification of tumour-specific protein markers for cancers including brain,[58,59] colon,[60] and prostate,[61] as well as markers for neurodegenerative diseases.[62,63] Through consecutive imaging of serial sections, it became possible to map the distributions of these proteins across a reconstructed 3D sample.[64]

Despite its principal use in protein analysis, MALDI has the propensity for some low molecular mass molecules to ionise through the formation of radicals, ions, or by proton transfer.[6] This enabled the simultaneous spatial analysis of a wider range of masses; from drugs and metabolites, to small proteins. MALDI with a quadrupole ion trap mass spectrometer was used in 1999 to detect pharmaceutical compounds within intact tissue.[65] Spectra were recorded at various locations of the tumour to analyse the drug's distribution, and MS fragmentation (MS/MS) was used to confirm the identity of the drug at trace levels in human ovarian tumours.[17] Simultaneously mapping the distributions of a drug and its metabolites using MALDI-MSI was first employed in 2001, whereby clozapine – an antipsychotic drug – was shown to localise to the cerebral cortex and striatum, but was absent in the corpus callosum.[6]

Later work observed a bronchodilator drug in rat lungs and used serial dilutions to produce a calibration curve for quantification.[66]

MALDI-MSI has been employed to map the distributions of drugs and proteins in a range of samples sizes, from cells[67] and tissues,[68] to whole organisms.[48] As a result of its ability to produce global, label-free spatial information, MALDI-MSI provides a promising tool for elucidating the efficacy of a drug's absorption, distribution, metabolism and excretion (ADME), and plays an important role in drug discovery.[39]

As well as its application in drug discovery, MALDI-MSI of small molecules has been applied to quantify neurotransmitters in brain sections,[69] detect drugs within hair samples,[70] identify biocontrol agents for plants diseases,[71] and classify markers for patient survival prognosis.[72] Its application to solve biological problems has significantly increased since its initial development, and MSI is regularly combined with other analytical techniques including histology markers,[73] magnetic resonance imaging,[74] and Raman spectroscopy[75] to produce complementary informative data on biological samples (figure 1.16).

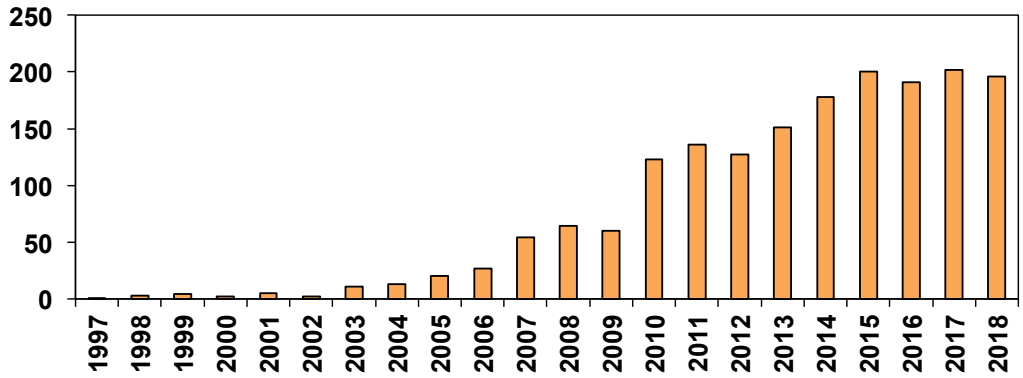

Figure 1.16. Web of Science search for articles containing the subject MALDI mass spectrometry imaging between 1997 and 2018. Data correct as of December 2018.

Since the first application of MALDI-MSI in 1997, delocalisation of molecules has been a major limitation of the technique.[55] Early MALDI imaging data produced an imaging resolution down to 50 μm, but recent publications have achieved a spatial resolution of 1.4 μm, making the reduction of delocalisation more important than ever.[42,76] The majority of delocalisation is caused by inconsistent and sub-optimal sample preparation. To ensure the biological validity of the data obtained, sample

preparation needs to be carefully considered and optimised to produce high resolution and meaningful data.[40] For this reason, reproducible sample preparation has been a focus in the development of the MALDI-MSI field.[9,40] Publications have focused on the optimisation of sectioning conditions,[77] automation of matrix application,[78–80] and sample storage conditions.[81] The next section will cover the methods utilised to prepare a tissue sample for MALDI-MSI.

1.2.1.1 Sample Preparation

Tissue sample preparation can be categorised into four stages: sample collection, processing, post-sectioning, and ionisation treatment (figure 1.17).[40] In order to produce biologically relevant results, it is imperative that the spatial distribution and abundance of molecules in biological samples remains as close to a native state as possible throughout each stage of sample preparation.[9] The failure to optimise each stage produces an amplified effect on the sensitivity, reproducibility, accuracy, and overall quality of the results obtained, thus producing a non-representative distribution or abundance of the molecules in the tissue.[40]

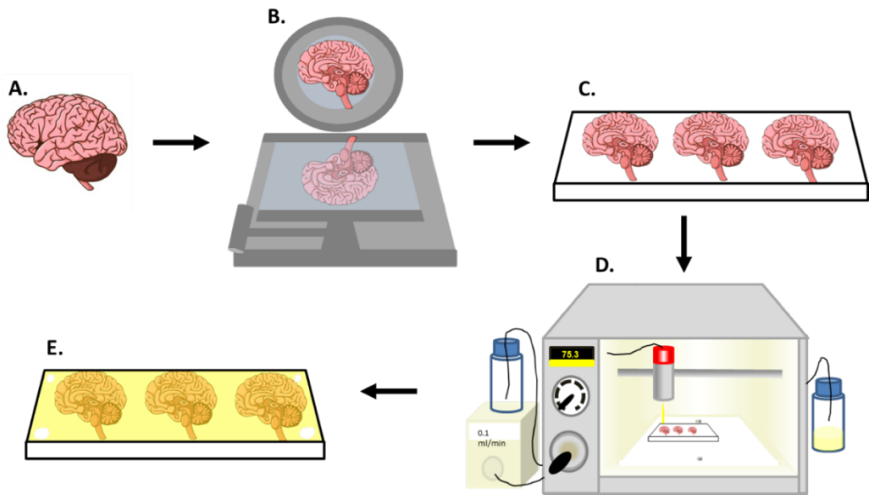

Figure 1.17. Schematic of MALDI-MSI preparation workflow for tissues. (A) The tissue or sample of interest is (B) sectioned using a cryostat and (C) thaw-mounted onto a conductive slide. (D) This slide is coated in matrix and (E) teach points are added for calibration of the area to be imaged.

1.2.1.1.1 Sample collection

As soon as a tissue sample is removed from the *in vivo* environment, a cascade of biological processes commences that will alter the abundance of important molecules within the cells.[40] Therefore, efficient and consistent collection protocols are important to prevent the rapid delocalisation and degradation of target compounds. Histological samples can be preserved using formalin fixation and paraffin embedding (FFPE), but the covalent cross-linking and degradation of some lipids limits the use of these samples for MSI.[78] Furthermore, the sample preparation for FFPE can cause delocalisation of some small molecules.[40] Alternatively, immediately freezing the sample in liquid nitrogen and storing it at -80 °C preserves the integrity of the tissue's structure and protects the biological compounds from degradation. However, once the temperature increases, the degradation and proteolytic activity will resume.[9,40] Storage of a mouse brain at sub-zero temperatures for seven months exhibited no significant lipid degradation, though there was no analysis carried out for proteins or other small molecules.[81] Moreover, it has been shown that upon returning sectioned tissue to room temperature, the abundance of low molecular weight compounds changes in a tissue-specific manner in as little as 30 seconds.[82]

Small and fragile samples are often embedded in compounds including binding agar,[55] carboxymethylcellulose (CMC),[83] ice,[48] gelatin,[84] and optimal cutting temperature (OCT).[85] However the latter can contaminate the sample because it readily ionises and causes ion suppression of less abundant species.

1.2.1.1.2 Sample processing

Once the sample is prepared, it undergoes sectioning to expose the contents of the cells.[40] Initial work used a manual microtome blade,[55] but modern cryostats ensure accurate sectioning with minimal contamination by keeping the sample frozen during this stage of the process.[9] Thicker sections are easier to manipulate, but take longer to dry and may not be electrically conductive once in the spectrometer.[9] Thinner sections increase the number of signals detected, but are difficult to manipulate and can tear easily.[77] Whilst molecules are detected as deep as 40 μm, sections are typically between 10 to 20 μm as a compromise between tissue fragility and ion abundance, as well as being approximately the diameter of a mammalian cell.[9,86]

Once a section is taken, it is mounted onto a flat, conductive surface. Early conduction plates used metal[55] or adhesive tape,[6] but the majority of work now employs conductive indium-tin oxide (ITO) coated slides.[64] Samples are most commonly transferred through thaw-mounting, whereby the slide is cooled prior to the sample being added, and once the sample is on the slide, the two are both heated simultaneously.[9] Thaw-mounting prevents the loss of water-soluble proteins, as any ice crystals produced are transferred onto the plate alongside the section, but differing levels of heating can cause inter-sample variation.[9,87]

To ensure all water is removed from the slides before matrix coating and to reduce delocalisation, the samples are often dried using a stream of nitrogen gas.[88] Some samples are washed with an organic solvent to remove the salts responsible for ion suppression, but this process affects the analyte composition and is avoided if small molecules such as drugs or metabolites are the target of interest.[40] Mounted samples are stored at -80 °C before being placed in a desiccator prior to matrix application, although this freeze-thaw cycle can result in increased analyte diffusion.[89] To reduce inter-sample variability, comparable sections are mounted on the same slide to enable normalisation and identical processing.[40]

To improve the sensitivity of detecting low abundance proteins, early studies employed sample blotting. This involves blotting the tissue sample onto specially prepared targets containing an adsorbent material.[55] This method maximises sensitivity by removing interfering lipids and salt peaks while maintaining the spatial arrangements of molecules in the sample.[55]

1.2.1.1.3 Post-sectioning processing

MALDI-MSI requires the addition of a matrix for ionisation. The principal aim of the matrix is to co-crystallise with molecules in the tissue sample and extract the analytes for ionisation.[2] Subtle changes in matrix application rate, drying times, matrix composition and thickness all affect the ionisation efficiency, the propensity to detect low abundance compounds, and the reproducibility of the results obtained.[40] The Einstein-Smoluchowski relation (equation 1.12) shows the effect of matrix application on the diffusion of molecules in the absence of convection.[86] If a matrix takes longer to dry, it has the benefit of extracting more molecules from deeper within the tissue slice, but has the disadvantage of lateral diffusion.[86]

$$\tau = d^2/2D$$

Equation 1.12

Where d is the average distance travelled by a molecule in interval τ, and D is the diffusion coefficient for a given molecule; a value that is increased by the solvent content of the matrix solution.[86]

Analyte diffusion is the major concern during matrix application, as the spatial resolution in MALDI-MSI is limited to the size of the matrix crystals.[90] Therefore, the selection of the most appropriate matrix and optimisation of its application parameters is required to obtain high quality and biologically relevant spectra directly from tissue samples.[9,40] Whilst insufficient matrix application can lead to unstable ion signals, excessive wetting augments analyte migration, altering the true biological distribution of compounds within the tissue.[65]

Matrix can be applied discretely as spots or continuously as a coating, either manually or using an automated system.[9] Early MALDI-MSI matrix application utilised airbrushes,[6] droplet spotting,[65] or even immersion,[55] however, these manual methods produced results that were inconsistent between researchers. Now, fully automated matrix application is routine and has improved inter user reproducibility.[90] Key tuning parameters are wetting, droplet size, incubation time and drying time, which together determine both the sensitivity and spatial resolution of the image obtained.

Depositing discrete spots of matrix is reproducible with minimal delocalisation, but the image resolution is limited to the size and spacing of the spots.[78,91] The matrix-solvent mixture diffuses below the tissue surface to produce signals that are more intense than those observed using continuous coatings.[86,92] Notwithstanding, due to the heterogeneity of any given tissue, adjacent spots produce varying levels of ionisation propensity, producing hotspots for detectable molecules.[78] Droplet deposition can be done using a capillary that makes contact with the sample, however there is a greater chance of cross-contamination compared to non-contact methods, as well as less control over the size and placement of each droplet.[78] Typically the volume deposited using this method is between 200–300 nL, whilst automated methods deposit significantly smaller volumes, improving the potential

resolution of the image produced.[86] Alternatively, increasing the solvent percentage decreases the droplet volume, dispensing a drier matrix with less spreading.[78] Samples can be washed with ethanol to improve the distinction between spots, but this washes off low molecular weight compounds and so cannot be used for analytes in a low mass range.[91]

Continuous application can be done in a number of ways, but can be prone to analyte delocalisation if the application is too wet.[40] The sample is held 20 to 30 cm from the nozzle of the sprayer and coated using repetitive cycles of matrix application. In each cycle, small volumes of matrix solution are deposited to produce a dense matrix coat whilst minimising the time the sample remains wet.[9] The most common manual spray techniques use an airbrush or electrospray to deposit the matrix solution directly onto the tissue.[78] Manual matrix application permits a user-defined velocity and homogeneity, but is often not reproducible.[93,94] Inadequate coverage of the tissue sample can result in unstable analyte ion signals, whereas an excessively wet application can lead to soluble analyte migration and large crystal formation.[95] Furthermore, if the temperature or the solvent concentration is too high during matrix application, the crystals will form in transit to the slide, minimising the incorporation of molecules into the crystals and thus reducing the ionisation efficiency.[9]

Automated sprayers remove the variability between users and significantly increase the number of metabolites detected by robotically controlling the temperature, flow rate, velocity of the spraying nozzle and the number of passes.[95] A number of automated systems are available, including the Bruker ImagePrep, the Shimadzu CHIP-1000, and the HTX-TM-Sprayer.[95] In order to increase access to automated matrix applications, a number of alternative cheaper methods have been developed, such as a converted inkjet printer.[79]

A combination of the two applications, known as the spray-droplet method, improved both the crystal density and homogeneity, resulting in an improved sensitivity and S/N compared to the droplet method alone.[92] The application of this method on tissue samples produced a 9.4 fold improved S/N with approximately 90 uniquely identified peaks that were not observed in the droplet method. However, the slide became wet during matrix deposition and required a five-minute interval

between each coat, which would have caused delocalisation in an imaging run with a spatial resolution below 100 µm. A large disadvantage to both the spray and spot deposition methods is the potential of blocking the capillary or nozzle as a result of solvent volatility combined with a saturated matrix concentration.[78]

An alternative 'dry' application using a 20 µm sieve to finely distribute matrix over the tissue controls both the crystal size and reduces the variability between different operators.[53] The application of this method to detect drugs in a mouse brain produced fewer signals above *m/z* 1000 than traditional 'wet' methods, but also uniquely identified marker ions that were not identified using the spray application.[88] By simplifying the sample preparation and avoiding the use of an organic solvent, there are fewer conditions to optimise.[53]

Alternatively, sublimation deposition uses a simple set up, and has been shown to produce high spatial resolution down to 10 µm, an improved lipid intensity, and a reduced laser spot-to-spot variation.[96,97] During sublimation, it is common to place the slide into a humidity chamber for 45 minutes to increase the number of signals observed at higher *m/z* values, however this can result in analyte diffusion of smaller molecules.[94]

MALDI's primary limitations are that the signal efficiency varies heavily in a tissue-dependent manner, abundant species can suppress other signals, and overlapping peaks can lead to ambiguous molecular identification.[17,18] Furthermore, tissue sections often have high concentrations of sodium and potassium ions, which can cluster with matrix ions, producing numerous peaks for each molecular species.[17]

1.2.1.2 Spatial resolution

The spatial resolution of the MSI image refers to the distance between the centre of adjacent spots.[18] The resolution of the image is a function of both the size of the crystals produced during matrix application and laser diameter.[9,40] Once the crystal size becomes smaller than the diameter of the laser, the laser beam becomes the limiting factor in imaging resolution.[9] The laser diameter is selected during experimental set-up by varying the laser spot size and step increment. Improving the spatial resolution enables more discrete localisation patterns to be observed throughout a tissue. However, since improving spatial resolution decreases the area

of tissue ionised, there is a trade-off between spatial resolution and sensitivity. Furthermore, with increasing resolution, data processing becomes more difficult as a result of the exponentially larger file sizes.[49]

Several strategies have been developed to increase the spatial resolution achievable using MALDI-MSI. Laser ablation of a sample produces a Gaussian distribution pattern, with incomplete ionisation around the outside of the pixel. Oversampling uses a raster increment smaller than the diameter of the laser beam coupled with complete matrix ablation to produce an image with a resolution smaller than the diameter of the laser (figure 1.18).[98] Alternatively, adjusting the geometry of the ionisation source can further reduce the laser size applied. For example, Spengler and co-workers reported a lateral spatial resolution of 1.4 μm on an atmospheric pressure MALDI, allowing for the visualisation of subcellular distributions of lipids, metabolites, and peptides.[76] Meanwhile, on a vacuum pressure MALDI, a spatial resolution of 5 μm has been reported.[99]

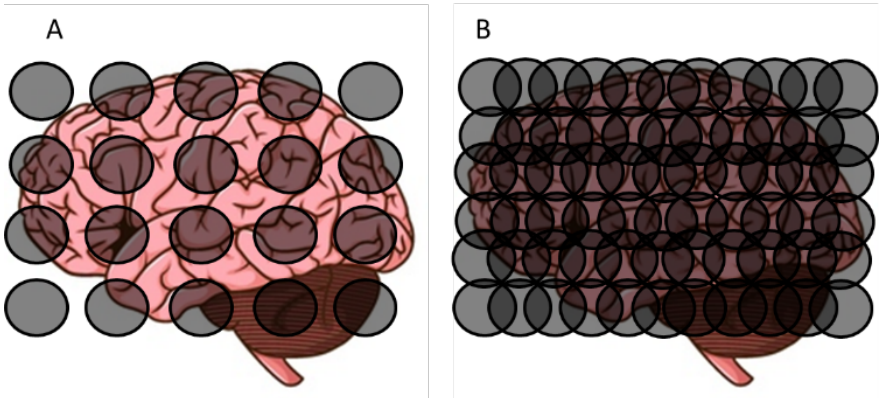

Figure 1.18. (A) Under-sampling leaves gaps between adjacent laser spots whereas (B) over-sampling produces overlapping spots that are smaller than the diameter of the laser to increase the resolution with a larger laser size.

1.2.1.3 Data analysis

Ongoing instrumental developments and improved spatial resolution are causing an exponential growth in data file sizes.[49] To address this challenge and ensure that analyses remain possible without the loss of valuable information, important advancements in software have been developed.

The most important information obtained from an imaging experiment is the visualisation of the distribution of analytes throughout the tissue. Early imaging experiments required over one minute per pixel,[55] however the development of automated software continues to effectively reduce the acquisition and processing time.[56] Each pixel of an imaging experiment contains an entire mass spectrum, so special software is required to handle the multi-dimensional information held within the datasets. FlexImaging and SCiLS are commercially available platforms, whereas the development of open access platforms such as MSiReader[100] and SpectralAnalysis[101] have widened the accessibility of MSI.

Data sizes can be reduced to simplify handling and distribution. Several compression strategies including binning mass spectra and compression based on region of interest (ROI) have been implemented to reduce the size of data while still retaining the important information.[49] Further processing of the data can be utilised to reduce experimental variance, extract relevant information, and improve the accuracy of subsequent statistical analysis.[49]

Manual analysis involves selecting an *m/z* value unique to the ROI and generating an image of its distribution. However, a number of software programmes are capable of further analysis, including colocalisation analyses, spatial segmentation, and classification model calculations.[101] Statistical analyses can be applied to determine differences that exist between regions within a sample or between two samples. One example of this is principal component analysis (PCA), which reduces the dimensionality of the data set by plotting the two components that cause the greatest variation on the x and y-axis to induce groupings of related pixels in the data sets.[102] It can also be used to remove noise and any signals which are poorly connected with variability between groups.[101] Alternatively, partial least-squares (PLS) regression is similar to PCA, but classes of data are annotated with known labels.

Data storage and sharing of the final results across laboratories is important for the standardisation of MSI as a technique. Imaging depositories such as METASPACE[103] are being developed to enable inter-laboratory comparison of results.

1.2.1.4 Quantification

The signal intensity of an ion irradiated from any point is assumed to be proportional to the concentration of the target analyte.[6,104] However, this view is over simplistic, as heterogeneity across a tissue influences the ionisation efficiency of the analytes.[83,105] The comparison of relative ion intensities using the 2D ion density maps can be utilised as a semi-quantitative tool. However, this provides a relative intensity and not an absolute quantification, thus MSI is currently considered a qualitative technique.[106] Notwithstanding, the correct procedure, processing, and software enables quantitative information to be extracted, although the degree of accuracy remains under close scrutiny.

Normalisation can be used to rationalise the signal intensity and enable some sort of quantification of the compound of interest.[105] Total ion count (TIC) normalisation is commonly applied to convert the spectra into the same intensity ranges and to compare the intensities of different ions. This process is based on the assumption that there is a comparable number of signals in each spectrum, and ensures that all spectra have the same integrated area.[107] Alternatively, normalisation can be completed using: endogenous molecules that are consistently expressed throughout the whole tissue, an external standard applied during matrix application, or reporter ions.[108] In the latter case, when the standard is ionised by the laser, it fragments into distinct reporter ions; the ratios of which are compared to other molecules to calculate their relative abundance.[109]

Whilst relative quantification is useful, calculating the true concentration of a molecule is highly desirable for drug distribution studies. However, as a result of sample heterogeneity and ion suppression, using an external spotted calibration curve adjacent to the sample yields inaccurate concentrations. Alternatively, an on-tissue calibration curve can be used to calculate the tissue-specific ionisation efficiency, and each signal intensity can be scaled to compensate for suppression (figure 1.19).[66,83,105] Other work has utilised a labelled form of the compound of interest; either using a compound with similar ionisation properties,[91] or a deuterated standard combined with matrix.[54]

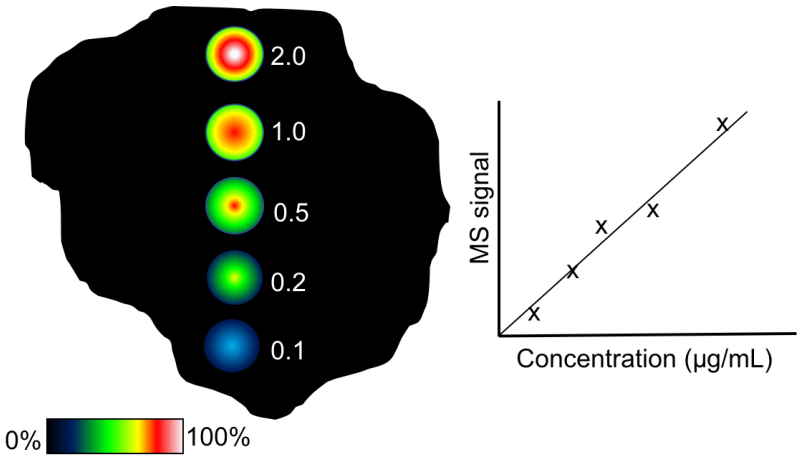

Figure 1.19. Representative diagram showing how a serial dilution of a drug or standard can be placed onto the tissue of interest to create a calibration curve. Using this curve, the intensity of the compound can be compared and quantified.

1.3 Three-dimensional cell culture

Currently, more than half of all drugs fail in Phase II and Phase III clinical trials.[110] One of the most promising areas expected to improve the success rates in drug development is the availability of new preclinical models that better recapitulate *in vivo* biology and microenvironmental factors. Conventionally, initial drug development is tested on cells grown in two-dimensional (2D) culture under carefully controlled conditions with supplemented medium to aid growth.[111] Whilst these homogeneous conditions provide effective experimental consistency, *in vivo* tissue microenvironments are not typically composed of a homogenous cell population, but are complex structures with intricate relationships.[112,113] 3D cell culture combines the simplicity of cell culture systems with the interplay of factors resembling the multifaceted physiology of tissues *in vivo*.[84,114] Unlike conventional culture formats, 3D cell culture is capable of mimicking the various cell-cell and cell-matrix interactions that make up the complex architecture *in vivo*.[112,115]

A number of cancer cell lines form microscale spherical cell clusters, known as multicellular tumour spheroids (MTS), which self-assemble spontaneously in the absence of attachment to another surface.[113,116] The layered structure of MTS commonly exhibits an increased resistance to radiotherapy and drug treatments, making them an effective *ex vivo* model of cancer, and useful in the development of potential treatments.[117]

1.3.1 Spheroid formation

A number of methods are available for MTS generation, including using either spinner flasks or rotary vessels to prevent the cells settling. Spheroids produced using these methods vary in size and rely on specialist equipment.[115] An alternative, more labour intensive method relies on gravity to induce the formation of uniformly sized aggregates from a suspension of cells, known as the hanging drop method.[115] Developed by Kelm et al, this method involves the placement of an aliquot of cell suspension onto the lid of a petri dish. The lid is subsequently inverted, and the droplet is held in place by surface tension.[118] By varying the number of cells seeded into the droplet, the size of the spheroid produced can be varied up to a diameter of approximately 1 mm.[111] Cells accumulate at the liquid-air interface and proliferate to produce highly organised, tissue-like spheroids with their own extracellular matrix (ECM) (figure 1.20).[119] However, the volume of the drop is the limiting factor with this method, as above 50 µL the surface tension no longer holds the drop in place.[118]

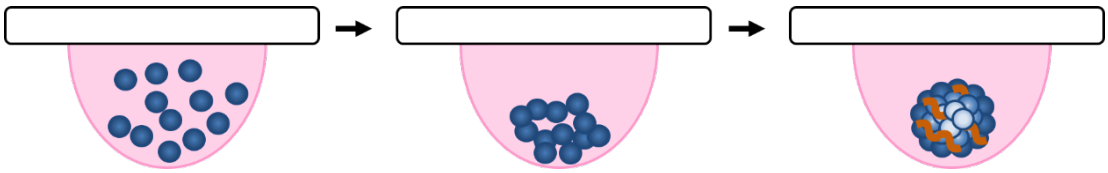

Figure 1.20. Formation of spheroids using the hanging drop method. The lack of interactions between the cells and a surface causes the cells attach to one another and produce a spheroid.

The formation of spheroids is a three-staged process (figure 1.21). Initially, cell-surface integrins and long-chain ECM fibres with multiple arginine-glycine-aspartate (RGD)-containing binding sites organise cells into loose aggregates with high permeability.[120] Subsequently, there is a delay phase during which cadherin expression is upregulated to increase the intercellular interactions, after which homophilic cadherin-cadherin interactions augment cell cohesion between two adjacent cells.[121] In some cell lines, the outer compacted cells then differentiate into smooth tightly packed, polarised cells.[120] Whilst the process remains relatively conserved across spheroids, the ECM fibres and cadherins vary between cell types.[120]

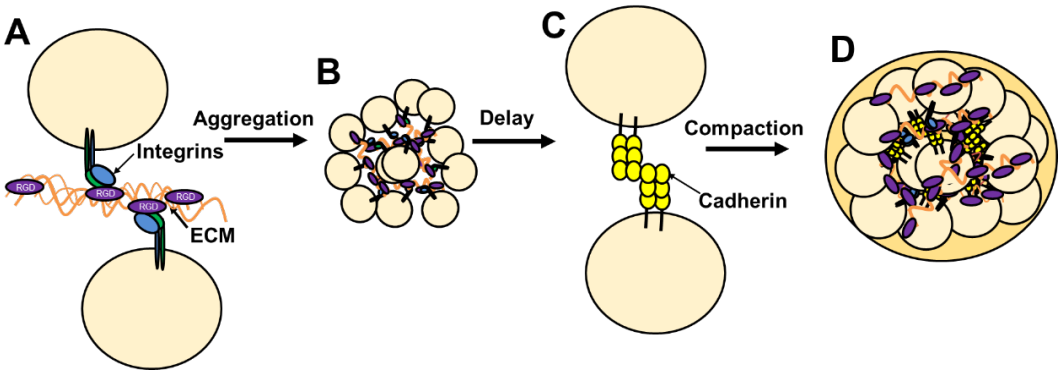

Figure 1.21. Formation of spheroids. (A) Integrins bind to ECM via RGD binding motifs producing (B) loose aggregates with high permeability. After a delay period, upregulated cadherin expression leads to (C) homophilic cadherin binding and subsequent compaction. This produces (D) differentiated and polarised outer cells.

Each cell line reacts differently when cultured using the same method, and not all cell lines are capable of producing spheroids.[111] Furthermore, the MTS currently available omit the vascularisation aspect of tumour development, which is a hugely significant part of tumorigenesis.[111] Co-culturing multiple cell-types and incorporating cultivation methods that enable the angiogenesis process could more accurately mimic tumours and provide a better representation of the *in vivo* environment.[115]

1.3.2 MTS structure

Due to the rapid proliferative properties and poor vasculature observed in tumours, cells furthest from the blood supply experience gradients of oxygen, nutrients, and waste.[122] Similarly, with a radius greater than *ca.* 200 μm, MTS display these same diffusional limits. Above this threshold, the centre of the spheroid experiences hypoxic conditions and forms a concentric three-layered structure (figure 1.22).[84,115] At the centre is a necrotic core, surrounded by a layer of quiescent cells, and at the spheroid periphery is a rim of proliferating cells.[84,116] The thickness of each layer is dependent on the cell type and the growth conditions. For example, increasing the concentration of oxygen and glucose increases the thickness of the outer proliferating layer.[123,124] It has also been suggested that the central hypoxic cells can adapt their metabolism to the environment and maintain intracellular homeostasis until shortly before cell death. With an increasing size, Freyer and co-workers found that the levels of high-energy phosphates and intracellular pH remained constant,

suggesting that the quiescent cells adapt their metabolism under the environmental conditions until the point of cell death.[125]

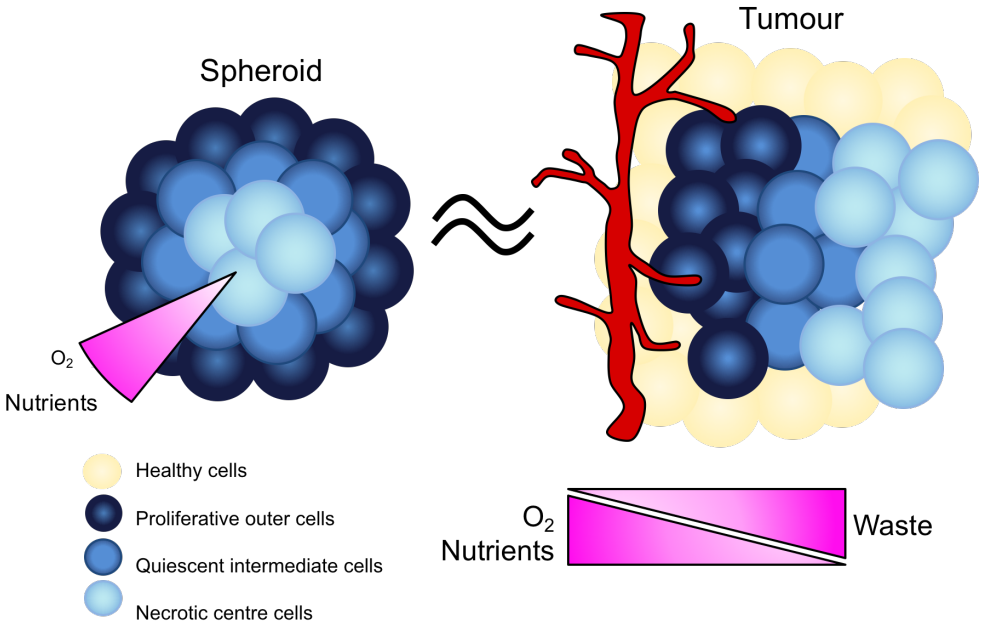

Figure 1.22. Spheroids experience a three-layered structure. At the centre is a necrotic core, surrounded by a layer of quiescent cells. At the periphery, the cells have access to oxygen and nutrients, so can rapidly divide.

The primary limitation of MTS is their upper size limit of 1 mm, limiting the range of tumour sizes that can be investigated. Tumour explants have been developed that bypass the current size limitations of some small-growing spheroids, and are useful for cancer cell lines which do not form spheroids.[126] Additionally, the development of organoids has the potential to provide a more accurate model than current spheroids. Organoids are self-organising, self-renewing 3D cell cultures derived from primary tissue, embryonic stem cells, or induced pluripotent stem cells.[127] Organoid cultures have a similar functionality to the tissue from which the cells originate, and have been described for normal and disease models of the digestive tract, prostate, lung, kidney, and brain.[127,128]

1.4 MSI of MTS

Early investigations of the structure of MTS employed serial trypsinisation and subsequent LC-MS/MS for identification of each spheroid layer.[129] More recently,

imaging techniques such as confocal Raman microscopy (CRM)[75] and MSI[84] have been utilised. MSI was first applied to MTS in 2011 to examine the distribution of biological molecules in human carcinoma (HCT-116) spheroids.[84] There are now a total of 20 papers published including the subject 'MALDI mass spectrometry imaging' and 'spheroids;' with the number of publications steadily increasing over the last four years (figure 1.23).

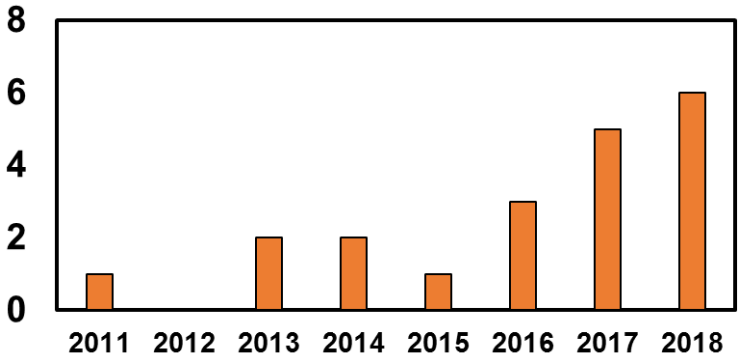

Figure 1.23. Web of science search of subjects containing MALDI mass spectrometry imaging and spheroids over the past 10 years. A total of 20 publications have been produced. Data correct as of January 2019.

In 2011, Li and co-workers developed a method for MALDI-MSI of MTS to observe how the cellular proteome responded to the formation of these molecular gradients.[84] They observed the distribution of a limited number of intact proteins which localised to the central necrotic region. To complement this MSI study, nano liquid chromatography (LC) MS/MS was used to identify cytochrome C and histone H4, both of which distributed uniformly across the spheroid.[84] Later work applied multivariate statistical analyses including PCA, *k* means clustering and linear discriminant analysis (LDA) to visualise the differences in protein expression levels across HCT-116 MTS.[130] They were able to identify a number of *m/z* values that uniquely localised to the central hypoxic and proliferative outer regions, however the values were not identified.

As well as elucidating how the proteome is affected by gradients of oxygen and waste, MSI has been used to characterise the endogenous lipids in HCT-116 spheroids, and compare these distributions to both monolayer culture and tumour tissue.[131] Using MALDI-ToF in both positive and negative mode, Hiraide and co-

workers identified an arachidonic-containing phosphatidylinositol that localised to the periphery of the spheroids and at the stromal interface of the tumour. However, the lipid species was absent in the monolayer culture, suggesting that 3D cell culture provides a more accurate model for tumour biology.[131]

MALDI-MSI of MTS is most commonly employed for observing the time-dependent penetration of drugs as an *ex vivo* model of cancer.[38] This application was first developed in 2013 whereby HCT-116 spheroids were sectioned at 60 µm intervals and MSI was used to observe the time-dependent penetration of the chemotherapeutic drug irinotecan and its metabolites at 75 µm resolution.[132] Irinotecan was shown to distribute evenly across the spheroid after 24 hours, and using LC-MS/MS, 10 metabolites were observed after 72 hours of incubation.[132] This work was later repeated on patient-derived colorectal tumour organoids (CTOs) to predict the therapeutic response of individual patients.[133] Unlike in the homogenously populated HCT-116 spheroids, the heterogeneous CTOs showed that the active metabolite had a localisation unique from the parent drug and inactive metabolites.

However, the static dosing method employed in these drug penetration studies involves a single exchange of media at the beginning of the time course. This method provides a poor mimic of *in vivo* drug studies as it lacks the flow component of nutrients and waste products. LaBonia employed a 3D printed fluidic device to dynamically dose HCT-116 spheroids with irinotecan over 24 hours. They identified that whilst irinotecan distributed throughout the spheroid, its active metabolite was localised to the outer rim of proliferating cells.[134] From these results, they suggested that dynamic dosing gives a more realistic representation of the ADME of an *in vivo* system because it allows for nutrient exchange and the diffusion of toxic metabolites and waste products away from the spheroid.[134]

Whilst irinotecan has been widely used for drug studies in MTS, other drugs have been investigated, including comparing the distribution of liposomal-encased doxorubicin and free doxorubicin over 72 hours of treatment.[135] Both forms of the chemotherapeutic drug distributed throughout the HCT-116 spheroid after 12 hours of treatment, suggesting that liposomal encasement did not severely affect the rate of drug diffusion into spheroids. However, the free drug was at its highest intensity in

the outer region of the cells after six hours compared to 12 hours in the liposomal time course. This delay in permeation of the encased drug was proposed to have been caused by the time it took to bind the liposome to the lipid bilayer and release the drug into the cells.

A number of drugs are not detectable by MALDI, and so derivatisation can be used to improve the sensitivity of the analysis. In 2016, colorectal spheroids were dosed with the platinum-based anti-cancer drug oxaliplatin and imaged using MALDI-ToF MSI.[136] The derivatisation reagent diethyldithiocarbamate (DDTC) was incubated with the sectioned spheroids to extract and chelate the platinum to form a dimer or a trimer, which is detectable by MALDI-ToF. In the absence of DDTC, they identified the presence of an inactive metabolite but were unable to detect the parent drug. However, with derivatisation they identified that after 90 minutes exposure, oxaliplatin is present in the outer and intermediate regions of the MTS, suggesting the necrotic core has limited penetration. Furthermore, they identified that a reaction with methionine produces an inactive metabolite in the necrotic core.

MALDI-MSI has been combined with other proteomic analysis methods to obtain complementary information about MTS. This has been used to further elucidate the structure of MTS,[75] and examine the effects of therapeutic drugs on post-translational modifications[129] and the proteome.[137]

MSI and CRM were used to obtain complementary information on the layered structure of MTS.[75] CRM revealed differences in cellular integrity and protein secretion, whilst MSI was used to observe the distributions of small molecules. Using these techniques, Ahlf and co-workers employed PCA to identify the most chemically informative elements and suggested that these primarily localised to the necrotic core of the HCT-116 spheroids.

Feist et al analysed HCT-116 spheroids by both MSI and nanoLC-MS/MS to observe the epigenetic response to UNC1999; a drug that inhibits the methylation of histone H3 lysine 27 (H3K27).[129] After 72 hours, MSI showed that UNC1999 distributed throughout the spheroid and serial trypsinisation followed by nanoLC-MS/MS on a parallel spheroid identified and quantified 258 differentially modified histone peptides. This included a reduction of methylated H3K27, which caused a decreased diameter of the MTS. Furthermore, most of the epigenetic and proteomic

changes observed were localised to the outer and intermediate regions, consistent with the concept that the central necrotic core has reduced enzymatic activity.

MSI is currently a qualitative tool, however quantification can be completed using complementary information from isobaric tag for relative and absolute quantitation (iTRAQ). iTRAQ records reporter ion intensities for each peptide via MS/MS. This method allows for protein identification along with fold-change quantification between samples. This technique was used in conjunction with MSI to evaluate the synergistic effects of chemotherapy in tandem with glucose restriction and autophagy inhibition in HCT-116 spheroids.[138] MALDI ToF MSI showed that the chemotherapeutic compound (irinotecan) and the autophagy inhibition compound (chloroquine) distributed uniformly throughout the spheroid under both normal and nutrient-restricted conditions. Using iTRAQ, significant changes to proteins involved in autophagy and metabolism were quantified, as well as an upregulation of various tumour suppression proteins. Furthermore, when glucose restriction was combined with autophagy inhibition and chemotherapy, all of the phenotypic results were intensified, suggesting that chemotherapy in combination with nutrient restriction is more effective than chemotherapy alone.

Later work employed a similar method to observe the distribution of a combination of chemotherapy drugs using dynamic dosing. Folinic acid, 5-fluorouracil, and irinotecan (FOLFIRI) were dynamically dosed over 24 hours, and iTRAQ was used to quantify the proteomic changes.[137] After 24 hours, folinic acid and irinotecan were localised to the necrotic core, however the active metabolite of folinic acid localised to the outer proliferative region. 5-fluorouracil was not detectable by MS. Using iTRAQ, over 5400 proteins were identified and quantified. After 24 hours, 171 unique proteins with roles in histone regulation and protein synthesis were differentially regulated with a fold change of more than two, and 269 proteins after 48 hours. The Eukaryotic Initiation Factor 2 (eIF2) signalling pathway was the most significantly downregulated pathway, including several ribosomal proteins with roles in the initiation of mRNA translation, suggesting protein synthesis was significantly affected.

Chapter 2.

Project aims

2.1 Project aims

When MTS are grown to a radius greater than 200 μm, they display gradients of oxygen, nutrients, and waste. These gradients produce a three-layered structure comprised of a necrotic centre, an intermediate quiescent region, and an outer layer of rapidly proliferating cells. MALDI-MSI provides a global untargeted approach for investigating how these gradients influence the proteome and metabolome across the spheroid. This project aims to use high spatial resolution MALDI-MSI to elucidate the biological environments within MTS.

The most widely employed protocol for MALDI-MSI of MTS was developed by the Hummon group in 2011. Using agarose-coated well plates, human carcinoma (HCT-116) spheroids were grown to diameters of approximately 1 mm over 14–20 days. For imaging, gelatin was used to embed up to six spheroids in a well of a 24-well microtiter plate. Sectioning of the gelatin block produced up to 16 spheroid sections per slide. This project aims to optimise a method for MALDI-MSI of breast cancer (MCF-7) and prostate cancer (PC3) spheroids grown using the hanging drop method to a diameter of approximately 500 μm. By exploring the use of different embedding procedures, this project aims to simplify sample preparation and increase the number of sections that can be mounted onto a slide.

The high spectral resolution of FT-ICR MS affords sufficient mass accuracy and resolution to assign elemental formulae from accurate mass measurements. Therefore, MALDI MS FT-ICR MS in positive and negative polarities will be used to compile comprehensive lists of tentative metabolite assignments with sub-ppm errors.

The oxygen, nutrient, and waste gradients experienced across MTS result in the formation of various microenvironments. Using a targeted MSI approach, this project will use metabolite markers to indicate regions of increased oxidative stress and hypoxia within the spheroid. Furthermore, to investigate how the various spheroid microenvironments affect the regional flux through specific metabolic branch pathways, untargeted discriminatory analysis will be performed to observe metabolites that colocalise to these regions.

Pimonidazole is a widely used immunohistochemical marker of hypoxia. MALDI-MSI has been employed to observe the distribution of pimonidazole within tumours, and

a number of its metabolites have been found to colocalise with regions of hypoxia. This project aims to use MALDI-MSI to observe the localisation of pimonidazole and its metabolites within MTS. By treating spheroids with pimonidazole over a time course, MALDI-MSI will be used to simultaneously observe the distribution of the parent drug and its metabolites at high spatial and spectral resolution.

Commercially available matrix application platforms are expensive, limiting the accessibility into the MALDI-MSI field. Alternative options have been developed, including an inkjet printer, but this is prone to blockage and regularly needs replacing. This project aims to use a 3D printer and components regularly found in an analytical chemistry laboratory to develop a cheaper alternative for matrix application. Using rhodamine B microarrays and fluorescence scanning, various matrix application conditions will be tested, and the optimised parameters will be identified. Using MALDI-MSI, the optimised conditions can be compared to the commercially available application devices.

Chapter 3.

Materials and methods

3.1 Reagents

Human breast cancer cell line (MCF-7) at passage 52 were obtained in 1 mL aliquots from the Queen's Medical Research Institute (University of Edinburgh, Little France, EH16 4UU) and stored in liquid nitrogen. Human prostate cancer cell line (PC3) (20 µL) was purchased at passage 6 from Sigma-Aldrich. Phosphate buffered saline (PBS) was acquired from Thermo-Fisher Scientific. For cell culture, Roswell Park Memorial Institute (RPMI) medium (Thermo-Fisher) or Dulbecco Modified Eagle's Medium (DMEM) (Thermo-Fisher) was supplemented with fetal bovine serum (FBS) (Sigma-Aldrich) and penicillin (Thermo-Fisher). Trypsin was acquired from Sigma-Aldrich. Dimethyl sulfoxide (DMSO) (Sigma-Aldrich) was used to solubilise pimonidazole (Sigma-Aldrich). ITO-coated slides were purchased directly from Bruker (Bremen, Germany). Trifluoroacetic acid (TFA), CHCA, DHB and 9AA for the imaging data were purchased from Sigma-Aldrich. HPLC-grade solvents were provided by Sigma-Aldrich. Haematoxylin, eosin and acid alcohol for histological staining were purchased from Sigma-Aldrich.

3.2 Cell culture

3.2.1 MCF-7 cells

Both monolayer cells and spheroids were grown in DMEM media supplemented with FBS (10% v/v) and Penicillin-Streptomycin (10000 units penicillin/mL, 10 mg streptomycin/mL, 3 mL). Monolayer cells were routinely seeded every four days at approximately 80% confluence in a 75 cm^3 flask. For seeding the cells, the media was poured off, cells were washed twice with PBS (10 mL) and incubated with trypsin (5 minutes). Supplemented media (10 mL) was added to arrest trypsin activity, and the contents of the flask was transferred into a falcon tube (50 mL) and centrifuged (2.0 rpm, 4 minutes). The media was poured off and the cells re-suspended in fresh supplemented DMEM media (10 mL). Re-suspended cells (2 mL) were placed into a new 75 cm^3 flask with fresh supplemented DMEM media (8 mL). The media was replaced every 48 hours.

3.2.2 PC3 cells

Both monolayer cells and spheroids were grown in RPMI media supplemented with FBS (10% v/v) and Penicillin-Streptomycin (10000 units penicillin/mL, 10 mg

streptomycin/mL, 3 mL). Monolayer cells were routinely seeded every four days at approximately 80% confluence in a 75 cm^3 flask. The process of seeding is the same as section 3.2.1. The media was replaced every 48 hours.

3.2.3 Spheroid preparation

Spheroids were obtained using the hanging drop method.[139] Approximately 6000 cells were seeded into droplets (20 µL) that were then suspended from the lid of a petri dish. A reservoir of fresh media (10 mL) was placed in the bottom of the dish. Media (15 µL) was removed and fresh media (15 µL) was added every 72 hours. Spheroids were incubated at 36.5 °C, 5% CO_2 and 95% humidity for up to 14 days before imaging.

3.2.3.1 Spheroid dosing with pimonidazole

For dosing the spheroids, media (15 µL) was removed from the droplets. For control spheroids, fresh supplemented RPMI media (20 µL) was added for the equivalent time course. For the dosed spheroids, a stock of pimonidazole (4 mM) in DMSO was diluted into fresh supplemented media to a final concentration of 200 µM and was added to the spheroids (20 µL). Spheroids were then incubated under the same conditions as previously stated for various time points over 24 hours.

3.3 MSI sample preparation

3.3.1 Embedding

Media (20 µL) was removed, and spheroids were washed with ammonium formate (20 µL, 50 mM). Each spheroid was picked up using a 100 µL pipette and placed into a droplet from which the maximum amount of liquid was removed. To aid spheroid detection during sectioning, gelatin (3 mL, 17.5% (w/v)) was prepared using blue food colouring (2.5 mL water, 0.5 mL Sainsbury's food colouring) at 37.5 °C using a heated stirrer plate. 20 µL was initially placed onto the spheroids using a P100 pipette. A second layer (20 µL) was added, and the gelatin-embedded spheroids were frozen on isopentane and dry ice (-78 °C, 2 minutes). The gelatin blocks were then snap frozen in liquid nitrogen and stored (-80 °C) until sectioning.

3.3.2 Sectioning

Sectioning was performed using a cryostat (-21 ºC) (Leica CM 1900 (Leica Biosystems, Nussloch, Germany). Water (*ca.* 1.5 mL) was frozen onto a chuck (3 minutes) and faced off to provide a flat surface. Then, gelatin-embedded spheroids were frozen onto the chuck using water (*ca.* 500 µL, 30 seconds). Sections (15 µm) were cut and thaw mounted onto conductive ITO-coated glass slides. Consecutive sections were taken for haematoxylin and eosin (HE) staining (see section 3.3.4). The slides were then placed into a slide adapter and the image scanned (4800 dpi).

3.3.3 Matrix application

3.3.3.1 CHCA

For matrix application of CHCA (5 mg/mL, 70% acetonitrile (ACN), 0.1% TFA) a TM-sprayer™ (HTX Technologies, LLC, NC, USA) was used to apply eight coats of matrix at a flow rate of 0.1 mL/minute at 80 °C with a gas pressure of 10 psi and a velocity of 1100 mm/minute. These parameters took approximately 20 minutes to coat a slide and resulted in a matrix density of 0.22 mg/cm^2.

3.3.3.2 DHB

For matrix application of DHB (10 mg/mL, 80% ACN), a TM-sprayer™ was used to apply eight coats of matrix at a flow rate of 0.1 mL/minute at 80 °C with a gas pressure of 10 psi and a velocity of 1100 mm/minute. These parameters took approximately 20 minutes to coat a slide and resulted in a matrix density of 0.15 mg/cm^2.

3.3.3.3 9AA

For matrix application of 9AA (5 mg/mL 70% ACN), a TM-sprayer™ was used to apply eight coats of matrix at a flow rate of 0.1 mL/minute at 80 °C with a gas pressure of 10 psi and a velocity of 1100 mm/minute. These parameters took approximately 20 minutes to coat a slide and resulted in a matrix area density of 0.11 mg/cm^2.

9AA matrix was also applied using a converted 3D printer. The optimised conditions consisted of eight coats of matrix (5 mg/mL, 70% ACN) at a flow rate of 0.1

mL/minute at 40 °C with a gas pressure of 50 psi and a z height of 30 mm. The velocity was set within the G-code as F1000, which resulted in a velocity of 1100 mm/minute. These parameters took approximately 15 minutes to coat a slide and resulted in a matrix area density of 0.11 mg/cm^2 (for further details, see chapter 7).

3.3.4 H&E staining

Alternate spheroid sections were thaw-mounted onto a glass slide and stored in a vacuum desiccator (room temperature, 18 hours). Sections were covered with haematoxylin (3 minutes) and washed with running water. The slide was coated with tap water (1 minute), then acid alcohol (20 seconds) and then washed using water. Eosin was added (1 minute) and then washed with water. The stained cells were then air dried before being imaged under the 40x objective on an inverted AE2000 (Motic, Hong Kong) microscope.

3.4 MALDI MS

3.4.1 Steel plate MALDI MS

For MALDI MS of pimonidazole, the UltraFlex MS equipped with a MALDI ionisation source (Bruker Daltonics) was used. Mass spectra were acquired in reflectron positive-ion mode with 500 laser shots per spot. Spectra were acquired across a mass range of *m/z* 100–1000 using a laser spot size of 35 µm with a SmartWalk raster of 50 µm. A sampling frequency of 2 kHz was used, and the laser intensity was set at 65% for CHCA and 47% for DHB. 100 µM pimonidazole was mixed with either DHB (70% ACN, 0.1% TFA) or CHCA (50% ACN, 0.1% TFA) and 15 spectra were averaged. Calibration was carried out using red phosphorus.

3.4.2 MALDI MS of spheroids

For MALDI MS analysis, a 12T SolariX FT-ICR MS equipped with an infinity ICR cell and a MALDI ionisation SmartBeam II UV laser (Bruker Daltonics, Bremen, Germany) was used. Spectra were acquired in positive-ion mode (using CHCA and DHB matrices) and negative-ion mode (using DHB and 9AA matrices). Typically, an *m/z* range of 98-1500 was acquired in broadband mode with a Time Domain for Acquisition of 2 MWord. 300 shots were accumulated across 20 scans with 15%, 9%, and 7% laser power for CHCA, 9AA, and DHB matrices respectively.

3.4.2.1 Accurate mass assignment

The resulting mass spectra were internally calibrated using five known species for each matrix and confirmed using the DataAnalysis SmartFormula tool (tables 3.1 – 3.4). A mass list for each matrix was produced using FTMS peak detection with a S/N > 3 in DataAnalysis 4.4. The calibrated *m/z* values were then identified using the Human Metabolome Database (HMDB) using an error tolerance of 1 ppm (http://www.hmdb.ca/spectra/ms/search) and LipidMaps using an error tolerance of 0.001 *m/z* (http://www.lipidmaps.org/tools/ms/lm_mass_form.php). This was subsequently manually filtered to errors within 1 ppm. For positive-ion mode, formulae were assigned with the adducts $[M+H]^+$, $[M+Na]^+$ and $[M+K]^+$. For negative-ion mode, formulae were assigned with the adducts $[M-H]^-$, $[M+Na-2H]^-$ and $[M+K-2H]^-$.

Table 3.1. Calibration list for CHCA in positive mode.

m/z	**Neutral formula**	**Adduct**
190.04987	$C_{10}H_7NO_3$	$[M+H]^+$
379.09246	$C_{10}H_7NO_3$	$[2M+H]^+$
666.48330	$C_{36}H_{70}NO_6P$	$[M+Na]^+$
725.55680	$C_{39}H_{79}N_2O_6P$	$[M+Na]^+$
851.64028	$C_{47}H_{93}N_2O_6P$	$[M+K]^+$

Table 3.2. Calibration list for DHB in positive mode.

m/z	**Neutral formula**	**Adduct**
155.03389	$C_7H_6O_4$	$[M+H]^+$
283.01894	$C_6H_{13}O_9P$	$[M+Na]^+$
348.07036	$C_{10}H_{14}N_5O_7P$	$[M+H]^+$
428.03669	$C_{10}H_{15}N_5O_{10}P_2$	$[M+H]^+$
703.57485	$C_{39}H_{79}N_2O_6P$	$[M+H]^+$

Table 3.3. Calibration list for DHB in negative mode.

m/z	Neutral formula	Adduct
153.01933	$C_7H_6O_4$	$[M-H]^-$
241.01188	$C_6H_{11}O_8P$	$[M-H]^-$
402.99492	$C_9H_{14}N_2O_{12}P_2$	$[M-H]^-$
505.98847	$C_{10}H_{16}N_5O_{13}P_3$	$[M-H]^-$
834.52906	$C_{46}H_{78}NO_{10}P$	$[M-H]^-$

Table 3.4. Calibration list for 9AA in negative mode.

m/z	Neutral formula	Adduct
193.07712	$C_{13}H_{10}N_2$	$[M-H]^-$
346.05581	$C_{10}H_{14}N_5O_7P$	$[M-H]^-$
426.02214	$C_{10}H_{15}N_5O_{10}P_2$	$[M-H]^-$
611.14469	$C_{20}H_{32}N_6O_{12}S_2$	$[M-H]^-$
885.549985	$C_{47}H_{83}O_{13}P$	$[M-H]^-$

3.4.3 Continual accumulation of selected ions (CASI)

CASI was used for negative mode MS with a CASI window of *m/z* 30 and a Q1 mass of *m/z* 506, 426 and 346 for adenosine triphosphate (**ATP**), adenosine diphosphate (**ADP**), and adenosine monophosphate (**AMP**) respectively. 300 shots were accumulated across 20 scans using the 12T SolariX FT-ICR MS in negative-ion mode with a 7% laser power. A Time Domain for Acquisition of 2 MWord and an ICR transient length of 0.5 seconds in broadband mode was used.

For MS of pimonidazole, a Q1 mass of *m/z* 240 and an isolation window of *m/z* 40 was used. 300 shots were accumulated across 20 scans in positive-ion mode with 15% laser power, an ICR transient length of 0.5 seconds, and a Time Domain for Acquisition of 2 MWord.

3.5 MALDI-MSI

3.5.1 ToF MSI

ToF MSI experiments were performed on an UltraFlex MS equipped with a MALDI ionisation source (Bruker Daltonics, Germany). Mass spectra were acquired in

reflectron positive-ion mode with 500 laser shots per spot. Mass spectra were acquired in a mass range of *m/z* 100–1000 using a laser spot size of 35 µm and a SmartWalk raster of 50 µm. A sampling frequency of 2 kHz was used, and the laser intensity was set at 65% for CHCA and 47% for DHB. Quadratic calibration was completed prior to the imaging run using red phosphorus and resulting images were further calibrated using internal DHB and CHCA matrix peaks (tables 3.5 and 3.6). Images were processed with FlexImaging 4.1 and SCiLS version 2019a (Bruker Daltonics, Bremen, Germany) with TIC normalisation to generate ion maps.

Table 3.5. DHB calibration list for ToF data.

m/z	**Neutral formula**	**Adduct**
137.02332	$C_7H_4O_3$	$[M+H]^+$
155.03389	$C_7H_6O_4$	$[M+H]^+$
273.03936	$C_{14}H_8O_6$	$[M+H]^+$
409.05541	$C_{21}H_{12}O_9$	$[M+H]^+$
545.07145	$C_{28}H_{16}O_{12}$	$[M+H]^+$
681.08750	$C_{35}H_{20}O_{15}$	$[M+H]^+$
817.10354	$C_{42}H_{24}O_{18}$	$[M+H]^+$

Table 3.6. CHCA calibration list for ToF data.

m/z	**Neutral formula**	**Adduct**
190.04987	$C_{10}H_7NO_3$	$[M+H]^+$
379.09246	$C_{10}H_7NO_3$	$[2M+H]^+$
401.07441	$C_{10}H_7NO_3$	$[2M+Na]^+$
417.04834	$C_{10}H_7NO_3$	$[2M+K]^+$
568.13506	$C_{10}H_7NO_3$	$[3M+H]^+$

3.5.2 FT-ICR MSI

FT-ICR experiments were performed on a 12T SolariX FT-ICR MS equipped with an infinity ICR cell and a MALDI SmartBeam II UV laser (Bruker Daltonics, Bremen, Germany). Spectra were acquired in positive-ion mode (using CHCA and DHB matrices) and negative-ion mode (using DHB and 9AA matrices). An *m/z* range of 98-1500 was acquired in broadband mode with a Time Domain for Acquisition of

2 MWord. Ions were accumulated across 300 laser shots for each mass analysis. The method settings were as follows: 100 V offset, 280 V defector plate, 18% sweep excitation power, 100 sweep frequency density, 10 s sweep time. The laser was set to minimum spot size (laser diameter of *ca.* 15 μm), 1000 Hz laser frequency, minimum laser focus, and a 50 μm Smart Walk for each matrix. The dwell time per pixel was 1000-1500 ms, which resulted in a total data acquisition time of *ca.* 20 minutes per spheroid section. Images were processed using FlexImaging 4.1 and SCiLS version 2019a software with TIC normalisation to generate ion maps. Pixels were exported to DataAnalysis 4.4 and quadratic calibration was carried out using a pre-determined list of internal calibrants for each matrix (tables 3.1 – 3.4).

3.5.2.1 CASI MSI

CASI imaging was performed using the 12T SolariX FT-ICR mass spectrometer. For pimonidazole, a Q1 mass of *m/z* 240 and an isolation window of *m/z* 40 was used. 300 shots were accumulated across 20 scans in positive-ion mode with 15% laser power. An ICR transient length of 0.5 seconds in broadband mode with a Time Domain for Acquisition of 2 MWord was used. The laser raster increment was set to 40 μm along both the x and y axis with a smart walk of 50 μm. Laser focus was set to minimum, with a frequency of 1000 Hz. Ions were accumulated across 300 laser shots for each mass analysis.

3.6 Discriminatory analysis

.mis files were imported into SCiLS version 2019a and the raw data was converted into the .ibd SCiLS format without baseline removal. TIC normalisation was applied to the data once it was imported. The spheroids were segregated into the ‘outer’ and ‘central’ region based on 50% of the radius. For automatically finding *m/z* values discriminating the outer and central regions, the receiver operating characteristic (ROC) tool was employed and the area under the ROC curve (AUC) was calculated. A threshold was set for the top five discriminatory *m/z* values. Using a representative pixel from either region, the calibrated *m/z* values were then assigned formulae using HMDB with an error tolerance of 1 ppm for the $[M-H]^-$ ion. For comparison of the ion abundances of individual species between regions of spheroids, ion abundance distributions were represented as box and whisker plots using SCiLS software.

3.7 Production and imaging of rhodamine microarrays

45 spots containing 50 droplets of 350 pL 0.01% rhodamine (w/v) in water (Sigma Aldrich) was dispensed. A microarray printer (SciFLEXARRAYER S5 (Scienion AG)) equipped with a Piezo Dispense Capillary (PDC 80) with a 50 µm nozzle aperture was used to print onto a SuperFrost™ glass slide. The fluorescence was measured using a BioAnalyzer 4F/4S (LaVision BioTec) fluorescence scanner at 70 ms exposure time and a Cy5 filter. The area of observed fluorescence was measured using ImageJ before and after matrix application. 9AA (5 mg/mL, 70% ACN) was used as the matrix.

3.8 Scanning electron microscopy

Matrix-coated rhodamine B slides were mounted on aluminium stubs with carbon tabs attached and sputter coated with 20 nm gold palladium (Emscope). The samples were viewed using a Hitachi S-4700 scanning electron microscope.

Chapter 4.

Method development for mass spectrometry imaging of multicellular tumour spheroids

4.1 Introduction

MSI was first applied to MTS in 2011 to examine the distribution of biological molecules in human carcinoma (HCT 116) spheroids.[84] In this report, by Li et al., HCT-116 spheroids were grown over 14–20 days to approximately 1 mm in diameter, embedded in gelatin (350 mg/mL) and sectioned. This workflow embedded up to five spheroids and produced up to 16 spheroid sections on each slide. Using MALDI ToF MSI in positive mode with 75 µm resolution, Li and co-workers observed the distribution of a limited number of intact proteins that localised to the central necrotic region. To complement this MSI study, nanoLC MS/MS was used to identify cytochrome C and histone H4, both of which distributed uniformly across the spheroid. Since this first report, several other studies have applied a similar workflow to investigate MTS in a spatially-resolved manner. These include observing the distribution of lipids,[131] metabolites,[80] and the time-dependent penetration of drugs.[129,132,136,140]

Although several reports have demonstrated the feasibility of MSI analysis of spheroids, no standardised sample preparation protocol has been universally adopted. Therefore, our initial work focused on the development of a robust, reliable and reproducible protocol for the sample preparation, MSI data collection, and data processing of MTS cultures.

Specifically, we have optimised a method for MALDI ToF and FT-ICR MSI of breast cancer (MCF-7) spheroids. Initial MALDI MS analysis was used to create peak lists in positive and negative polarities, and formulae were tentatively assigned with sub-ppm errors. These mass lists were subsequently employed to assign formulae to exported spectra from an imaging run. Metabolites that displayed localised distributions to specific regions – in this case outer and centre – were assigned based on accurate mass and metabolome database searches.

4.2 Results and discussion

4.2.1 Method development for MALDI MS of MTS

For all work carried out, the spheroids were produced using the hanging drop method.[113] 20 µL containing approximately 6000 cells were placed onto the lid of a petri dish (figure 4.1). The droplets were suspended over a reservoir containing

fresh media (10 mL) supplemented with FBS (10% v/v) and Penicillin-Streptomycin (10000 units penicillin/mL, 10 mg streptomycin/mL, 3 mL). 15 µL of media was removed and replaced every third day over a total of seven to 21 days of culture. Above 21 days, spheroids became fragile and easily damaged during sample preparation, as shown by H&E staining (figure 4.2).

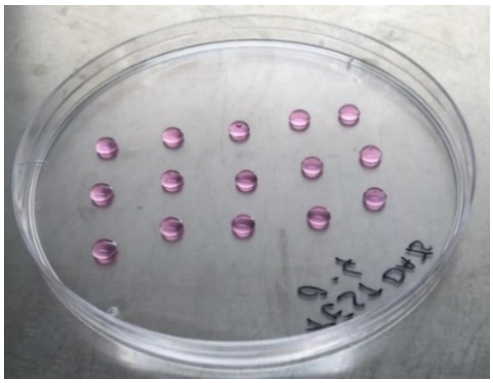

Figure 4.1. Spheroids were produced using the hanging drop method. This involved placing 20 µL of approximately 6000 cells onto the lid of a petri dish. The lid was then inverted, and a reservoir of 10 mL of media was placed in the bottom of the petri dish.

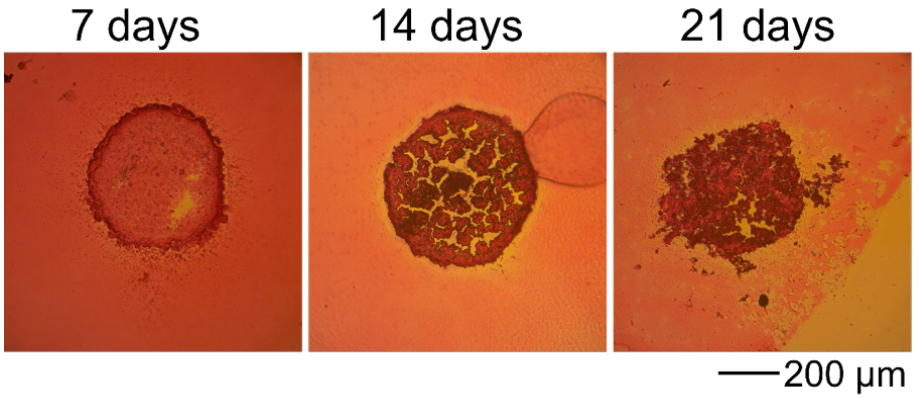

Figure 4.2. H&E staining of embedded and sectioned MCF-7 spheroids after culturing for seven, 14, and 21 days.

After seven days, the spheroids reached an approximate diameter of 500 µm. They were prepared for imaging by removing the media and washing the spheroids twice with PBS (20 µL). During this stage, spheroids are very fragile and likely to be damaged, and so extra care is required when washing the spheroids. Gelatin (3 mL, 17.5% (w/v)) was used as the embedding medium. It was prepared using a stirrer

plate at 37 °C to reduce heat damage to the spheroids, and a Sainsbury's own brand blue food colouring dye (0.5 mL) was added in order to visualise the spheroids during sectioning. Embedding was initially carried out using moulds, including a silica well plate and a 3D printed block with a lid to make individual wells (figure 4.3). However, both of these methods prevented visualisation of the spheroids within the mould during embedding, and the gelatin block was regularly damaged during removal. A simplified protocol was developed using the petri dish lid on which the spheroids were grown. After the second wash with PBS, spheroids were picked up with a 100 µL pipette tip and placed into a single droplet from which maximal liquid was removed. Blue gelatin (20 µL) was then added to the spheroids. An additional 'blanket' layer of gelatin (20 µL) was added on top once the first layer had set to ensure the spheroids were fully embedded. Up to eight spheroids were embedded in each droplet.

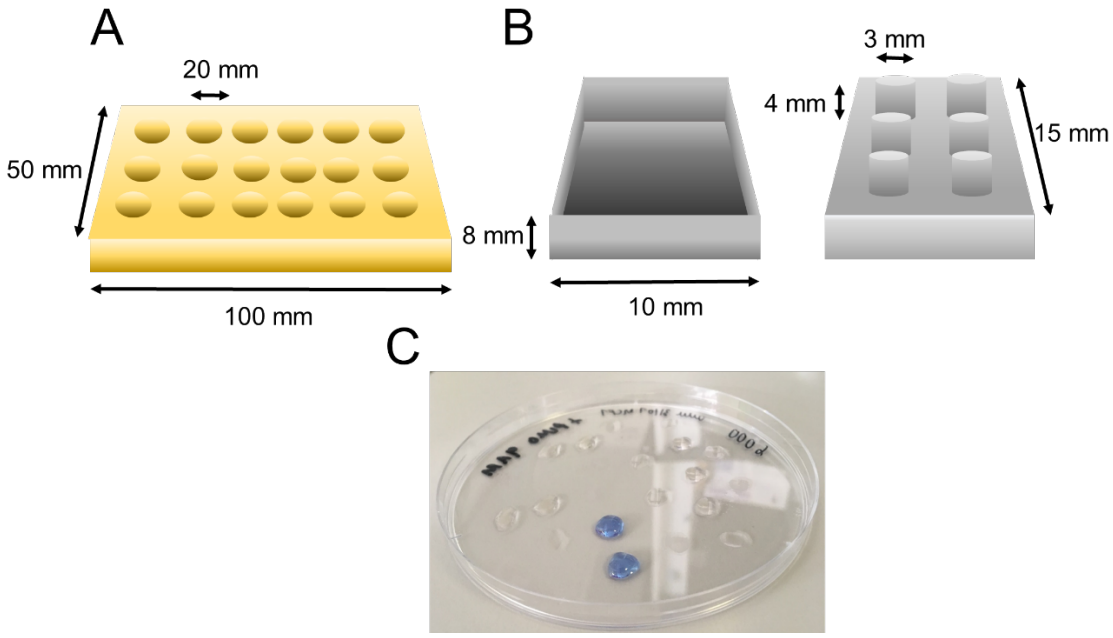

Figure 4.3. Schematic of moulds used for initial MALDI-MSI of spheroids. (A) Silica mould containing individual wells for spheroids. (B) 3D-printed plastic mould containing four wells for spheroids. (C) Gelatin droplets were placed directly onto the petri dish where the spheroid was cultured.

To prevent degradation of biological molecules, embedded spheroids were immediately frozen. To reduce the size of the water crystals in the gelatin, spheroids were frozen on dry ice with isopentane, then snap-frozen in liquid nitrogen and

stored at -80 °C until use. Sectioning thickness is commonly between 10 and 20 µm as a compromise between minimising tissue fragility and maximising ion abundance.[9,86] Therefore, the embedded spheroids were sectioned at 15 µm thickness using the cryostat (-21 °C) and thaw mounted onto ITO-coated glass slides. Cryostat temperatures above -10 °C resulted in unsuccessful sectioning due to thawing of the edges of the gelatin.

During sectioning, alternate sections were taken for H&E staining to confirm the structural integrity of the spheroid sections. Using this method, a single slide could mount up to 24 gelatin sections. Therefore, depending on the number of spheroids per section, up to 100 spheroid sections were mounted onto one slide. The slide was then scanned at 4800 dpi and this image was used to calibrate the imaging run and identify the locations of the spheroids (figure 4.4). Slides were scanned prior to matrix coating to improve the visibility of the sectioned spheroids.

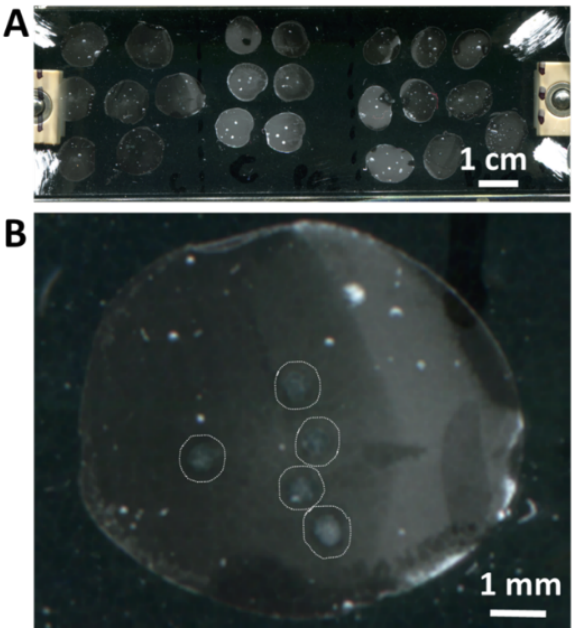

Figure 4.4. Scanned image of (A) a slide with gelatin-embedded spheroids mounted. (B) A single gelatin section with spheroids identified by the dotted white lines. Additional marks are the result of air bubbles in the gelatin.

Each spheroid-mounted slide was coated in a matrix for MALDI ionisation. Depending on the polarity of ionisation and the analyte of interest, a number of matrices were used; including DHB, CHCA and 9AA. A TM-sprayer™ was used for

matrix application, and the solvent composition, number of passes, temperature, spray velocity, and gas pressure were all optimised (figure 4.5). For each condition, the quality of the matrix coverage was observed using glass slides without a sample mounted to observe how changing each parameter affected the quality of matrix deposition. The optimised conditions for the TM-sprayer™ were identified as 80 °C, 0.1 mL/minute flow rate, 10 psi gas pressure, and a velocity of 1100 mm/minute. These conditions took approximately 20 minutes to coat a slide and resulted in a matrix density of 0.22 mg/cm^2 for CHCA, 0.15 mg/cm^2 for DHB, and 0.11 mg/cm^2 for 9AA (figure 4.6).

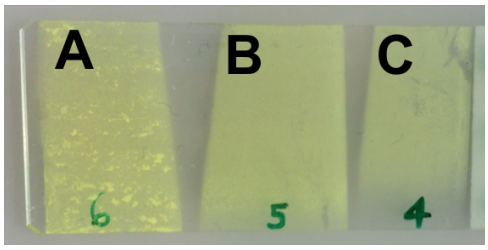

Figure 4.5. Optimisation of matrix application conditions for 9AA matrix application. (A) 50 °C produced an inhomogeneous coverage of large crystals. (B) 80 °C produced a dense homogeneous coverage of small crystals. (C) 90°C produced an uneven coverage, and the nozzle became blocked during application. All conditions shown used 10 psi gas pressure, 0.1 mL/minute flow rate, and a velocity of 1100 mm/minute.

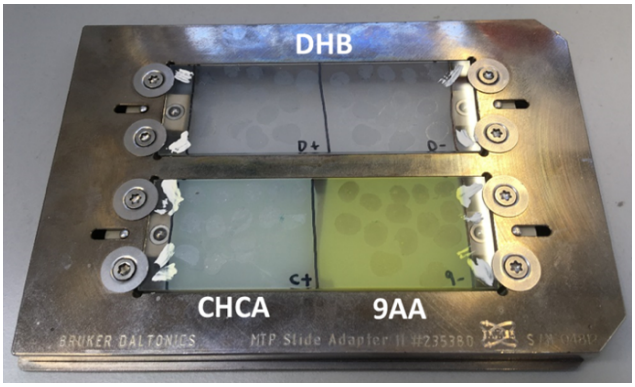

Figure 4.6. Representative image of a MALDI slide holder with two spheroid-mounted ITO slides. The slide was coated in a variety of matrices (DHB, CHCA, and 9AA), placed into a slide holder and stored in a desiccator until use on the same day.

Once the spheroids were coated, FlexImaging 4.4 was used to calibrate the scanned image with the slide to align the laser with the spheroids. Spheroid sections had a diameter of approximately 500 µm, so a minimum laser size (*ca.* 15 µm) with a step size of 40 µm was employed. For each instrument and each matrix, the number of accumulated shots and laser power were optimised to produce an intense signal for the analytes of interest. For FT-ICR MS, this was identified as 15%, 9%, and 7% laser power for CHCA, 9AA, and DHB matrices respectively. For ToF MS, this was identified as 65%, 50%, and 47% laser power for CHCA, 9AA, and DHB matrices respectively. All conditions fully ablated the sample. The ToF instrument was quadratically calibrated using red phosphorus prior to analysis, and re-calibrated using internal matrix peaks after acquisition. FT-ICR spectra were calibrated after acquisition. For FT-ICR imaging runs, a representative pixel was exported from the ion density map and calibrated using internal peaks (see methods section 3.4.1).

4.2.2 MALDI MS global metabolite analysis of MTS

This high spectral resolution of the FT-ICR affords sufficient mass accuracy and resolution to assign elemental formulae from accurate mass measurements. These elemental formulae can then be searched against metabolite databases in order to propose potential metabolite assignments. Therefore, FT-ICR MS can be used to produce a mass list of the ionisable metabolome of a spheroid.

However, during an MSI experiment, only a single spectrum is acquired per pixel, thus low intensity ions may not be observed. Consequently, in order to gain a more comprehensive picture of the ionisable metabolome in MTS, a MALDI MS method was employed. During MALDI MS data acquisition, multiple spectra are accumulated and averaged, increasing the signal of the less abundant metabolites and as a result more peaks can be assigned.

For MALDI MS analysis, eight-day-old MCF-7 spheroids were prepared using the previously outlined method. Sections were taken close to the hemisphere of each spheroid to improve the reproducibility. For ionisation, CHCA and DHB matrices were employed for positive-ion mode, and DHB and 9AA matrices were used for negative-ion mode. All experiments were completed in triplicate. For each matrix, a single spheroid was used to sum and average 20 spectra between *m/z* 100 and

1500. This enabled ionisation of metabolites from the entire area of the sectioned spheroid and produced a final spectrum containing a representative snapshot of the ionisable metabolome of an eight-day-old MCF-7 spheroid. By summing multiple spectra, a greater S/N for each metabolite is obtained, and therefore more formulae can be tentatively identified. However, the limitation of this method is the lack of spatial information. This could result in some low abundance localised species within the spheroid to be below the S/N threshold required for assignment.

For each matrix, a mass resolution above 100000 was achieved and over 1000 peaks were observed with S/N >3. After internal calibration, the obtained peak lists could be searched against metabolite and lipid databases (HMDB and Lipidmaps) to produce potential metabolite assignments based on accurate mass alone (figure 4.7).

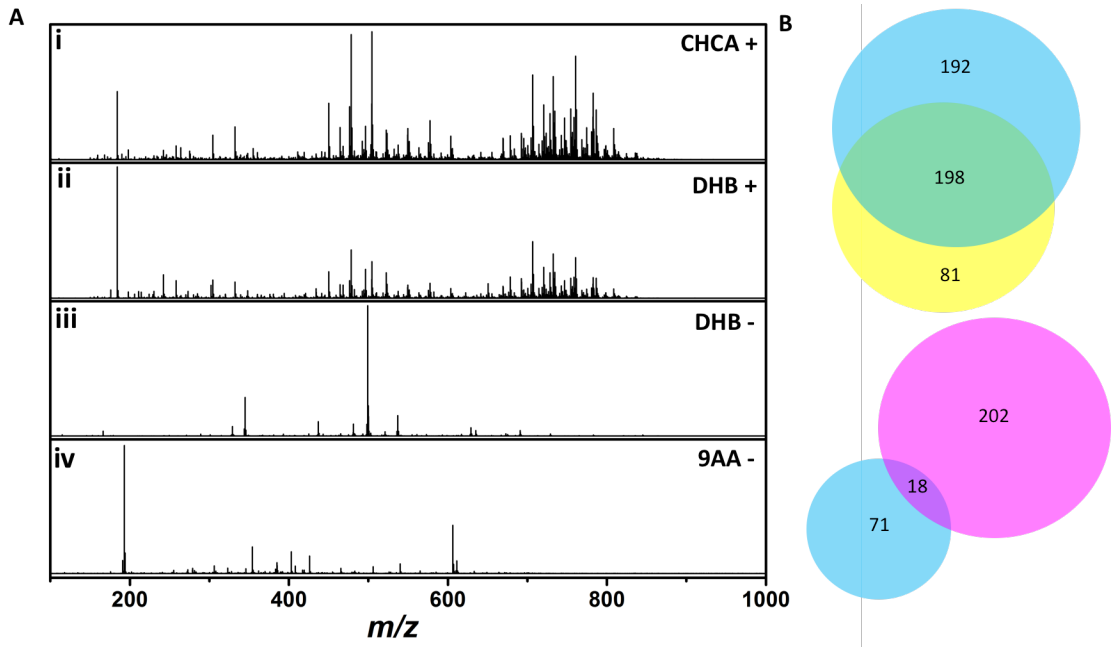

Figure 4.7. (A) MALDI FT-ICR MS analysis of sectioned MCF-7 spheroids. Accumulation of 20 shots manually acquired across a spheroid between m/z 100–1500 using various MALDI matrices. (i) CHCA positive mode, (ii) DHB positive mode, (iii) DHB negative mode (iv) 9AA negative mode. (B) Venn diagrams showing the identification of metabolites in (top) positive and (bottom) negative mode. Blue corresponds to DHB, yellow corresponds to CHCA and pink corresponds to 9AA. For each matrix, the mass resolution was greater than 102000 at m/z 300.

Using positive mode ionisation, 279 and 390 metabolites formulae were tentatively assigned with sub-ppm error using CHCA and DHB as matrices respectively. In negative mode using DHB, 89 metabolites were assigned, and 220 assignments were made using 9AA as a matrix. Considering all matrices used, overall, 471 different species were assigned putative metabolite identities in positive mode, and 291 metabolites were assigned in negative mode (see appendix for tentative metabolite formulae assignments). Of the metabolites assigned, 198 formulae were reproducibly assigned for both matrices in positive mode and 18 were reproducibly assigned in negative mode.

In some cases, for a single peak, the online databases identified multiple different formulae within the pre-determined error tolerance. Therefore, for each of these assignments, the biological relevance of the assigned metabolite was used to select the most likely formula. For example, if the formula corresponded to a metabolite uniquely identified in fruit, this would be an unlikely metabolite to be observed within a spheroid. In order to increase the confidence of these assignments, MS/MS is required to analyse neutral mass losses for each assignment observed.

4.2.3 FT-ICR and ToF MSI of MTS

In an imaging experiment, the spatial distributions of hundreds to thousands of metabolites are mapped simultaneously.[141] MCF-7 spheroids were imaged at 40 μm spatial resolution in positive mode using ToF and FT-ICR MSI. Each spheroid section imaged took approximately 10 minutes using the ToF and 20 minutes using the FT-ICR. The profile spectrum produced from each spheroid was highly complex, and the distributions of various *m/z* values could be observed (figure 4.8).

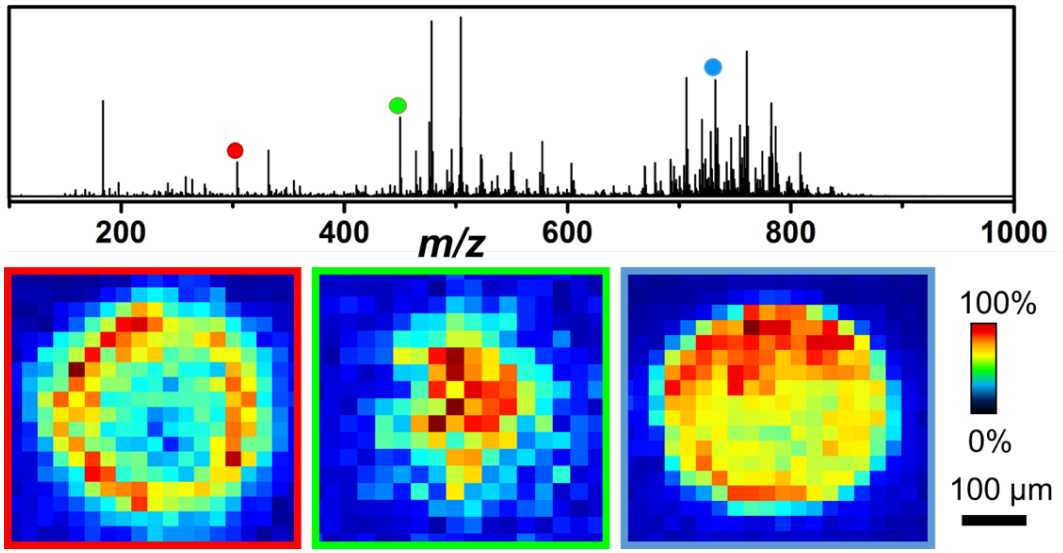

Figure 4.8. Profile spectrum and ion density maps of various m/z values from ToF MSI of MCF-7 spheroids in positive mode with CHCA as the matrix at 40 µm spatial resolution. The resolution obtained was 20000 at m/z 300.

ToF mass analysers have a mass resolving power of up to 50000, whereas FT-ICR instruments have a mass resolving power of up to 1 million.[34] By exporting a representative pixel from each of the imaging datasets, the improved mass resolution of the FT-ICR is shown through its capability to separate overlapping peaks (figure 4.9). Using a S/N >3, 232 peaks were picked from the ToF spectrum, whereas 1495 peaks were picked from the FT-ICR spectrum. Furthermore, FT-ICR data acquired a resolution of over 100000, whereas ToF imaging data produced a resolution of 20000 at *m/z* 300.

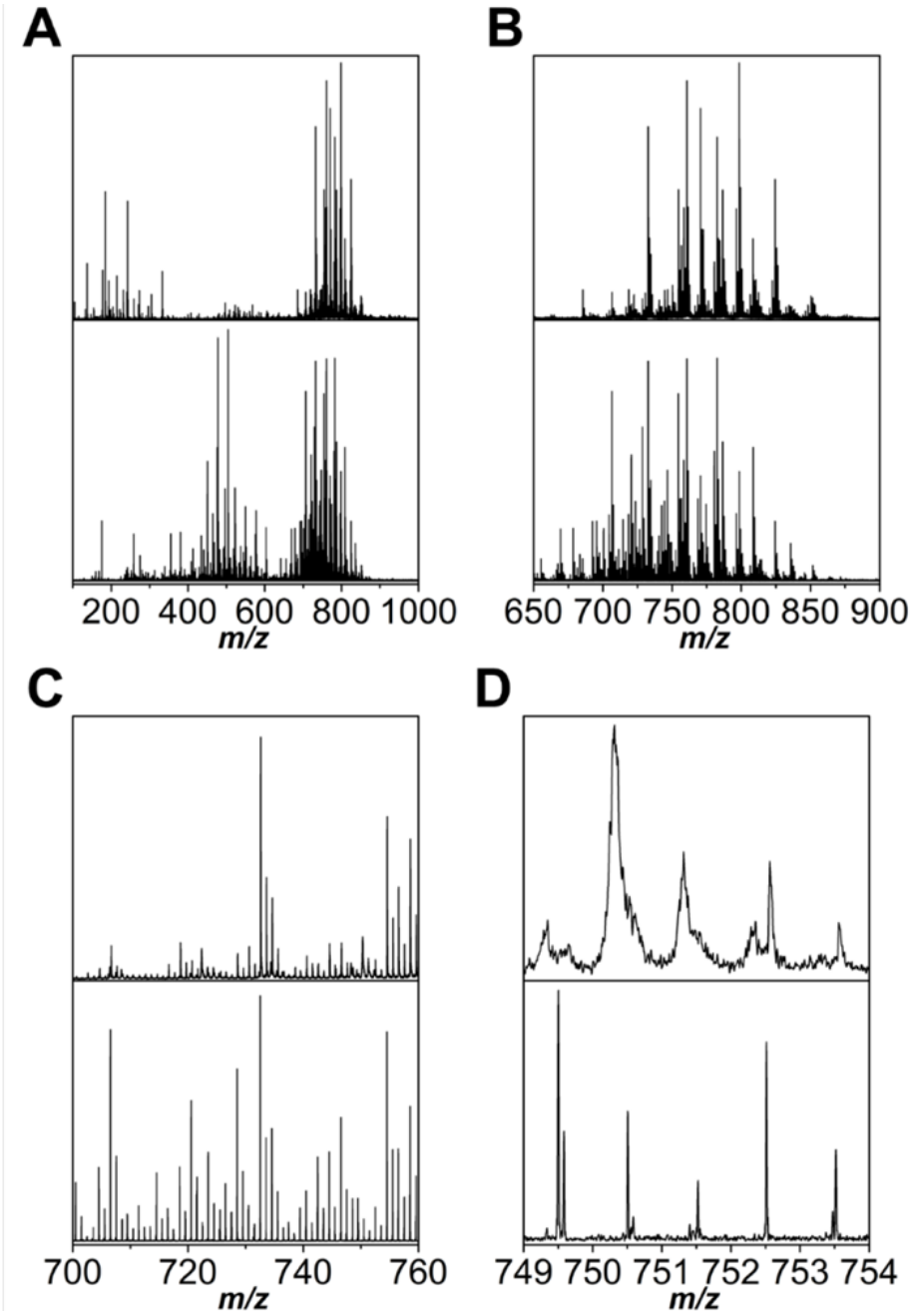

Figure 4.9. Profile spectrum of an MCF-7 spheroid using CHCA as the matrix for (top) ToF and (bottom) FT-ICR MSI. (A) m/z *100–1000 (B)* m/z *600–1000 (C)* m/z *700–760 and (D)* m/z *749–754.*

The high mass resolution of FT-ICR enables the assignment of elemental formulae without the requirement for targeted MS/MS approaches.[142] To observe the benefits of the high spectral resolution of FT-ICR imaging, formula assignments of the peaks between *m/z* 772 and 775 were carried out using online databases (figure 4.10).

The FT-ICR peak list assigned $C_{43}H_{76}NO_7P$ (*m/z* 772.52516) and $C_{43}H_{82}NO_8P$ (*m/z* 772.58509) with 0.254 and 0.210 ppm errors respectively. In contrast, the data collected by ToF was unable to resolve these two species and single feature is observed at *m/z* 772.529; consequently, neither can be assigned with confidence. Database searching based on this signal feature matches $C_{43}H_{76}NO_7P$ with a 4.984 ppm error and $C_{43}H_{82}NO_8P$ with an error of 72.587 ppm. This demonstrates that the high spectral resolution of the FT-ICR is required for global analysis as it is capable of assigning elemental formulae from accurate *m/z* measurements, whereas ToF MSI lacks the resolving power required. Furthermore, the two mass analysers display unique distribution patterns for the *m/z* value imaged, however the reason for this is unknown.

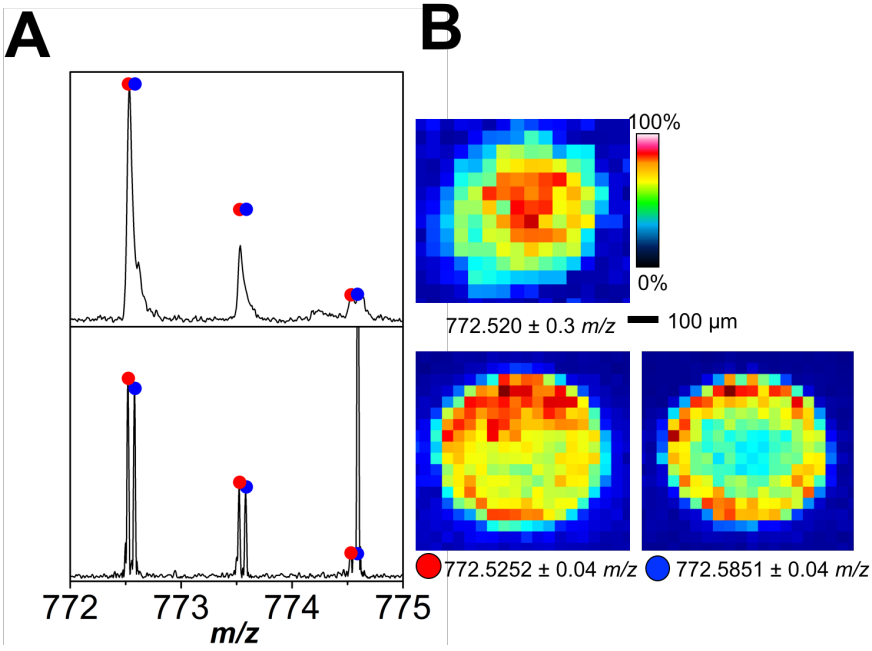

Figure 4.10 (A) Spectra of exported pixel from (top) ToF and (bottom) FT-ICR MSI of MTS at 40 µm resolution in positive mode with CHCA as the matrix. (B) Ion density maps from (top) ToF and (bottom) FT-ICR showing the distribution of the identified lipids. Overlaid spectra show the (red) $C_{43}H_{76}NO_7P$ $[M+Na]^+$ and the (blue) $C_{43}H_{82}NO_8P$ $[M+H]^+$ adduct.

4.2.3.1 Elucidating spheroid microenvironments

To elucidate how the various microenvironments across a spheroid influence its metabolome, MCF-7 3D cell cultures were grown over eight days to form spheroids

of approximately 500 μm in diameter and prepared for MSI as previously discussed. Spheroid sections were coated in 9AA matrix and subjected to MALDI FT-ICR MSI at 40 μm spatial resolution between *m/z* 98–1500 in negative mode. This matrix was selected to preferentially ionise metabolites including nucleotides and phosphates,[143] as these are important in understanding the biology of cancer.[144] Figure 4.11 highlights the differences in the profile mass spectra produced from areas across the diameter of the spheroid (in this case, the central and outer regions). By inspection of an exported representative pixel from the outer and centre region, it is clear that spectra from the spheroid are highly complex, and significant differences in the profile mass spectra are apparent in the two regions (Figure 4.11A). Across the entire spectrum, formulae were assigned to each peak with sub-ppm error and database searches offered tentative metabolite identifications. A narrow region of each spectrum is shown in Figure 4.11B, highlighting the variation in abundance of species between the outer and centre region of the spheroid. The intensities of these peaks are consistent across the spheroid as shown by the ion density maps (Figure 4.11C).

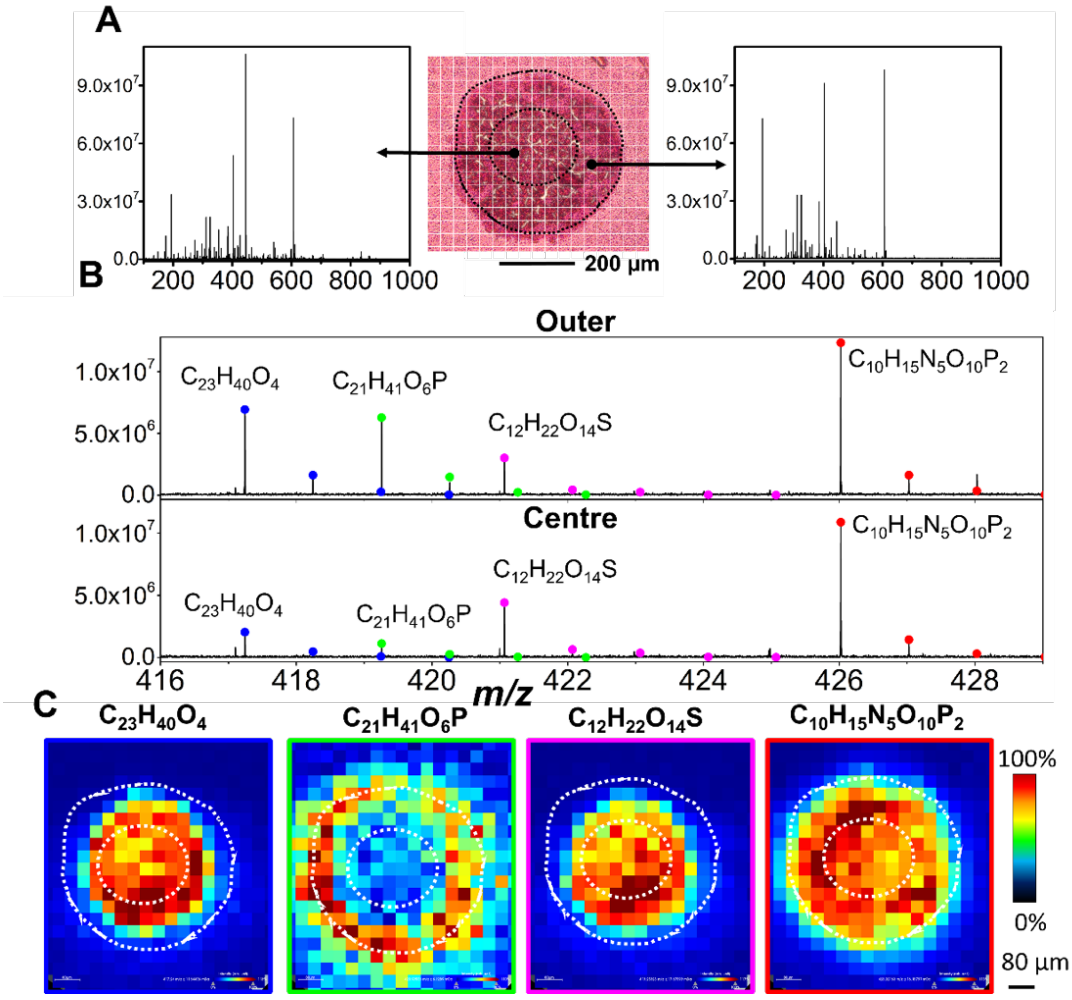

Figure 4.11. (A) A representative H&E stained section of the MCF-7 spheroids used in this study. An FT-ICR mass spectrum from a representative pixel in the outer and centre regions of the MCF-7 spheroid is shown. (B) Representative pixels from the (top) outer and (bottom) centre region of an MCF-7 spheroid imaged at 40 µm resolution. Using HMDB, each peak could be assigned with sub-ppm error and the relative intensity compared between the regions. The errors identified were 0.0719, 0.3816, 0.2375 and 0.1174 ppm for each assigned formula respectively. (C) The ion density maps for each of the formulae assigned.

By exporting and calibrating a representative spectrum from the outer and centre region (see section 3.4.1 in materials and methods for detailed description of calibration process), peaks with a S/N >3 were assigned formulae with sub-ppm errors using online databases HMDB and LipidMaps. In total, 100 peaks were assigned using the imaging data from both pixels. Furthermore, of the peaks

assigned, four peaks were unique to the outer region and eight peaks were unique to the centre region (figure 4.12). Based on the formulae assigned to the unique peaks, tentative metabolite identifications were made (tables 4.1 and 4.2).

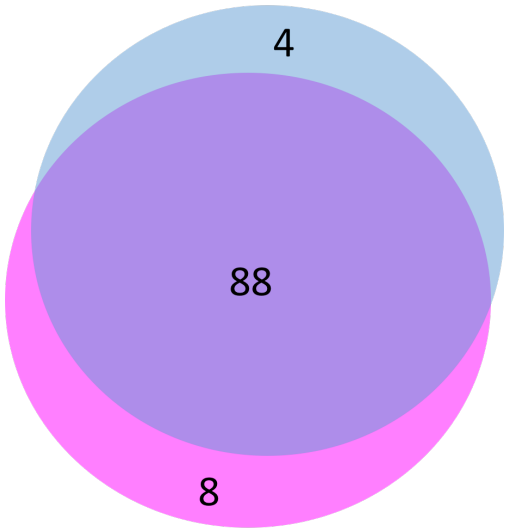

Figure 4.12. Venn diagram showing the identified molecules in the (blue) outer and (pink) centre of the spheroid. Of the 100 formulae assigned, four were unique to an outer pixel and eight were unique to a centre pixel of the eight-day-old spheroid.

Table 4.1. m/z values assigned uniquely to a pixel in the outer region of a spheroid with sub-ppm error using HMDB and LipidMaps. Tentative metabolite identifications were made based on the accurate masses and formulae.

Observed *m/z*	**Expected *m/z***	**Error (ppm)**	**Tentative neutral formula**	**Adduct**	**Tentative identity**
424.97684	424.97687	0.05883	$C_9H_{14}N_2O_{12}P_2$	[M+Na-2H]-	Uridine 5'-diphosphate
481.97734	481.97724	-0.21578	$C_9H_{16}N_3O_{14}P_3$	[M-H]-	Cytidine triphosphate
558.06435	558.06440	0.08422	$C_{15}H_{23}N_5O_{14}P_2$	[M-H]-	Adenosine diphosphate ribose
628.05599	628.05624	0.39328	$C_{17}H_{27}N_3O_{17}P_2$	[M+Na-2H]-	Uridine diphosphate-N-acetylglucosamine

Table 4.2. m/z values assigned uniquely to a pixel in the centre region of a spheroid with sub-ppm error using HMDB and LipidMaps. Tentative metabolite identifications were made based on the accurate masses and formulae. ***PA****, Phosphatidic acid,* ***CMP-NeuNAc*** *Cytidine monophosphate N-acetylneuraminic acid.*

Observed *m/z*	Expected *m/z*	Error (ppm)	Tentative neutral formula	Adduct	Tentative identity
214.04859	214.04860	0.03270	$C_5H_{14}NO_6P$	[M-H]-	Glycerylphosphorylethanolamine
253.05000	253.04998	-0.07508	$C_7H_{14}N_2O_6S$	[M-H]-	5-L-Glutamyl-taurine
304.03403	304.03401	-0.06578	$C_9H_{12}N_3O_7P$	[M-H]-	Cytidine 2',3'-cyclic phosphate
334.07143	334.07144	0.04191	$C_{11}H_{17}N_3O_7S$	[M-H]-	S-Formylglutathione
340.99458	340.99464	0.18475	$C_{10}H_{13}N_2O_7P$	[M+K-2H]-	Thymidine 3',5'-cyclic monophosphate
459.06859	459.06872	0.27883	$C_{17}H_{19}N_4O_8P$	[M+Na-2H]-	Riboflavin cyclic-4',5'-phosphate
613.13971	613.13999	0.45667	$C_{20}H_{31}N_4O_{16}P$	[M-H]-	CMP-NeuNAc
669.45021	669.45008	-0.19568	$C_{37}H_{67}O_8P$	[M-H]-	PA(20:2(11Z,14Z)/14:1(9Z))

An advantage of MSI over MALDI MS is the spatial information provided within the data. The initial assignment of formulae from an exported pixel can be complemented by observing the spatial distribution of each assignment across the spheroids. Of the metabolites uniquely assigned in the outer pixel, all of the assignments involved nucleotides, two of which are uridine phosphates. The ion density maps show that both uridine diphosphate (**UDP**) (*m/z* 424.97684) and UDP-N-Acetylglucosamine (**UDP-GlcNAc**) (*m/z* 628.05599) display higher intensities in the outer region of the spheroid, which agrees with the pixel assignments (figure 4.13). Furthermore, both of these metabolites are associated with the hexosamine biosynthetic pathway (**HBP**), which has been shown to be downregulated in hypoxic conditions.[145,146] **ADP ribose** (*m/z* 628.05599) also displays a clear distribution to the outer region of the spheroid. This metabolite is suggested to play an important role in DNA repair,[147] which could explain its absence from the hypoxic central regions of the spheroid.

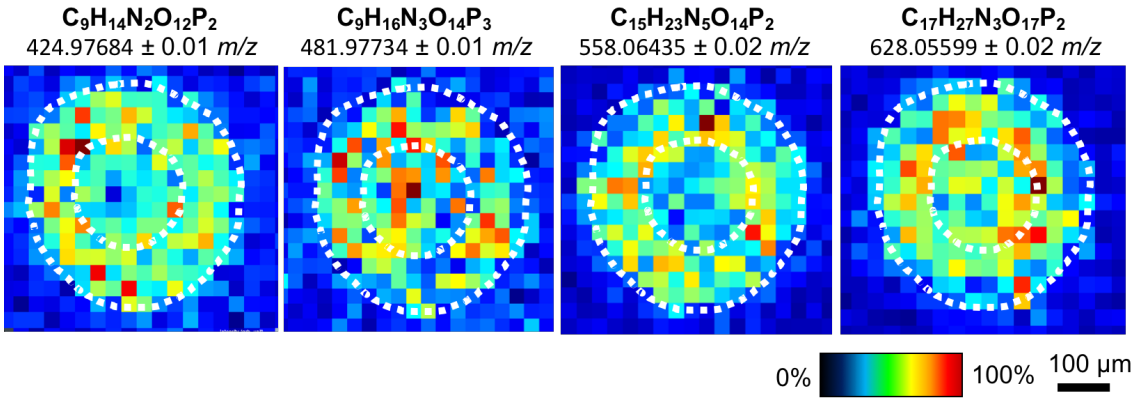

Figure 4.13. Ion density maps showing metabolites that were uniquely assigned from a representative exported pixel from the outer region of the eight-day-old MCF-7 spheroid. The white line denotes the outer and centre regions of the spheroid. From left to right, tentative identifications are ***UDP****,* ***CTP****,* ***ADP ribose*** *and* ***UDP-GlcNAc****.*

Despite the unique assignment of cytidine triphosphate (**CTP**) (*m/z* 481.97734) in the exported spectrum from an outer region, the ion density map suggests that it has a uniform distribution across the spheroid. **CTP** is present at a low intensity throughout the spheroid, and the exported pixel did not contain the peak corresponding to **CTP**, resulting in a false positive assignment of this nucleotide to the outer region (figure 4.14). This shows the limitations of using a representative pixel from the ion density map, whereby a single pixel is not representative of the heterogeneous distributions of metabolites.

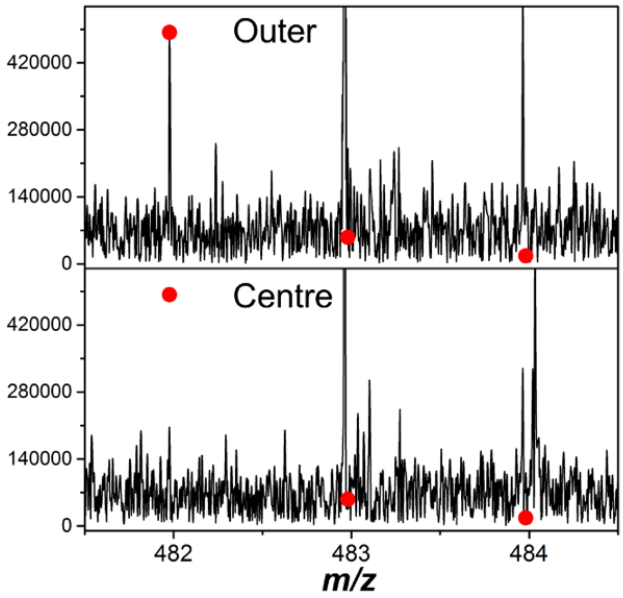

*Figure 4.14. Exported pixels shows that the peak corresponding to **CTP** (m/z 481.97734) in the (top) outer and (bottom) centre of the spheroid produced a false positive result for the discriminatory distribution of this analyte to the outer region. The predicted isotope pattern is plotted as a scatter plot over the data.*

In the centre of the spheroid, four of the eight metabolites assigned are nucleotides, two of which are cytidine phosphates (figure 4.15). Based on the ion density maps, seven of the metabolites identified display distinctly localised distributions towards the centre of the spheroid. However, phosphatidic acid (**PA**) (*m/z* 669.45021) displays a consistent distribution across the structure. Comparably to the pixel analysis of the outer region, this false positive is the result of the exported pixel possessing a S/N <3 (figure 4.16). These results suggest that whilst pixel analysis is effective in identifying unique distributions of metabolites, a threshold of S/N >3 is not consistently low enough to identify low abundance peaks.

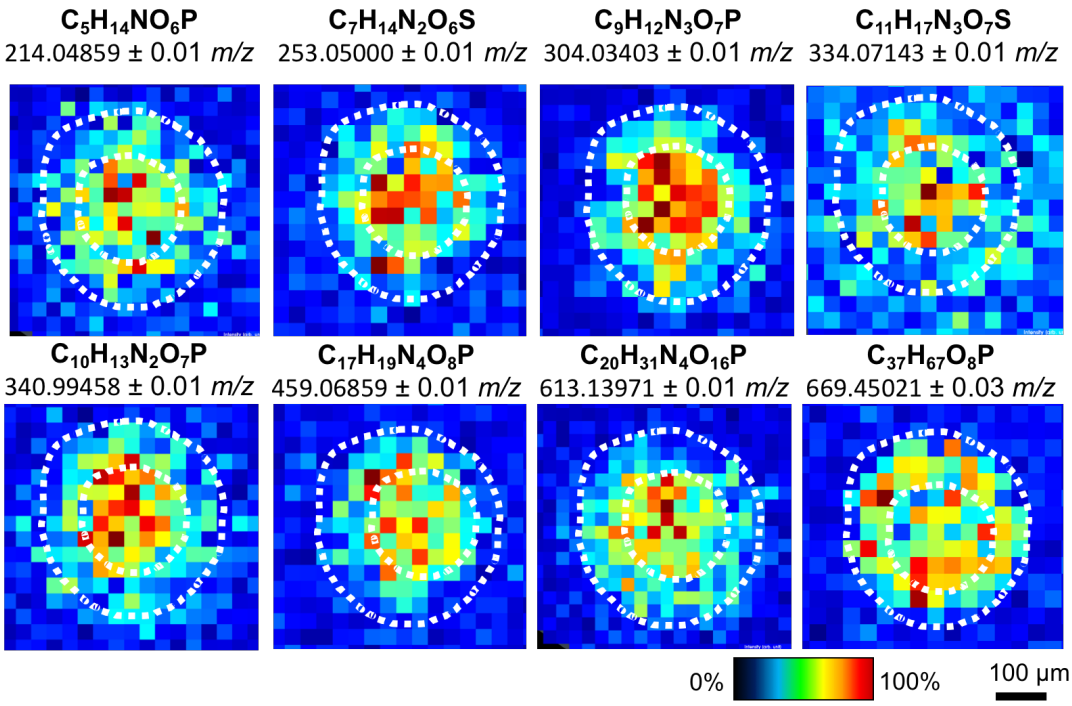

Figure 4.15. Ion density map showing the distribution of the metabolites that were assigned uniquely in the centre region using pixel analysis. The white line denotes the outer and centre regions of the spheroid. From left to right top row Glycerylphosphorylethanolamine, 5-L-Glutamyl-taurine, Cytidine 2',3'-cyclic phosphate, S-Formylglutathione. Bottom row LysoPA (0:0/18:2(9Z,12Z)), Riboflavin cyclic-4',5'-phosphate, ***CMP****, N-acetylneuraminic acid,* ***PA*** *(20:2(11Z,14Z)/14:1(9Z)).*

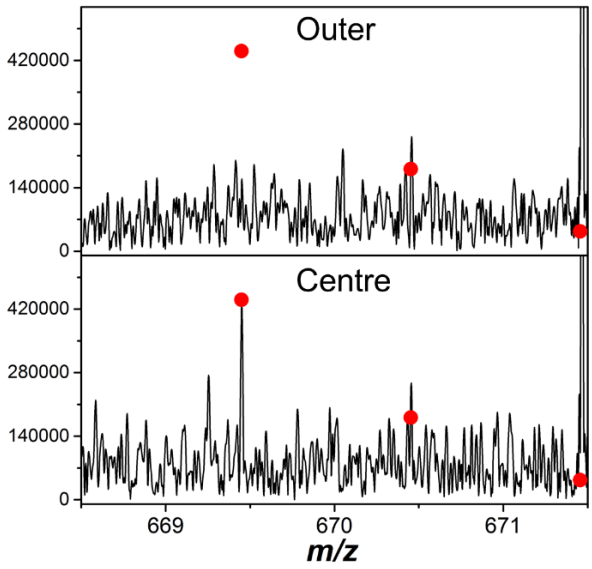

*Figure 4.16. Exported pixels shows that the peak corresponding to **PA** (m/z 669.45021) in the (top) outer and (bottom) centre of the spheroid produced a false positive result for the discriminatory distribution of this analyte to the centre region. The predicted isotope pattern is plotted as a scatter plot over the data.*

4.3 Conclusions

Here we have shown the method development for MALDI-MSI of MTS. Using a simplified gelatin-embedding process, the handling of spheroids is effectively minimised to prevent damage. The conditions of matrix composition and matrix application were effectively optimised to enable successful MSI at high spatial resolution using both FT-ICR and ToF MSI. Using MALDI MS analysis, tentative formulae assignment lists were compiled. These were used to assign metabolites from representative pixels of an imaged spheroid, and metabolites that uniquely localised to different regions of the spheroid – in this case the outer and centre – were observed. However, the primary limitation of this method is the low S/N of a number of metabolites, resulting in identification of false positives during peak selection.

Chapter 5.

Untargeted metabolite mapping in 3D cell culture models using high spectral resolution Fourier-transform ion cyclotron resonance mass spectrometry imaging

5.1. Introduction

Despite the recent advances in MSI of spheroids, the majority of the work has been carried out using ToF MS.[38] Whilst ToF-MS instruments provide high sensitivity and relatively fast acquisition of MSI data, they typically have a mass resolving power of up to ~50000 and mass accuracies of 1–5 ppm after external calibration.[34] As a result, these instruments lack the resolving power and mass accuracy required for definitive determination of elemental formulae. In contrast, FT-ICR MS can achieve a mass resolution above 300000 and mass accuracies between 0.1–1 ppm, which is sufficient to assign elemental formulae from accurate mass measurements.[148] For this reason, FT-ICR MS is widely used for characterisation of unknown metabolites and biomarkers.[149,150] The high spectral resolution can be combined with spatial information using MSI to observe the distribution of known metabolites without employing targeted MS/MS techniques.[151]

In this chapter, the high spectral resolution of the 12T FT-ICR is combined with high spatial resolution imaging for the analysis of metabolites within MCF-7 spheroids. Initially, a targeted approach was used to indicate regions of increased hypoxia and oxidative stress within spheroids. Subsequently, an untargeted approach of discriminatory analysis was employed to identify metabolites that colocalise to these areas. Finally, the tentative assignments were used to investigate the regional flux through specific biochemical pathways.

5.2 Results and discussion

5.2.1 MS imaging highlights redox and energy gradients across MTS

During MSI, the signal abundance of an ion irradiated from any point is assumed to be proportional to the concentration of the targeted analyte. However, this view is over simplistic, as the analytes present could be ionised to varying extents as a result of ion suppression and sample heterogeneity.[40] Alternatively, the proportional abundance of individual ions can be used to compare how their ratios change in different locations across the tissue.[16] Using this approach, a targeted method can be used to compare the distributions of known metabolites within MTS. The distributions of oxidised/reduced glutathione and high energy adenosine phosphates were analysed, as these are thought to be affected by the nutrient and oxygen gradients within MTS.[113] This study was performed with MCF-7 3D cell cultures

grown over eight days to form spheroids of approximately 500 μm in diameter and prepared for MSI as previously discussed. Spheroid sections were coated in 9AA matrix and subjected to MALDI FT-ICR MSI.

5.2.1.1 An increased distribution of ATP in the outer region of the spheroid indicates a decreasing oxygen gradient through the spheroid.

Almost every cellular process requires energy, converting **ATP** to **ADP** and phosphate. As a result, one of the fundamental parameters that all living cells must maintain is a high ratio of **ATP** to **ADP**. Under intracellular conditions, the equilibrium ratio of **ATP:ADP** is around 10^{-7}:1; however, in living cells, this ratio is maintained at 10:1; 10^{8} orders of magnitude away from equilibrium.[152] This ratio is a central control parameter of intracellular energy metabolism that determines the free-energy change for **ATP** hydrolysis and therefore the driving force for many reactions.[153] For example, in glucose metabolism, the **ATP:ADP** ratio determines whether the reaction flux through phosphoglycerate kinase is in the glycolytic or gluconeogenic direction.[153] If mitochondrial **ATP** synthesis becomes compromised when the cell is under stress, such as during hypoxia, the **ATP:ADP** ratio drops dramatically. This results in stimulation of glycolysis to generate **ATP** anaerobically. The **ATP** yield per mole of glucose is much lower for glycolysis compared to mitochondrial oxidative phosphorylation (2 moles of **ATP** vs. ~35 moles of **ATP** per mole of glucose, respectively).[154] Interestingly, the total **ATP:ADP** ratio in spheroids is thought to be reduced compared to monolayer cell culture.[155] Furthermore, as spheroids age and increase in size, the rate of glycolysis increases.[155] This suggests that whilst monolayer and small spheroids rely primarily on oxidative phosphorylation for energy production, larger spheroid's energy demand is predominantly supported by the glycolytic pathway.[155] As a result, the ability to observe changes in the **ATP:ADP** ratio can be used to visualise energy changes in cells.[156]

Ions corresponding to **ATP**, **ADP**, and **AMP** are all seen in the MSI data of MCF-7 spheroids. The distributions of the $[M-H]^-$ *m/z* value of **ATP** (*m/z* 505.98847) localised distinctly towards the outer region of the MCF-7 spheroid with 0.140 ppm mass error (figure 5.1). In contrast, **ADP** (*m/z* 426.02214) and **AMP** (*m/z* 346.05581) are more uniformly localised across the spheroid with 0.167 and 0.179 ppm errors respectively. This observation suggests that that there is a lower rate of

ATP production relative to dephosphorylation in this central region of the spheroid. This implies that the cellular environment is energy depleted, and potentially hypoxic compared to the outer region of the spheroid. Biological replicates show that all three biomolecules displayed consistent gradients across multiple separately imaged spheroids (figure 5.2).

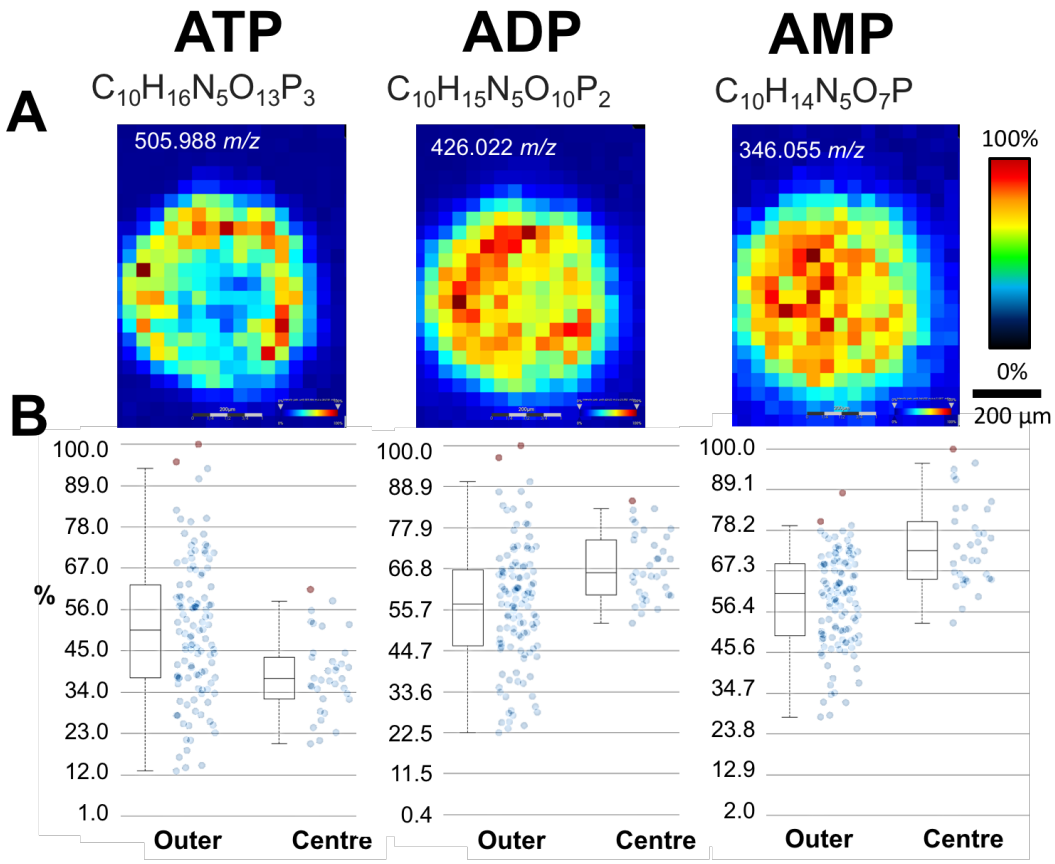

*Figure 5.1. (A) Ion density map of **ATP**, **ADP** and **AMP** across an MCF-7 spheroid imaged at 40 µm resolution using the FT-ICR. (B) Box and whisker plot showing the intensity of the peak for each pixel in the allocated outer and centre regions.*

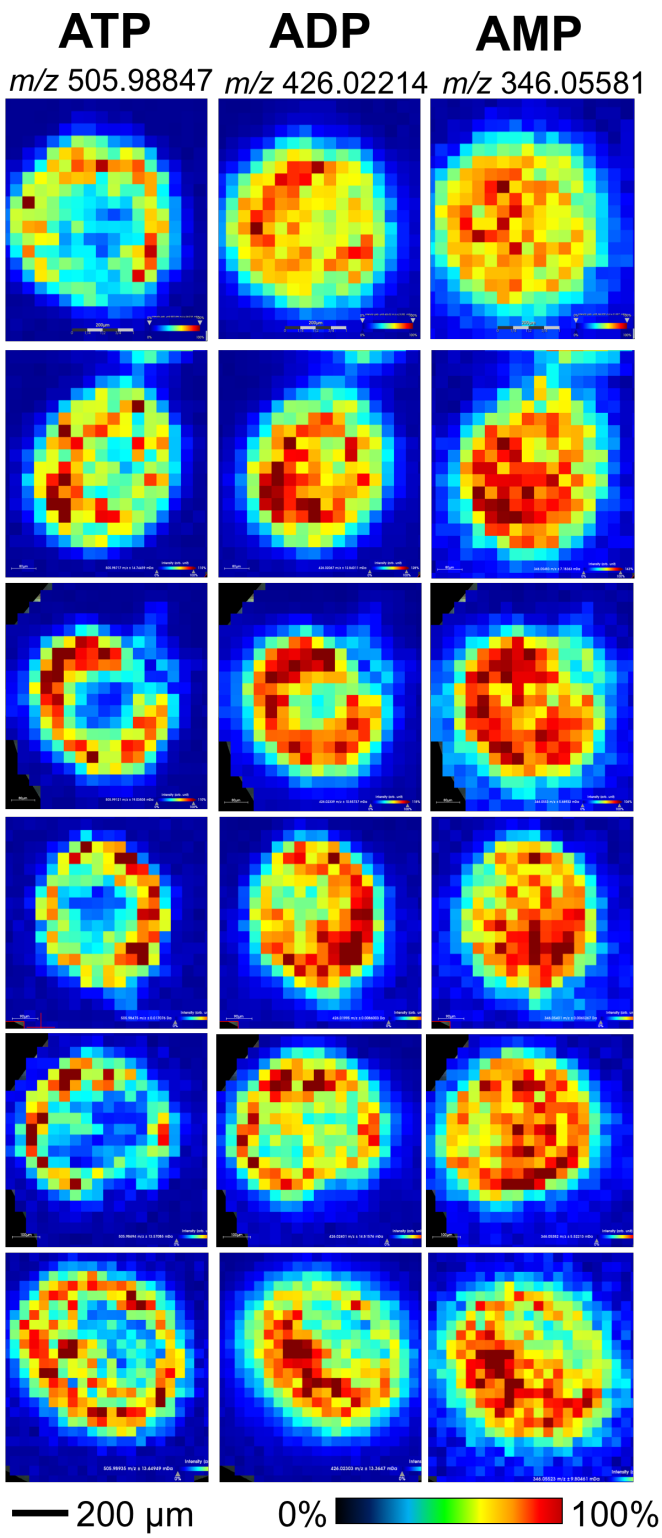

*Figure 5.2. Biological replicates of the distributions of **ATP**, **ADP** and **AMP** across individually imaged MCF-7 spheroids.*

The high spectral resolution obtainable by FT-ICR MALDI MS enables the observation of isotopic fine structure (IFS) of the first isotope peak for **ATP**, **ADP**, and **AMP** (i.e. the mass discrepancy between ^{13}C and ^{15}N) to increase the confidence of the formula assignments (figure 5.3).

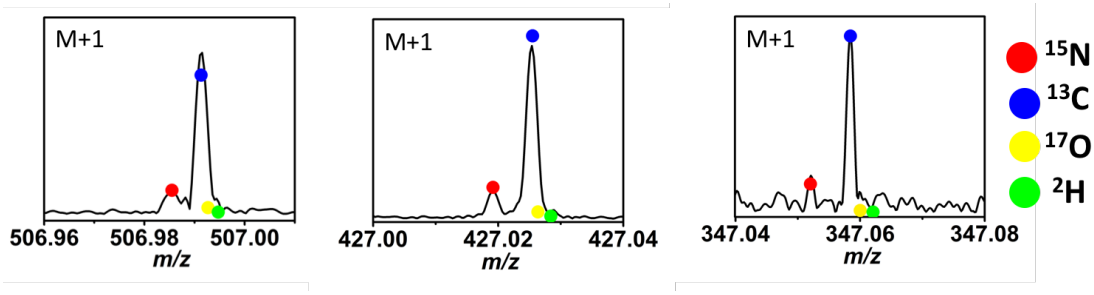

*Figure 5.3. The fine structure of the first isotope for **ATP**, **ADP**, and **AMP** observed by MALDI MS analysis (left to right). The predicted isotope fine structure is plotted over the data as scatter plots. 15 spectra were summed using a CASI window of m/z 15 for each nucleotide, For all species the signal for the ^{13}C and ^{15}N stable isotope are sufficiently resolved.*

5.2.1.2 An increased ratio of glutathione disulfide to glutathione is indicative of hypoxic environment in the central region of the spheroid

The tripeptide glutathione (**GSH**) plays an important role in maintaining the cellular redox homeostasis through oxidation of its sulfhydryl group to form glutathione disulfide (**GSSG**).[157] The overall concentration of **GSH** varies between organisms, however it exists *in vivo* predominantly in the reduced form to maintain the **GSH:GSSG** ratio and avert oxidative stress and apoptosis.[158] Under conditions of oxidative stress, **GSH** is oxidised. This results in an intracellular redox imbalance reflected by a decreased **GSH:GSSG** ratio.[159] Thus, the ratio of **GSH:GSSG** has been proposed to be a marker for the oxidative nature of the cellular environment and a potential indicator of oxidative stress.

The distributions of the $[M-H]^-$ *m/z* values of **GSSG** (*m/z* 611.14469) and **GSH** *(m/z* 306.07653) were imaged within the MCF-7 spheroid with 0.294 ppm and 0.289 ppm errors respectively (figure 5.4). Overall, both **GSSG** and **GSH** increase in intensity towards the centre of the spheroid (figure 5.4A). However, the observed ratio of ion abundance for the **GSH:GSSG** ions differs in the two regions, with a clear decrease of this ratio in the inner region (figure 5.4B). This observation suggests that the

oxidised form is present at a higher relative abundance compared to the reduced form in the central region of the spheroid. This is consistent with greater oxidative stress experienced in this central region. This observation was reproducible across independently imaged spheroids (figure 5.5).

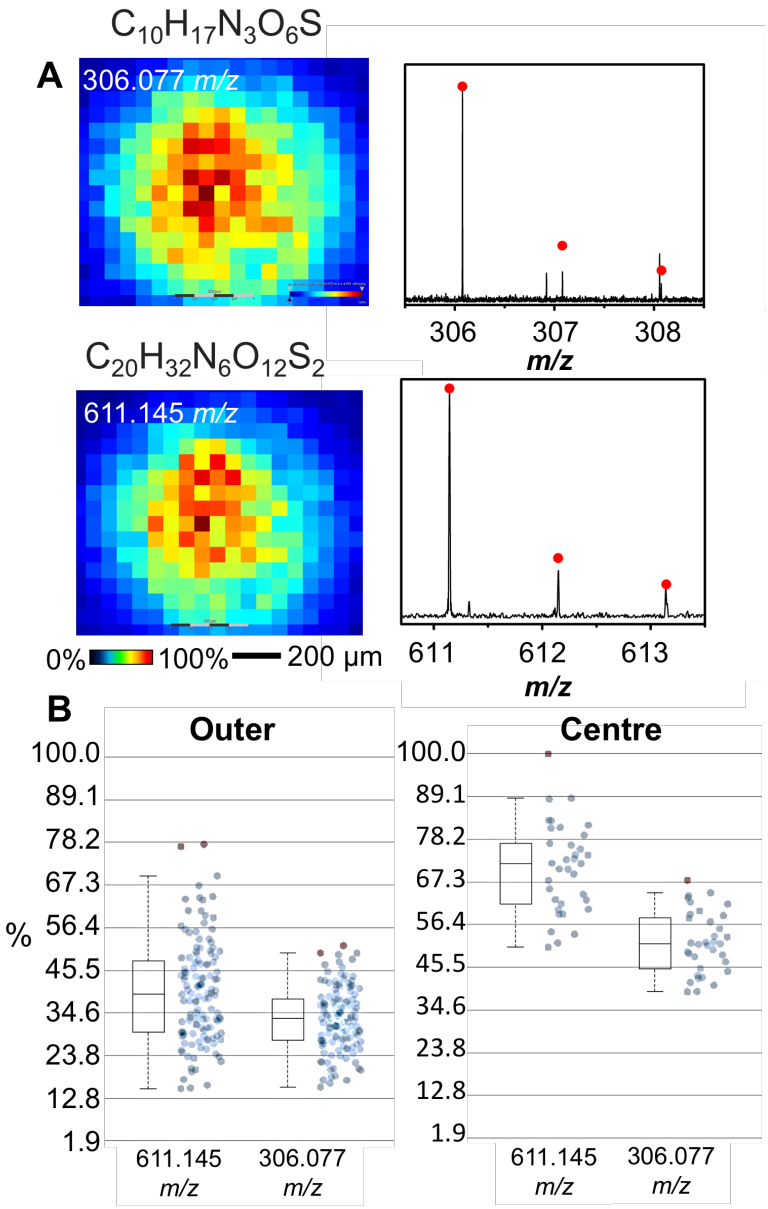

Figure 5.4. (A) Ion density map of oxidised (m/z 611.14469) and reduced (m/z 306.07653) glutathione with overlaid spectra showing with 0.294 ppm and 0.289 ppm errors respectively. (B) The box and whisker plots correspond to the intensity of the m/z value for each pixel allocated to the outer and centre region. The values are normalised against the highest peak intensity.

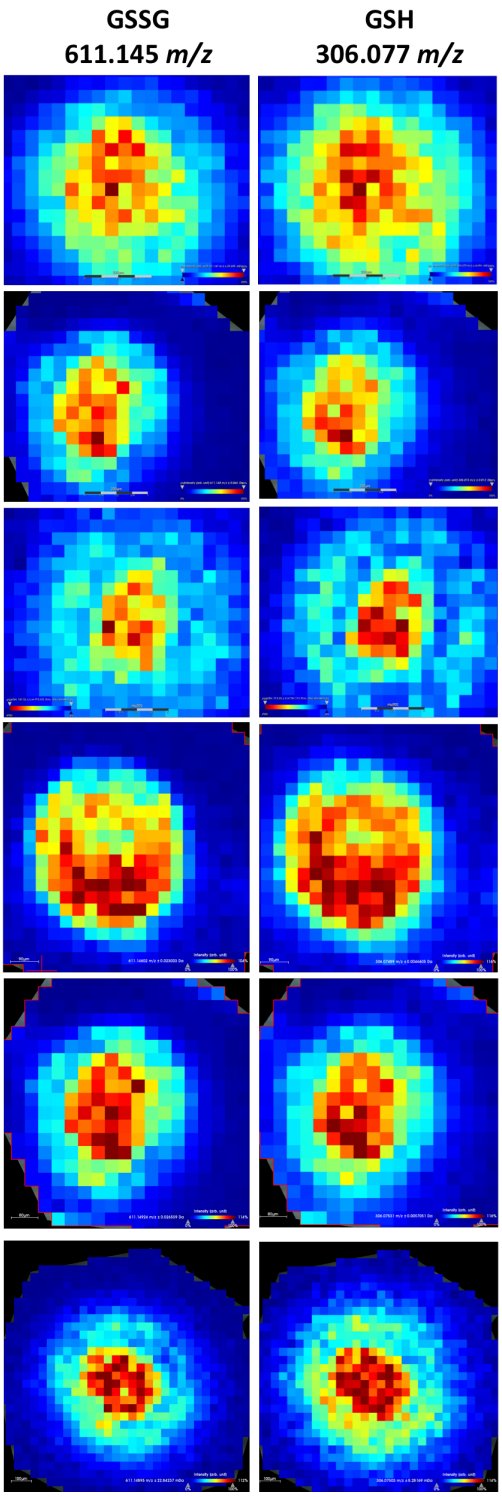

*Figure 5.5. Biological replicates of the distributions of oxidised (**GSSG**) and reduced (**GSH**) glutathione across independently imaged MCF-7 spheroids.*

Taken together, the ratios of **ATP:ADP** and **GSSG:GSH** observed using MSI are indicative of both oxidative stress and hypoxia occurring within the central region of the spheroid. Whilst this may sound paradoxical, the co-occurrence of these biological states in the same tissue environment is well documented, as hypoxia is known to increase the production of reactive oxygen species (ROS), thereby increasing cellular oxidative stress. In fact, ROS signalling is directly responsible for stabilisation of the transcription factor hypoxia-inducible factor (HIF-1α); the primary transcriptional response to hypoxic stress.[160] In turn, HIF-1α has been shown to cause a metabolic switch in tumour cells by modulating expression of genes including pyruvate dehydrogenase kinase, resulting in an increased flux through the glycolytic pathway.[161]

5.2.2 Identifying metabolites which display ion abundance gradients within MTS

Discriminatory analysis was performed to identify the metabolites that are most affected by the hypoxia-induced oxidative stress produced across the spheroid's diameter. For this analysis, two regions were defined within a spheroid as the 'outer' and 'centre' based on 50% of the radius (figure 5.6). For each *m/z* value the area under the receiver operating characteristic curve (AUC of ROC) was determined and the top five discriminatory metabolites in each region were tentatively identified based on their *m/z* using HMDB.

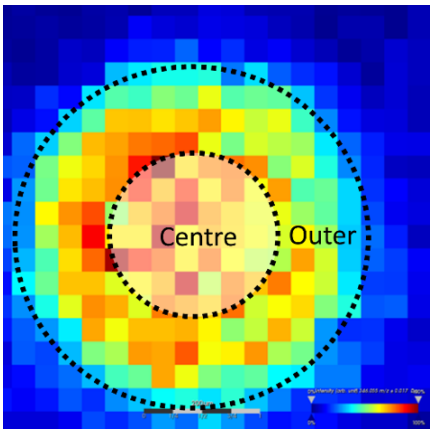

Figure 5.6. Regions were drawn on the SCiLS software corresponding to the 'outer' and 'centre' regions of the spheroid based on 50% of the radius. Using these regions, discriminatory analysis was performed.

5.2.2.1 High energy uridine phosphates are localised to areas of high oxygen availability

The five molecules that discriminated most strongly towards the outer region were identified using the HMDB with a sub-1 ppm error (figure 5.7). Remarkably, all five of the discriminatory molecules were identified as uridine phosphates based on their *m/z* values. This is in agreement with recent findings that hypoxia is associated with decreased abundance of uridine nucleosides.[144,162]

In our data, uridine triphosphate (**UTP**) (AUC = 0.960), **UDP** (AUC = 0.992) and UDP-N-acetyl hexose isomers, such as **UDP-GlcNAc** (AUC = 0.887) display gradients across the diameter of a spheroid. These distributions were reproducible across biological replicates of independently imaged spheroids (figure 5.8) These species play central roles in the HBP from which the high energy end product **UDP-GlcNAc** is catabolised from glucose, glutamine, acetyl-CoA and **UTP**.[163] **UDP-GlcNAc** goes on to play an important role in proliferation by contributing to the synthesis of glycosaminoglycans, proteoglycans, and glycolipids, which regulate cell signalling and enzyme activity in primary metabolism.[164,165]

m/z	Mass error (ppm)	Neutral formula	Assignment	Ion density map	ROC plot	Box and whisker plot	Isotope distribution
300.049	0.303	$C_8H_{16}NO_9P$	N-acetylglucosamine-1-phosphate		AUC = 0.918	Outer Centre	300 301 302
323.029	0.464	$C_9H_{13}N_2O_9P$	Uridine monophosphate		AUC = 0.824	Outer Centre	323 324 325
402.995	0.022	$C_9H_{14}N_2O_{12}P_2$	Uridine diphosphate		AUC = 0.992	Outer Centre	403 404 405
482.961	0.019	$C_9H_{15}N_2O_{15}P_3$	Uridine triphosphate		AUC = 0.960	Outer Centre	483 484 485
606.075	0.169	$C_{17}H_{27}N_3O_{17}P_2$	Uridine diphosphate-N-acetyl glucosamine		AUC = 0.887	Outer Centre	606 607 608

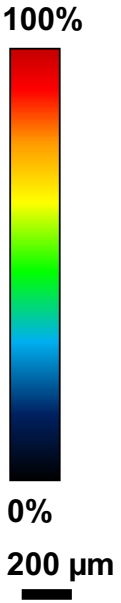

Figure 5.7. Discriminatory analysis for the identified five outer discriminatory molecules. Formulae were assigned with a sub-ppm error. For each formula identified, the ion density map, ROC, box and whisker plot, and isotope pattern are shown. Expected isotope pattern is overlaid as a scatter plot on the spectrum.

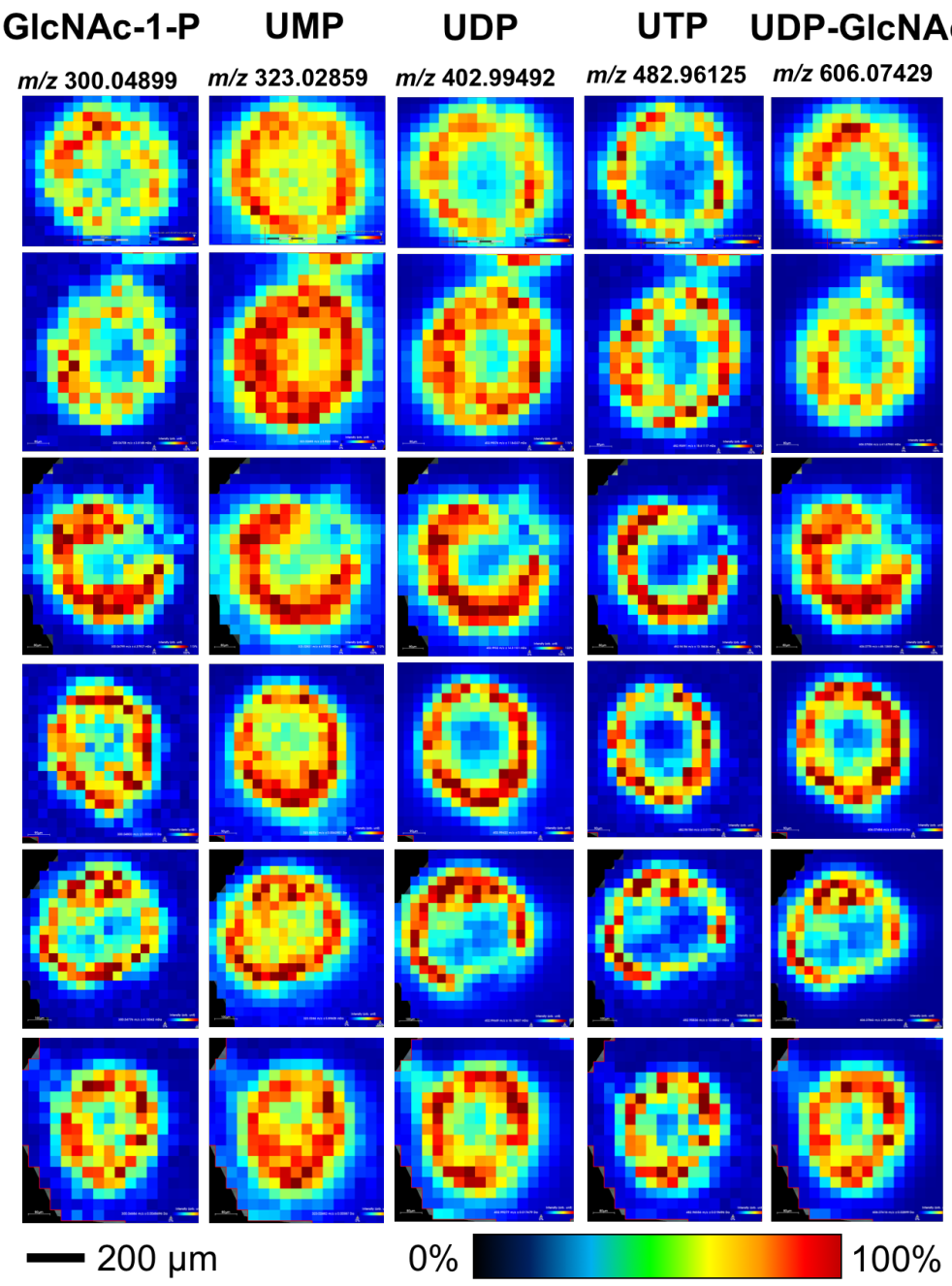

Figure 5.8. Biological replicates of the distributions of the discriminatory molecules identified in the outer region of an MCF-7 spheroid.

It is thought that under conditions of energetic surplus, 10% of glycolysis flux is redirected into the HBP to produce **UDP-GlcNAc**. However, as a result of insufficient oxygen, glucose is re-directed through glycolysis to produce **ATP** as an energy source, reducing the flux through the HBP.[145,146] This is supported by the

decreased levels of HBP intermediates in the centre of the spheroid. In addition, we observed upregulation of assigned glycolysis intermediates in the centre of the spheroid. This included $C_6H_{13}O_9P$ (*m/z* 259.02244) corresponding to hexose-monophosphates (e.g. glucose-6-phosphate (**G-6-P**), galactose-6-phosphate and fructose-6-phosphate (**F-6-P**)), as well as fructose-1,6-bisphosphate (**F-1,6-BisP**) (*m/z* 338.98877) (figure 5.9). The cleavage of F-1,6-BisP during the next steps of glycolysis produces dihydroxyacetone phosphate (**DHAP**) and glycerol-3-phosphate, whose distributions were not observed.

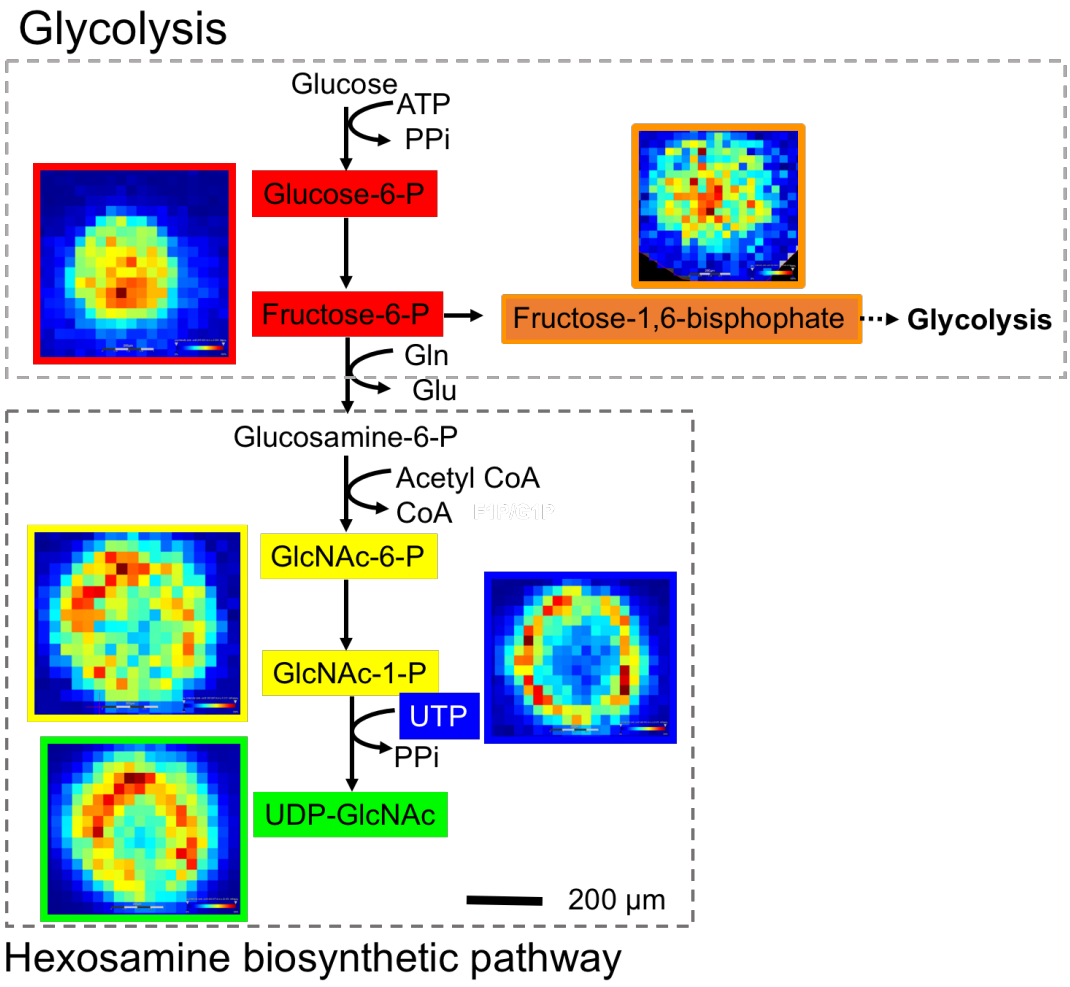

Figure 5.9. The elemental formula of the metabolites assigned can be mapped onto the HBP. Note how the HBP is upregulated in the outer region, whereas glycolysis intermediates are upregulated in the centre region. Glucosamine-6-phosphate was not observed using MSI.

5.2.2.2 High energy cytidine phosphates localise in areas of low oxygen availability

The five molecules that discriminated most strongly towards the centre region were also identified using the HMDB with sub-1 ppm error. Four of these are related metabolites and all contain cytidine, including cytidine diphosphate (**CDP**) (AUC = 0.967), cytidine monophosphate (**CMP**) (AUC = 0.978), CDP-ethanolamine (AUC = 0.979), and cytidine-2',3'-cyclic phosphate (**cCMP**) (AUC = 0.950) (Figure 5.10). These distributions were reproducible across independently imaged biological replicates (figure 5.11). Cytidine and uridine have a mass difference of 0.98401 Da, (**UDP**: $[M-H]^-$ *m/z* 323.02859; **CDP**: $[M-H]^-$ *m/z* 322.04458). The high spectral resolution offered by FT-ICR allows the resolution of the monoisotopic peak of **UDP** to the first isotope of **CDP** with ease (figure 5.12).

m/z	Mass error (ppm)	Neutral formula	Assignment	Ion density map	ROC plot	Box and whisker plot	Isotope distribution
259.022	0.239	$C_6H_{13}O_9P$	Fructose-1-phosphate		AUC = 0.953	Outer Centre	259 260 261
304.034	0.658	$C_9H_{12}N_3O_7P$	Cytidine-2',3'-cyclic phosphate		AUC = 0.950	Outer Centre	304 305 306
322.045	0.543	$C_9H_{14}N_3O_8P$	Cytidine monophosphate		AUC = 0.978	Outer Centre	322 323 324
402.011	0.375	$C_9H_{15}N_3O_{11}P_2$	Cytidine disphosphate		AUC = 0.967	Outer Centre	402 403 404
445.053	0.189	$C_{11}H_{20}N_4O_{11}P_2$	Cytidine disphosphate -Ethanolamine		AUC = 0.979	Outer Centre	445 446 447

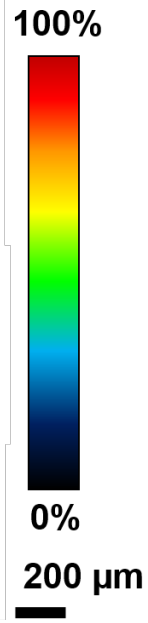

Figure 5.10. Discriminatory analysis for the identified five centre discriminatory molecules. Formulae were assigned with a sub-ppm error. For each formula identified, the ion density map, ROC, box and whisker plot, and expected isotope pattern are shown. Expected isotope pattern is overlaid as a scatter plot on the spectrum.

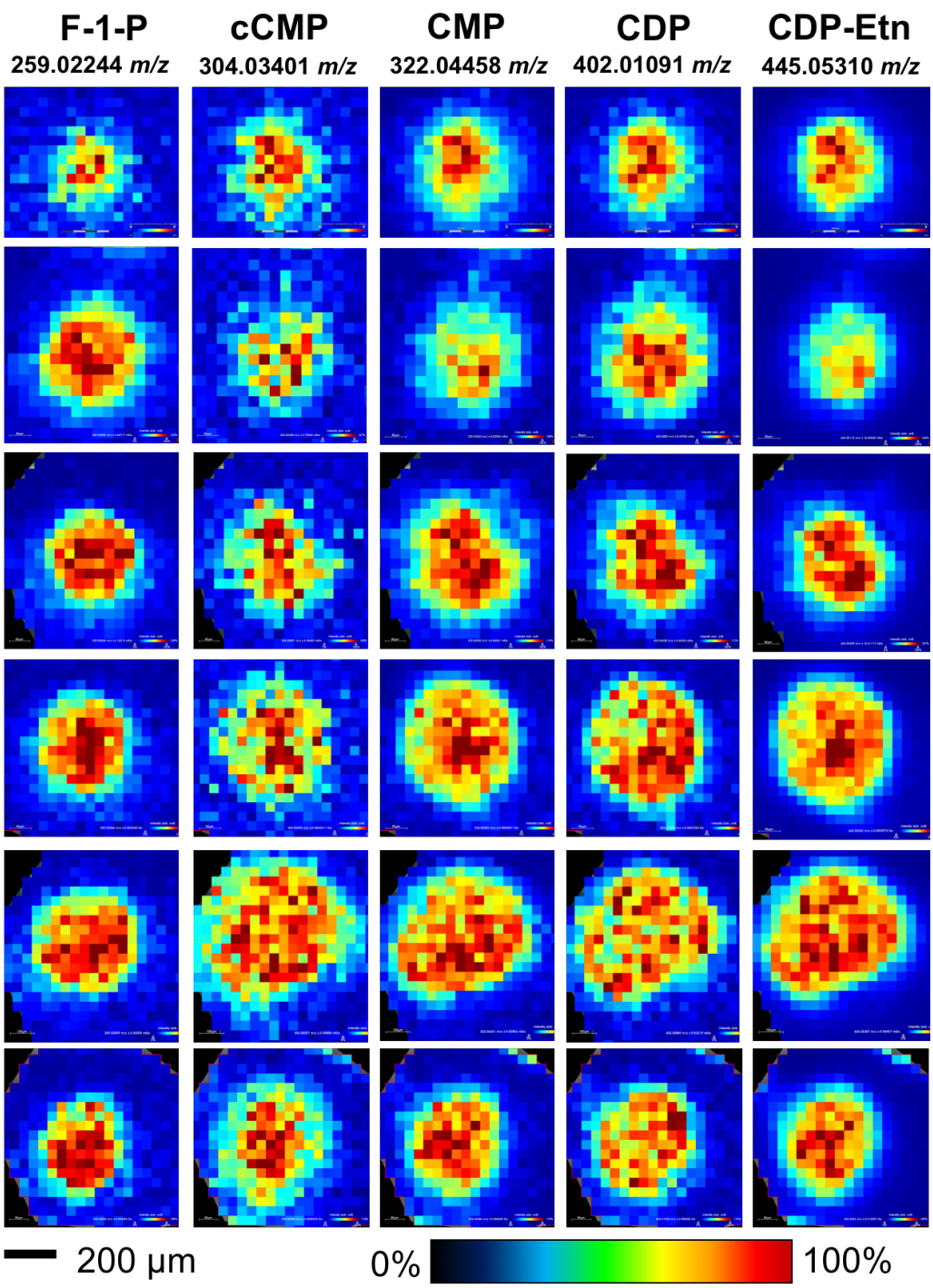

Figure 5.11. Biological replicates of the distributions of the discriminatory molecules identified in the centre region of an MCF-7 spheroid.

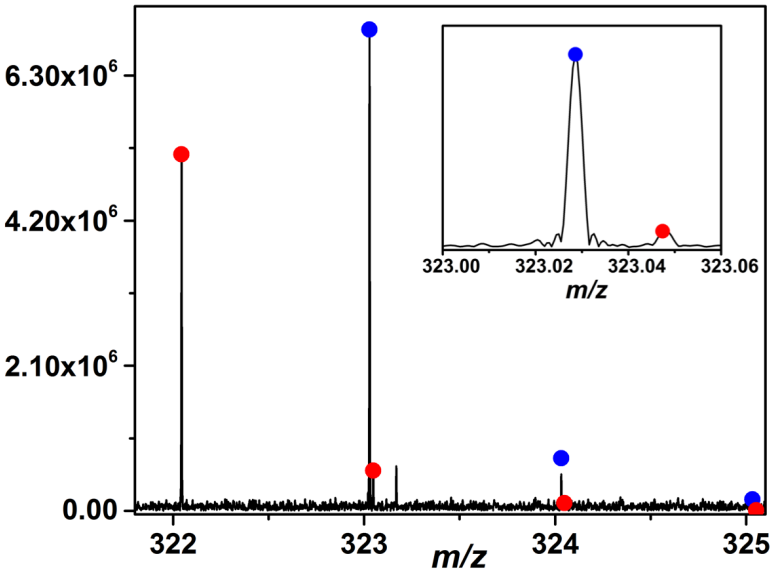

*Figure 5.12. The high resolution of the FT-ICR MS resolves the sub-1 Da mass difference between the monoisotopic peak of **UMP** (blue) and the first isotope peak of **CMP** (red).*

High-energy cytidine phosphates are utilised in the post-translational modification of glycoproteins and glycosylation of glycolipids with N-acetylneuraminic acid (**NeuNAc**). This modification is produced as an end-product of the sialic acid pathway (figure 5.13). Interestingly, there is evidence that cancer cells present elevated levels of neuraminic acid, which has been suggested to play an important role in malignancy and the evasion of the immune system.[165] Furthermore, it is thought that hypoxia further increases the expression of intracellular **NeuNAc**.[166]

In addition, the sialic acid pathway and the HBP are closely linked, whereby **NeuNAc** can be converted to **CMP-NeuNAc** for use in the sialic pathway, or alternatively isomerised to N-acetylmannosamine (**ManNAc**), which can be converted back into **GlcNAc** and salvaged back into the HBP (figure 5.13).[146] As shown in our data, the intermediates of both these pathways have distinct distributions in the MTS. The high energy uridine phosphates associated with the HBP are localised towards the outer proliferative regions (figure 5.9). In contrast, high energy cytidine phosphates distribute towards the oxidative hypoxic conditions of the central region (figure 5.10). These distibutions suggest that the microenvironments within MTS display distinct metabolic fluxes in these pathways.

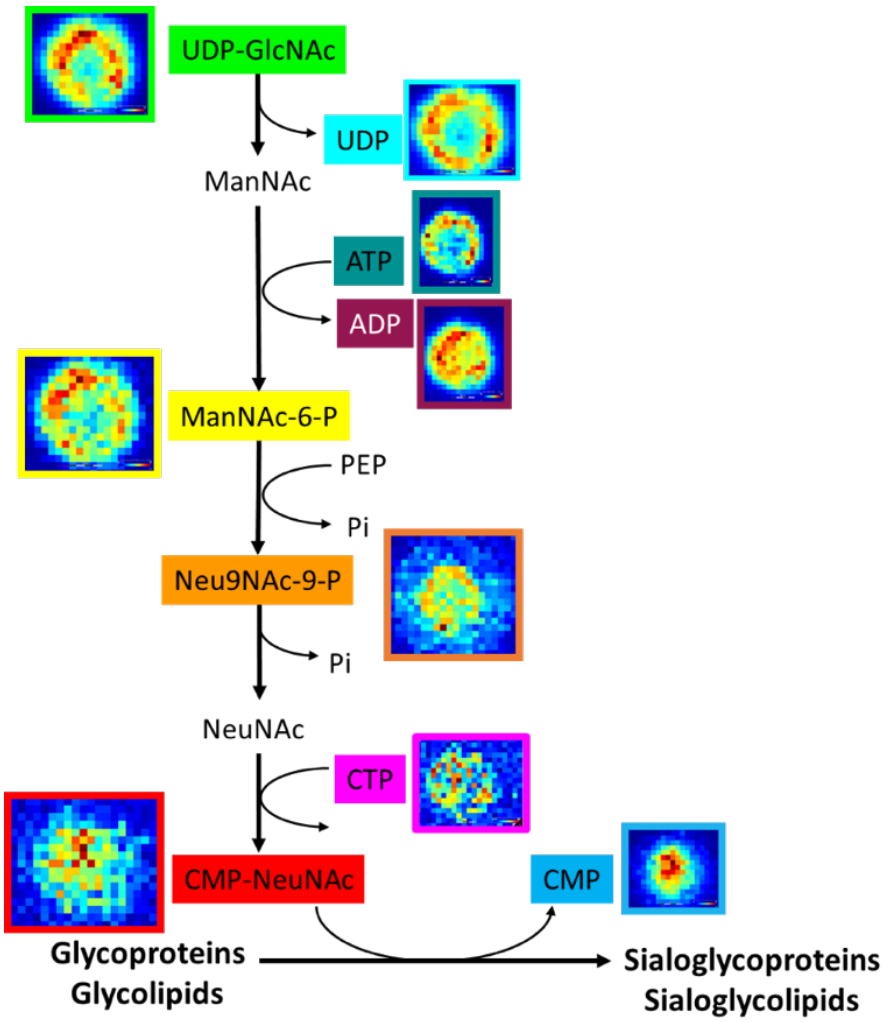

Figure 5.13. Sialic acid pathway. N-acetyl neuraminic acid (sialic acid) is formed by the end product of the HBP. ***UDP-GlcNAc*** *Uridine N-acetylglucosamine;* ***UDP*** *Uridine diphosphate;* ***ATP*** *adenosine triphosphate;* ***ADP*** *adenosine diphosphate;* ***ManNAc-6-P*** *N-acetylmannosamine-6-phosphate;* ***PEP*** *Phosphoenol pyruvate;* ***Neu9NAc-9-P*** *N-acetylneuraminic acid-9-phosphate;* ***NeuNAc*** *N-acetylneuraminic acid;* ***CMP-NeuAc*** *cytidine monophosphate N-acetylneuraminic acid;* ***CMP*** *cytidine monophosphate.*

5.3 Conclusions

Here, high resolution MSI has been used to determine metabolite distributions within MTS cell culture models. Metabolite markers have been employed to indicate regions of increased oxidative stress and hypoxia. In addition, the information obtained using this approach may be informative for investigating the regional flux

through biochemical pathways. Here, an upregulation of metabolic branch pathways such as the HBP in the regions of the spheroid with greater access to oxygen was observed. Conversely, there is greater glycolytic flux within the regions limited by hypoxia. However, the presence of ionisation bias enables the comparison of relative intensities, but prevents any definitive quantification of the distributions observed. This methodology shows great promise for applications in toxicity studies during drug development, whereby the ADME of the drug could be correlated with its effects on cellular metabolism.

Chapter 6.

Observing the distribution of a hypoxia marker within multicellular tumour spheroids

6.1 Introduction

Oxygen is vital for cell survival, as it is the terminal electron acceptor in cellular respiration. Under conditions of insufficient oxygen; a phenomenon known as hypoxia, cells die by necrosis or apoptosis.[167] Many solid tumours experience hypoxia and trigger complex responses for adaptation, survival, and metastasis.[168] Therefore, understanding the effects of these hypoxia-induced changes in tumours is essential for the development of effective cancer treatments.[168]

To detect hypoxic regions in tissues, various probes have been developed. A number of these contain a 2-nitroimidazole structure that readily undergoes reductive metabolism and uniquely accumulates in hypoxic regions.[169] Pimonidazole is a 2-nitroimidazole-based marker used for measuring tumour hypoxia in pathological research.[170,171] Under hypoxic conditions, the nitro group on the imidazole ring is reduced in a series of steps to produce highly reactive products, which can covalently bind to cellular nucleophiles such as thiol-containing proteins.[167,168]

Figure 6.1 outlines a suggested metabolism of pimonidazole reduction. First, a two-electron reduction produces nitroso-pimonidazole (2) through a highly reactive and short lived nitrenium intermediate.[168,170,172] A second two-electron reduction product forms pimonidazole hydroxylamine (3). This product can then covalently bind to nucleophilic macromolecules (5), or conjugate with glutathione (6) in cells.[170,172,173] Alternatively, the hydroxylamine can undergo a further reduction to yield an amine derivative (4).[168,172,174]

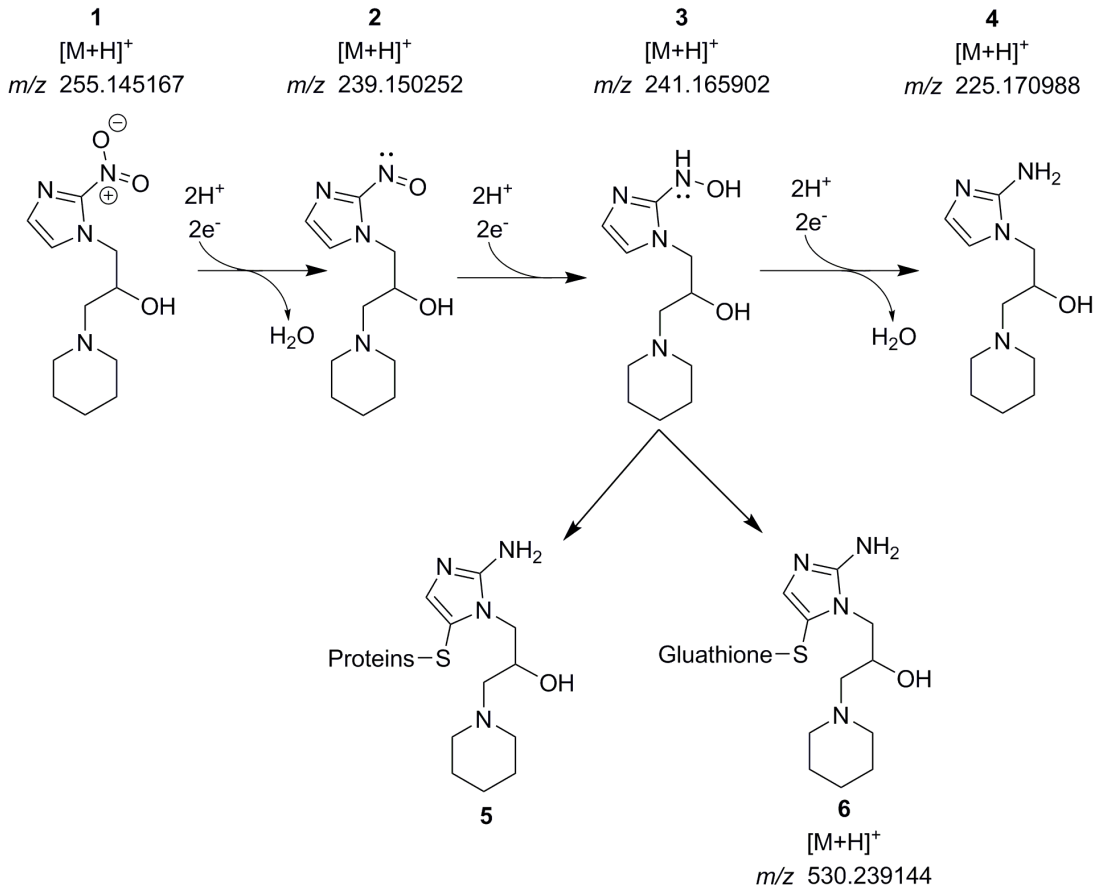

Figure 6.1. Suggested mechanism for the accumulation of pimonidazole in hypoxic tissue regions. Under hypoxic conditions, the nitro group on the imidazole ring is reduced in a series of steps to produce a product capable of covalently binding to proteins, glutathione, and other macromolecules within the cell.

MSI is advantageous over immunohistochemical techniques, as it provides an untargeted approach that does not require a specific label or antibody.[170] Because of the basic properties of the piperidine side chain, pimonidazole is suitable for mass spectral detection.[168] MSI has been applied to identify pimonidazole and a number of its reduced forms, including the glutathione conjugate, which was found to colocalise with the immunohistochemically stained areas corresponding to hypoxic tissue.[170]

In this chapter, the use of MALDI-MSI to map the distribution of pimonidazole within MTS will be discussed. Initially, human prostate cancer (PC3) spheroids were cultured over 14 days to approximately 500 μm in diameter. The spheroids were

subsequently dosed with pimonidazole for 24 hours, and MALDI ToF and FT-ICR MSI were carried out. CASI was employed to lower the limit of detection and increase the signal intensity of pimonidazole and its metabolites. Finally, a dosing time course was used to assess the time-dependent penetration of the hypoxia marker into the spheroids.

6.2 Results and discussion

6.2.1 Initial method development

To establish the ionisation efficiency of pimonidazole, MALDI MS was carried out. 100 μM pimonidazole was mixed with either DHB or CHCA and 15 spectra were averaged using ToF MS (see methods section 3.4.1 for details) (figure 6.2). DHB produced a signal 100-fold more intense than CHCA and did not present other significant peaks within the region of the monoisotopic peak. Unlike previously published literature,[168] fragmentation of the parent ion did not occur under the experimental conditions employed.

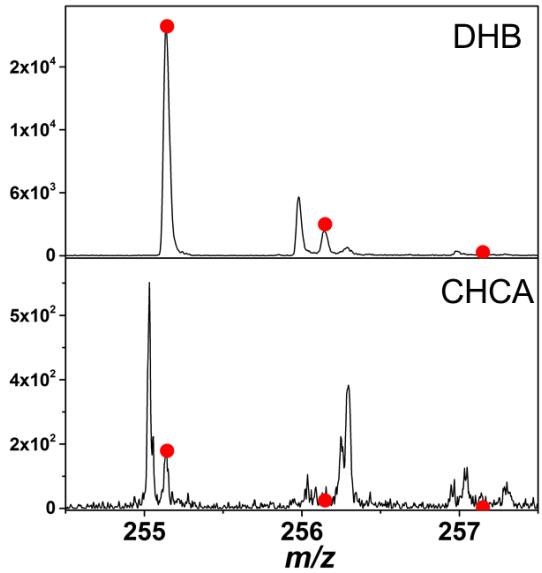

Figure 6.2. MALDI MALDI MS of pimonidazole on steel plates with (top) DHB and (bottom) CHCA as the matrix. Expected isotope pattern is overlaid as a scatter plot.

To establish the correct dosing concentration, 14-day-old PC3 spheroids were cultured using the hanging drop method and dosed with a range of pimonidazole concentrations from 100 μM to 1 mM for 24 hours. After dosing the spheroid at

concentrations below 200 μM, no peaks corresponding to pimonidazole or its metabolites were observed by MSI, whereas concentrations greater than 500 μM resulted in disintegration of the spheroid during incubation (figure 6.3). Therefore, a concentration of 200 μM was selected for further experiments.

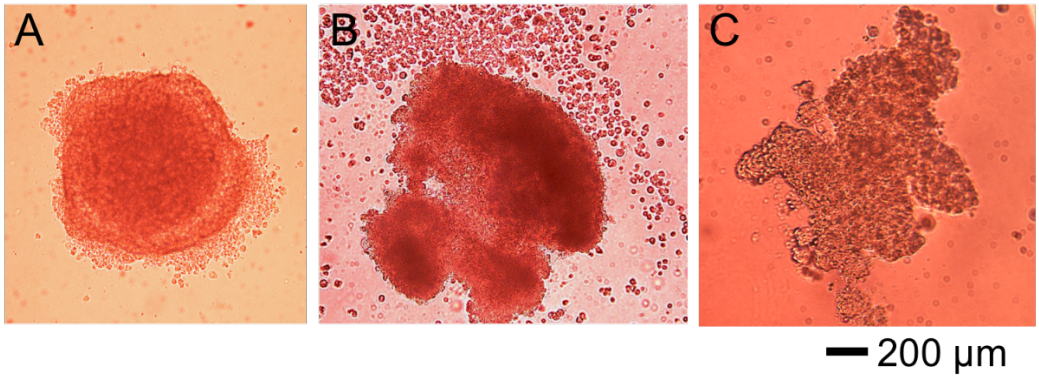

Figure 6.3. Microscope image of a PC3 spheroid dosed with (A) 200 μM (B) 500 μM and (C) 1 mM pimonidazole for 24 hours.

6.2.2 MSI of pimonidazole

To observe the distribution of pimonidazole and its metabolites after 24 hours, MALDI-MSI was employed. 14-day-old PC3 spheroids were dosed with 200 μM pimonidazole for 24 hours and prepared for imaging as previously discussed. DHB was used as the matrix and the spheroids were imaged in positive mode at 40 μm spatial resolution. H&E staining was used to confirm the structural integrity of the spheroids after sectioning.

6.2.2.1 ToF MSI of pimonidazole

Initially, positive mode MALDI ToF MSI was performed on dosed and untreated PC3 spheroids. Imaging runs were calibrated using red phosphorus prior to imaging and using internal DHB peaks post-imaging (see methods section 3.5.1 and table 3.5 for details). Using TIC normalisation, a low intensity peak consistent with pimonidazole at *m/z* 255.145 was observed in the treated spheroid and in the gelatin surrounding the control spheroid with a mass error of 1.2 ppm (figure 6.4). An exported pixel from the control and treated spheroid shows that the peak corresponding to pimonidazole is uniquely present within the dosed spheroids and absent in the control.

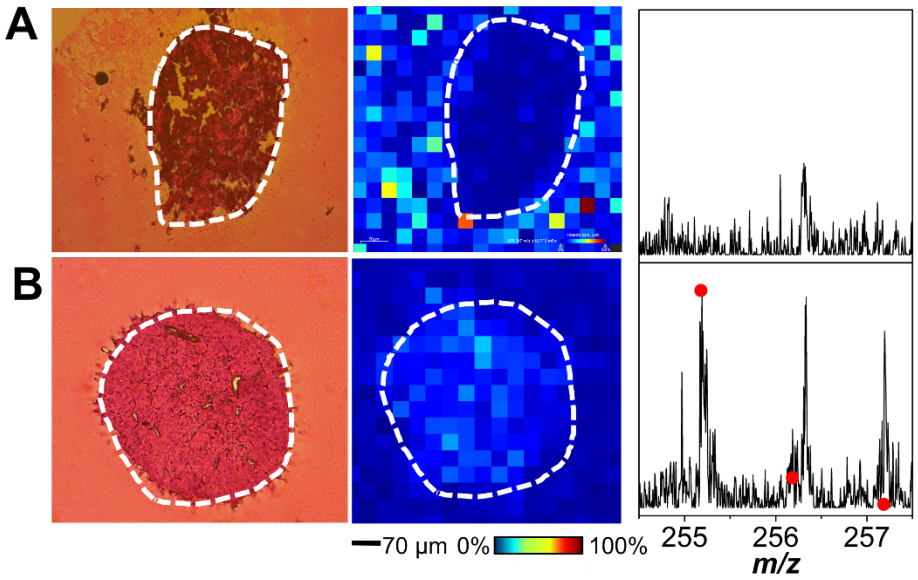

Figure 6.4. MALDI ToF MSI of pimonidazole (m/z 255.145) in (A) control and (B) dosed PC3 spheroids. H&E staining was used to confirm the morphology of the spheroid. The predicted isotope pattern is plotted over the data as a scatter plot with a 1.4 ppm error.

An advantage of MSI is the global untargeted analysis across the entire mass range imaged. This untargeted approach enables the visualisation of pimonidazole and its metabolites within the same spheroid (figure 6.5). The ion density maps show that all of the metabolites distribute uniformly across the spheroid. Furthermore, both the parent ion (**1**, *m/z* 255.145) and the nitroso ion (**2**, *m/z* 239.150) are present at significantly lower intensities than the subsequent reduction species. Whilst MSI is currently not a quantitative technique, the relative intensities of the metabolites can be observed using a box and whisker plot (figure 6.6). These show that pimonidazole and the nitroso ions have low relative intensities, whereas the hydroxylamine (**3**, *m/z* 241.166) and amine (**4**, *m/z* 225.171) derivatives are present at much higher relative intensities. Using an exported pixel, the S/N of the parent ion and its metabolites were 3, 6, 96 and 122 respectively. As a result of the low S/N for the ions observed, the control produces a false positive, however these values are all significantly lower than the dosed spheroid. The spectra are normalised using TIC, and the box and whisker plots are plotted as a percentage of the most abundant metabolite observed. The errors were calculated as 4.4, 4.8, and 1.3 ppm for the nitroso (**2**), hydroxylamine (**3**), and amine (**4**) metabolites respectively.

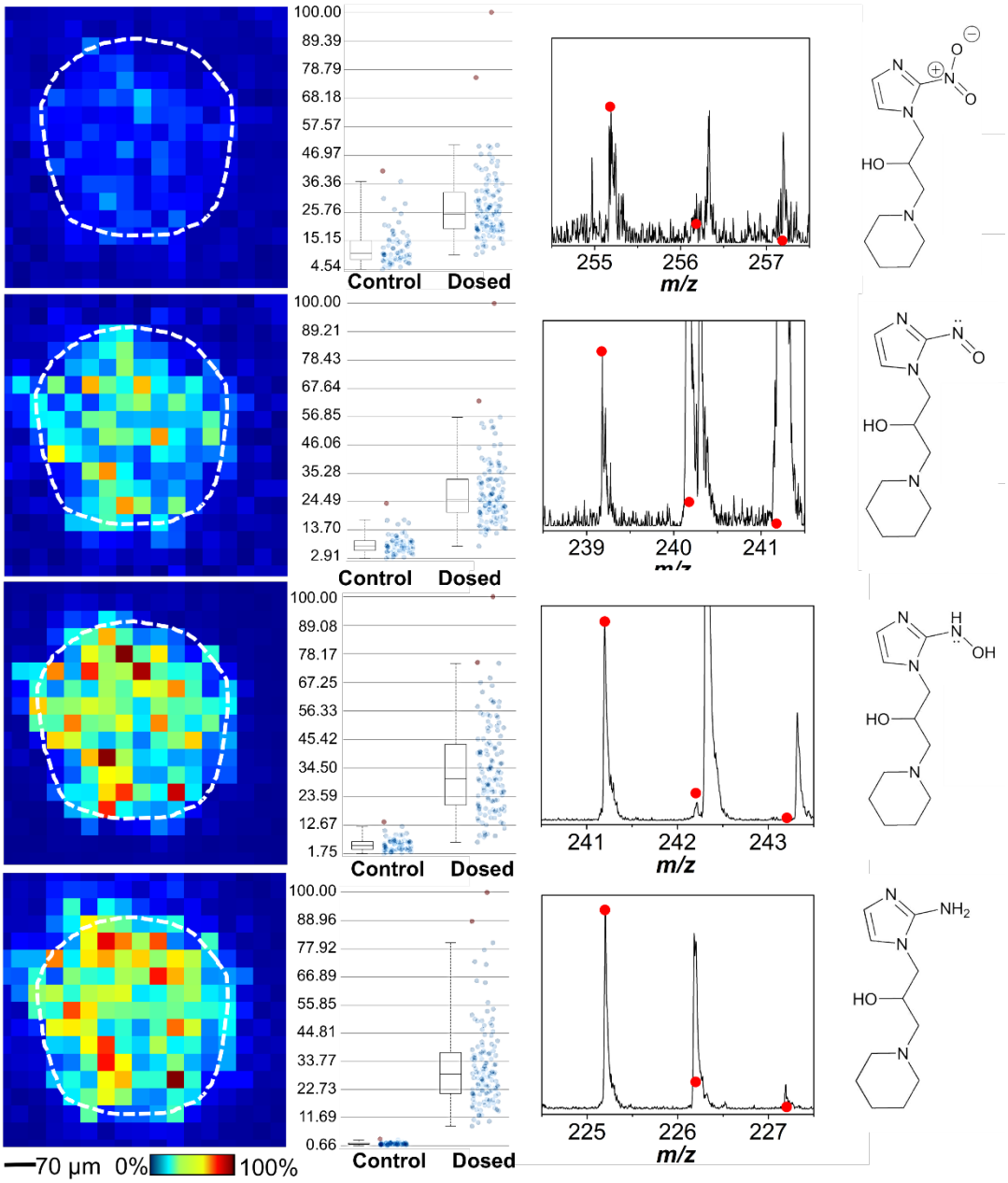

Figure 6.5. ToF MSI of pimonidazole-dosed spheroids over 24 hours. Ion density maps of pimonidazole (m/z 255.145), nitroso (m/z 239.150), hydroxylamine (m/z 241.166), and amine (m/z 225.171) derivatives. The box and whisker plots compare the intensity of each respective metabolite between the treated and control spheroids. The predicted isotope patterns are plotted over the data as scatter plots with 1.4, 4.4, 4.8, and 1.3 ppm errors respectively.

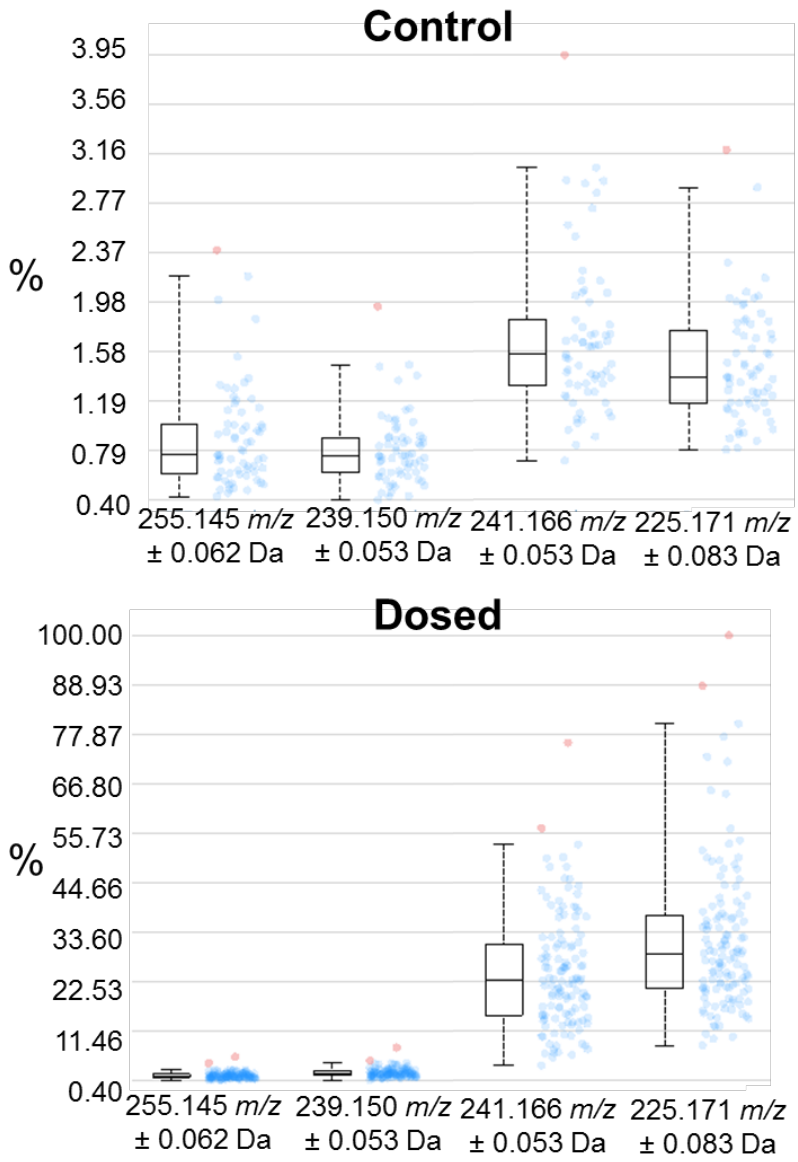

Figure 6.6. Box and whisker plots showing the intensity of the parent ion and each metabolite after 24 hours of dosing compared to an untreated spheroid (control). The values are normalised against the highest peak intensity within the regions selected.

Whilst the peaks are absent in the control, the high errors after calibration prevent confident assignment of the peaks using *m/z* values alone. Therefore, MALDI FT-ICR MSI was employed for confident assignment of the peaks without the requirement for MS/MS.

6.2.2.2 FT-ICR MSI of pimonidazole

PC3 spheroids were prepared as previously discussed and imaged at 40 µm resolution using the 12T FT-ICR in positive mode. Quadratic calibration of representative exported pixels post-imaging was carried out using internal peaks (see methods, table 3.2 for details). However, unlike ToF MSI, the pimonidazole parent ion was not observed in the ion density maps or an exported pixel (figure 6.7).

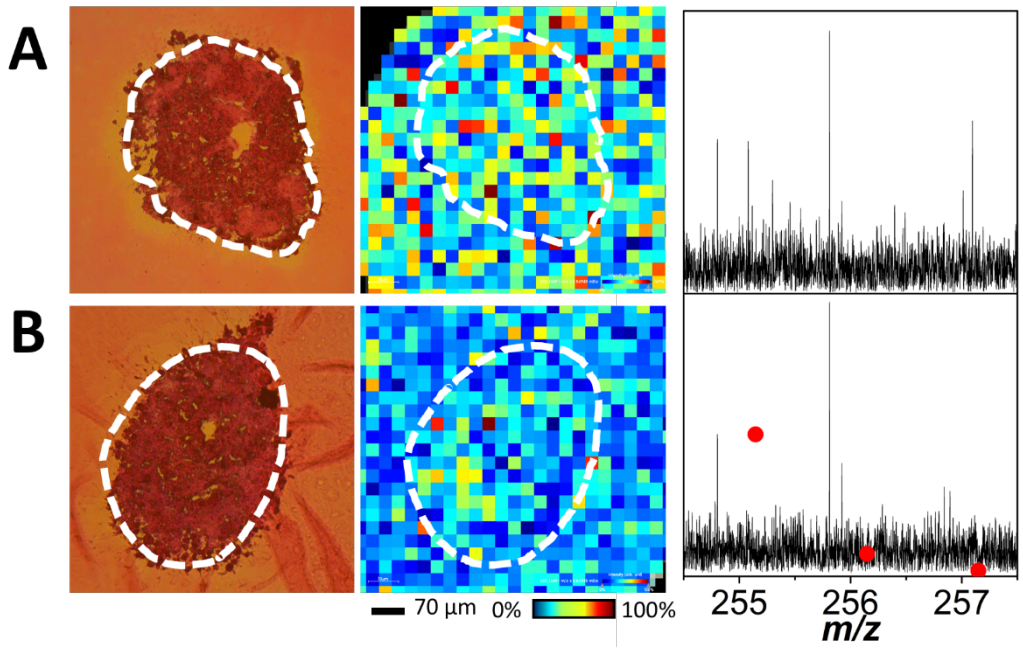

Figure 6.7. FT-ICR for pimonidazole (m/z 255.14517) in (A) control and (B) dosed PC3 spheroids. H&E staining was used to confirm the morphology of the spheroid. The predicted isotope pattern is plotted as a scatter plot over the data.

Despite the absence of pimonidazole, all three of the metabolites were observed within the spheroid at low intensity and with sub-ppm errors (figure 6.8). Furthermore, the distributions of the metabolites were unique from those observed by ToF. Whilst the nitroso ion (**2,** *m/z* 239.15025) displayed a uniform distribution across the spheroid, the other derivatives were localised towards the centre of the spheroid. This could be suggestive of the pimonidazole undergoing reduction as a result of the hypoxic environment at the centre of the spheroid.

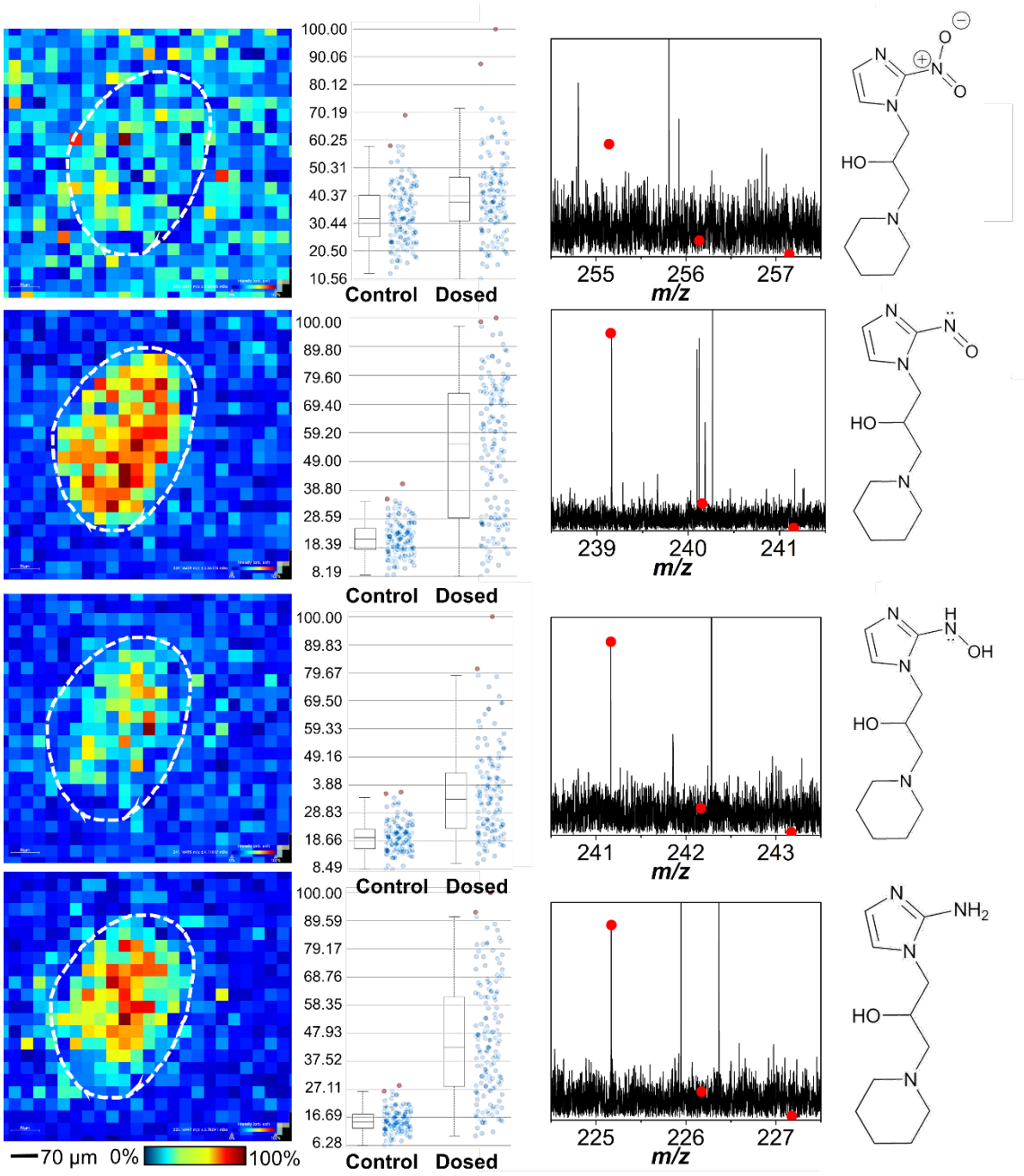

Figure 6.8. FT-ICR MSI of pimonidazole-dosed spheroids over 24 hours. Ion density maps of pimonidazole (m/z 255.14517), nitroso (m/z 239.15025), hydroxylamine (m/z 241.16590), and amine (m/z 225.17099) derivatives. The box and whisker plots compare the intensity of each respective metabolite between the treated and control spheroids. The predicted isotope patterns are plotted over the data as a scatter plots with calculated errors of 0.408, 0.482, and 0.222 ppm for each metabolite respectively.

The box and whisker plots show that pimonidazole is present at a value equivalent to the control, suggesting the peak is the result of the baseline noise, whereas the other metabolites are all present at higher intensities. Moreover, the nitroso (**2,** *m/z* 239.15025) and amine (**4**, *m/z* 225.17099) metabolites are present at the highest relative intensities of the metabolites observed, suggesting that pimonidazole is reduced over 24 hours within the spheroid (figure 6.9). The lower intensity of the hydroxylamine product could be the result of its reaction with intracellular macromolecules. However, due to the variety of proteins it can conjugate to within the cell, these are not observed within the mass range imaged.

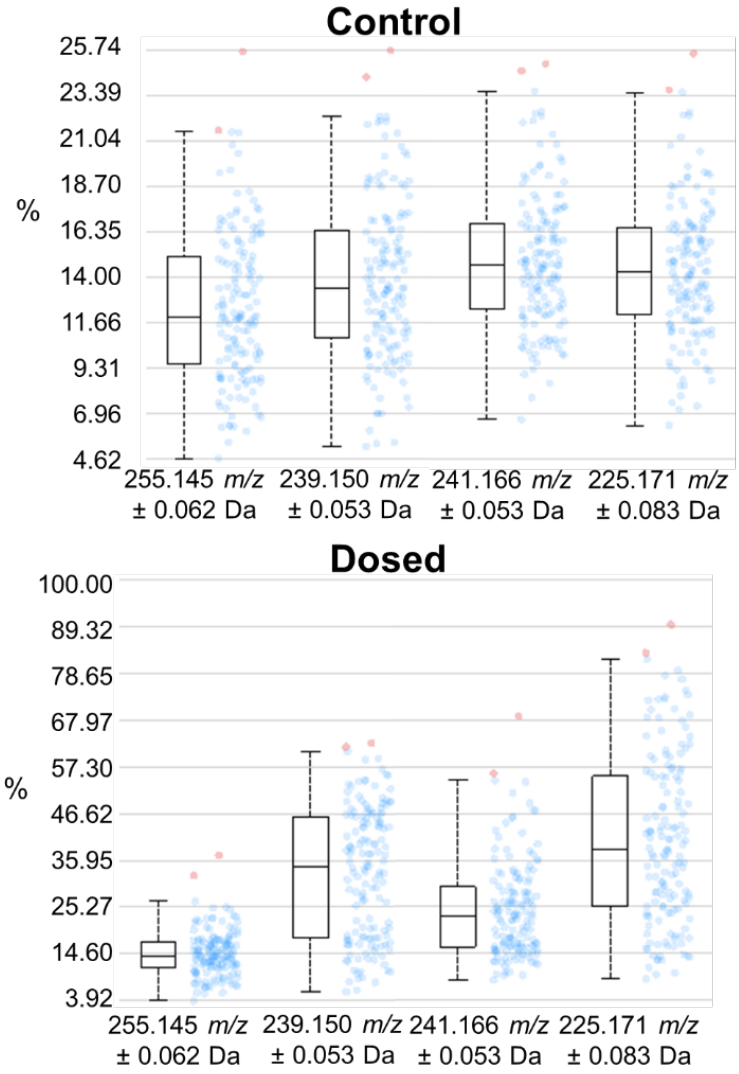

Figure 6.9. Box and whisker plot showing the intensity of pimonidazole and its metabolites after 24 hours. The values are normalised against the highest peak intensity.

Previous literature suggests that the glutathione conjugate of the hydroxylamine reduction product colocalises with regions of hypoxia. However, the glutathione conjugate (*m/z* 530.23914) was not observed by either MALDI ToF or FT-ICR MSI (figure 6.10). The ion density map produced a signal that was localised to the surrounding regions of the spheroid. However, this was present in both the control and the dosed spheroid, suggesting this could be the result of a matrix or gelatin-related peak.

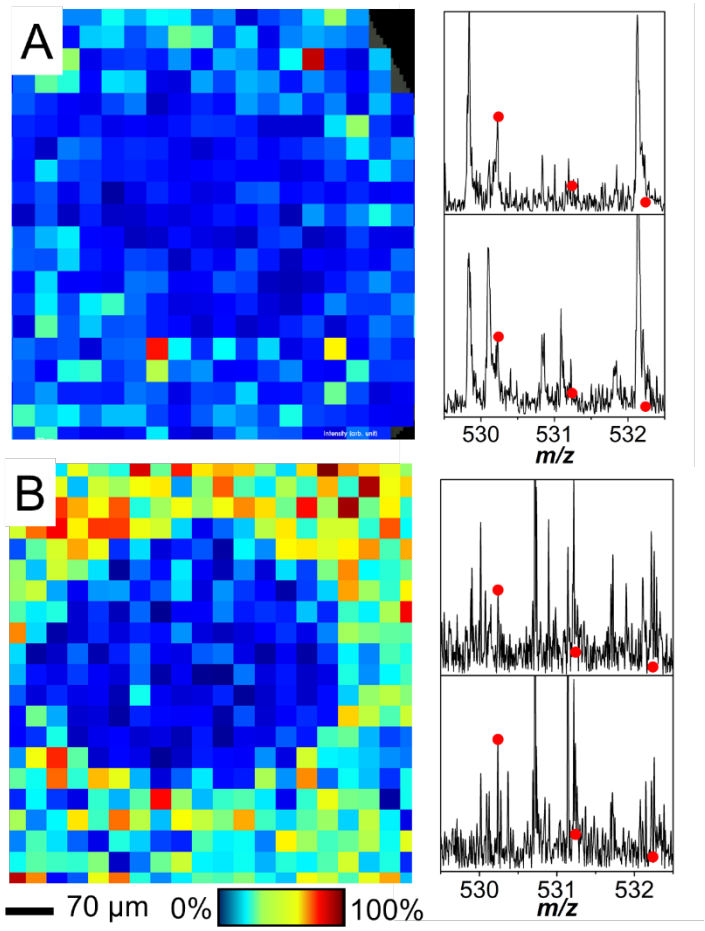

Figure 6.10. Ion density map showing the distribution of m/z 530.23914 corresponding to the pimonidazole glutathione conjugate in (A) ToF MSI and (B) FT-ICR MSI after 24 hours. The predicted isotope pattern is plotted over the data as a scatter plot.

Alternative literature has detected the presence of an additional pimonidazole reduction product at *m/z* 223.15528, which is suggested to colocalise with regions of hypoxia identified by immunohistochemical staining.[168] The identity of the ion was

proposed to have originated from a conjugate that undergoes in-source fragmentation to regenerate the nitrenium ion or a structurally related species.[167,168] The distribution of *m/z* 223.15528 was observed by both ToF and FT-ICR MSI (figure 6.11). Similarly to the metabolite products discussed, the distribution of this ion is uniformly localised when imaged by MALDI ToF MSI, whereas MALDI FT-ICR MSI suggests it is localised to the centre region. The S/N for this ion under ToF MSI was 120, whereas for FT-ICR the S/N was 3.8.

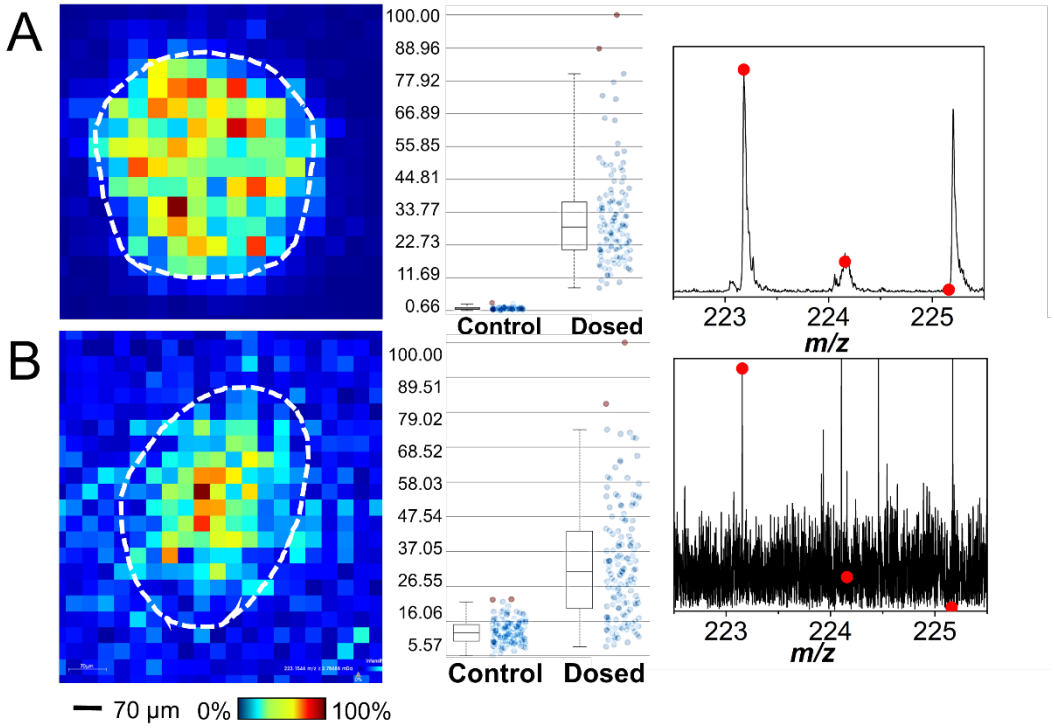

Figure 6.11. MALDI (A) ToF and (B) FT-ICR MSI of m/z 223.15528 in dosed spheroids over 24 hours. The box and whisker plots compare the intensity of each respective metabolite between the treated and control spheroids. The predicted isotope patterns are plotted over the data as scatter plots with a calculated error of 0.4 and 0.158 ppm errors by ToF and FT-ICR respectively.

6.2.3 CASI for improved signal-to-noise of selected ions

Whilst all three metabolites were observed using MALDI FT-ICR MSI, the S/N for each metabolite is very low. The nitroso (**2**), hydroxylamine (**3**), and amine (**4**) reduction products had S/N values of 17.5, 4.3, and 19.4 respectively. Therefore, CASI can be used to increase the S/N, achieve better sensitivity, and lower the limit

of detection for low abundance analytes without the need for MS/MS. In CASI mode, target ions are accumulated and enriched using quadrupoles, increasing the signal intensity of the selected ions.[33]

Initially, MALDI MS CASI was employed to detect the presence of pimonidazole and its metabolites in the spheroids. An average of 15 acquired spectra show that pimonidazole and all three reduction metabolites are observed using a Q1 mass of *m/z* 240 and CASI window of *m/z* 40 (figure 6.12). All four ions were observed at a resolution of over 98000. The S/N for each ion was 402.6, 119.1, 470.0, and 550.9 for pimonidazole (**1**, *m/z* 255.14517*)*, nitroso (**2**, *m/z* 239.15025), hydroxylamine (**3**, *m/z* 241.16590) and amine (**4**, *m/z* 225.17099) ions respectively. This is an increase of over 10-fold for each metabolite. Due to the narrow mass window, single-point calibration was carried out using the parent ion (*m/z* 255.14517).

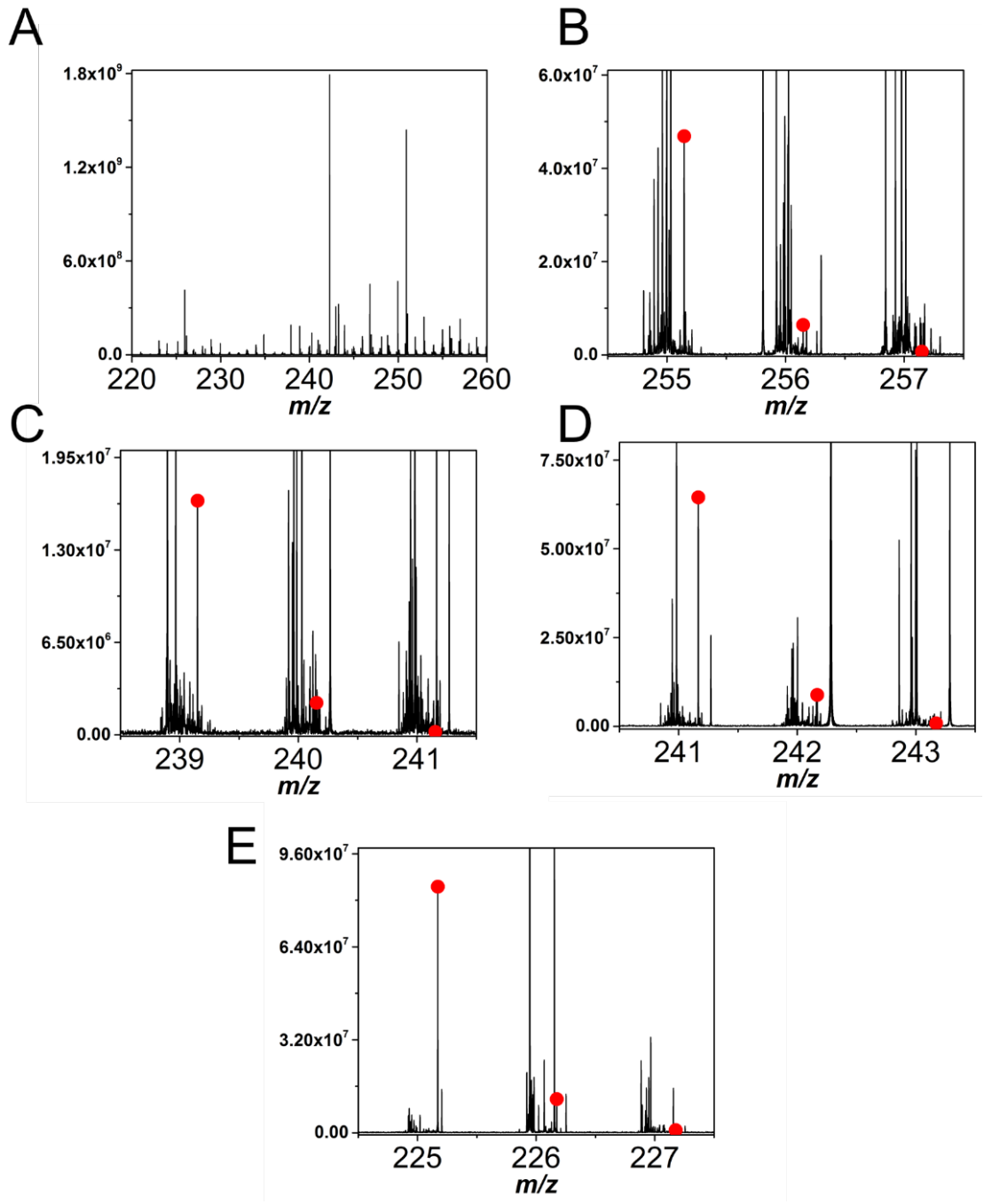

Figure 6.12. (A) MALDI MS of 15 averaged spectra with a CASI window of m/z 40 ionises pimonidazole and all three of its reduction metabolites. (B) Pimonidazole (m/z 255.14517), (C) nitroso (m/z 239.15025), (D) hydroxylamine (m/z 241.16590), and (E) amine (m/z 225.17099) derivatives. The predicted isotope patterns are plotted over the data as scatter plots with 0.000, 0.084, 0.105, and 0.124 ppm mass errors respectively.

As previously discussed, the high spectral resolution obtainable by FT-ICR enables the observation of IFS of the first isotope peak for each metabolite to increase the confidence of the formula assignment. Due to the low signal of the metabolites, the success of the analysis was limited. However, there is some evidence for the correct isotope ratios between the ^{13}C and ^{15}N (Figure 6.13).

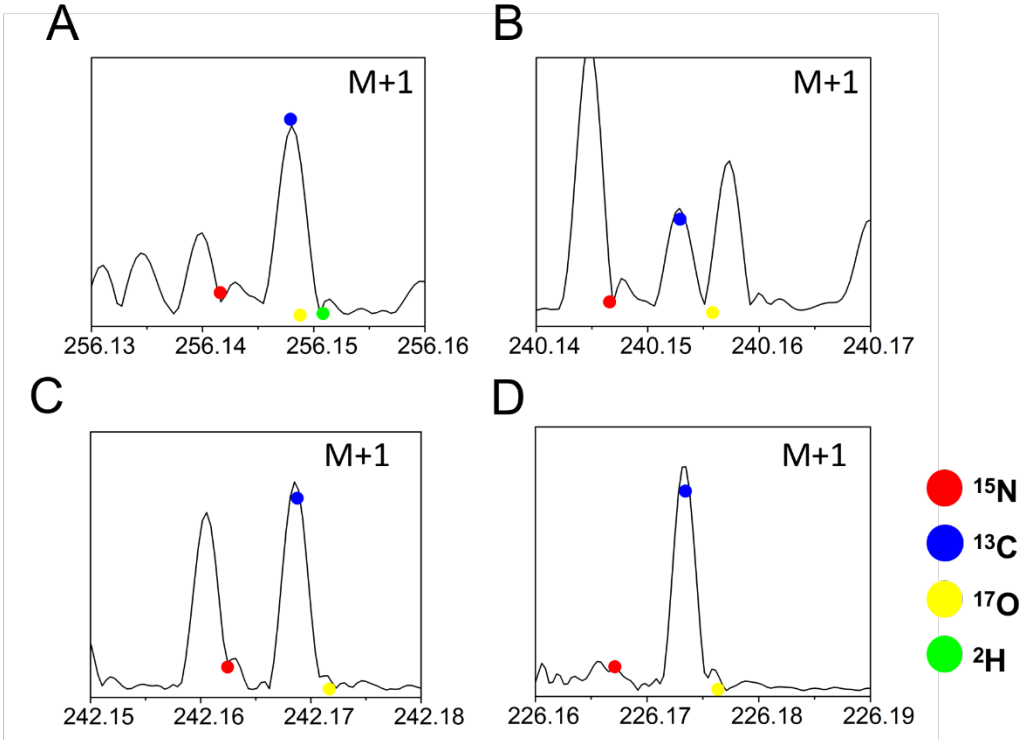

Figure 6.13. The fine structure of the first isotope for (A) pimonidazole and (B–D) its metabolites observed by MALDI MS analysis. (B) Nitroso, (C) hydroxylamine, and (D) amine. The predicted isotope fine structures are plotted over the data as scatter plots.

Based on the spectra obtained, CASI MSI of spheroids was carried out with a Q1 mass of *m/z* 240 and a window of *m/z* 40. Unlike the MALDI FT-ICR MSI data previously, the use of CASI improved the sensitivity and enabled the detection and visualisation of the pimonidazole parent ion (**1**, *m/z* 255.14517) within the spheroid (figure 6.14).

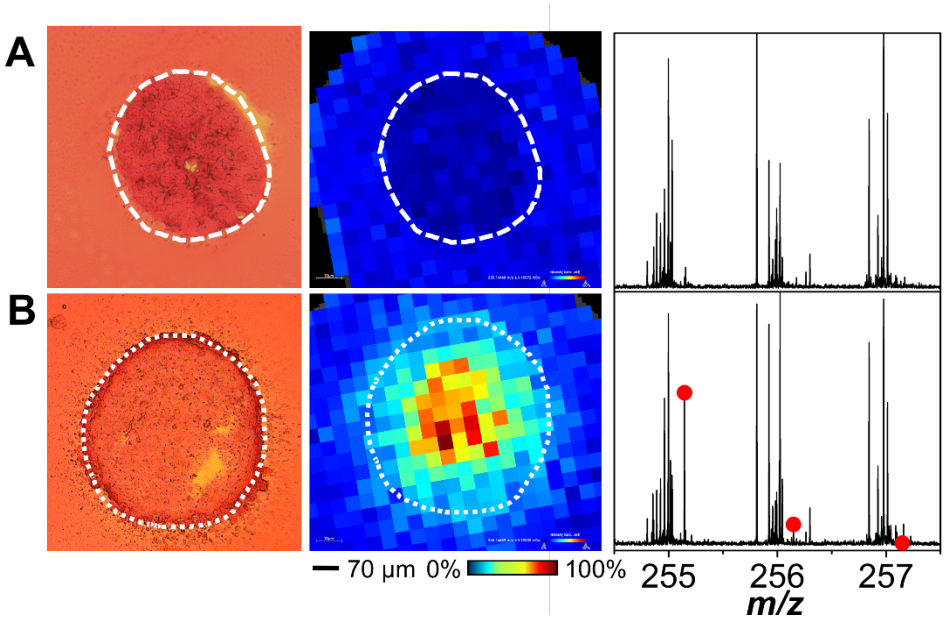

Figure 6.14. FT-ICR for pimonidazole in (A) control and (B) dosed PC3 spheroids with CASI. H&E staining was used to confirm the morphology of the spheroid. The isotope patterns are plotted over the data as scatter plots with a 0 ppm error.

Due to the window of *m/z* 40, it was possible to also observe the distribution of the reduction metabolites across the PC3 spheroid (figure 6.15). These show that pimonidazole and its metabolites all localise to the centre region of the spheroid. The ion density maps suggest that the hydroxylamine (**3**, *m/z* 241.16590) and amine (**4**, *m/z* 225.17099) metabolites are present at higher intensities compared to the parent ion. The S/N for the parent ion and its metabolites was 71.2, 169.9, 27.3, and 189.9 respectively.

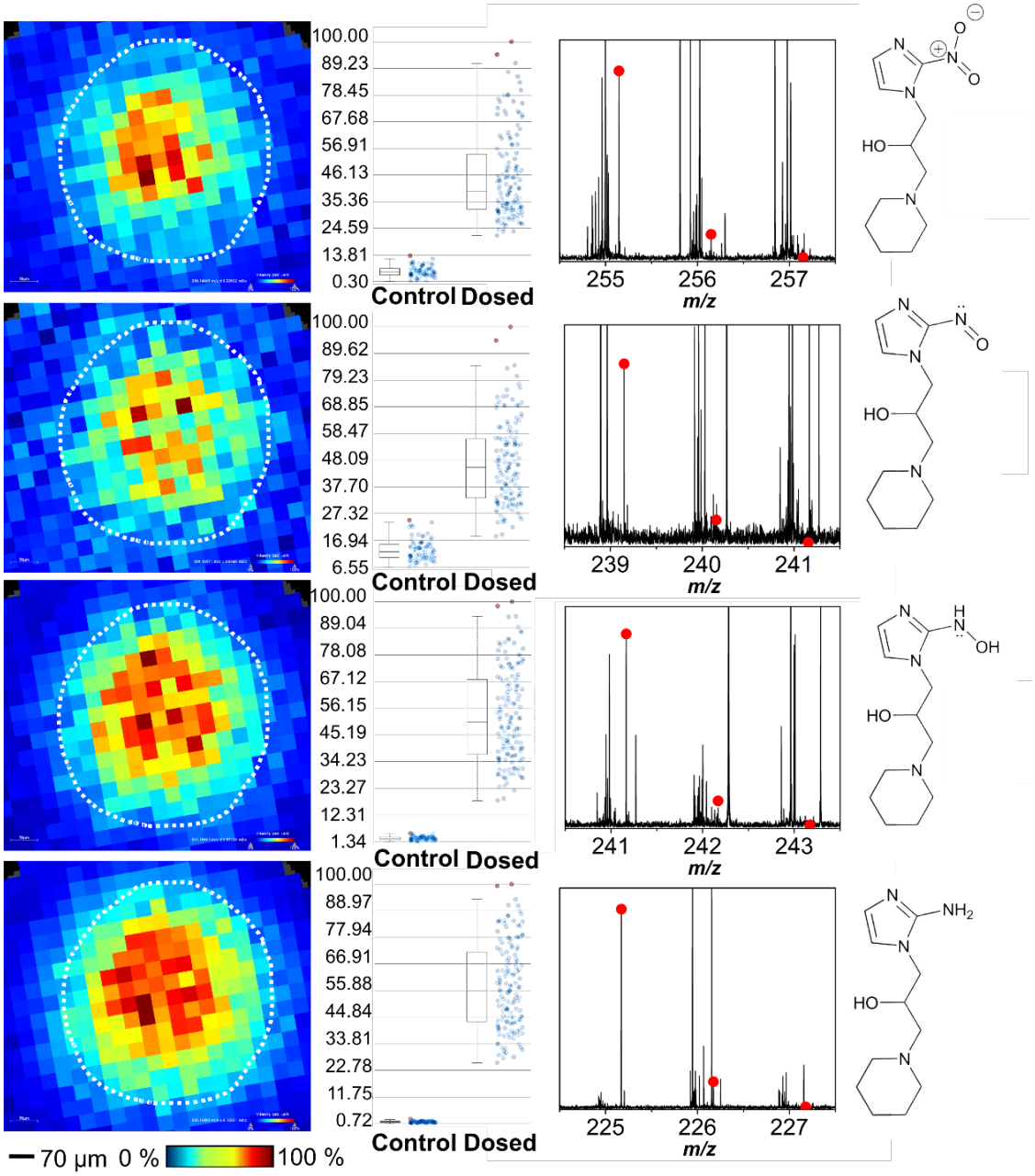

Figure 6.15. FT-ICR MSI of pimonidazole-dosed spheroids over 24 hours with a CASI window of m/z 40. Ion density maps of pimonidazole (m/z 255.14517) and its nitroso (m/z 239.15025), hydroxylamine (m/z 241.16590), and amine (m/z 225.17099) derivatives. The box and whisker plots compare the intensity of each respective metabolite between the treated and control spheroids. The predicted isotope patterns are plotted over the data as scatter plots with 0.000, 0.866, 0.788, and 0.666 ppm errors respectively.

The CASI window utilised also enabled the observation of the pimonidazole-derived reduction product at *m/z* 223.15528. This ion had a similar distribution to the other metabolites and localised towards the centre of the spheroid (figure 6.16). The S/N of this ion was 107.6.

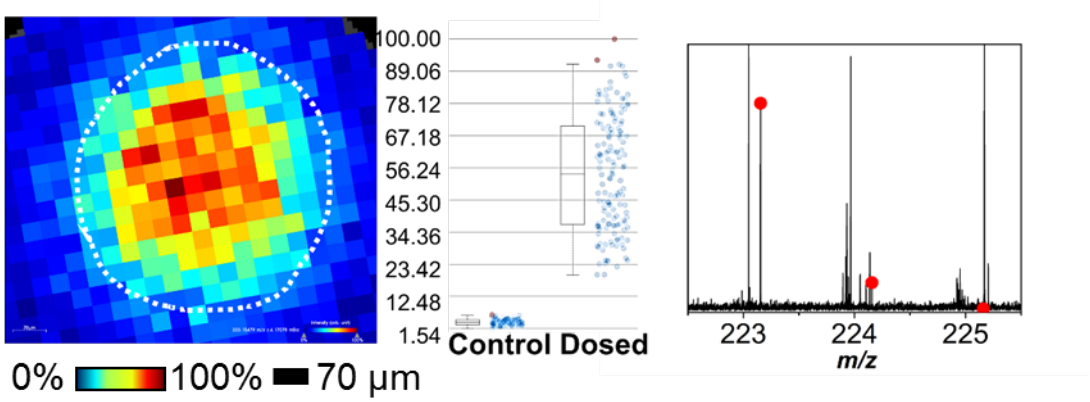

Figure 6.16. (A) FT-ICR MSI of pimonidazole-derived ion (m/z 223.15528). The box and whisker plot compares the intensity of the m/z 223.15528 peak between the dosed spheroid and the control. The predicted isotope pattern is plotted over the data as scatter plots with 0.809 ppm error.

The box and whisker plots of pimonidazole and its metabolites show that each successive reduction derivative increases in relative intensity. Furthermore, the amine (**4**) derivative displays the highest intensity compared to the other metabolites (figure 6.17). This implies that pimonidazole has undergone reduction into the amine (**4**, *m/z* 225.17099) derivative within the PC3 spheroids after 24 hours. However, the extent of conjugation of the hydroxylamine (**3**, *m/z* 241.16590) with other macromolecules within the cell is unknown. The average intensity of *m/z* 223.15528 is similar to the parent ion, however its point of production within the reduction pathway is uncertain.

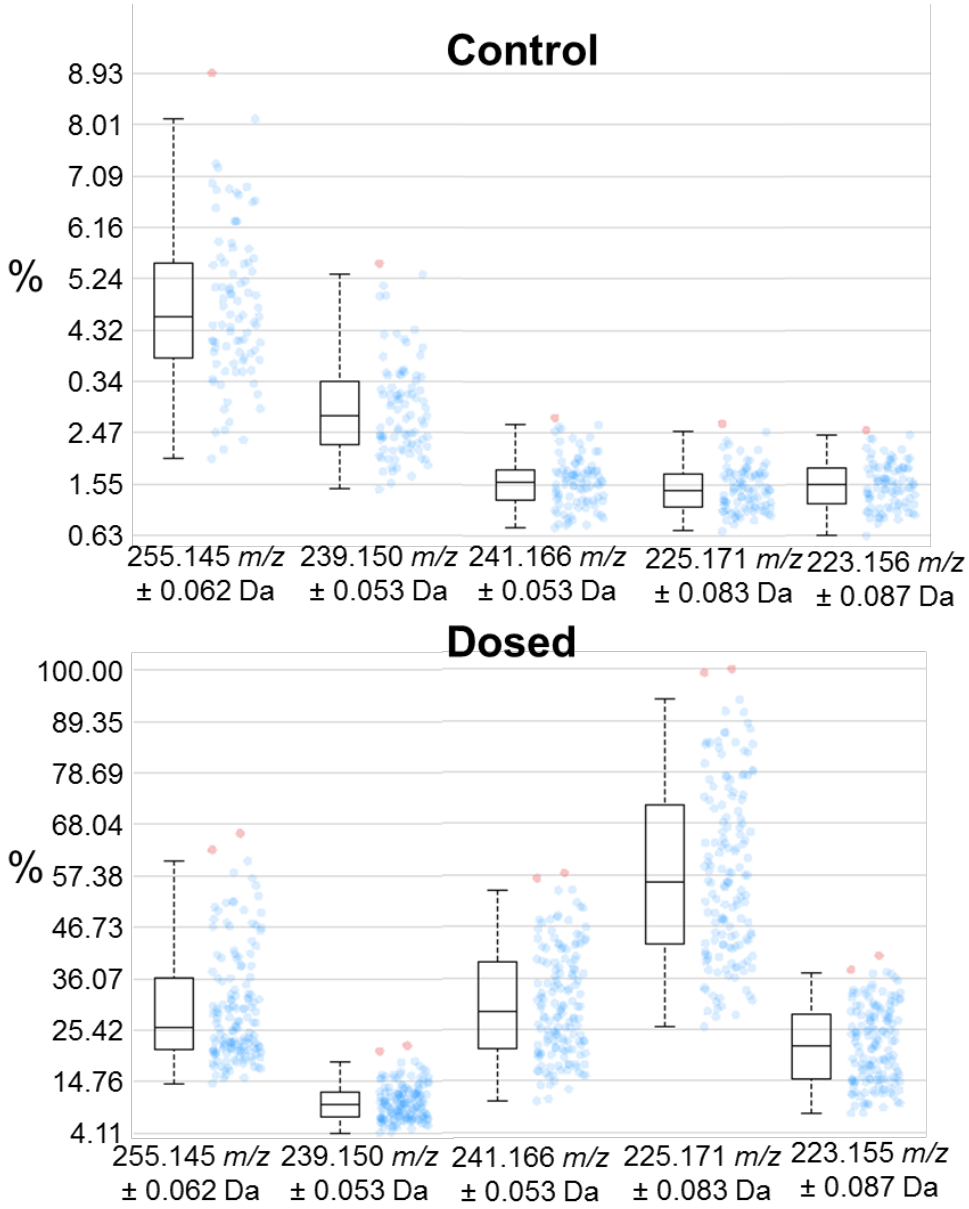

Figure 6.17. Box and whisker plot showing the intensity of pimonidazole and each metabolite after 24 hours. The values are normalised against the highest peak intensity.

In order to observe the glutathione conjugate, CASI at *m/z* 530 with a window of *m/z* 15 was employed. Single-point calibration with a DHB matrix peak at *m/z* 545.07145 was used for assignment. Whilst MALDI MS analysis produced a peak that corresponded to the conjugate with 0.945 ppm error (figure 6.18), the peak was only observed in the matrix surrounding the spheroid and was not present within the spheroid itself (figure 6.19). This suggests that the peak could be the result of the

matrix or gelatin. Furthermore, the large error associated with the peak is suggestive that it does not correspond to the glutathione conjugate.

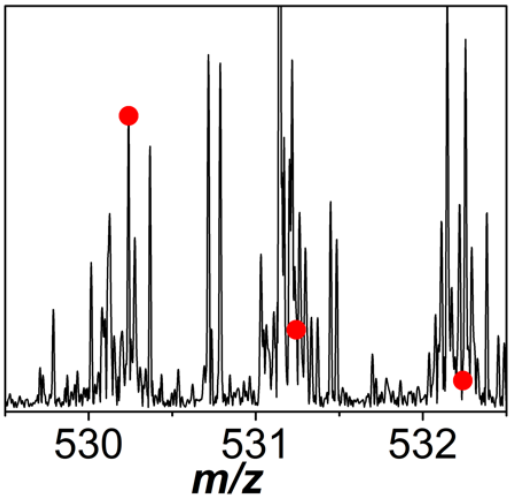

Figure 6.18 MALDI MS analysis of peak corresponding to glutathione conjugate (m/z 530.23914) in spheroids. The predicted isotope pattern is plotted over the data as a scatter plot.

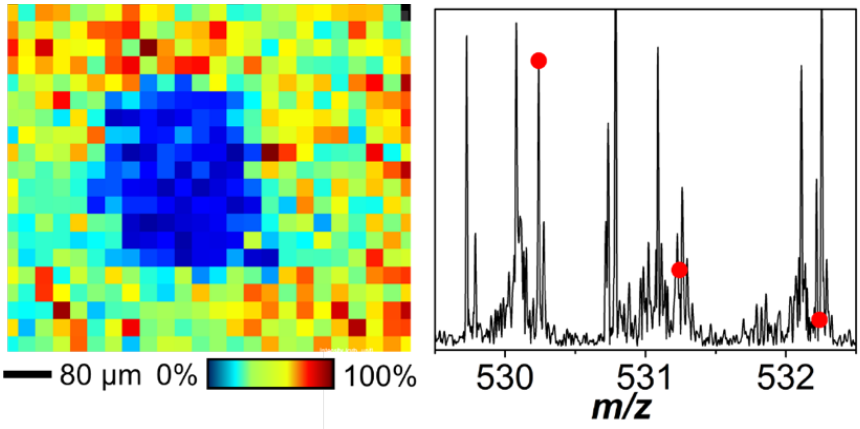

Figure 6.19. Ion density map corresponding to the pimonidazole glutathione conjugate (m/z 530.23914). The predicted isotope pattern is plotted over the data as a scatter plot.

6.2.4 Pimonidazole metabolism time course

To observe the time-dependent penetration and metabolism of pimonidazole over 24 hours within a spheroid, 14-day-old PC3 spheroids were dosed with 200 µM pimonidazole for six, 18 and 24 hours. Spheroids were sectioned and imaged using

MALDI FT-ICR MSI with a Q1 mass of *m/z* 240 and a CASI window of *m/z* 40. The distribution of the pimonidazole parent ion (**1**, *m/z* 255.14517) was observed at the first time point of six hours (figure 6.20). The box and whisker plot shows an increased uptake until 18 hours at which point the intensity of the peak corresponding to pimonidazole remains the same. The ion density maps show that pimonidazole is localised towards the centre at six hours but becomes distributed throughout the spheroid by 24 hours. This suggests that pimonidazole can penetrate and accumulate throughout the spheroid within this period.

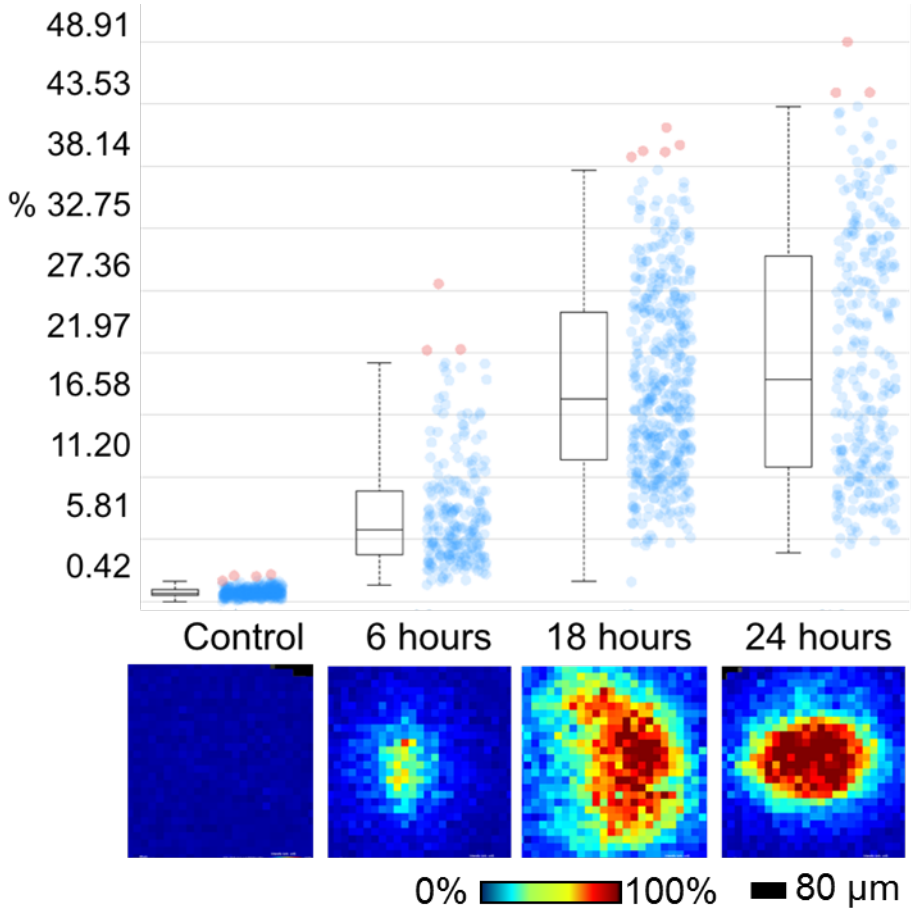

Figure 6.20. Box and whisker plot and ion density map showing the intensity of the pimonidazole parent ion over a 24-hour time course.

The distributions of the reduction metabolites over 24 hours were also observed (figure 6.21). All three reduction metabolites are present by six hours and become distributed throughout the spheroid over the time course, suggesting that pimonidazole diffuses into the spheroid and begins to undergo reduction within six

hours. Furthermore, the intensities of all three metabolites increase towards the central core, suggesting that pimonidazole is undergoing reduction from the centre of the spheroid.

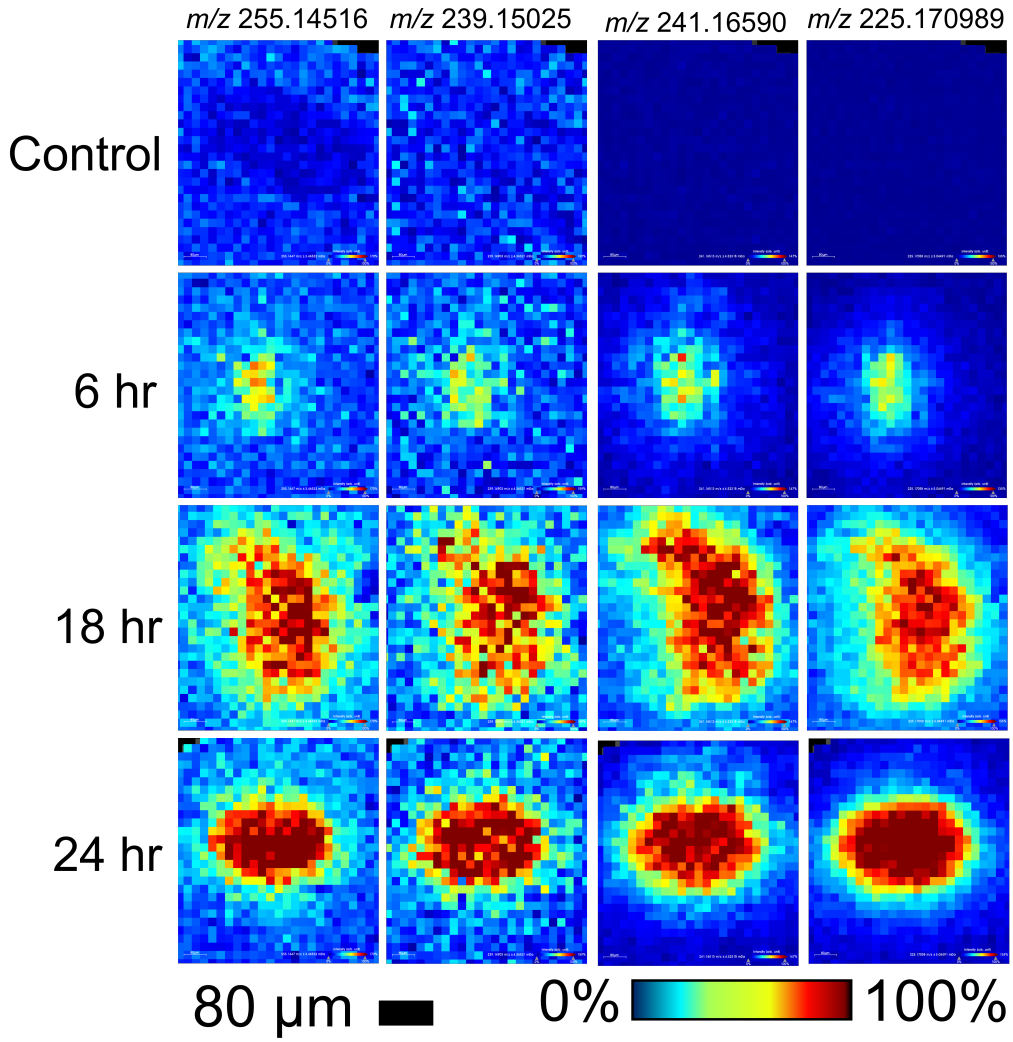

Figure 6.21. Ion density maps of pimonidazole (m/z 255.14517), nitroso (m/z 239.15025), hydroxylamine (m/z 241.16590), and amine (m/z 225.17099) derivatives over a 24-hour time course.

The box and whisker plots of pimonidazole metabolites show that the intensity of the nitroso (**2**, *m/z* 239.15025) and hydroxylamine (**3**, *m/z* 241.16590) derivatives increase up until 18 hours, at which point the average intensity plateaus, whereas the amine (**4**, *m/z* 225.17099) derivative continues to increase in intensity at the 24-hour timepoint (figure 6.22). This could suggest, that at 24 hours, the uptake of

pimonidazole is at an equivalent rate to its reduction (figure 6.22A), resulting in an accumulation of the final reduction amine derivative (figure 6.22D).

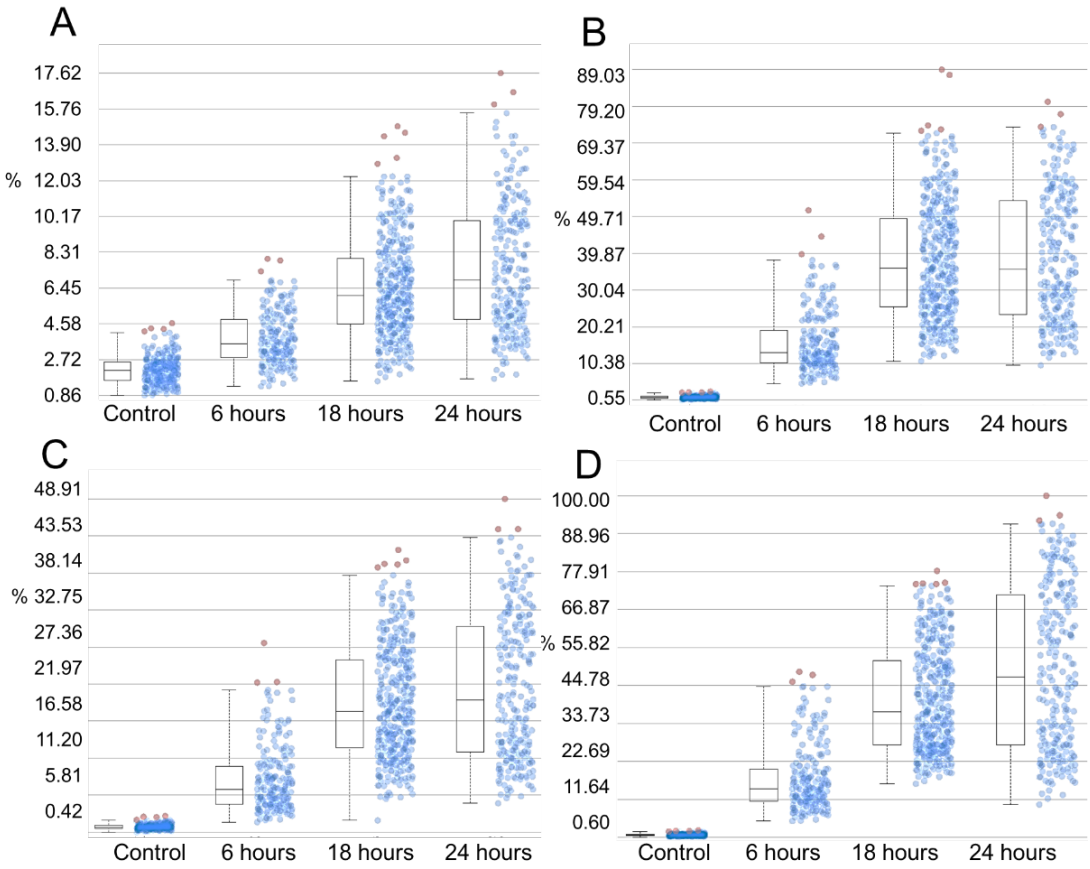

Figure 6.22. Box and whisker plot showing the intensity of (A) pimonidazole (m/z 255.14517) (B) nitroso (m/z 239.15025), (C) hydroxylamine (m/z 241.16590) and (D) amine (m/z 225.17099) over the 24-hour time course. The values are normalised against the highest peak intensity.

Moreover, by dividing the spheroid into an 'outer' and 'centre' region based on 50% of the radius, the box and whisker plots show that there is a greater accumulation of pimonidazole and its derivatives in the centre region compared to the outer region (figure 6.23). This further suggests that pimonidazole is becoming more reduced in the centre of the spheroid.

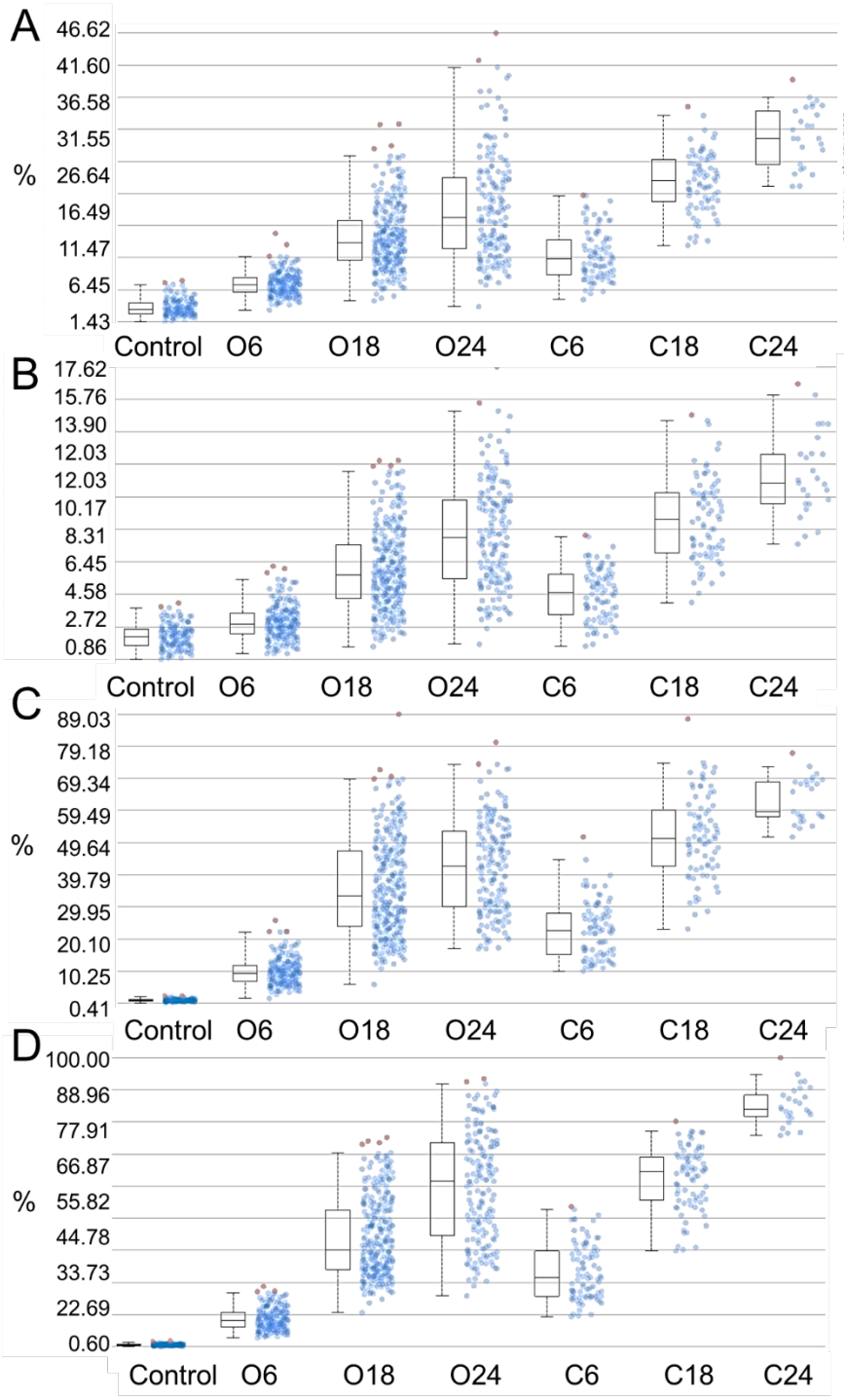

Figure 6.23. Box and whisker plots showing the intensity of (A) pimonidazole (m/z 255.14517) (B) nitroso (m/z 239.15025), (C) hydroxylamine (m/z 241.16590) and (D) amine (m/z 225.17099) derivatives over the 24-hour time course between the outer (O) and centre (C) of the spheroid. Each numerical value corresponds to the number of hours the spheroid was dosed.

Given that the imidazole ring is only reduced under hypoxic conditions, these results suggest that the centre of the spheroid is experiencing hypoxia.[167,168] This is in agreement with current literature, which indicates that spheroids with radii greater than 200 μm surpass oxygen diffusion limits and experience hypoxic conditions.[84,115] However, it has been suggested that MALDI-MSI of pimonidazole and its metabolites display a non-specific localisation, and their distributions do not correlate with the hypoxic regions of the cell. Therefore, the localisation of the reduction products through MALDI-MSI does not definitively identify the oxygen deficiency within the spheroid.

Similarly to the other metabolites, the intensity of the pimonidazole-derived ion (*m/z* 223.15528) increases up to 18 hours, at which point it remains the same (figure 6.24). The ion density maps show that the derivative was observed at the centre of the spheroid from six hours and becomes distributed throughout the spheroid over the time course. The increasing intensity towards the centre of the spheroid suggests that this could be a hypoxic region. Conversely, the localisation of this ion was similar to other metabolites within the spheroid, whereas previous literature observed a unique distribution.[168]

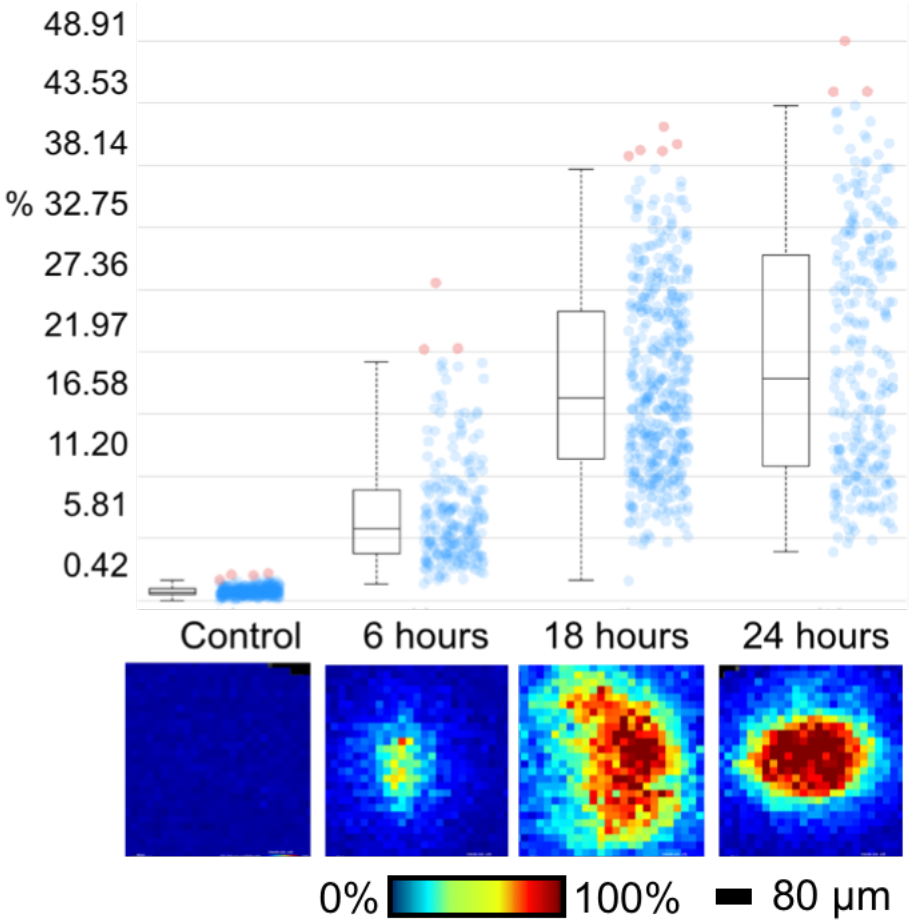

Figure 6.24. Box and whisker plot and ion density map showing the intensity of the m/z 223.15528 over a 24-hour time course. The box and whisker plot compares the relative intensity of each respective metabolite between the treated and control spheroids.

6.3 Conclusions

Here we show MALDI-MSI can be employed to observe the distribution of the hypoxia marker pimonidazole using both MALDI ToF and FT-ICR MSI. Furthermore, CASI provides an effective tool to improve the sensitivity of detecting both the parent ion and its metabolites. Finally, using high spatial resolution MSI, it is possible to simultaneously map the time-dependent distribution of pimonidazole and its metabolites over a 24-hour time course. Future work could complement this data with immunohistochemical to establish which metabolites colocalise with the hypoxic regions of the spheroid.

Chapter 7.

MALDI matrix application utilising a modified 3D printer for accessible high-resolution mass spectrometry imaging

7.1 Introduction

Sub-optimal matrix application conditions can cause extensive analyte diffusion, therefore the selection of the most appropriate matrix and optimisation of its application parameters is key to obtaining high quality and biologically relevant spectra directly from tissue samples.[9] Subtle changes in matrix application rate, drying times, matrix composition and thickness have all been demonstrated to affect the ionisation efficiency, the propensity to detect low abundance compounds and the reproducibility of the results obtained.[40,175]

Automated matrix application platforms remove the inter-user variability of manual applications by controlling the temperature, solvent flow rate, velocity of the spraying nozzle, and the number of passes; however they are generally slower than manual alternatives.[94] Several automated systems are commercially available, including the Bruker ImagePrep, the SunChrom SunCollect, and the HTX-TM-Sprayer, however the cost of this equipment limits many research facilities' accessibility to the technique.[95] A number of less expensive automated matrix application strategies have been developed in academic research laboratories, including an automated acoustic spotter,[78] the repurposing of an inkjet printer,[79] and the use of an pneumatic sprayer on top of a pneumatically moveable base (table 7.1).[95] After optimisation, these systems produced matrix crystals of 5 to 10 μm in diameter, and the mass spectra data collected displayed a high signal intensity and reproducibility.[95]

Table 7.1. A comparison of the cost of different automated matrix application methods as of March 2018.

Matrix deposition method	Company	Approximate cost ($)
HTX sprayer	Carrboro	60,000
ImagePrep	Bruker	45,000
Suncollect	SunChrom	20,000
Langartech	CIC EnergiGUNE	3,500
Inkjet printer	University of Florida	200
3D printer	University of Edinburgh	2,600

In this chapter, method development of matrix application will be discussed. A commercial 3D printer ($300) and other parts commonly found in an analytical chemistry lab were used to build a cost-effective alternative to commercial sprayers.

The extent of diffusion during matrix application was quantified using printed rhodamine B microarrays and fluorescence imaging. Optimisation of matrix application was carried out using experimental design to vary key experimental parameters including bed temperature, gas pressure, and nozzle height, which effectively reduced analyte diffusion on the rhodamine B microarrays. Subsequently, the home-built sprayer was used to observe metabolite distributions in MCF-7 spheroid sections with a consistently high spatial and spectral resolution.

7.2 Results and discussion

7.2.1 3D printer set-up

A WANHAO i3 duplicator 3D printer with a temperature-controlled build plate (0–120 ^{o}C) was used in this work. Adaptation of the printer takes approximately half an hour and costs a total of *ca.* $2600. First, the 3D printer was set up using the manual instructions provided by the manufacturer. A nebuliser housing block was designed using online software and printed in from poly lactic acid (PLA) plastic using the 3D printer (figure 7.1).

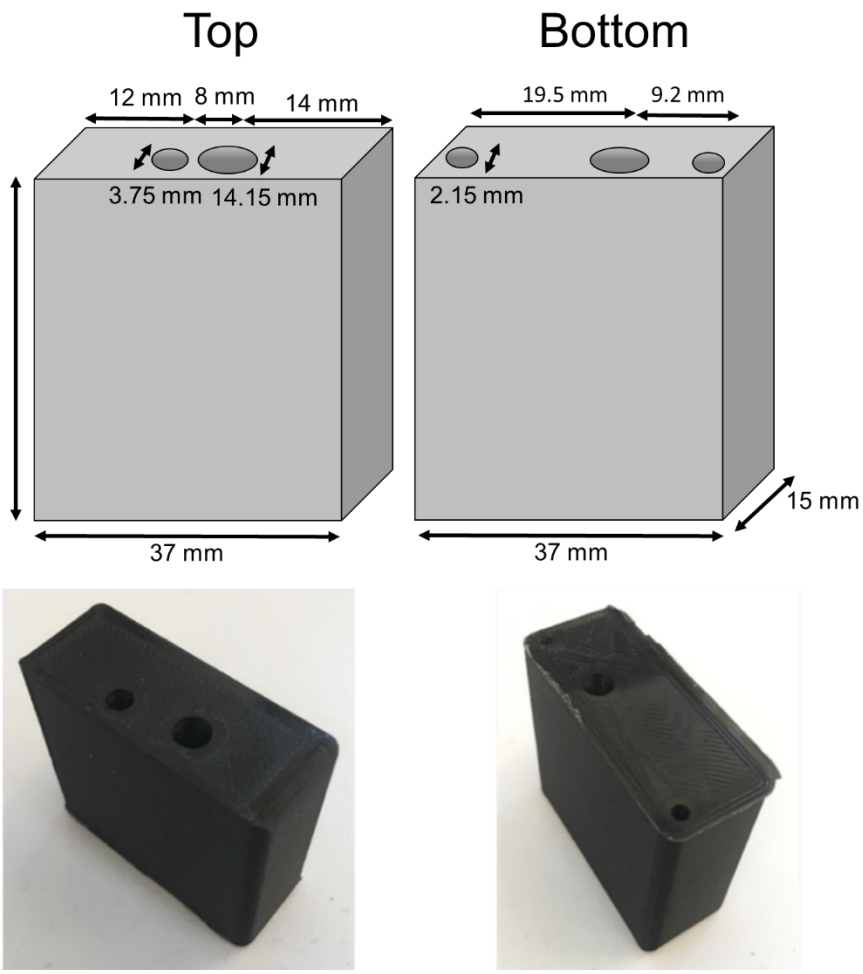

Figure 7.1. Online software was used to design a nebuliser housing block that held the nebuliser in place during matrix application. Holes were designed to secure the nebuliser above the sample as well as the block onto the converted printer. The file was converted into an .STL format and printed by the 3D printer according to the instructions provided by the manufacturer.

Once the block was printed, the 3D printer was converted into a matrix application platform. First, the printer's extruder and fans were removed to leave the empty extruder housing. Any remaining low voltage wires were insulated and secured in place with electrical tape (figure 7.2). The extruder and fans were stored to enable conversion back to the printer if required for future use.

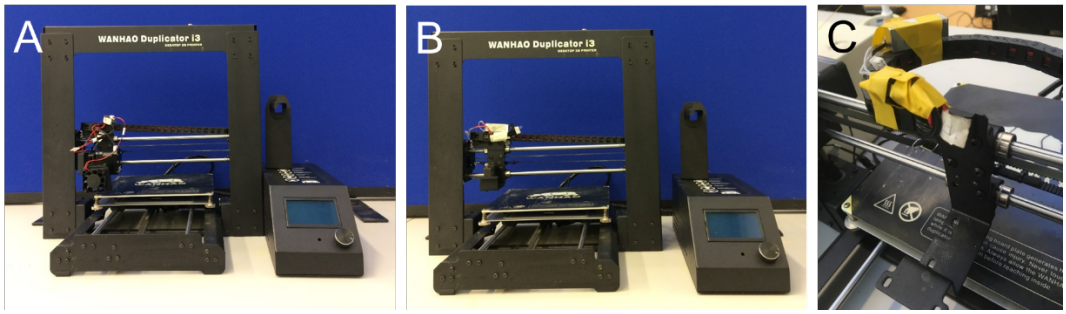

Figure 7.2. Outline of the printer set-up. (A) The 3D printer used was the WANHAO Duplicator i3. (B) The extruder and fans were removed to leave the empty extruder housing. (C) The remaining low voltage wires were insulated and secured in place with electrical tape.

A hex bolt was secured into the printed nebuliser housing block. The block was then attached onto the empty extruder housing using M3 Hex bolts on the underside of the housing (figure 7.3).

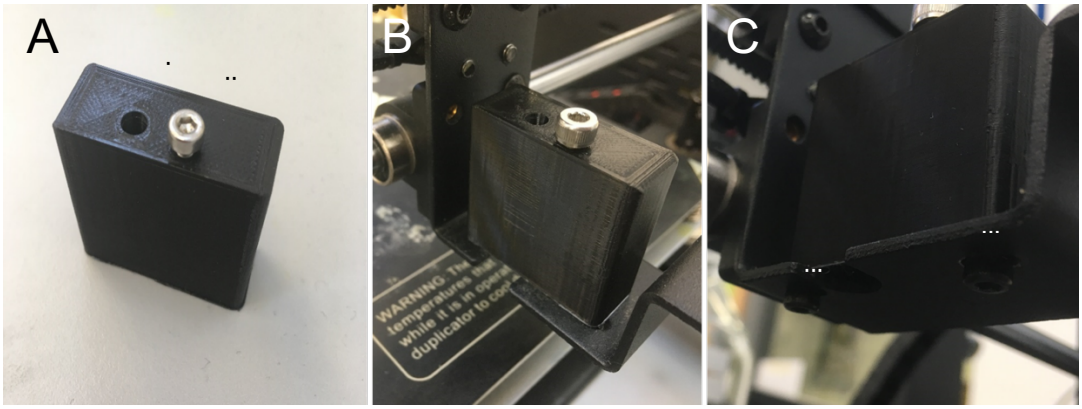

Figure 7.3. Outline of the printer set-up. (A) An M4 hex bolt was secured in the 3D printed nebuliser block. (B) The nebuliser block was then secured in place onto the empty extruder housing using (C) the M3 hex bolts on the underside of the 3D printed block.

Nitrogen was used as the nebuliser gas for matrix application (70 psi) and the gas pressure was set manually with an inline regulator. A Rheodyne C1-2006 6 port valve (Valco Instruments, Texas, USA) was attached on top of the printer (figure 7.4).

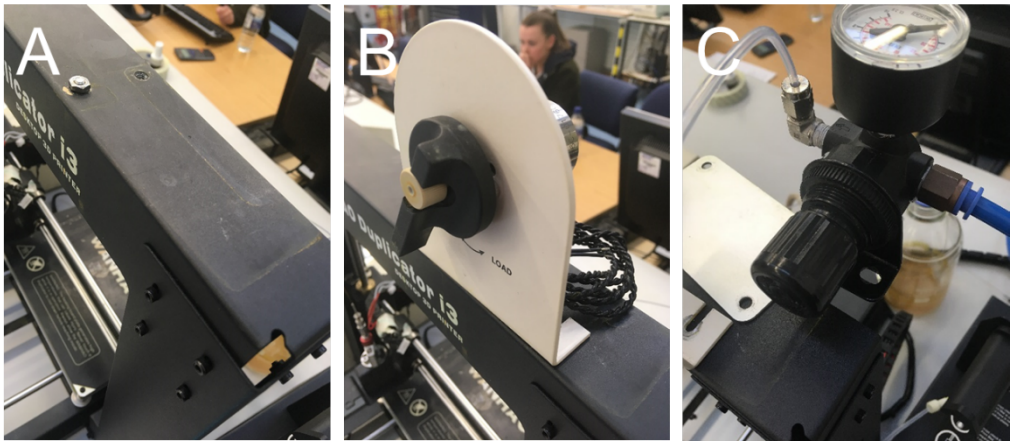

Figure 7.4. Outline of the printer set-up. (A) On the top side of the printer (B) a Rheodyne 6 port valve was attached. (C) A nitrogen gas supply (70 psi) was attached with an inline regulator. To prevent the entanglement of wires, a metal place was secured onto the printer and the regulator attached onto the plate.

The Rheodyne 6 port valve was equipped with a 5 mL sample loop, through which matrix could be injected and subsequently sprayed onto the slide. A Shimadzu LC-10ad HPLC pump was connected to the 6 port valve using 100 µm internal diameter fused silica tubing at a flow rate of 0.1 mL/min. A waste line was also connected (figure 7.5).

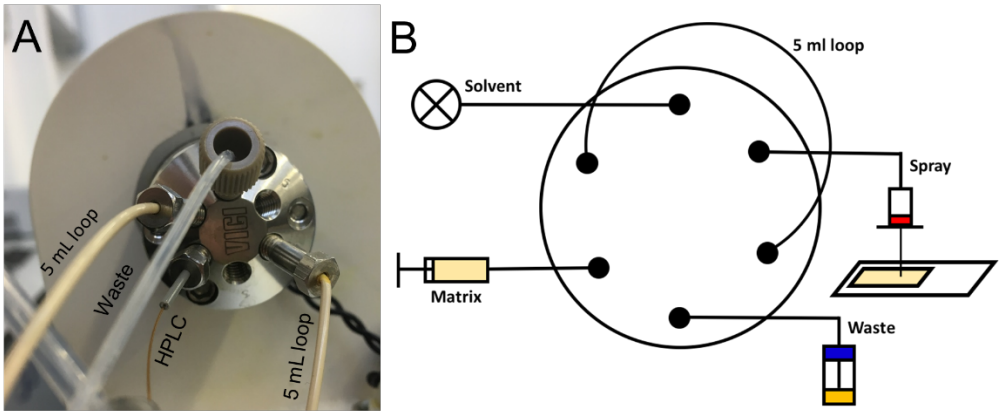

Figure 7.5. Outline of the printer set-up. (A) The 6 port valve was connected to a 5 mL loop. The valve was connected to the HPLC using 100 µm internal diameter fused silica tubing. A waste line was also connected to dispose of excess matrix and washes through the system. (B) A schematic of a 6 port valve. The matrix was injected through the front of the 6 port valve.

Matrix deposition was achieved by replacing the printing extruder with a commercially available Bruker Daltonics electrospray emitter for nebulisation without the addition of a voltage. The nebuliser was placed through the extruder housing block and secured in place using the M4 hex bolt. The 6 port valve was connected to the nebuliser using 100 µm internal diameter fused silica tubing and the gas line was connected from the inline regulator (figure 7.6).

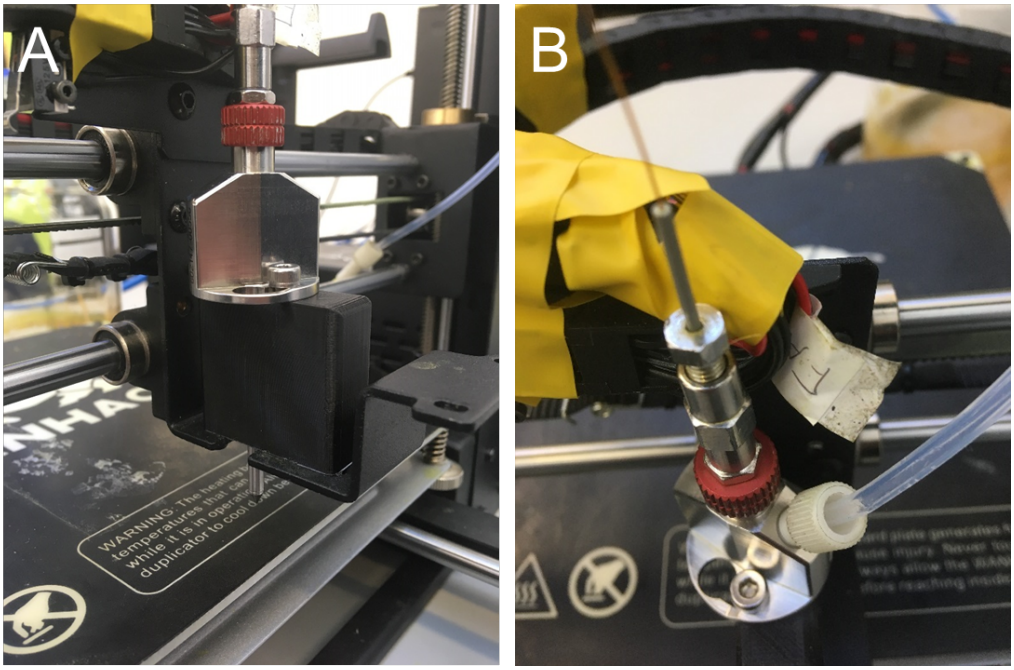

Figure 7.6. Outline of the printer set-up. (A) The nebuliser was placed through the 3D printed blocked on the printer and held in place using the hex bolt. (B) 100 µm internal diameter fused silica tubing was used to attach the 6 port valve to the nebuliser. A gas line from the regulator was attached to the nebuliser.

The x,y,z position and feed rate of the extruder was controlled with G-code instructions; a numerical control programme developed by Massachusetts Institute of Technology. The x,y range covered the area of a slide, whilst the z height

corresponded to the distance between the emitter and the bed height. The z height was calibrated to 0 when the nebuliser was 2 mm above the bed (figure 7.7).

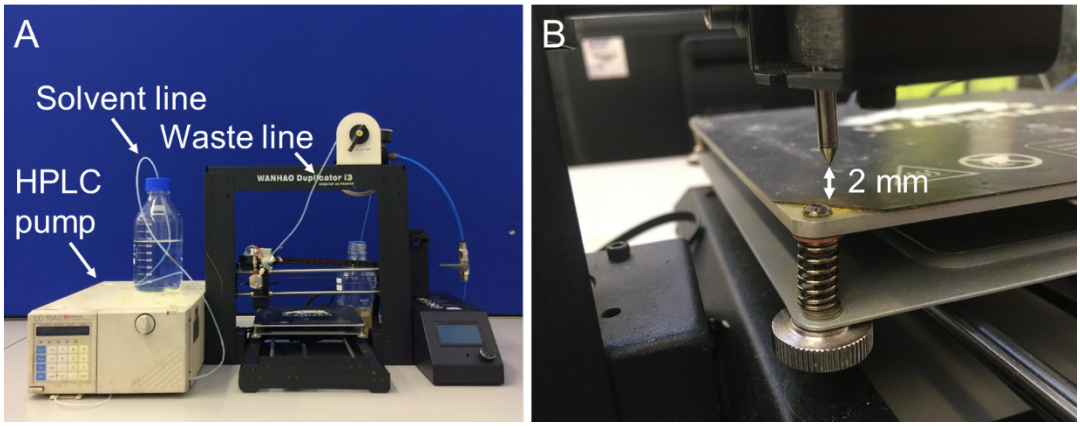

Figure 7.7. Outline of the printer set-up. (A) The final printer set-up. (B) The z height is calibrated to 0 by adjusting the platform to 2 mm distance from the nebuliser by turning the dials underneath the stage platform.

The matrix solution and application solvent used was 70% ACN. The mass of matrix deposited onto a glass slide using an optimised method on the commercial TM-sprayer™ was 2 mg. Therefore, the velocity of the spray head and the flow rate of the solvent were optimised to match this mass change. The velocity was set within the G-code as F1000, which created a velocity of 1100 mm/minute. The total time taken for eight coats of a glass slide was 20 minutes and produced an area density of 0.11 mg/cm^2. For consistent performance, regular wash cycles were done with 10 mL of solvent before and after use.

7.2.2 Generation, matrix coating and fluorescence imaging of rhodamine B microarrays

To quantify the extent of delocalisation as a result of matrix application, microarrays of rhodamine B – a water soluble fluorescent molecule – were used. As metabolites are commonly delocalised during matrix application, a water-soluble molecule provided a model system to replicate this phenomenon. Furthermore, fluorescence provided an efficient technique to assess a large number of conditions without requiring extensive sample preparation. 45 individual spots each containing 50 droplets of 350 pL rhodamine B in water were dispensed onto a SuperFrost™ glass slide using a SciFLEXARRAYER S5 microarray printer equipped with a PDC 80

dispense capillary with a 50 µm nozzle aperture. HPLC-grade water was used as the solvent which was degassed by sonication prior to printing (30 minutes). 45 spots provided a high number of replicates to improve the validity of the values calculated. The fluorescence was measured using a BioAnalyzer 4F/4S fluorescence scanner with a Cy5 filter before and after matrix application. The circle tool in ImageJ was used to measure the area (mm^2) before and after matrix application and the percentage change in area was used to quantify the extent of diffusion.

The concentration of rhodamine for the microarrays was chosen by measuring the change in fluorescence as a result of 9AA matrix application for a range of concentrations (0.001%–0.5% (w/v) in water) (figure 7.8). The sprayer conditions were kept consistent at 30 °C bed temperature, 20 mm z height, and 50 psi gas pressure. A 50 ms exposure time and a Cy5 filter was used for measuring the fluorescence at 540 nm. 0.001% (w/v) produced an average change in area of 44%, whilst 0.5% (w/v) produced a 942% area change after matrix application using the conditions (table 7.2). 0.5% rhodamine B (w/v) had a high standard deviation across the measured area of 45 spots and resulted in self-quenching of the fluorescence, whereas 0.001% (w/v) produced a more consistent spot size. However, the low concentration would make it difficult to detect smaller area changes that would occur after optimisation of the application parameters. As a result, a concentration of 0.01% (w/v) rhodamine B in water was selected, as it produced consistent spot sizes and the area change was large enough to cover a wider range of optimisation conditions.

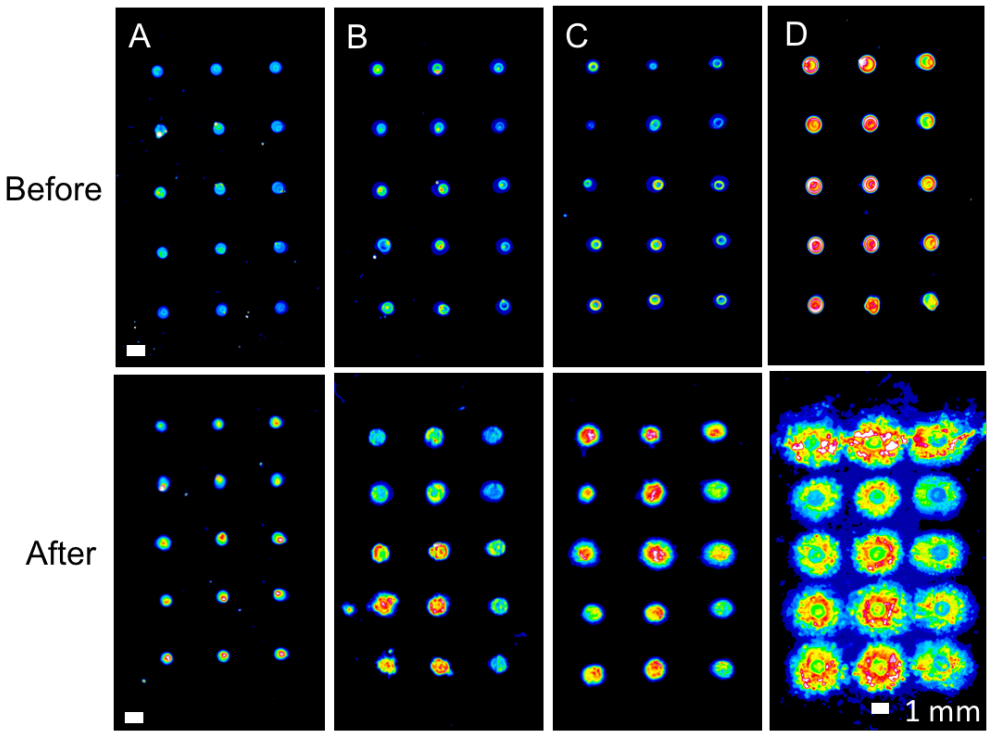

Figure 7.8.Fluorescence of printed microarrays at 540 nm wavelength of (A) 0.001% (B) 0.01% (C) 0.1% (D) 0.5% (w/v) rhodamine B in water before and after matrix application. The conditions used for the home-built sprayer were 30 °C bed temperature, 20 mm z height, 50 psi.

Table 7.2. Concentrations (w/v) of rhodamine B in water were assessed for the change in area measured after matrix application using the home-built printer prior to optimisation. The area was measured before and after matrix application for 45 spots and an average and standard deviation were calculated. The parameters used for the home-built sprayer were 30 °C, 20 mm z height, 50 psi.

Concentration % (w/v)	Average area before (mm^2)	SD	Average area after (mm^2)	SD	Percentage area change
0.001	0.446	0.036	0.646	0.102	44.803
0.01	0.675	0.054	1.437	0.371	113.032
0.1	0.539	0.136	1.760	0.546	226.540
0.5	0.843	0.059	8.718	1.173	934.378

To identify an exposure time that accurately represented the area change of a rhodamine B spot, a variety of fluorescence scanner exposure times were tested for their effect on the spot area. The area (mm^2) of 45 spots was measured using the ImageJ circle tool over three exposure times of 30, 60 and 90 ms prior to matrix application (figures 7.9 and 7.10). Increasing the exposure increased the measured area, however it also results in the saturation of more pixels.

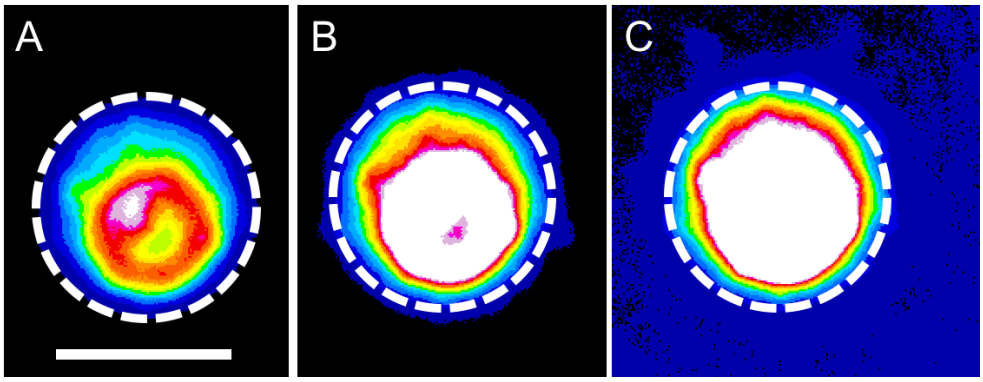

Figure 7.9. Fluorescence at 540 nm wavelength of a representative 0.01% (w/v) rhodamine B microarray spot in water imaged at (A) 30 ms (B) 60 ms (C) 90 ms exposure time with a Cy5 filter on a fluorescence scanner. The white dotted line depicts the initial size of the rhodamine B spot at 30 ms exposure. Note as the exposure increases, the size of the rhodamine spot also increases. Scale bar 1 mm.

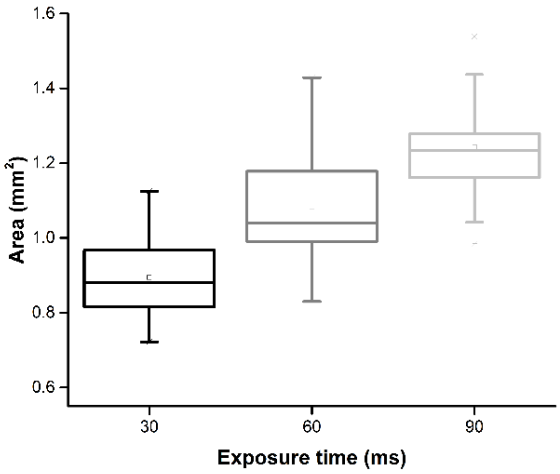

Figure 7.10. Box and whisker plot showing the effect of increasing exposure time on the area of the measured fluorescence at 540 nm wavelength across 45 rhodamine B spots. With an increasing exposure time, the area of fluorescence also increases.

To select an appropriate exposure time, the effect of the measured pixel area was compared to the extent of pixel saturation. To do this, the area and brightness across 45 rhodamine B spots were measured over exposure times ranging from 20 to 220 ms prior to matrix application (figure 7.11). As the exposure time increases, both the size and the average grayscale of the pixels increases. However, after approximately 120 ms exposure, the increase in area begins to level off. The brightness of each pixel also begins to plateau as more pixels become saturated at *ca.* 3000 (arbitrary units). The size of the spot plateaus before all the pixels become saturated, therefore the exposure time selected for the fluorescence measurements was 70 ms. At this exposure time, approximately 50% of the pixels are saturated and it is approximately 50% of the maximum spot size across the exposure times investigated. Applying a longer exposure time will result in an overestimation of area spot size, so any delocalisation observed will be reduced when applied to MSI of tissue samples.

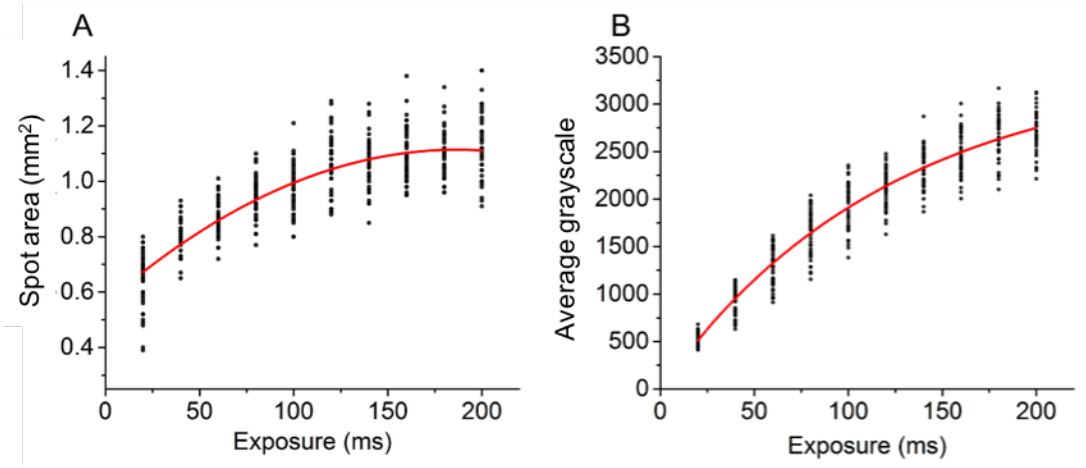

Figure 7.11. The (A) rhodamine area (mm^2) and (B) average brightness (arbitrary units) with increasing exposure measured by fluorescence at 540 nm wavelength across 45 microarray spots of 0.01% (w/v) rhodamine B. The line of best fit is plotted based on the average across 45 spots at each exposure increment.

Three common matrices – 9AA, DHB, and CHCA – were assessed to establish which matrix would benefit most from the optimisation using the converted 3D printer. Each matrix was applied to the rhodamine B printed microarray slides by means of the laboratory's current standard application protocols using a commercially available matrix application platform, the HTX TM-sprayer (Bruker

Daltonics, Bremen, Germany). For each matrix, the circle selection tool on ImageJ was used to measure the area of observed fluorescence for each rhodamine B spot before and after matrix application (figure 7.12). From this, the percentage change in area across the 45 spots could be calculated (table 7.3).

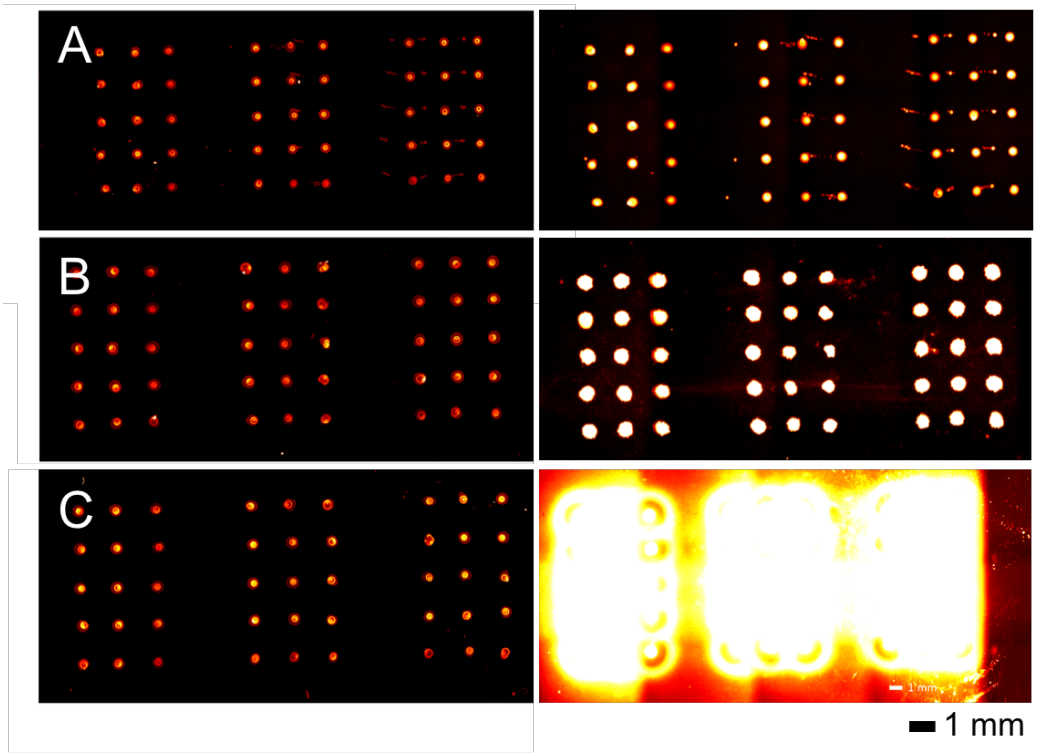

Figure 7.12. Measured fluorescence at 540 nm wavelength of 0.01% rhodamine B (w/v) microarray spots (left) before and (right) after matrix application using the optimised application of three common matrices by the HTX™ automated sprayer. (A) 9AA (B) DHB (C) CHCA. Scale bar 1 mm.

Table 7.3. Average change in fluorescence area at 540 nm wavelength after matrix application using an optimised method on the commercial HTX sprayer. Note that CHCA can not be calculated as the matrix itself is fluorescent.

Matrix	Average area before (mm^2)	SD	Average area after (mm^2)	SD	Average% change in area
9AA	0.713	0.058	0.892	0.076	25.214
DHB	0.850	0.087	2.119	0.256	150.540
CHCA	0.763	0.083	N/A	N/A	N/A

All three matrices showed some delocalisation despite using a standard optimised method for matrix application. CHCA was fluorescent and therefore fluorescence cannot be used to optimise its application. The optimised protocol for DHB application produced a 150% increase in rhodamine B area. This extensive delocalisation observed could be reduced using the converted 3D printer platform as an alternative method of application. However, a number of methods are available for DHB matrix application including sublimation, which has been shown to significantly reduce delocalisation compared to wet application methods.[176] 9AA produces poor results using sublimation and its optimised method using a commercial sprayer presented a 25% increase in spot area based on the changes in fluorescence (figure 7.13).[176] 5 mg/mL 9AA in 70% ACN was selected for optimisation of the 3D printer, as this is consistent with the current laboratory protocol.

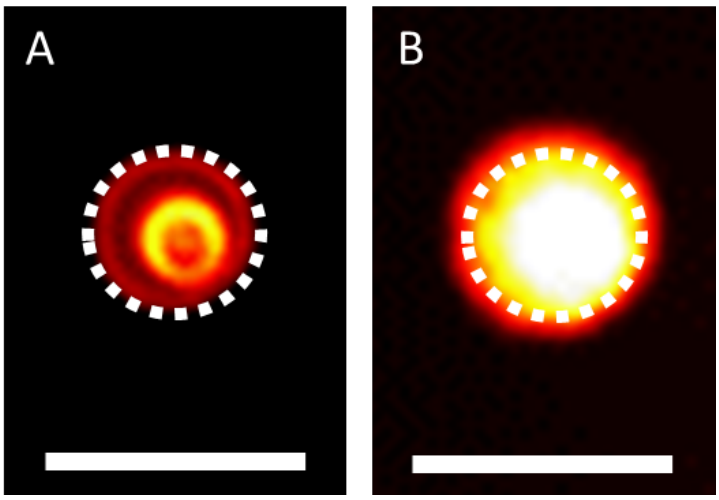

Figure 7.13. A representative rhodamine B spot (A) before and (B) after matrix application of 5 mg/mL 9-aminoacridine in 70% ACN imaged using fluorescence at 70 ms exposure time and 540 nm. Matrix application was carried out using the current optimised set-up in the laboratory with the HTX-TM sprayer. The dotted circle denotes the original area of the spot. Scale bar 1 mm.

To optimise the matrix application conditions using the home-built 3D printer, a user defined experimental design was compiled using Design Expert 10 (Stat-Ease, Minneapolis, USA) with discrete increments of 10 for three matrix application variables: nebulising gas pressure (40–60 psi), build-plate temperature (20–40 °C)

and nebuliser z height (i.e. height of nebuliser above the sample surface) (10–30 mm). This process produced a set of 27 discrete conditions for matrix application.

Microarrays of rhodamine B spots (0.01% w/v) were printed on glass slides (45 spots per slide) and each slide was coated with 9AA using one of the combinations of parameters identified. The fluorescence before and after matrix application was recorded using a fluorescence scanner at 70 ms exposure time. The area of each spot (mm^2) before and after matrix application was measured using imageJ as previously described (figure 7.14).

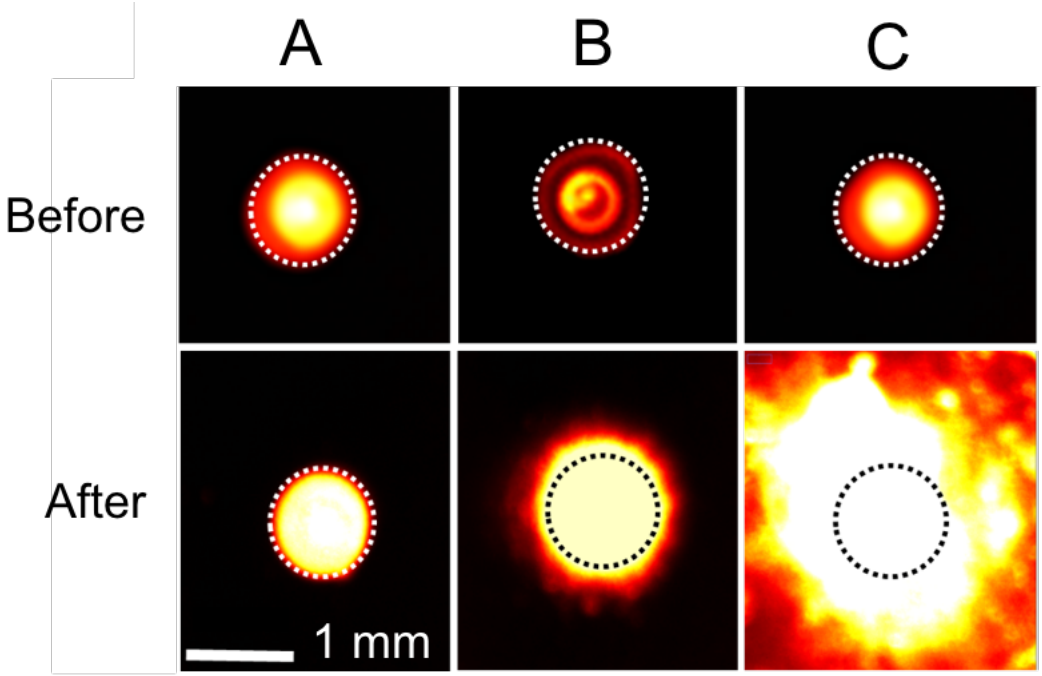

Figure 7.14. A representative rhodamine spot (0.01% w/v) imaged at 70 ms exposure using a fluorescence scanner at 540 nm wavelength before and after matrix application under various application conditions. (A) 40 °C, 30 mm, 50 psi, (B) 30 °C, 30 mm, 50 psi, and (C) 20 °C, 10 mm, 60 psi). Scale bar 1 mm.

The measured area across 45 spots was used to calculate the percentage area change for each combination of parameters identified using experimental design (figure 7.15 and table 7.4). The combination of a 40 °C build-plate temperature, 30 mm nebuliser z height and 50 psi gas pressure produced a dry matrix application with a 9.44% increase in area. This is smaller than the commercial matrix application, which produced a 25% increase in fluorescence area after matrix

application. In contrast, the worst conditions were identified as 20 °C, 10 mm z height and 60 psi gas pressure, producing a 403% increase in area of rhodamine B with visible smearing of the rhodamine B spots after matrix application.

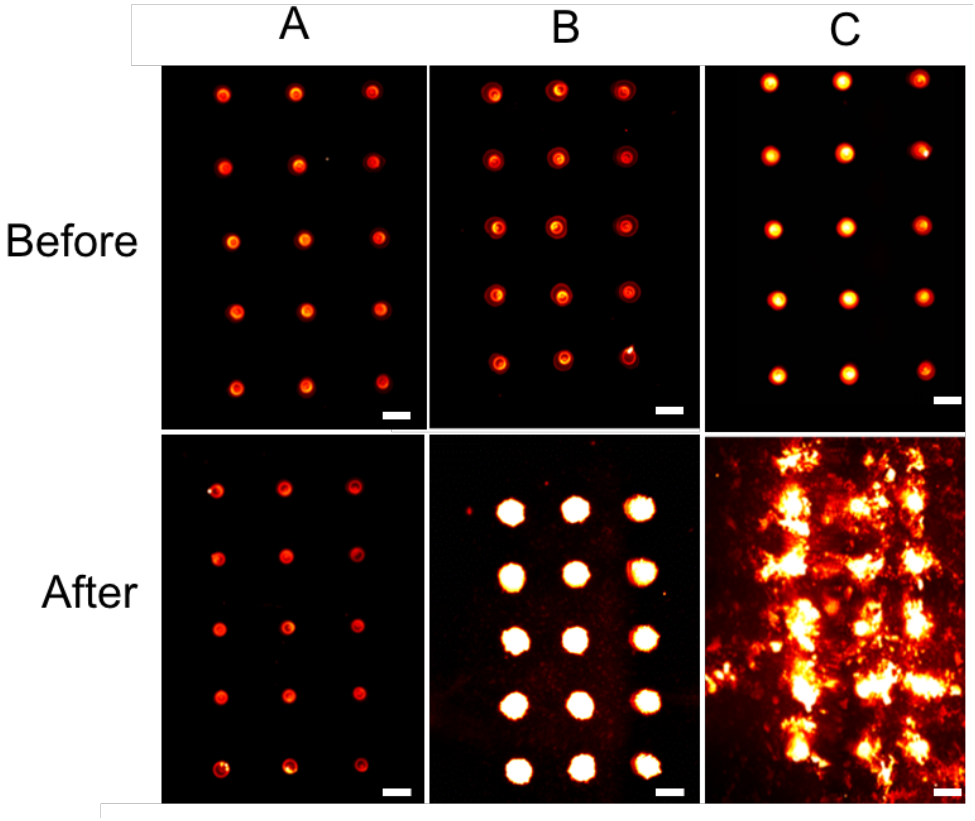

Figure 7.15. 45 Rhodamine B spots (0.01% w/v) were spotted using a microarray printer, and the fluorescence imaged at 70 ms exposure and 540 nm wavelength. The change in spot area after matrix application was measured for all 27 conditions identified using experimental design. Shown are the images of the optimised (A, 40 °C, 30 mm, 50 psi), intermediate (B, 30 °C, 30 mm, 50 psi) and worst (C, 20 °C, 10 mm, 60 psi) conditions before and after matrix application are shown. Scale bar 1 mm.

Table 7.4. Experimental design using a user defined method with discrete increments of 10 for three parameters: temperature (20–40 °C), z height (10–30 mm) and gas pressure (40–60 psi). This produced 27 different conditions for matrix application. The area of rhodamine fluorescence at 540 nm wavelength across 45 individual spots was measured before and after matrix application and the average percentage change in area with standard deviation (SD) was calculated.

Temperature (°C)	Z height (mm)	Gas pressure (psi)	Change in Mass (g)	Average Area Change (n=45) (mm^2)	SD
40	30	50	0.0016	9.4445	5.5831
40	20	40	0.0022	14.0961	8.4560
30	30	40	0.0017	15.4110	6.4115
40	30	60	0.0016	16.5411	8.4517
20	30	50	0.0015	25.8315	5.8350
30	30	60	0.0015	28.0233	13.1018
40	30	40	0.0014	31.2360	9.1229
30	30	50	0.0008	48.1635	9.8320
30	20	60	0.0018	54.1213	15.5157
20	20	50	0.0015	55.0061	14.3394
20	30	40	0.0015	56.5612	10.2006
40	20	50	0.0016	59.6784	18.8256
20	20	40	0.0017	60.7045	12.6046
30	20	40	0.0018	75.2751	26.9346
20	20	60	0.0020	88.5743	19.8371
40	10	60	0.0014	101.3613	25.0613
30	10	60	0.0022	150.3883	50.7967
20	30	60	0.0018	152.2325	14.7132
40	10	50	0.0014	180.3564	65.7270
20	10	50	0.0021	190.4001	26.6111
30	20	50	0.0020	207.4699	65.9244
40	10	40	0.0019	210.5439	60.6413
30	10	50	0.0026	271.8757	59.0557
20	10	40	0.0025	289.0410	78.5388
40	20	60	0.0019	346.0704	84.7562
30	10	40	0.0025	401.5536	95.6569
20	10	60	0.0020	403.3202	67.4806

A bubble plot was used to observe how changing each parameter affected the average area change of rhodamine B spots after matrix application (figure 7.16). At low temperatures and z heights there was a large change in area, however as both the z height and temperature increased, there was a smaller change after matrix application. In contrast, varying the gas pressure had a lesser effect on the extent of observed delocalisation, and at the highest z height and temperature, the gas pressure's effect on the area change was negligible.

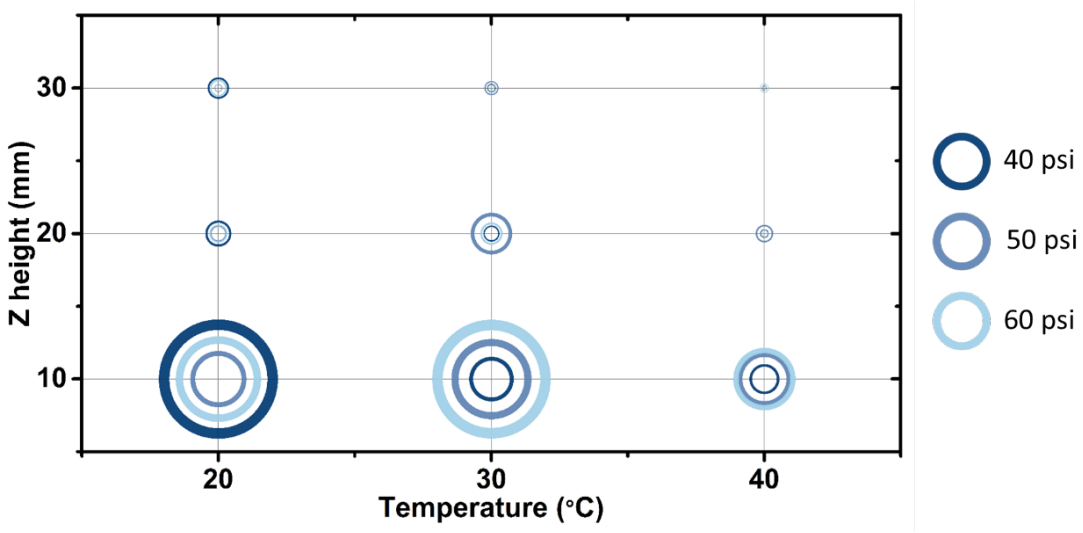

Figure 7.16. A bubble plot showing how the 27 matrix application conditions affect the change in area of rhodamine B fluorescence. The dark to pale blue colour scale is increasing gas pressure and the size of the circle is the percentage area change of after matrix application (diffusion). Note that as the temperature and z height increase, there is a smaller area change of the rhodamine B spot after matrix application under those combination of conditions.

7.2.3 Imaging the MALDI matrix crystal size using scanning electron microscopy (SEM)

The crystal size produced during matrix application defines the spatial resolution and the extent of analyte diffusion, thus reducing the crystal size achieves a greater spatial resolution.[1,40] SEM was used to assess the size of the matrix crystals produced for both the optimised and worst parameters using the modified 3D printer platform, as well as for the laboratory's standard application protocol using a commercially available system (the HTX TM-sprayer) (figure 7.17). SEM images

revealed that the sub-optimal conditions produced a non-uniform coverage of large inhomogeneous crystals. In contrast, the optimised conditions produced a more homogenous uniform coating of small regularly-sized crystals than those observed using the commercial printer.

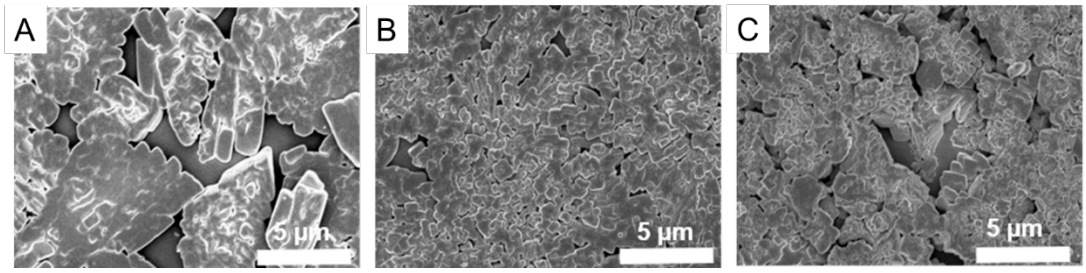

Figure 7.17. Scanning electron microscope images of the crystals produced under the (A) worst 3D printer conditions (B) optimised 3D printer conditions and (C) optimised commercial HTX-TM spraying conditions. The worst conditions produced large inhomogeneous crystals whilst the optimised method produced small crystals with a uniform coverage that were similar to those observed using the commercial sprayer.

7.2.4 MALDI imaging of metabolite distributions in 3D cell culture models

The optimised conditions identified corresponded to a 40 °C bed temperature, a 30 mm z height and a 50 psi gas pressure. Matrix application aims to extract the maximum amount of analyte whilst reducing analyte delocalisation.[40] Whilst the crystals were similar to the commercial sprayer, if the crystallisation occurs too quickly, there will be poor analyte incorporation and thus a poor ion signal.

As a result, it was important to apply the optimised conditions to an imaging run with a high spatial resolution. Sectioned MCF-7 spheroid samples were selected for this process due to their small size, as any delocalisation caused by matrix application can greatly affect the biological validity of the results obtained.

Eight-day-old MCF-7 spheroids were sectioned and coated with 9AA in 70% ACN using the optimised and worst conditions identified by experimental design of rhodamine B microarrays. The coated sections were imaged using MALDI FT-ICR MS at 40 µm imaging resolution in negative mode. The resulting MSI data achieved using the optimised and non-optimal 3D printer matrix application conditions were compared to the current laboratory standard protocol using an HTX-TM sprayer.

The spatial localisation of a number of metabolites including glutathione, **ATP** and **AMP** throughout the spheroid were observed, and an optical image of an adjoining H&E stained section validated the spheroid morphology after cryo-sectioning (figure 7.18).

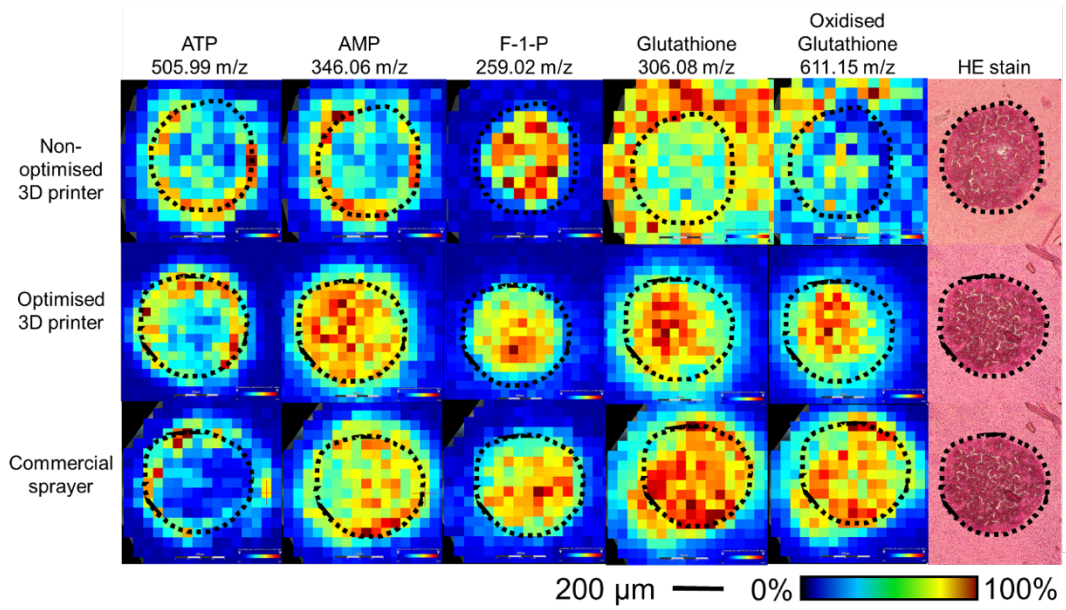

Figure 7.18. Eight-day MCF-7 spheroids were imaged at 40 µm lateral laser resolution using the FT-ICR. Distributions of molecules were observed and compared between the non-optimised and optimised parameters of the 3D printer compared to that of the current protocol using a commercially available sprayer. The H&E stain confirms the structural integrity of the sample. ***ATP*** *adenosine triphosphate;* ***AMP*** *adenosine monophosphate;* ***F-1-P*** *fructose-1-phoshate.*

ATP distributed to the outer region of the spheroid under all spraying conditions, however **ATP** was observed to localise in the embedding medium prior to optimisation. Furthermore, this distribution was reproducible across multiple spheroids using both the 3D printer and the optimised method (figure 7.19).

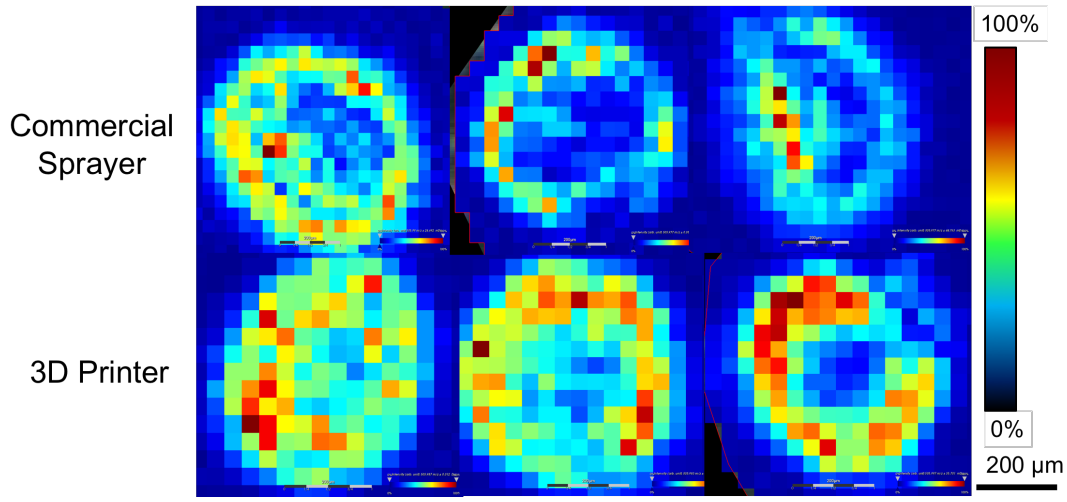

*Figure 7.19. Distribution of **ATP** across three different spheroids imaged in negative mode at 40 µm resolution using FT-ICR MS. **ATP** uniformly localises to the outer region of the spheroids and is reproducible across three different spheroids using both (top) the commercial sprayer and (bottom) the optimised application using the home-built sprayer.*

Prior to optimisation of the home-built sprayer, **AMP** localised outside of the spheroid in the embedding medium with a similar distribution to **ATP**. However, after optimisation, it localised uniformly throughout the spheroid with a similar distribution to the commercial sprayer. Fructose-1-phosphate (**F-1-P**) was uniformly distributed throughout the spheroid under sub-optimal conditions and using the commercial sprayer. However, the optimised conditions produced a unique distribution of **F-1-P** that was localised towards the centre of the spheroid. **F-1-P** is an intermediate in glycolysis and is likely localised to this central region as a result of the hypoxic conditions experienced at the centre of the spheroid.

Prior to optimisation, both reduced and oxidised glutathione had extensively delocalised out of the spheroid and diffused into the embedding medium. However, after optimisation, both the reduced and oxidised forms had a similar distribution towards the centre of the spheroid that was similar to the optimal matrix application using the commercial sprayer.

Under sub-optimal conditions, the converted 3D printer sprayer produced extensive diffusion of various molecules as discussed. These metabolites diffused out of the tissue and into the embedding medium, producing a biologically inaccurate

distribution. Under these spraying conditions, the nebuliser was located near the sample at a high gas pressure without the addition of a heated bed. At lower temperatures, matrix crystals form more slowly and therefore produce a heterogeneous distribution, incorporating analytes across larger regions with a poor S/N for the analytes observed.[40] However, after optimisation, these metabolites had distributions similar to those observed after matrix application using the commercially available sprayer. Furthermore, a number of molecules became more localised to the central region using the 3D printer, suggesting that there was some diffusion using the commercial sprayer that was altering the distribution of metabolites.

7.3 Conclusions

Here we have shown that a 3D printer can be converted into an effective automated MALDI matrix application platform and operates with minimal analyte diffusion during matrix application. Using fluorescent microarrays and experimental design, the conditions for 9AA matrix application were optimised. Incorporating a heated bed and increasing the z height of the sprayer minimised sample wetting and therefore reduced analyte diffusion. These optimised conditions were then used to reproducibly image MCF-7 spheroids at 40 μm resolution and identify numerous metabolites with reduced analyte delocalisation. The images had comparable distributions to those observed using a commercially available printer at a fraction of the set-up cost compared to commercially available systems.

Chapter 8.

Conclusions

8.1 Conclusions

Here, we have developed a method for high spectral and spatial resolution MALDI-MSI of MCF-7 and PC3 spheroids. By preparing the gelatin at 37 °C and embedding the spheroids on the petri dish lid, this effectively reduced the handling of spheroids and minimised damage during sample preparation. For each matrix, FT-ICR MS MALDI MS analysis was used to compile tentative formula assignment lists at sub-ppm errors. Whilst formulae can be tentatively assigned, MS/MS is required to provide confidence on the metabolite isoforms. Furthermore, to improve the confidence of the assignments, the IFS for each metabolite should be investigated.

Using the developed protocol, we have shown the application of high resolution MSI to determine metabolite distributions within MTS cell culture models. Initially, **ATP** and glutathione were employed as targeted metabolite markers to indicate regions of increased oxidative stress and hypoxia. Subsequently, untargeted discriminatory analysis was used to investigate how these microenvironments affect the regional flux through metabolic branch pathways. Here we have shown that there is an upregulation of the HBP in regions of the spheroid with greater access to oxygen; whereas there is greater glycolytic flux within the regions limited by hypoxia. Nevertheless, whilst it is possible to compare the relative intensities of these metabolites in the different microenvironments, ionisation bias prevents any definitive quantification of the distributions observed.

MALDI-MSI has also been employed to observe the distribution of pimonidazole and its metabolites within PC3 MTS over a 24-hour time course. CASI effectively increased the S/N and achieved better sensitivity of the hypoxia marker and its reduction products. We have shown that pimonidazole accumulated at the centre of the spheroid by six hours and underwent reduction over the time course. However, due to the various conjugates the hydroxylamine derivative can form, it was not possible to observe all of the reaction products. In addition, previous MSI literature has suggested that pimonidazole displays a non-specific localisation to regions of hypoxia. Therefore, future work could complement this data with immunohistochemical staining to establish which metabolites colocalise with the hypoxic regions of the spheroid.

Finally, we have shown that a 3D printer can be converted into an effective automated MALDI matrix application platform. Using fluorescent microarrays and experimental design, the conditions for 9AA matrix application were optimised. Incorporating a heated bed and increasing the z height of the sprayer minimised sample wetting and reduced analyte diffusion. These optimised conditions were then used to reproducibly image MCF-7 spheroids and observe numerous metabolites with reduced analyte delocalisation. The images had comparable distributions to those observed using a commercially available printer at a fraction of the set-up cost.

MSI using FT-ICR provides unparalleled spectral resolution for confident elemental assignment. By increasing the transient recording time, FT-ICR produces an approximately linear improvement of mass resolution.[177] However, this results in an inherently slow acquisition time, as the high mass resolving power requires long transients to be acquired for each pixel.[34] Given that a typical MS image can consist of tens of thousands of pixels, acquisition time may become a constraining factor. This can result in a trade-off between spectral resolution and data aquisition time. Notwithstanding, in comparison to animal tissue samples, the small size of MTS mitigates this disadvantage somewhat, allowing multiple biological replicates to be analysed on realistic timescales.

Bibliography

(1) Chaurand, P.; Schwartz, S. A.; Reyzer, M. L.; Caprioli, R. M. *Toxicol. Pathol.* **2005**, *33* (1), 92–101.

(2) Di Girolamo, F.; Lante, I.; Muraca, M.; Putignani, L. *Curr. Org. Chem*. **2013**, *17* (23), 2891–2905.

(3) Ren, J.; Zhang, A.; Kong, L.; Wang, X. *RSC Adv.* **2018**, *8*, 22335–22350.

(4) Tanaka, K.; Waki, H.; Ido, Y.; Akita, S.; Yoshida, Y.; Yoshida, T.; Matsuo, T. *Rapid Commun. Mass Spectrom*. **1988,** *2* (8), 151–153.

(5) Fenn, J. B.; Mann, M.; Meng, C. K.; Fu, W. S.; Whitehouse, C. M. *Science* **1989**, *246*, 64–71.

(6) Todd, P. J.; Schaaff, T. G.; Chaurand, P.; Caprioli, R. M. *J. Mass Spectrom.* **2001**, *36* (4), 355–369.

(7) Takáts, Z.; Wiseman, J. M.; Gologan, B.; Cooks, G. *Science* **2004**, *306* (5695), 471–473.

(8) Kertesz, V.; Van Berkel, G. J.; *J. Mass. Spectrom*. **2010**, *45*, 252–260.

(9) Schwartz, S. A.; Reyzer, M. L.; Caprioli, R. M. *J. Mass Spectrom*. **2003**, *38* (7), 699–708.

(10) Dreisewerd, K. *Anal. Bioanal. Chem*. **2014**, *406* (9), 2261–2278

(11) de Hoffmann, E.; Stroobant, V. Mass spectrometry: Principles and Applications, 3rd ed.; Wiley, **2007**.

(12) Chaurand, P.; Schwartz, S. A; Caprioli, R. M. *Anal. Chem.* **2004**, *33* (1), 92–101.

(13) Lu, I.; Lee, C.; Lee, Y.; Ni, C. Annu. Rev. Anal. Chem. **2015**, *8*, 21–39.

(14) Niehaus, M.; Soltwisch, J. *Sci. Rep.* **2018**, *7755*, 1–10.

(15) Weaver, E. M.; Hummon, A. B. *Adv. Drug Deliv. Rev*. **2013**, *65* (8), 1039–1055.

(16) Chughtai, K.; Heeren, R. M. *Chem. Rev.* **2010**, *110* (5), 3237–3277.

(17) Reyzer, M. L.; Hsieh, Y.; Ng, K.; Korfmacher, W. A.; Caprioli, R. M. *J. Mass Spectrom.* **2003**, *38* (10), 1081–1092.

(18) Liu, X.; Hummon, A. B. *Anal. Chem.* **2015**, *87* (19), 9508–9519.

(19) Garrison, B. J.; Delcorte, A.; Zhigilei, L. V; Itina, T. E.; Krantzman, K. D.; Yingling, Y. G.; Mcquaw, C. M.; Smiley, E. J.; Winograd, N. *Appl. Surf. Sci* **2003**, *204*, 69–71.

(20) Benninghoven, A.; Rudenauer, F. G.; Werner, H. W. Secondary Ion Mass Spectrometry: Basic Concepts, Instrumental Aspects, Applications, and Trends; Wiley: New York, **1987**.

(21) Ho, C. S.; Lam, C. W.; Chan, M. H.; Cheung, R. C.; Law, L. K.; Lit, L. C.; Ng, K. F.; Suen, M. W.; Tai, H. L. *Clin. Biochem. Rev* **2003**, *24* (1), 3–12.

(22) Whitehouse, C. M.; Dreyer, R. N.; Yamashita, M.; Fenn, J. B*. Anal. Chem.* **1985**, *57* (3), 675–679.

(23) Iribarne, J. V.; Thomson, B. A*. J. Chem. Phys*. **1976**, *64* (6), 2287–2294.

(24) De La Mora, J. F. *Anal. Chim. Acta* **2000**, *406* (1), 93–104.

(25) Nguyen, S.; Fenn, J. B. *PNAS* **2007**, *104* (4), 1–7.

(26) Konermann, L.; Rodriguez, A. D.; Liu, J. *Anal. Chem.* **2012**, *84* (15), 6798–6804.

(27) Van Berkel, G. J.; Sanchez, A. D.; Quirke, J. M*. Anal. Chem*. **2002**, *74* (24), 6216–6223.

(28) Venter, A.; Sojka, P. E.; Cooks, R. G. *Anal. Chem*. **2006**, *78* (24), 8549–8555.

(29) Costa, A. B.; Cooks, R. G. *Chem. Phys. Lett*. **2008**, *464*, 1–8.

(30) Gaskell, S. J. *J. Mass. Spectrom.* **1997**, *32* (7), 677–688.

(31) Ifa, D. R.; Wu, C.; Ouyang, Z.; Cooks, R. G. *Analyst* **2010**, *135* (4), 669–681.

(32) Takáts, Z.; Wiseman, J. M.; Cooks, R. G. *J. Mass Spectrom.* **2005**, *40* (10), 1261–1275.

(33) Awad, H.; Khamis, M. M.; El-Aneed, A. *Appl. Spectrosc. Rev.* **2015**, *50* (2), 158–175.

(34) Jungmann, J. H.; Heeren, R. M. A. J. *Proteomics* **2012**, 75 (16), 5077–5092.

(35) Amster, I. J. J. Mass Spectrom. *J. Mass. Spectrom.* **1996**, *31* (12), 1325–1337.

(356 Marshall, A. G.; Hendrickson, C. L.; Jackson, G. S. *Mass. Spectrom. Rev.* **1998**, *17* (1), 1–35.

(37) Lee, D. Y.; Bowen, B. P.; Northen, T. R. *Biotechniques* **2010**, *49* (2), 557–565.

(38) Acland, M.; Mittal, P.; Lokman, N. A.; Klingler-Hoffmann, M.; Oehler, M. K.; Hoffmann, P. *Proteomics Clin. Appl.* **2018**, *12* (3), 1–13.

(39) Nilsson, A.; Goodwin, R. J. A.; Shariatgorji, M.; Vallianatou, T.; Webborn, P. J. H.; Andrén, P. E. *Anal. Chem*. **2015**, *87* (3), 1437–1455.

(40) Goodwin, R. J. A. J. *Proteomics* **2012**, *75* (16), 4893–4911.

(41) Spengler, B. *Anal. Chem*. **2015**, 87, 64–82.

(42) Chaurand, P.; Schwartz, S. A.; Caprioli, R. M. *Curr. Opin. Chem. Biol.* **2002**, *6* (5), 676–681.

(43) Todd, P. J.; Mcmahon, J. M.; Short, R. T. McCandlish, C. A.; *Anal. Chem.* **1997**, *69* (17), 529–535.

(44) Vickerman, J. C. *Analyst* **2011**, *136* (11), 2199–2217.

(45) Okutan, S.; Hansen, H. S.; Janfelt, C. *Proteomics* **2016**, *16* (11), 1634–1641.

(46) Griffiths, R. L.; Simmonds, A. L.; Swales, J. G.; Goodwin, R. J. A.; Cooper, H. J. *Anal. Chem.* **2018**, *90* (22), 13306–13314.

(47) Griffiths, R. L.; Cooper, H. J*. Anal. Chem.* **2016**, *88*, 606–609.

(48) Khatib-Shahidi, S.; Andersson, M.; Herman, J. L.; Gillespie, T. A.; Caprioli, R. M. *Anal. Chem.* **2006**, *78* (18), 6448–6456.

(49) Buchberger, A. R.; DeLaney, K.; Johnson, J.; Li, L. *Anal. Chem*. **2018**, *90* (1), 240–265.

(50) Swales, J. G.; Tucker, J. W.; Strittmatter, N.; Nilsson, A.; Cobice, D.; Clench, M. R.; Mackay, C. L.; Andren, P. E. Takáts, Z.; Webborn, P. J.; Goodwin, R. J.; *Anal. Chem.* **2014**, *86* (8), 8473−8480.

(51) Laskin, J.; Heath, B. S.; Roach, P. J.; Cazares, L.; Semmes, O. J. *Anal. Chem*. **2012**, *84* (1), 141–148.

(52) Doerr, A. *Nat. Methods* **2018**, *15* (1), 32.

(53) Puolitaival, S. M.; Burnum, K. E.; Cornett, D. S.; Caprioli, R. M. *J. Am. Soc. Mass Spectrom.* **2008**, *19* (6), 882–886.

(54) Goodwin, R. J. A.; Scullion, P.; Macintyre, L.; Watson, D. G.; Pitt, A. R. *Rapid Commun. Mass Spectrom.* **2010**, *24* (1), 1682–1686.

(55) Caprioli, R. M.; Farmer, T. B.; Gile, J. *Anal. Chem.* **1997**, *69* (23), 4751–4760.

(56) Stoeckli, M.; Farmer, T. B.; Caprioli, R. M. *J. Am. Soc. Mass. Spectrom.* **1999**, *10* (1), 67–71.

(57) Chaurand, P.; Caprioli, R. M. *Electrophoresis* **2002**, *23* (18), 3125–3135.

(58) Chaurand, P.; DaGue, B. B.; Ma, S.; Kasper, S.; Caprioli, R. M. *Biochemistry* **2001**, *40* (32), 9725–9733.

(59) Stoeckli, M.; Chaurand, P.; Hallahan, D. E.; Caprioli, R. M. *Nat. Med*. **2001**, *7* (4), 493–496.

(60) Chaurand, P.; Dague, B. B.; Pearsall, R. S.; Threadgill, D. W.; Caprioli, R. M. *Proteomics* **2001**, *1* (10), 1320–1326.

(61) Cazares, L. H.; Troyer, D.; Mendrinos, S.; Lance, R. A.; Nyalwidhe, J. O.; Beydoun, H. A.; Clements, M. A.; Drake, R. R.; Semmes, O. *J. Clin. Cancer Res.* **2009**, *15* (17), 5541–5551.

(62) Stoeckli, M.; Staab, D.; Staufenbiel, M.; Wiederhold, K.; Signor, L. *Anal. Biochem.* **2002**, *311* (1), 33–39.

(63) Stauber, J.; Lemaire, R.; Franck, J.; Bonnel, D.; Croix, D.; Day, R.; Wisztorski, M.; Fournier, I.; Salzet, M. *J. Proteome Res*. **2008**, *7* (3), 969–978.

(64) Crecelius, A. C.; Cornett, D. S.; Caprioli, R. M.; Williams, B.; Dawant, B. M.; Bodenheimer, B. *J. Am. Soc. Mass. Spectrom.* **2005**, *16* (7), 1093–1099.

(65) Troendle, F. J.; Reddick, C. D.; Yost, R. A. *J. Am. Soc. Mass Spectrom.* **1999**, *10* (12), 1315–1321.

(66) Nilsson, A.; Fehniger, T. E.; Gustavsson, L.; Andersson, M.; Kenne, K.; Marko-Varga, G.; Andrén, P. E. *PLoS One* **2010**, *5* (7), 1–8.

(67) Chaurand, P.; Fouchécourt, S.; DaGue, B. B.; Xu, B. J.; Reyzer, M. L. *Proteomics* **2003**, *3* (11), 2221–2239.

(68) Hsieh, Y.; Chen, J.; Korfmacher, W. A. *J. Pharmacol. Toxicol. Methods* **2007**, *55* (2), 193–200.

(69) Shariatgorji, M.; Nilsson, A.; Goodwin, R. J. A.; Källback, P.; Schintu, N.; Zhang, X.; Crossman, A. R.; Bezard, E.; Svenningsson, P.; Andren, P. E. *Neuron*. **2014**, *84* (4), 697–707.

(70) Beasley, E.; Francese, S.; Bassindale, T. *Anal. Chem*. **2016**, *88* (20), 10328–10334.

(71) Araújo, F. D.; Araújo, W. L.; Eberlin, M. N. *J. Am. Soc. Mass. Spectrom*. **2017**, *28* (5), 901–907.

(72) Gemoll, T.; Strohkamp, S.; Schillo, K.; Thorns, C.; Havermann, J. K. *Oncotarget* **2015**, *6* (41), 43869–43880.

(73) Koomen, J. M.; Stoeckli, M.; Caprioli, R. M. *J. Mass. Spectrom*. **2000**, *35* (2), 258–264.

(74) Seeley, E. H.; Wilson, K. J.; Yankeelov, T. E.; Johnson, R. W.; Gore, J. C.; Caprioli, R. M.; Matrisian, L. M.; Sterling, J. A. *Bone* **2014**, *61*, 208–216.

(75) Ahlf, D. R.; Masyuko, R. N.; Hummon, A. B.; Bohn, P. W. *Analyst* **2014**, *139* (18), 4578–4585.

(76) Kompauer, M.; Heiles, S.; Spengler, B. *Nat. Methods* **2017**, *14* (1), 90–96.

(77) Sugiura, Y.; Shimma S; Setou, M. *J. Mass Spectrom. Soc. Jpn.* **2006**, *54* (2), 45–48.

(78) Aerni, H. R.; Cornett, D. S.; Caprioli, R. M. *Anal. Chem*. **2006**, *78* (3), 827–834.

(79) Baluya, D. L.; Garrett, T. J.; Yost, R. A. *Anal. Chem*. **2007**, *79* (17), 6862–6867.

(80) Tucker, L. H.; Conde-González, A.; Cobice, D.; Hamm, G. R.; Goodwin, R. J. A.; Campbell, C. J.; Clarke, D. J.; Mackay, C. L. *Anal. Chem*. **2018**, *90* (15), 8742–8749.

(81) Dill, A. L.; Eberlin, L. S.; Costa, A. B.; Ifa, D. R.; Cooks, R. G. *Anal. Bioanal. Chem*. **2011**, *401* (6), 1949–1961.

(82) Goodwin, R. J.; Iverson, S. L.; Andren, P. E. *Rapid Commun. Mass Spectrom.* **2012**, *26* (5), 494–498.

(83) Stoeckli, M.; Staab, D.; Schweitzer, A. *Int. J. Mass Spectrom.* **2007**, *260* (2), 195–202.

(84) Li, H.; Hummon, A. B. *Anal. Chem*. **2011**, *83* (22), 8794–8801.

(85) Pierson, J.; Norris, J. L.; Aerni, H.; Svenningsson, P.; Caprioli, R. M.; Andren, P. E. *J. Proteome Res*. **2004**, *3* (2), 289–295.

(86) Crossman, L.; McHugh, N. A.; Hsieh, Y.; Korfmacher, W. A.; Chen, *J. Rapid Commum. Mass. Spectrom*. **2006**, *20* (2), 284–290.

(87) Goodwin, R. J. A.; Dungworth, J. C.; Cobb, S. R.; Pitt, A. R. *Proteomics* **2008**, *8* (18), 3801–3808.

(88) Goodwin, R. J. A; Pitt, A. R.; Harrison, D.; Weidt, S. K.; Langridge-Smith, P. R.; Barrett, M. P.; MacKay, C. L. *Rapid Commun. Mass Spectrom*. **2011**, *25* (7), 969–972.

(89) Wang, H.J., Jackson, S.N., Post, J., Woods, A. S. *Int. J. Mass Spectrom*. **2008**, *278*, 143–149.

(90) Heeren, R. M. A. *Int. J. Mass Spectrom*. **2015**, *377*, 672–680.

(91) Jackson, P.; Attalla, M. I. *Rapid Commun. Mass Spectrom*. **2010**, *24* (24), 3567–3577.

(92) Sugiura, Y.; Shimma, S.; Setou, M. *Anal. Chem.* **2006**, *78* (24), 8227–8235.

(93) Eriksen, J.; Jørgensen, T. N.; Gether, U. *J. Neurochem*. **2010**, *113* (1), 27–41.

(94) Gemperline, E.; Rawson, S.; Li, L. *Anal. Chem*. **2014**, *86*, 10030–10035.

(95) Mounfield, W. P.; Garrett, T. *J. Am. Soc. Mass Spectrom*. **2012**, *23* (3), 563–569.

(96) Murphy, R. C.; Hankin, J. A.; Barkley, R. M.; Berry, K. A. Z. *Biochim. Biophys. Acta.* **2012**, *1811* (11), 970–975.

(97) Hankin, J. A.; Barkley, R. M.; Murphy, R. C. *J. Am. Mass. Spectrom.* **2007**, *18* (9), 1646–1652.

(98) Jurchen, J. C.; Rubakhin, S. S.; Sweedler, J. V. *J. Am. Soc. Mass Spectrom*. **2005**, *16* (10), 1654–1659.

(99) Feenstra, A. D.; Dueñas, M. E.; Lee, Y. J. *J. Am. Mass. Spectrom*. **2017**, *28* (3), 434–442.

(100) Robichaud, G.; Garrad, K. P.; Barry, J. A.; Muddiman, D. C. *J. Mass Spectrom*. **2014**, *24* (5), 718–721.

(101) Race, A. M.; Palmer, A. D.; Dexter, A.; Steven, R. T.; Styles, I. B.; Bunch, J. *Anal. Chem.* **2016**, *88* (19), 9451–9458.

(102) Bro, R.; Smilde, A. K. *Anal. Methods* **2014**, *6*, 2812–2831.

(103) Alexandrov, T. Metaspace http://metaspace2020.eu.

(104) Hsieh, Y.; Wang, G.; Wang, Y.; Chackalamannil, S.; Korfmacher, W. A. *Anal. Chem.* **2003**, *75* (8), 1812–1818.

(105) Hamm, G.; Bonnel, D.; Legouffe, R.; Pamelard, F.; Delbos, J. M.; Bouzom, F.; Stauber, J. *J. Proteomics* **2012**, *75* (16), 4952–4961.

(106) Ait-Belkacem, R.; Sellami, L.; Villard, C.; DePauw, E.; Calligaris, D.; Lafitte, D. *Trends Biotechnol.* **2012**, *30* (9), 466–474.

(107) Fonville, J. M.; Carter, C.; Cloarec, O.; Nicholson, J. K.; Lindon, J. C.; Bunch, J.; Holmes, E. *Anal. Chem*. **2012**, *84* (3), 1310–1319.

(108) Cobice, D. F.; Livingstone, D. E. W.; Mackay, C. L.; Goodwin, R. J. A.; Smith, L. B.; Walker, B. R.; Andrew, R. *Anal. Chem*. **2016**, *88* (21), 10362–10367.

(109) Wang, H.; DeGnore, J. P.; Kelly, B. D.; True, J.; Bieniarz, C. *J. Mass. Spectrom.* **2015**, *50* (9), 1088–1095.

(110) Arrowsmith, J.; Miller, P. *Nat. Rev. Drug Dicsov*. **2013**, *12* (8), 569.

(111) Breslin, S.; O'Driscoll, L. *Drug Discov. Today* **2013**, *18* (5), 240–249.

(112) Fennema, E.; Rivron, N.; Rouwkema, J.; van Blitterswijk, C.; De Boer, J. *Trends Biotechnol*. **2013**, *31* (2), 108–115.

(113) Jamieson, L. E.; Harrison, D. J.; Campbell, C. J. *Analyst* **2015**, *140*, 3910–3920.

(114) Asthana, A.; Kisaalita, W. S. *Drug Discov. Today* **2016**, *21* (3), 395–399.

(115) Mehta, G.; Hsiao, A. Y.; Ingram, M.; Luker, G. D.; Takayama, S. *J. Control. Release* **2012**, *164* (2), 192–204.

(116) Kunz-Schughart, L. A.; Kreutz, M.; Knuechel, R. *Int. J. Exp. Pathol.* **1998**, *79* (1), 1–23.

(117) He, W.; Kuang, Y.; Xing, X.; Simpson, R. J.; Huang, H.; Yang, T.; Chen, J.; Yang, L.; Liu, E.; Gu, J. *J. Proteome Res*. **2014**, *13* (5), 2272–2281.

(118) Kelm, J. M.; Timmins, N. E.; Brown, C. J.; Fussenegger, M.; Nielsen, L. K. *Biotechnol. Bioeng.* **2003**, *83* (2), 173–180.

(119) Lin, R. Z.; Chang, H. Y. *Biotechnol. J.* **2008**, *3* (9–10), 1172–1184.

(120) Lin, R. Z.; Chou, R. L. *Cell Tissue Res*. **2006**, *324*, 411–422.

(121) Ivascu, A.; Kubbies, M. *Int. J. Oncol.* **2007**, *31* (6), 1403–1413.

(122) Trédan, O.; Galmarini, C. M.; Patel, K.; Tannock, I. F. *J. Natl. Cancer Inst.* **2007**, *99* (19), 1441–1454.

(123) Freyer, J. P.; Sutherland, R. M. *Cancer Research* **1986**, *46*, 3504–3512.

(124) Franko, A. J.; Sutherland, R. M. *Radiation Research* **1979**, *79* (3), 439–453.

(125) Freyer, J. P.; Schor, P. L.; Jarrett, K. A.; Neeman, M.; Sillerud, L. O. *Cancer Research* **1991**, *51*, 3831–3838.

(126) David, B. P.; Dubrovskyi, O.; Speltz, T. E.; Wol, J. J.; Frasor, J.; Sanchez, L. M.; Moore, T. W. *Med. Chem. Lett.* **2018**, *9* (7), 768–772.

(127) Clevers, H. *Cell* **2016**, *165* (7), 1586–1597.

(128) Fatehullah, A.; Tan, S. H.; Barker, N. *Nat. Cell Biol.* **2016**, *18* (3), 246–254.

(129) Feist, P. E.; Sidoli, S.; Liu, X.; Schroll, M. M.; Rahmy, S.; Fujiwara, R.; Garcia, B. A.; Hummon, A. B. *Anal. Chem*. **2017**, *89* (5), 2773–2781.

(130) Weaver, E. M.; Hummon, A. B.; Keithley, R. B. *Anal. Methods* **2015**, *7* (17), 7208–7219.

(131) Hiraide, T.; Ikegami, K.; Sakaguchi, T.; Morita, Y.; Hayasaka, T.; Masaki, N.; Waki, M.; Sugiyama, E.; Shinriki, S.; Takeda, M.; Shibasaki, Y.; Miyazaki, S.; Kikuchi, H.; Okuyama, H.; Inoue, M.; Setou, M.; Konno, H. *Sci. Rep.* **2016**, *6*, 1–11.

(132) Liu, X.; Weaver, E. M.; Hummon, A. B. *Anal. Chem*. **2013**, *85* (13), 6295–6302.

(133) Liu, X.; Flinders, C.; Mumenthaler, S. M.; Hummon, A. B. *J. Am. Soc. Mass Spectrom.* **2017**, *29* (3), 516–526.

(134) LaBonia, G. J.; Lockwood, S. Y.; Heller, A. A.; Spence, D. M.; Hummon, A. B. *Proteomics* **2016**, *16* (11–12), 1814–1821.

(135) Lukowski, J. K.; Weaver, E. M.; Hummon, A. B. *Anal. Chem.* **2017**, *89* (16), 8453–8458.

(136) Liu, X.; Hummon, A. B. *Sci. Rep*. **2016**, *6*, 1–10.

(137) LaBonia, G. J.; Ludwig, K. R.; Mousseau, C. B.; Hummon, A. B. *Anal. Chem.* **2018**, *90* (2), 1423–1430.

(138) Schroll, M. M.; LaBonia, G. J.; Ludwig, K. R.; Hummon, A. B. *J. Proteome Res*. **2017**, *16* (8), 3009–3018.

(139) Jamieson, L. E.; Camus, V. L.; Bagnaninchi, P. O.; Fisher, K. M.; Stewart, G. D.; Nailon, W. H.; McLaren, D. B.; Harrison, J.; Campbell, C. J. *Nanoscale* **2016**, *8* (37), 16710–16718.

(140) Niehoff, A. C.; Grünebaum, J.; Moosmann, A.; Mulac, D.; Söbbing, J.; Niehaus, R.; Buchholz, R.; Kröger, S.; Wiehe, A.; Wagner, S.; Sperling, M.; von Briesen, H.; Langer, K.; Karst, U. *Anal. Chim. Acta* **2016**, *938*, 106–113.

(141) Palmer, A.; Phapale, P.; Chernyavsky, I.; Lavigne, R.; Fay, D.; Tarasov, A.; Kovalev, V.; Fuchser, J.; Nikolenko, S.; Pineau, C. *Nat. Methods* **2016**, *14* (1), 57–60. https://doi.org/10.1038/nmeth.4072.

(142) Dilillo, M.; Ait-Belkacem, R.; Esteve, C.; Pellegrini, D.; Nicolardi, S.; Costa, M.; Vannini, E.; De Graaf, E. L.; Caleo, M.; McDonnell, L. A. *Sci. Rep*. **2017**, *7* (1), 1–11.

(143) Benabdellah, F.; Touboul, D.; Brunelle, A.; Laprévote, O. *Anal. Chem.* **2009**, *81* (13), 5557–5560.

(144) Nagana Gowda, G. A.; Barding, G. A.; Dai, J.; Gu, H.; Margineantu, D. H.; Hockenbery, D. M.; Raftery, D. *Front. Mol. Biosci.* **2018**, *15* (5), 1–13.

(145) Ma, Z.; Vosseller, K. *Amino Acids* **2013**, *45* (4), 719–733.

(146) Badr, H. A.; Alsadek, D. M. M.; Mathew, M. P.; Li, C.; Djansugurova, L. B.; Yarema, K. J. Ahmed, H. *Biomaterials* **2015**, *70*, 23–36.

(147) Herceg, Z.; Wang, Z. *Mutat. Res*. **2001**, *477* (1–2), 97–110.

(148) Cornett, D. S.; Frappier, S. L.; Caprioli, R. M. *Anal. Chem.* **2008**, *80* (14), 5648–5653

(149) Zhang, T.; Zhang, A.; Qiu, S.; Yang, S.; Wang, X. *Crit. Rev. Anal. Chem*. **2016**, *46* (4), 342–351.

(150) Navas-Carrillo, D.; Rodriguez, J. M.; Montoro-García, S.; Orenes-Piñero, E. *Crit. Rev. Clin. Lab. Sci.* **2017**, *54* (7–8), 446–457.

(151) Prentice, B. M.; W, C. C.; Caprioli, R. M. *J. Mass Spectrom.* **2016**, *50* (4), 703–710.

(152) Hardie, D. G.; Scott, J. W.; Pan, D. A.; Hudson, E. R. *FEBS Lett.* **2003**, *546* (1), 113–120.

(153) Veech, R. L.; Lawson, J. W.; Cornell, N. W.; Krebs, H. A. *J. Biol. Chem.* **1979**, *254* (14), 6538–6547.

(154) Maldonado, E. N.; Lemasters, J. *J. Mitochondrion* **2014**, *19* (1), 78–84.

(155) Rodriguez-Enriquez, S.; Gallardo-Pérez, J. C.; Avilés-Salas, A.; Marin-Hernández, A.; Carreño-Fuentes, L.; Maldonado-Laguna, V.; Moreno-Sánchez, R. *J. Cell Physiol.* **2008**, *216*, 189–197.

(156) Tantama, M.; Martínez-François, J. R.; Mongeon, R.; Yellen, G. *Nat. Commun.* **2013**, *4* (2250), 1–27.

(157) Balendiran, G. K.; Dabur, R.; Fraser, D. *Cell Biochem. Funct.* **2004**, *22* (1), 343–352.

(158) Deponte, M. *Antioxid. Redox Signal.* **2017**, *27* (15), 1130–1161.

(159) Circu, M. L.; Yee Aw, T. *Biochem. Biophys. Acta.* **2012**, *1823* (10), 1767–1777.

(160) Chandel, N. S.; McClintock, D. S.; Feliciano, C. E.; Wood, T. M.; Melendez, J. A.; Rodriguez, A. M.; Schumacker, P. T. *J. Biol. Chem*. **2000,** *275* (33), 25130–25138.

(161) Kim, J. W.; Tchernyshyov, I.; Semenza, G. L.; Dang, C. V. *Cell Metab*. **2006**, *3* (3), 177–185.

(162) Shirato, K.; Nakajima, K.; Korekane, H.; Shinji Takamatsu, Congxiao Gao, T. Angata, T.; Ohtsubo, K.; Taniguchi, N. *J. Clin. Biochem.* **2011**, *48* (1), 20–25.

(163) Ruan, H. Bin; Singh, J. P.; Li, M. D.; Wu, J.; Yang, X. *Trends Endocrinol. Metab.* **2013**, *24* (6), 301–309.

(164) Clark, P. M.; Dweck, J. F.; Mason, D. E.; Hart, C. R.; Buck, S. B.; Peters, E. C.; Agnew, B. J.; Hsieh-Wilson, L. C. *J. Am. Chem. Soc.* **2008**, *130* (35), 11576–11577.

(165) Pearce, O. M. T.; Läubli, H. *Glycobiology* **2016**, *26* (2), 111–128.

(166) Go, S.; Sato, C.; Yin, J.; Kannagi, R.; Kitajima, K. *Biochem. Biophys. Res. Commun.* **2007**, *357*, 537–542.

(167) Krohn, K. A.; Link, J. M.; Mason, R. P. *J. Nucl. Med*. **2008**, *49,* 129–149.

(168) Mascini, N. E.; Cheng, M.; Jiang, L.; Rizwan, A.; Podmore, H.; Bhandari, D. R.; Ro, A.; Glunde, K.; Heeren, R. M. A. *Anal. Chem.* **2016**, *88* (6), 3107–3114.

(169) Nunn, A.; Linder, K.; Strauss, H. W. Eur. *J. Nucl. Med*. **1995**, *22* (3), 265–280.

(170) Masaki, Y.; Shimizu, Y.; Yoshioka, T.; Feng, F.; Zhao, S. Higashino, K.; Numata, Y.; Kuge, Y. *PLoS One* **2016**, *11* (8), 1–11.

(171) Masaki, Y.; Shimizu, Y.; Yoshioka, T.; Tanaka, Y. Nishijima, K.; Zhao, S.; Higashino, K.; Sakamoto, S.; Numata, Y.; Yamaguchi, Y.; Tamaki, N.; Kuge, Y. *Sci. Rep.* **2015**, *5,* 1–9.

(172) Varghese, A. J.; Whitmore, G. F. *Chem. Biol. Interact.* **1985**, *56* (2–3), 269–287.

(173) Raleigh, J. A.; Koch, C. *J. Biochem. Pharmacol.* **1990**, *40* (11), 2457–2464.

(174) Varghese, A. J.; Whitmore, G. F. *Cancer Res*. **1980**, *40* (7), 165–169.

(175) Heeren, R. M. A.; Kükrer-Kaletas, B.; Taban, I. M.; MacAleese, L.; McDonnell, L. A. *Appl. Surf. Sci*. **2008**, *255* (4), 1289–1297.

(176) Thomas, A.; Charbonneau, J. L.; Fournaise, E.; Chaurand, P. *Anal. Chem.* **2012**, *84* (4), 2048–2054.

(177) Hendrickson, C. L.; Quinn, J. P.; Kaiser, N. K.; Smith, D. F.; Blakney, G. T.; Chen, T.; Marshall, A. G.; Weisbrod, C. R.; Beu, S. C. *Am. Soc. Mass Spectrom*. **2015**, *26*, 1626–1632.

Appendices

CHCA mass list positive mode

Observed *m/z*	Expected *m/z*	Error (ppm)	Tentative neutral formula	Adduct
272.12560	272.12571	0.41892	$C_{14}H_{19}NO_3$	[M+Na]+
275.13877	275.13902	0.90500	$C_{15}H_{18}N_2O_3$	[M+H]+
280.09184	280.09205	0.73190	$C_8H_{20}NO_6P$	[M+Na]+
282.09704	282.09721	0.61681	$C_{13}H_{15}NO_6$	[M+H]+
282.27888	282.27914	0.92462	$C_{18}H_{35}NO$	[M+H]+
283.01872	283.01894	0.77380	$C_6H_{13}O_9P$	[M+Na]+
285.24224	285.24242	0.63455	$C_{17}H_{32}O_3$	[M+H]+
286.31024	286.31044	0.70204	$C_{18}H_{39}NO$	[M+H]+
294.10987	294.11006	0.65962	$C_{16}H_{17}NO_3$	[M+Na]+
296.06579	296.06598	0.64850	$C_8H_{20}NO_6P$	[M+K]+
298.08980	298.08972	-0.25831	$C_{11}H_{17}NO_7$	[M+Na]+
299.25791	299.25807	0.53800	$C_{18}H_{34}O_3$	[M+H]+
308.06572	308.06552	-0.65246	$C_{16}H_{13}O_5$	[M+Na]+
311.25792	311.25807	0.48513	$C_{19}H_{34}O_3$	[M+H]+
317.24504	317.24510	0.19228	$C_{19}H_{34}O_2$	[M+Na]+
331.13750	331.13740	-0.31407	$C_6H_7N_5O$	[2M+H]+
341.30500	341.30502	0.06446	$C_{21}H_{40}O_3$	[M+H]+
344.11297	344.11286	-0.30804	$C_{18}H_{17}NO_6$	[M+H]+
365.10534	365.10543	0.25198	$C_{12}H_{22}O_{11}$	[M+Na]+
370.12878	370.12851	-0.71867	$C_{20}H_{19}NO_6$	[M+H]+
374.14331	374.14349	0.47843	$C_{15}H_{21}N_5O_5$	[M+Na]+
376.35746	376.35739	-0.18068	$C_{25}H_{45}NO$	[M+H]+
379.09244	379.09246	0.06067	$C_{10}H_7NO_3$	[2M+H]+
388.12151	388.12142	-0.23962	$C_{14}H_{23}NO_{10}$	[M+Na]+
390.37319	390.37304	-0.37912	$C_{26}H_{47}NO$	[M+H]+
391.22443	391.22452	0.22493	$C_{21}H_{36}O_4$	[M+K]+
391.28432	391.28429	-0.08689	$C_{24}H_{38}O_4$	[M+H]+
393.30004	393.29994	-0.26443	$C_{24}H_{40}O_4$	[M+H]+
405.24011	405.24002	-0.23196	$C_{25}H_{34}O_3$	[M+Na]+
406.16966	406.16970	0.10833	$C_{16}H_{25}N_5O_6$	[M+Na]+
408.32381	408.32369	-0.30368	$C_{26}H_{43}NO$	[M+Na]+
411.06290	411.06293	0.07785	$C_{23}H_{16}O_5$	[M+K]+
413.04209	413.04220	0.25663	$C_{22}H_{14}O_6$	[M+K]+
413.09587	413.09554	-0.80853	$C_{18}H_{18}N_2O_8$	[M+Na]+
413.26618	413.26623	0.12099	$C_{24}H_{38}O_4$	[M+Na]+
415.22206	415.22200	-0.15413	$C_{19}H_{37}O_6P$	[M+Na]+
417.24012	417.24017	0.11504	$C_{23}H_{38}O_4$	[M+K]+
419.25572	419.25570	-0.04293	$C_{21}H_{39}O_6P$	[M+H]+
419.31578	419.31559	-0.46266	$C_{26}H_{42}O_4$	[M+H]+
422.33921	422.33934	0.29834	$C_{27}H_{45}NO$	[M+Na]+
429.24049	429.24017	-0.75016	$C_{24}H_{38}O_4$	[M+K]+
431.21717	431.21691	-0.60063	$C_{19}H_{37}O_7P$	[M+Na]+
433.27142	433.27132	-0.24003	$C_{27}H_{38}O_3$	[M+Na]+
436.28225	436.28222	-0.08022	$C_{26}H_{39}NO_3$	[M+K]+
436.35502	436.35514	0.27042	$C_{25}H_{51}NO_2$	[M+K]+
439.22219	439.22200	-0.44169	$C_{21}H_{37}O_6P$	[M+Na]+
441.23782	441.23765	-0.39435	$C_{21}H_{39}O_6P$	[M+Na]+

441.29772	441.29753	-0.42828	$C_{26}H_{42}O_4$	[M+Na]+
443.25303	443.25330	0.60011	$C_{21}H_{41}O_6P$	[M+Na]+
445.27156	445.27147	-0.20662	$C_{25}H_{42}O_4$	[M+K]+
448.28247	448.28237	-0.22977	$C_{24}H_{43}NO_4$	[M+K]+
448.35524	448.35514	-0.22750	$C_{26}H_{51}NO_2$	[M+K]+
450.29799	450.29802	0.05996	$C_{24}H_{45}NO_4$	[M+K]+
457.23287	457.23256	-0.67580	$C_{21}H_{39}O_7P$	[M+Na]+
457.27179	457.27147	-0.70418	$C_{26}H_{42}O_4$	[M+K]+
459.24848	459.24821	-0.58574	$C_{21}H_{41}O_7P$	[M+Na]+
461.26421	461.26386	-0.75662	$C_{21}H_{43}O_7P$	[M+Na]+
464.31377	464.31367	-0.22183	$C_{25}H_{47}NO_4$	[M+K]+
468.30856	468.30847	-0.20072	$C_{22}H_{46}NO_7P$	[M+H]+
473.19740	473.19720	-0.41843	$C_{15}H_{12}N_2O$	[2M+H]+
473.30281	473.30277	-0.08874	$C_{27}H_{46}O_4$	[M+K]+
476.21724	476.21740	0.32968	$C_{20}H_{40}NO_7P$	[M+K]+
482.32425	482.32412	-0.27782	$C_{23}H_{48}NO_7P$	[M+K]+
485.26400	485.26386	-0.28644	$C_{23}H_{43}O_7P$	[M+Na]+
489.17720	489.17686	-0.69300	$C_{13}H_{12}N_2O_3$	[2M+H]+
490.29063	490.29041	-0.44871	$C_{22}H_{46}NO_7P$	[M+Na]+
490.32936	490.32932	-0.08770	$C_{27}H_{49}NO_4$	[M+K]+
492.34498	492.34497	-0.02640	$C_{27}H_{51}NO_4$	[M+K]+
494.32426	494.32412	-0.29131	$C_{24}H_{48}NO_7P$	[M+H]+
495.44090	495.44079	-0.22808	$C_{31}H_{58}O_4$	[M+H]+
496.33991	496.33977	-0.29012	$C_{24}H_{50}NO_7P$	[M+H]+
501.31451	501.31436	-0.30520	$C_{21}H_{40}N_8O_6$	[M+H]+
506.36056	506.36050	-0.11652	$C_{26}H_{52}NO_6P$	[M+H]+
508.21917	508.21869	-0.94841	$C_{20}H_{39}NO_{10}S$	[M+Na]+
508.34018	508.33977	-0.81442	$C_{25}H_{50}NO_7P$	[M+H]+
509.45657	509.45644	-0.26106	$C_{32}H_{60}O_4$	[M+H]+
510.35568	510.35542	-0.51729	$C_{25}H_{52}NO_7P$	[M+H]+
516.30642	516.30606	-0.69726	$C_{24}H_{48}NO_7P$	[M+Na]+
517.42295	517.42273	-0.42325	$C_{31}H_{58}O_4$	[M+Na]+
518.32200	518.32171	-0.55950	$C_{24}H_{50}NO_7P$	[M+Na]+
518.36059	518.36050	-0.17170	$C_{27}H_{52}NO_6P$	[M+H]+
519.36423	519.36399	-0.45633	$C_{13}H_{25}NO_4$	[2M+H]+
520.34002	520.33977	-0.48814	$C_{26}H_{50}NO_7P$	[M+H]+
520.37642	520.37627	-0.29402	$C_{29}H_{55}NO_4$	[M+K]+
521.45671	521.45644	-0.52353	$C_{33}H_{60}O_4$	[M+H]+
522.35554	522.35542	-0.23739	$C_{26}H_{52}NO_7P$	[M+H]+
522.52473	522.52446	-0.52246	$C_{34}H_{67}NO_2$	[M+H]+
523.47229	523.47209	-0.38780	$C_{33}H_{62}O_4$	[M+H]+
524.37118	524.37107	-0.21740	$C_{26}H_{54}NO_7P$	[M+H]+
530.27019	530.27009	-0.19235	$C_{28}H_{45}NO_4S$	[M+K]+
531.43877	531.43838	-0.73198	$C_{32}H_{60}O_4$	[M+Na]+
532.07190	532.07218	0.52812	$C_{23}H_{17}NO_{14}$	[M+H]+
532.33757	532.33736	-0.39449	$C_{25}H_{52}NO_7P$	[M+Na]+
535.29064	535.29016	-0.89858	$C_{29}H_{42}O_9$	[M+H]+
536.37155	536.37107	-0.90236	$C_{27}H_{54}NO_7P$	[M+H]+
536.37155	536.37107	-0.90236	$C_{27}H_{54}NO_7P$	[M+H]+
537.48797	537.48774	-0.43350	$C_{34}H_{64}O_4$	[M+H]+
538.35071	538.35033	-0.70400	$C_{26}H_{52}NO_8P$	[M+H]+
538.38682	538.38672	-0.19317	$C_{27}H_{56}NO_7P$	[M+H]+

539.13380	539.13366	-0.26153	$C_{31}H_{22}O_9$	[M+H]+
543.43863	543.43838	-0.45819	$C_{33}H_{60}O_4$	[M+Na]+
544.33762	544.33736	-0.47764	$C_{26}H_{52}NO_7P$	[M+Na]+
544.50674	544.50640	-0.62258	$C_{34}H_{67}NO_2$	[M+Na]+
545.45424	545.45403	-0.38317	$C_{33}H_{62}O_4$	[M+Na]+
547.47237	547.47209	-0.51692	$C_{35}H_{62}O_4$	[M+H]+
550.38687	550.38672	-0.27980	$C_{28}H_{56}NO_7P$	[M+H]+
551.50362	551.50339	-0.42248	$C_{35}H_{66}O_4$	[M+H]+
559.47015	559.46968	-0.83829	$C_{34}H_{64}O_4$	[M+Na]+
560.40764	560.40745	-0.33547	$C_{30}H_{58}NO_6P$	[M+H]+
563.50357	563.50339	-0.32475	$C_{36}H_{66}O_4$	[M+H]+
564.40185	564.40237	0.91424	$C_{29}H_{58}NO_7P$	[M+H]+
565.51931	565.51904	-0.48274	$C_{36}H_{68}O_4$	[M+H]+
572.36895	572.36866	-0.50667	$C_{28}H_{56}NO_7P$	[M+Na]+
575.50370	575.50339	-0.54387	$C_{37}H_{66}O_4$	[M+H]+
577.51926	577.51904	-0.38613	$C_{37}H_{68}O_4$	[M+H]+
578.38216	578.38163	-0.91462	$C_{29}H_{56}NO_8P$	[M+H]+
578.41841	578.41802	-0.68117	$C_{30}H_{60}NO_7P$	[M+H]+
581.19566	581.19587	0.35272	$C_{19}H_{14}O_3$	[2M+H]+
585.48570	585.48533	-0.63025	$C_{36}H_{66}O_4$	[M+Na]+
588.43904	588.43875	-0.48943	$C_{32}H_{62}NO_6P$	[M+H]+
589.26976	589.27021	0.76705	$C_{12}H_{22}O_8$	[2M+H]+
589.51919	589.51904	-0.25953	$C_{19}H_{34}O_2$	[2M+H]+
591.53496	591.53469	-0.46151	$C_{38}H_{70}O_4$	[M+H]+
592.39773	592.39728	-0.75794	$C_{30}H_{58}NO_8P$	[M+H]+
593.12668	593.12671	0.05732	$C_{25}H_{30}O_{14}$	[M+K]+
595.33934	595.33955	0.34770	$C_{34}H_{52}O_6$	[M+K]+
600.36322	600.36358	0.59131	$C_{29}H_{56}NO_8P$	[M+Na]+
601.51919	601.51904	-0.25436	$C_{39}H_{68}O_4$	[M+H]+
603.53481	603.53469	-0.20380	$C_{39}H_{70}O_4$	[M+H]+
605.23543	605.23587	0.72699	$C_{29}H_{42}O_{11}$	[M+K]+
606.41291	606.41293	0.03463	$C_{31}H_{60}NO_8P$	[M+H]+
606.44935	606.44932	-0.05606	$C_{32}H_{64}NO_7P$	[M+H]+
613.34785	613.34759	-0.42227	$C_{30}H_{55}O_9P$	[M+Na]+
614.37974	614.37923	-0.83824	$C_{30}H_{58}NO_8P$	[M+Na]+
617.55061	617.55034	-0.44207	$C_{20}H_{36}O_2$	[2M+H]+
619.56627	619.56599	-0.45677	$C_{40}H_{74}O_4$	[M+H]+
620.42898	620.42858	-0.64310	$C_{32}H_{62}NO_8P$	[M+H]+
622.40807	622.40785	-0.35989	$C_{31}H_{60}NO_9P$	[M+H]+
627.53457	627.53469	0.18644	$C_{41}H_{70}O_4$	[M+H]+
628.39523	628.39488	-0.56493	$C_{31}H_{60}NO_8P$	[M+Na]+
629.55074	629.55034	-0.64014	$C_{41}H_{72}O_4$	[M+H]+
631.56627	631.56599	-0.44809	$C_{41}H_{74}O_4$	[M+H]+
632.42878	632.42858	-0.31466	$C_{33}H_{62}NO_8P$	[M+H]+
634.44423	634.44423	0.00158	$C_{33}H_{64}NO_8P$	[M+H]+
636.42372	636.42350	-0.35197	$C_{32}H_{62}NO_9P$	[M+H]+
638.45197	638.45200	0.04072	$C_{34}H_{66}NO_6P$	[M+Na]+
639.36319	639.36324	0.07977	$C_{32}H_{57}O_9P$	[M+Na]+
640.46815	640.46765	-0.78692	$C_{34}H_{68}NO_6P$	[M+Na]+
641.41555	641.41528	-0.42718	$C_{33}H_{63}O_8P$	[M+Na]+
646.44449	646.44423	-0.40065	$C_{34}H_{64}NO_8P$	[M+H]+
647.37865	647.37897	0.50048	$C_{36}H_{54}O_{10}$	[M+H]+

648.42414	648.42350	-0.99318	$C_{33}H_{62}NO_9P$	[M+H]+
648.46009	648.45988	-0.32230	$C_{34}H_{66}NO_8P$	[M+H]+
648.62904	648.62892	-0.18192	$C_{42}H_{81}NO_3$	[M+H]+
650.43935	650.43915	-0.31363	$C_{33}H_{64}NO_9P$	[M+H]+
653.55044	653.55034	-0.15760	$C_{43}H_{72}O_4$	[M+H]+
655.43110	655.43093	-0.26547	$C_{34}H_{65}O_8P$	[M+Na]+
659.59747	659.59729	-0.27744	$C_{43}H_{78}O_4$	[M+H]+
664.45524	664.45480	-0.66822	$C_{34}H_{66}NO_9P$	[M+H]+
664.49172	664.49118	-0.81115	$C_{35}H_{70}NO_8P$	[M+H]+
666.43441	666.43406	-0.52518	$C_{33}H_{64}NO_{10}P$	[M+H]+
666.48328	666.48330	0.02401	$C_{36}H_{70}NO_6P$	[M+Na]+
667.43078	667.43093	0.21875	$C_{35}H_{65}O_8P$	[M+Na]+
668.49926	668.49895	-0.46971	$C_{36}H_{72}NO_6P$	[M+Na]+
669.44684	669.44658	-0.39436	$C_{35}H_{67}O_8P$	[M+Na]+
670.61100	670.61087	-0.19982	$C_{42}H_{81}NO_3$	[M+Na]+
672.42104	672.42109	0.07436	$C_{33}H_{64}NO_9P$	[M+Na]+
675.54410	675.54355	-0.81268	$C_{37}H_{75}N_2O_6P$	[M+H]+
676.45486	676.45480	-0.09461	$C_{35}H_{66}NO_9P$	[M+H]+
676.49117	676.49118	0.01626	$C_{36}H_{70}NO_8P$	[M+H]+
678.50696	678.50683	-0.19012	$C_{36}H_{72}NO_8P$	[M+H]+
681.44643	681.44658	0.21425	$C_{36}H_{67}O_8P$	[M+Na]+
683.46238	683.46223	-0.22386	$C_{36}H_{69}O_8P$	[M+Na]+
685.46805	685.46813	0.12109	$C_{35}H_{71}N_2O_6P$	[M+K]+
688.41594	688.41601	0.09442	$C_{33}H_{64}NO_{10}P$	[M+Na]+
690.50691	690.50683	-0.11441	$C_{37}H_{72}NO_8P$	[M+H]+
692.52258	692.52248	-0.14296	$C_{37}H_{74}NO_8P$	[M+H]+
693.44664	693.44658	-0.09229	$C_{37}H_{67}O_8P$	[M+Na]+
695.46226	695.46223	-0.04745	$C_{37}H_{69}O_8P$	[M+Na]+
698.43855	698.43915	0.85333	$C_{37}H_{64}NO_9P$	[M+H]+
699.54138	699.54115	-0.33450	$C_{37}H_{77}N_2O_6P$	[M+Na]+
700.48869	700.48878	0.12277	$C_{36}H_{72}NO_8P$	[M+Na]+
703.57481	703.57485	0.05827	$C_{39}H_{79}N_2O_6P$	[M+H]+
704.52254	704.52248	-0.08374	$C_{38}H_{74}NO_8P$	[M+H]+
705.59098	705.59050	-0.67886	$C_{39}H_{81}N_2O_6P$	[M+H]+
706.53831	706.53813	-0.25335	$C_{38}H_{76}NO_8P$	[M+H]+
709.47768	709.47788	0.27767	$C_{38}H_{71}O_8P$	[M+Na]+
711.43721	711.43676	-0.62690	$C_{22}H_{29}NO_3$	[2M+H]+
714.50443	714.50443	-0.00560	$C_{37}H_{74}NO_8P$	[M+Na]+
716.46290	716.46271	-0.26100	$C_{36}H_{72}NO_8P$	[M+K]+
718.53820	718.53813	-0.09603	$C_{39}H_{76}NO_8P$	[M+H]+
719.54146	719.54162	0.22653	$C_{19}H_{37}NO_5$	[2M+H]+
720.55405	720.55378	-0.37194	$C_{39}H_{78}NO_8P$	[M+H]+
721.47778	721.47788	0.13445	$C_{39}H_{71}O_8P$	[M+Na]+
721.53770	721.53780	0.13444	$C_{39}H_{77}O_9P$	[M+H]+
723.49365	723.49353	-0.17001	$C_{39}H_{73}O_8P$	[M+Na]+
725.45352	725.45418	0.91391	$C_{45}H_{66}O_5$	[M+K]+
725.55654	725.55680	0.35283	$C_{39}H_{79}N_2O_6P$	[M+Na]+
726.50399	726.50443	0.60013	$C_{38}H_{74}NO_8P$	[M+Na]+
727.52744	727.52723	-0.28590	$C_{41}H_{75}O_8P$	[M+H]+
728.52003	728.52008	0.06314	$C_{38}H_{76}NO_8P$	[M+Na]+
732.55382	732.55378	-0.05187	$C_{40}H_{78}NO_8P$	[M+H]+
735.55348	735.55345	-0.04486	$C_{40}H_{79}O_9P$	[M+H]+

737.50912	737.50918	0.07729	$C_{40}H_{75}O_8P$	[M+Na]+
740.49951	740.49910	-0.55503	$C_{39}H_{76}NO_7P$	[M+K]+
740.52003	740.52008	0.06212	$C_{39}H_{76}NO_8P$	[M+Na]+
742.51527	742.51475	-0.70167	$C_{39}H_{78}NO_7P$	[M+K]+
742.53573	742.53573	-0.00539	$C_{39}H_{78}NO_8P$	[M+Na]+
743.55902	743.55850	-0.70472	$C_{47}H_{76}O_5$	[M+Na]+
744.49433	744.49401	-0.42579	$C_{38}H_{76}NO_8P$	[M+K]+
746.56950	746.56943	-0.09108	$C_{41}H_{80}NO_8P$	[M+H]+
747.49367	747.49353	-0.19131	$C_{41}H_{73}O_8P$	[M+Na]+
747.57276	747.57292	0.21804	$C_{20}H_{39}NO_5$	[2M+H]+
749.50910	749.50918	0.10273	$C_{41}H_{75}O_8P$	[M+Na]+
753.48599	753.48548	-0.67287	$C_{47}H_{70}O_5$	[M+K]+
754.51439	754.51475	0.47580	$C_{40}H_{78}NO_7P$	[M+K]+
754.53583	754.53573	-0.13783	$C_{40}H_{78}NO_8P$	[M+Na]+
756.49420	756.49401	-0.24719	$C_{39}H_{76}NO_8P$	[M+K]+
758.51029	758.50966	-0.82662	$C_{39}H_{78}NO_8P$	[M+K]+
758.56964	758.56943	-0.27420	$C_{42}H_{80}NO_8P$	[M+H]+
759.55123	759.55104	-0.24751	$C_{40}H_{81}O_9P$	[M+Na]+
760.58509	760.58508	-0.01052	$C_{42}H_{82}NO_8P$	[M+H]+
766.48705	766.48649	-0.73061	$C_{38}H_{72}NO_{12}P$	[M+H]+
766.53515	766.53573	0.75143	$C_{41}H_{78}NO_8P$	[M+Na]+
767.53819	767.53752	-0.87422	$C_{49}H_{76}O_4$	[M+K]+
768.55132	768.55138	0.07286	$C_{41}H_{80}NO_8P$	[M+Na]+
770.50951	770.50951	0.00130	$C_{43}H_{74}NO_7P$	[M+Na]+
772.58550	772.58508	-0.54104	$C_{43}H_{82}NO_8P$	[M+H]+
774.60053	774.60073	0.26078	$C_{43}H_{84}NO_8P$	[M+H]+
777.54077	777.54048	-0.37683	$C_{43}H_{79}O_8P$	[M+Na]+
777.59534	777.59464	-0.90021	$C_{52}H_{82}O_2$	[M+K]+
778.53603	778.53573	-0.39048	$C_{42}H_{78}NO_8P$	[M+Na]+
780.55114	780.55138	0.30235	$C_{42}H_{80}NO_8P$	[M+Na]+
782.56715	782.56703	-0.15845	$C_{42}H_{82}NO_8P$	[M+Na]+
784.52533	784.52531	-0.02167	$C_{41}H_{80}NO_8P$	[M+K]+
784.56924	784.56994	0.89348	$C_{42}H_{83}NO_9$	[M+K]+
785.56868	785.56910	0.53083	$C_{44}H_{81}O_9P$	[M+H]+
786.57719	786.57735	0.20214	$C_{42}H_{86}NO_7P$	[M+K]+
786.60061	786.60073	0.15510	$C_{44}H_{84}NO_8P$	[M+H]+
794.56663	794.56703	0.49838	$C_{43}H_{82}NO_8P$	[M+Na]+
796.52578	796.52531	-0.58630	$C_{42}H_{80}NO_8P$	[M+K]+
796.58284	796.58268	-0.20588	$C_{43}H_{84}NO_8P$	[M+Na]+
798.54126	798.54096	-0.37193	$C_{42}H_{82}NO_8P$	[M+K]+
800.61617	800.61638	0.26480	$C_{45}H_{86}NO_8P$	[M+H]+
801.54082	801.54048	-0.42793	$C_{45}H_{79}O_8P$	[M+Na]+
802.63279	802.63203	-0.94439	$C_{45}H_{88}NO_8P$	[M+H]+
802.63279	802.63203	-0.94439	$C_{45}H_{88}NO_8P$	[M+H]+
804.55136	804.55138	0.01989	$C_{44}H_{80}NO_8P$	[M+Na]+
807.63569	807.63505	-0.79739	$C_{45}H_{89}N_2O_6P$	[M+Na]+
808.58290	808.58268	-0.27703	$C_{44}H_{84}NO_8P$	[M+Na]+
810.60017	810.60073	0.69331	$C_{46}H_{84}NO_8P$	[M+H]+
813.56168	813.56161	-0.09096	$C_{43}H_{83}O_{10}P$	[M+Na]+
813.68453	813.68440	-0.15731	$C_{47}H_{93}N_2O_6P$	[M+H]+
814.63225	814.63203	-0.26761	$C_{46}H_{88}NO_8P$	[M+H]+
815.70058	815.70005	-0.64730	$C_{47}H_{95}N_2O_6P$	[M+H]+

824.55699	824.55661	-0.45722	$C_{44}H_{84}NO_8P$	[M+K]+
824.61472	824.61398	-0.90224	$C_{45}H_{88}NO_8P$	[M+Na]+
827.57718	827.57726	0.09183	$C_{44}H_{85}O_{10}P$	[M+Na]+
827.70063	827.70005	-0.69832	$C_{48}H_{95}N_2O_6P$	[M+H]+
828.55137	828.55138	0.00724	$C_{46}H_{80}NO_8P$	[M+Na]+
828.64794	828.64768	-0.31135	$C_{47}H_{90}NO_8P$	[M+H]+
830.56755	830.56703	-0.63089	$C_{46}H_{82}NO_8P$	[M+Na]+
832.58451	832.58508	0.68702	$C_{48}H_{82}NO_8P$	[M+H]+
834.60117	834.60073	-0.52480	$C_{48}H_{84}NO_8P$	[M+H]+
835.64183	835.64223	0.47389	$C_{51}H_{88}O_7$	[M+Na]+
835.66681	835.66635	-0.55525	$C_{47}H_{93}N_2O_6P$	[M+Na]+
837.68283	837.68200	-0.99560	$C_{47}H_{95}N_2O_6P$	[M+Na]+
838.63271	838.63203	-0.80846	$C_{48}H_{88}NO_8P$	[M+H]+
839.68869	839.68882	0.15244	$C_{50}H_{95}O_7P$	[M+H]+
841.71562	841.71570	0.09742	$C_{49}H_{97}N_2O_6P$	[M+H]+
842.66363	842.66333	-0.35364	$C_{48}H_{92}NO_8P$	[M+H]+
851.64026	851.64028	0.02701	$C_{47}H_{93}N_2O_6P$	[M+K]+
852.58849	852.58791	-0.67559	$C_{46}H_{88}NO_8P$	[M+K]+
852.64476	852.64528	0.60518	$C_{47}H_{92}NO_8P$	[M+Na]+
854.66075	854.66093	0.20593	$C_{47}H_{94}NO_8P$	[M+Na]+
858.59895	858.59833	-0.72677	$C_{48}H_{86}NO_8P$	[M+Na]+
859.60325	859.60347	0.25710	$C_{45}H_{89}O_{11}P$	[M+Na]+
862.63262	862.63203	-0.68163	$C_{50}H_{88}NO_8P$	[M+H]+
863.63652	863.63718	0.76074	$C_{47}H_{91}O_{11}P$	[M+H]+
864.64706	864.64768	0.71937	$C_{50}H_{90}NO_8P$	[M+H]+

DHB mass list positive mode

Observed *m/z*	Expected *m/z*	Error (ppm)	Tentative neutral formula	Adduct
155.03387	155.03389	0.09675	$C_7H_6O_4$	[M+H]+
198.08894	198.08909	0.74209	$C_8H_{17}NO_2$	[M+K]+
203.22295	203.22302	0.35921	$C_{10}H_{26}N_4$	[M+H]+
204.12294	204.12303	0.46051	$C_9H_{17}NO_4$	[M+H]+
211.06007	211.06010	0.14214	$C_{10}H_{10}O_5$	[M+H]+
217.04950	217.04954	0.16125	$C_{12}H_8O_4$	[M+H]+
218.13869	218.13869	-0.02292	$C_{10}H_{19}NO_4$	[M+H]+
222.08889	222.08909	0.88703	$C_{10}H_{17}NO_2$	[M+K]+
224.10459	224.10459	-0.02231	$C_{13}H_{15}NO$	[M+Na]+
226.08389	226.08385	-0.18135	$C_{12}H_{13}NO_2$	[M+Na]+
229.04948	229.04954	0.24012	$C_{13}H_8O_4$	[M+H]+
229.07063	229.07067	0.15279	$C_{10}H_{12}O_6$	[M+H]+
230.24781	230.24784	0.13464	$C_{14}H_{31}NO$	[M+H]+
232.15433	232.15434	0.02154	$C_{11}H_{21}NO_4$	[M+H]+
240.09950	240.09950	-0.00416	$C_{13}H_{15}NO_2$	[M+Na]+
245.04441	245.04445	0.16324	$C_{13}H_8O_5$	[M+H]+
251.05265	251.05261	-0.16331	$C_{10}H_{12}O_6$	[M+Na]+
256.09440	256.09457	0.64820	$C_{10}H_{19}NO_4$	[M+K]+
256.26349	256.26349	0.00390	$C_{16}H_{33}NO$	[M+H]+
258.11009	258.11010	0.03874	$C_8H_{20}NO_6P$	[M+H]+
258.27912	258.27914	0.08131	$C_{16}H_{35}NO$	[M+H]+
263.14619	263.14623	0.15201	$C_4H_9N_3O_2$	[2M+H]+
264.09953	264.09950	-0.11738	$C_{15}H_{15}NO_2$	[M+Na]+
265.25254	265.25259	0.19604	$C_{18}H_{32}O$	[M+H]+
270.31553	270.31553	-0.01110	$C_{18}H_{39}N$	[M+H]+
273.00465	273.00481	0.59706	$C_9H_{14}O_2S_3$	[M+Na]+
280.09203	280.09205	0.05355	$C_8H_{20}NO_6P$	[M+Na]+
280.26118	280.26109	-0.33897	$C_{16}H_{35}NO$	[M+Na]+
282.11010	282.11022	0.41119	$C_{12}H_{21}NO_4$	[M+K]+
282.27910	282.27914	0.14525	$C_{18}H_{35}NO$	[M+H]+
283.01894	283.01894	-0.00353	$C_6H_{13}O_9P$	[M+Na]+
284.29478	284.29479	0.03869	$C_{18}H_{37}NO$	[M+H]+
285.03927	285.03936	0.32978	$C_{15}H_8O_6$	[M+H]+
285.24247	285.24242	-0.17178	$C_{17}H_{32}O_3$	[M+H]+
286.31043	286.31044	0.03842	$C_{18}H_{39}NO$	[M+H]+
294.11011	294.11006	-0.15640	$C_{16}H_{17}NO_3$	[M+Na]+
296.06593	296.06598	0.17564	$C_8H_{20}NO_6P$	[M+K]+
296.12591	296.12587	-0.14859	$C_{13}H_{23}NO_4$	[M+K]+
296.23496	296.23502	0.21267	$C_{16}H_{35}NO$	[M+K]+
298.09678	298.09684	0.19121	$C_{11}H_{15}N_5O_3S$	[M+H]+
298.10512	298.10498	-0.47299	$C_{15}H_{17}NO_4$	[M+Na]+
299.25802	299.25807	0.17042	$C_{18}H_{34}O_3$	[M+H]+
302.07879	302.07876	-0.08607	$C_{17}H_{13}NO_3$	[M+Na]+
308.06577	308.06552	-0.81476	$C_{16}H_{13}O_5$	[M+Na]+
310.31027	310.31044	0.55106	$C_{20}H_{39}NO$	[M+H]+
311.25812	311.25807	-0.15743	$C_{19}H_{34}O_3$	[M+H]+
312.12068	312.12063	-0.16340	$C_{16}H_{19}NO_4$	[M+Na]+
319.00628	319.00621	-0.23511	$C_9H_{12}O_{10}$	[M+K]+
320.08932	320.08933	0.02812	$C_{17}H_{15}NO_4$	[M+Na]+
322.14132	322.14136	0.13659	$C_{18}H_{21}NO_3$	[M+Na]+
330.07296	330.07303	0.20299	$C_{10}H_{17}N_3O_6S$	[M+Na]+
336.15701	336.15701	0.01190	$C_{19}H_{23}NO_3$	[M+Na]+
341.30502	341.30502	0.00586	$C_{21}H_{40}O_3$	[M+H]+
348.07037	348.07036	-0.02586	$C_{10}H_{14}N_5O_7P$	[M+H]+
349.19103	349.19105	0.06873	$C_{22}H_{24}N_2O_2$	[M+H]+
350.17267	350.17266	-0.01713	$C_{20}H_{25}NO_3$	[M+Na]+
353.26863	353.26864	0.01698	$C_{21}H_{36}O_4$	[M+H]+

354.13117	354.13119	0.06495	$C_{18}H_{21}NO_5$	[M+Na]+
355.28459	355.28429	-0.85565	$C_{21}H_{38}O_4$	[M+H]+
360.06928	360.06899	-0.81373	$C_{15}H_{15}NO_8$	[M+Na]+
364.18833	364.18831	-0.04393	$C_{21}H_{27}NO_3$	[M+Na]+
365.10540	365.10543	0.08765	$C_{12}H_{22}O_{11}$	[M+Na]+
365.11044	365.11079	0.96409	$C_{18}H_{18}N_2O_5$	[M+Na]+
366.20394	366.20396	0.06554	$C_{21}H_{29}NO_3$	[M+Na]+
376.32096	376.32101	0.12224	$C_{24}H_{41}NO_2$	[M+H]+
376.35734	376.35739	0.13817	$C_{25}H_{45}NO$	[M+H]+
378.20416	378.20396	-0.51824	$C_{22}H_{29}NO_3$	[M+Na]+
381.29993	381.29994	0.01574	$C_{23}H_{40}O_4$	[M+H]+
388.12132	388.12142	0.24992	$C_{14}H_{23}NO_{10}$	[M+Na]+
391.22434	391.22452	0.45498	$C_{21}H_{36}O_4$	[M+K]+
392.21985	392.21962	-0.59915	$C_{23}H_{31}NO_3$	[M+Na]+
393.30000	393.29994	-0.16273	$C_{24}H_{40}O_4$	[M+H]+
394.12599	394.12611	0.29940	$C_{20}H_{21}NO_6$	[M+Na]+
395.06071	395.06089	0.45056	$C_{17}H_{14}O_{11}$	[M+H]+
396.17802	396.17814	0.31299	$C_{21}H_{27}NO_5$	[M+Na]+
399.14473	399.14452	-0.53865	$C_{15}H_{22}N_6O_5S$	[M+H]+
400.10061	400.10044	-0.42739	$C_{15}H_{23}NO_9$	[M+K]+
404.35215	404.35231	0.38580	$C_{26}H_{45}NO_2$	[M+H]+
405.24010	405.24002	-0.20728	$C_{25}H_{34}O_3$	[M+Na]+
408.32372	408.32384	0.28899	$C_{23}H_{47}NO_2$	[M+K]+
413.26611	413.26623	0.29037	$C_{24}H_{38}O_4$	[M+Na]+
415.22198	415.22200	0.03853	$C_{19}H_{37}O_6P$	[M+Na]+
416.35204	416.35231	0.63888	$C_{27}H_{45}NO_2$	[M+H]+
417.23994	417.24005	0.26843	$C_{21}H_{37}O_6P$	[M+H]+
419.25565	419.25582	0.40071	$C_{23}H_{40}O_4$	[M+K]+
421.33102	421.33124	0.51266	$C_{13}H_{22}O_2$	[2M+H]+
422.23022	422.23033	0.26289	$C_{21}H_{37}NO_5$	[M+K]+
422.33927	422.33949	0.51617	$C_{24}H_{49}NO_2$	[M+K]+
428.03672	428.03669	-0.06775	$C_{10}H_{15}N_5O_{10}P_2$	[M+H]+
431.21688	431.21691	0.07189	$C_{19}H_{37}O_7P$	[M+Na]+
433.27137	433.27132	-0.12463	$C_{27}H_{38}O_3$	[M+Na]+
436.28224	436.28237	0.29110	$C_{23}H_{43}NO_4$	[M+K]+
436.35499	436.35514	0.33917	$C_{25}H_{51}NO_2$	[M+K]+
439.22206	439.22200	-0.14571	$C_{21}H_{37}O_6P$	[M+Na]+
439.34190	439.34180	-0.22534	$C_{26}H_{46}O_5$	[M+H]+
439.37793	439.37819	0.58492	$C_{27}H_{50}O_4$	[M+H]+
441.23764	441.23765	0.01360	$C_{21}H_{39}O_6P$	[M+Na]+
441.29789	441.29753	-0.81351	$C_{26}H_{42}O_4$	[M+Na]+
443.25302	443.25330	0.62267	$C_{21}H_{41}O_6P$	[M+Na]+
445.23265	445.23256	-0.19990	$C_{20}H_{39}O_7P$	[M+Na]+
445.27133	445.27147	0.30992	$C_{25}H_{42}O_4$	[M+K]+
448.28223	448.28237	0.30561	$C_{24}H_{43}NO_4$	[M+K]+
448.35513	448.35514	0.01784	$C_{26}H_{51}NO_2$	[M+K]+
450.29784	450.29802	0.39307	$C_{24}H_{45}NO_4$	[M+K]+
457.23260	457.23256	-0.08530	$C_{21}H_{39}O_7P$	[M+Na]+
457.27150	457.27147	-0.06998	$C_{26}H_{42}O_4$	[M+K]+
459.24821	459.24821	0.00218	$C_{21}H_{41}O_7P$	[M+Na]+
461.26371	461.26386	0.32736	$C_{21}H_{43}O_7P$	[M+Na]+
462.29805	462.29802	-0.07138	$C_{25}H_{45}NO_4$	[M+K]+
462.37069	462.37079	0.21195	$C_{27}H_{53}NO_2$	[M+K]+
464.31353	464.31367	0.29506	$C_{25}H_{47}NO_4$	[M+K]+
465.35770	465.35745	-0.53507	$C_{28}H_{48}O_5$	[M+H]+
465.39396	465.39384	-0.26429	$C_{29}H_{52}O_4$	[M+H]+
466.29300	466.29282	-0.39460	$C_{22}H_{44}NO_7P$	[M+H]+
467.40978	467.40949	-0.62686	$C_{29}H_{54}O_4$	[M+H]+
468.30841	468.30847	0.11958	$C_{22}H_{46}NO_7P$	[M+H]+

469.09753	469.09767	0.29205	$C_{20}H_{20}O_{13}$	[M+H]+
477.39383	477.39384	0.01466	$C_{15}H_{26}O_2$	[2M+H]+
480.30845	480.30847	0.03331	$C_{23}H_{46}NO_7P$	[M+H]+
482.32405	482.32412	0.13684	$C_{23}H_{48}NO_7P$	[M+H]+
485.26385	485.26386	0.02267	$C_{23}H_{43}O_7P$	[M+Na]+
487.27968	487.27951	-0.34682	$C_{23}H_{45}O_7P$	[M+Na]+
490.29032	490.29041	0.18356	$C_{22}H_{46}NO_7P$	[M+Na]+
490.32917	490.32932	0.29980	$C_{27}H_{49}NO_4$	[M+K]+
490.40163	490.40209	0.93393	$C_{29}H_{57}NO_2$	[M+K]+
491.33254	491.33269	0.31140	$C_{12}H_{23}NO_4$	[2M+H]+
492.34480	492.34497	0.33919	$C_{27}H_{51}NO_4$	[M+K]+
493.42531	493.42514	-0.35061	$C_{31}H_{56}O_4$	[M+H]+
494.32404	494.32412	0.15375	$C_{24}H_{48}NO_7P$	[M+H]+
494.49290	494.49316	0.51972	$C_{32}H_{63}NO_2$	[M+H]+
495.40450	495.40440	-0.19984	$C_{30}H_{54}O_5$	[M+H]+
496.33971	496.33977	0.11283	$C_{24}H_{50}NO_7P$	[M+H]+
501.31437	501.31436	-0.02593	$C_{21}H_{40}N_8O_6$	[M+H]+
504.30618	504.30606	-0.23795	$C_{23}H_{48}NO_7P$	[M+Na]+
504.34484	504.34485	0.02181	$C_{26}H_{50}NO_6P$	[M+H]+
506.26418	506.26435	0.33184	$C_{22}H_{46}NO_7P$	[M+K]+
506.36035	506.36050	0.29821	$C_{26}H_{52}NO_6P$	[M+H]+
507.44103	507.44079	-0.47887	$C_{32}H_{58}O_4$	[M+H]+
508.00268	508.00302	0.67322	$C_{10}H_{16}N_5O_{13}P_3$	[M+H]+
508.33981	508.33977	-0.08656	$C_{25}H_{50}NO_7P$	[M+H]+
509.12901	509.12897	-0.08446	$C_{23}H_{24}O_{13}$	[M+H]+
509.45637	509.45644	0.13151	$C_{32}H_{60}O_4$	[M+H]+
510.35539	510.35542	0.05094	$C_{25}H_{52}NO_7P$	[M+H]+
511.09621	511.09655	0.66915	$C_{14}H_{26}N_4O_{11}P_2$	[M+Na]+
513.29503	513.29516	0.25521	$C_{25}H_{47}O_7P$	[M+Na]+
516.28393	516.28369	-0.45711	$C_{22}H_{45}NO_{10}S$	[M+H]+
516.30594	516.30606	0.23242	$C_{24}H_{48}NO_7P$	[M+Na]+
517.38614	517.38635	0.39816	$C_{30}H_{54}O_5$	[M+Na]+
517.42287	517.42273	-0.26864	$C_{31}H_{58}O_4$	[M+Na]+
518.32168	518.32171	0.05788	$C_{24}H_{50}NO_7P$	[M+Na]+
518.36024	518.36050	0.50351	$C_{27}H_{52}NO_6P$	[M+H]+
519.36405	519.36399	-0.10975	$C_{13}H_{25}NO_4$	[2M+H]+
520.27952	520.28000	0.91874	$C_{23}H_{48}NO_7P$	[M+K]+
520.33966	520.33977	0.20371	$C_{26}H_{50}NO_7P$	[M+H]+
521.45637	521.45644	0.12849	$C_{33}H_{60}O_4$	[M+H]+
522.35531	522.35542	0.20293	$C_{26}H_{52}NO_7P$	[M+H]+
522.52446	522.52446	-0.00574	$C_{34}H_{67}NO_2$	[M+H]+
523.32239	523.32252	0.25223	$C_{12}H_{23}NO_5$	[2M+H]+
523.47202	523.47209	0.12799	$C_{33}H_{62}O_4$	[M+H]+
524.37097	524.37107	0.18308	$C_{26}H_{54}NO_7P$	[M+H]+
525.47821	525.47784	-0.70222	$C_{35}H_{60}N_2O$	[M+H]+
531.43835	531.43838	0.05833	$C_{32}H_{60}O_4$	[M+Na]+
532.33698	532.33736	0.71383	$C_{25}H_{52}NO_7P$	[M+Na]+
532.37615	532.37615	0.00376	$C_{28}H_{54}NO_6P$	[M+H]+
534.29535	534.29565	0.55774	$C_{24}H_{50}NO_7P$	[M+K]+
536.37108	536.37107	-0.02610	$C_{27}H_{54}NO_7P$	[M+H]+
537.48768	537.48774	0.10605	$C_{34}H_{64}O_4$	[M+H]+
538.35030	538.35033	0.05758	$C_{26}H_{52}NO_8P$	[M+H]+
538.38658	538.38672	0.25261	$C_{27}H_{56}NO_7P$	[M+H]+
538.38658	538.38672	0.25261	$C_{27}H_{56}NO_7P$	[M+H]+
543.43847	543.43838	-0.16377	$C_{33}H_{60}O_4$	[M+Na]+
544.33739	544.33736	-0.05511	$C_{26}H_{52}NO_7P$	[M+Na]+
544.50681	544.50640	-0.75114	$C_{34}H_{67}NO_2$	[M+Na]+
545.45407	545.45403	-0.07150	$C_{33}H_{62}O_4$	[M+Na]+
546.35299	546.35301	0.03661	$C_{26}H_{54}NO_7P$	[M+Na]+

547.47206	547.47209	0.04932	$C_{35}H_{62}O_4$	[M+H]+
549.48763	549.48774	0.19473	$C_{35}H_{64}O_4$	[M+H]+
550.35027	550.35029	0.04361	$C_{32}H_{49}NO_5$	[M+Na]+
550.38662	550.38672	0.17442	$C_{28}H_{56}NO_7P$	[M+H]+
551.35371	551.35382	0.20314	$C_{13}H_{25}NO_5$	[2M+H]+
551.50330	551.50339	0.15775	$C_{35}H_{66}O_4$	[M+H]+
552.32943	552.32960	0.29873	$C_{26}H_{50}NO_9P$	[M+H]+
552.36623	552.36598	-0.45079	$C_{27}H_{54}NO_8P$	[M+H]+
559.46966	559.46968	0.03754	$C_{34}H_{64}O_4$	[M+Na]+
560.31122	560.31130	0.13921	$C_{26}H_{52}NO_7P$	[M+K]+
560.33218	560.33228	0.16954	$C_{26}H_{52}NO_8P$	[M+Na]+
560.40745	560.40745	0.00357	$C_{30}H_{58}NO_6P$	[M+H]+
561.48730	561.48774	0.77829	$C_{18}H_{32}O_2$	[2M+H]+
563.50330	563.50339	0.15439	$C_{36}H_{66}O_4$	[M+H]+
564.40215	564.40237	0.38271	$C_{29}H_{58}NO_7P$	[M+H]+
565.51897	565.51904	0.11848	$C_{36}H_{68}O_4$	[M+H]+
566.38189	566.38163	-0.45729	$C_{28}H_{56}NO_8P$	[M+H]+
571.46956	571.46968	0.21173	$C_{35}H_{64}O_4$	[M+Na]+
572.36839	572.36866	0.47172	$C_{28}H_{56}NO_7P$	[M+Na]+
575.50330	575.50339	0.15117	$C_{37}H_{66}O_4$	[M+H]+
577.51895	577.51904	0.15064	$C_{37}H_{68}O_4$	[M+H]+
578.38165	578.38163	-0.03285	$C_{29}H_{56}NO_8P$	[M+H]+
578.41764	578.41802	0.65005	$C_{30}H_{60}NO_7P$	[M+H]+
579.38531	579.38512	-0.32448	$C_{14}H_{27}NO_5$	[2M+H]+
580.36098	580.36090	-0.14646	$C_{28}H_{54}NO_9P$	[M+H]+
582.27281	582.27295	0.23357	$C_{21}H_{39}N_7O_{12}$	[M+H]+
585.35326	585.35268	-0.99769	$C_{29}H_{55}O_8P$	[M+Na]+
585.48562	585.48533	-0.49361	$C_{36}H_{66}O_4$	[M+Na]+
589.51896	589.51904	0.13061	$C_{19}H_{34}O_2$	[2M+H]+
591.53461	591.53469	0.13017	$C_{38}H_{70}O_4$	[M+H]+
592.39719	592.39728	0.15361	$C_{30}H_{58}NO_8P$	[M+H]+
594.37635	594.37655	0.32807	$C_{29}H_{56}NO_9P$	[M+H]+
594.41308	594.41293	-0.25067	$C_{30}H_{60}NO_8P$	[M+H]+
597.35320	597.35268	-0.87720	$C_{30}H_{55}O_8P$	[M+Na]+
597.48526	597.48533	0.11883	$C_{37}H_{66}O_4$	[M+Na]+
598.38652	598.38672	0.32755	$C_{32}H_{56}NO_7P$	[M+H]+
599.50142	599.50098	-0.73228	$C_{37}H_{68}O_4$	[M+Na]+
600.36309	600.36358	0.80784	$C_{29}H_{56}NO_8P$	[M+Na]+
601.51882	601.51904	0.36075	$C_{39}H_{68}O_4$	[M+H]+
603.53453	603.53469	0.26013	$C_{39}H_{70}O_4$	[M+H]+
604.25508	604.25489	-0.31444	$C_{21}H_{39}N_7O_{12}$	[M+Na]+
605.55038	605.55034	-0.07101	$C_{39}H_{72}O_4$	[M+H]+
606.41285	606.41293	0.13357	$C_{31}H_{60}NO_8P$	[M+H]+
606.44921	606.44932	0.17479	$C_{32}H_{64}NO_7P$	[M+H]+
607.41610	607.41642	0.53176	$C_{15}H_{29}NO_5$	[2M+H]+
608.39184	608.39220	0.58515	$C_{30}H_{58}NO_9P$	[M+H]+
611.36793	611.36833	0.64773	$C_{31}H_{57}O_8P$	[M+Na]+
613.34748	613.34759	0.18097	$C_{30}H_{55}O_9P$	[M+Na]+
614.37897	614.37923	0.41505	$C_{30}H_{58}NO_8P$	[M+Na]+
616.35812	616.35849	0.60030	$C_{29}H_{56}NO_9P$	[M+Na]+
618.41298	618.41293	-0.07924	$C_{32}H_{60}NO_8P$	[M+H]+
619.56641	619.56599	-0.68274	$C_{40}H_{74}O_4$	[M+H]+
620.42850	620.42858	0.13055	$C_{32}H_{62}NO_8P$	[M+H]+
622.40773	622.40785	0.18637	$C_{31}H_{60}NO_9P$	[M+H]+
622.44413	622.44423	0.16226	$C_{32}H_{64}NO_8P$	[M+H]+
627.36270	627.36324	0.86234	$C_{31}H_{57}O_9P$	[M+Na]+
628.39466	628.39488	0.34214	$C_{31}H_{60}NO_8P$	[M+Na]+
631.56611	631.56599	-0.19475	$C_{41}H_{74}O_4$	[M+H]+
632.42837	632.42858	0.33363	$C_{33}H_{62}NO_8P$	[M+H]+

633.58207	633.58164	-0.68342	$C_{41}H_{76}O_4$	[M+H]+
634.40781	634.40785	0.05675	$C_{32}H_{60}NO_9P$	[M+H]+
634.44437	634.44423	-0.21909	$C_{33}H_{64}NO_8P$	[M+H]+
635.44789	635.44772	-0.26281	$C_{16}H_{31}NO_5$	[2M+H]+
636.42322	636.42350	0.43367	$C_{32}H_{62}NO_9P$	[M+H]+
636.45974	636.45988	0.22154	$C_{33}H_{66}NO_8P$	[M+H]+
638.40222	638.40276	0.84586	$C_{31}H_{60}NO_{10}P$	[M+H]+
639.36300	639.36324	0.37694	$C_{32}H_{57}O_9P$	[M+Na]+
640.46749	640.46765	0.24357	$C_{34}H_{68}NO_6P$	[M+Na]+
641.37936	641.37889	-0.73124	$C_{32}H_{59}O_9P$	[M+Na]+
641.41494	641.41528	0.52384	$C_{33}H_{63}O_8P$	[M+Na]+
644.38949	644.38979	0.46556	$C_{31}H_{60}NO_9P$	[M+Na]+
644.42622	644.42618	-0.06983	$C_{32}H_{64}NO_8P$	[M+Na]+
645.42854	645.42797	-0.88468	$C_{40}H_{62}O_4$	[M+K]+
646.44434	646.44423	-0.16861	$C_{34}H_{64}NO_8P$	[M+H]+
648.42323	648.42350	0.41023	$C_{33}H_{62}NO_9P$	[M+H]+
648.45962	648.45988	0.40249	$C_{34}H_{66}NO_8P$	[M+H]+
648.62920	648.62892	-0.42860	$C_{42}H_{81}NO_3$	[M+H]+
650.43884	650.43915	0.47045	$C_{33}H_{64}NO_9P$	[M+H]+
651.45784	651.45789	0.08136	$C_{18}H_{31}NO_4$	[2M+H]+
652.41821	652.41841	0.30655	$C_{32}H_{62}NO_{10}P$	[M+H]+
653.55032	653.55034	0.02601	$C_{43}H_{72}O_4$	[M+H]+
654.41012	654.41053	0.61888	$C_{33}H_{62}NO_8P$	[M+Na]+
655.43053	655.43093	0.60418	$C_{34}H_{65}O_8P$	[M+Na]+
657.38863	657.38921	0.88836	$C_{33}H_{63}O_8P$	[M+K]+
658.40491	658.40544	0.80498	$C_{32}H_{62}NO_9P$	[M+Na]+
658.44191	658.44183	-0.12909	$C_{33}H_{66}NO_8P$	[M+Na]+
659.59707	659.59729	0.32899	$C_{43}H_{78}O_4$	[M+H]+
660.36348	660.36373	0.37404	$C_{31}H_{60}NO_9P$	[M+K]+
662.43849	662.43915	0.99028	$C_{34}H_{64}NO_9P$	[M+H]+
662.47593	662.47553	-0.60229	$C_{35}H_{68}NO_8P$	[M+H]+
664.41815	664.41841	0.39132	$C_{33}H_{62}NO_{10}P$	[M+H]+
664.45437	664.45480	0.64113	$C_{34}H_{66}NO_9P$	[M+H]+
664.49082	664.49118	0.54327	$C_{35}H_{70}NO_8P$	[M+H]+
666.43376	666.43406	0.45016	$C_{33}H_{64}NO_{10}P$	[M+H]+
666.48269	666.48330	0.90925	$C_{36}H_{70}NO_6P$	[M+Na]+
666.63932	666.63949	0.25051	$C_{42}H_{83}NO_4$	[M+H]+
667.39438	667.39454	0.24124	$C_{34}H_{61}O_9P$	[M+Na]+
668.49865	668.49895	0.44278	$C_{36}H_{72}NO_6P$	[M+Na]+
669.44632	669.44658	0.38241	$C_{35}H_{67}O_8P$	[M+Na]+
670.40480	670.40544	0.95465	$C_{33}H_{62}NO_9P$	[M+Na]+
670.61047	670.61087	0.59051	$C_{42}H_{81}NO_3$	[M+Na]+
671.40482	671.40486	0.06553	$C_{34}H_{65}O_8P$	[M+K]+
672.42071	672.42109	0.56512	$C_{33}H_{64}NO_9P$	[M+Na]+
672.45714	672.45748	0.49817	$C_{34}H_{68}NO_8P$	[M+Na]+
674.43969	674.43915	-0.80660	$C_{35}H_{64}NO_9P$	[M+H]+
674.47487	674.47553	0.98002	$C_{36}H_{68}NO_8P$	[M+H]+
675.54313	675.54355	0.62320	$C_{37}H_{75}N_2O_6P$	[M+H]+
676.45436	676.45480	0.64454	$C_{35}H_{66}NO_9P$	[M+H]+
676.49183	676.49118	-0.95936	$C_{36}H_{70}NO_8P$	[M+H]+
677.55903	677.55920	0.25238	$C_{37}H_{77}N_2O_6P$	[M+H]+
678.47014	678.47045	0.45101	$C_{35}H_{68}NO_9P$	[M+H]+
678.50641	678.50683	0.62048	$C_{36}H_{72}NO_8P$	[M+H]+
680.44994	680.44971	-0.33801	$C_{34}H_{66}NO_{10}P$	[M+H]+
683.40473	683.40486	0.19608	$C_{35}H_{65}O_8P$	[M+K]+
683.46191	683.46223	0.46382	$C_{36}H_{69}O_8P$	[M+Na]+
685.42034	685.42051	0.25386	$C_{35}H_{67}O_8P$	[M+K]+
686.43616	686.43674	0.84494	$C_{34}H_{66}NO_9P$	[M+Na]+
686.47279	686.47313	0.48946	$C_{35}H_{70}NO_8P$	[M+Na]+

688.39463	688.39503	0.57670	$C_{33}H_{64}NO_9P$	[M+K]+
688.41573	688.41601	0.39947	$C_{33}H_{64}NO_{10}P$	[M+Na]+
688.49126	688.49118	-0.11474	$C_{37}H_{70}NO_8P$	[M+H]+
690.47015	690.47045	0.42869	$C_{36}H_{68}NO_9P$	[M+H]+
690.50625	690.50683	0.84141	$C_{37}H_{72}NO_8P$	[M+H]+
692.52206	692.52248	0.60792	$C_{37}H_{74}NO_8P$	[M+H]+
694.46499	694.46536	0.53278	$C_{35}H_{68}NO_{10}P$	[M+H]+
695.46161	695.46223	0.88718	$C_{37}H_{69}O_8P$	[M+Na]+
697.47803	697.47788	-0.21936	$C_{37}H_{71}O_8P$	[M+Na]+
697.52502	697.52550	0.68098	$C_{37}H_{75}N_2O_6P$	[M+Na]+
698.43645	698.43674	0.41521	$C_{35}H_{66}NO_9P$	[M+Na]+
699.43659	699.43616	-0.60906	$C_{36}H_{69}O_8P$	[M+K]+
699.54126	699.54115	-0.16296	$C_{37}H_{77}N_2O_6P$	[M+Na]+
700.45308	700.45239	-0.98508	$C_{35}H_{68}NO_9P$	[M+Na]+
700.48823	700.48878	0.77946	$C_{36}H_{72}NO_8P$	[M+Na]+
703.57444	703.57485	0.58416	$C_{39}H_{79}N_2O_6P$	[M+H]+
704.48624	704.48610	-0.20440	$C_{37}H_{70}NO_9P$	[M+H]+
704.52199	704.52248	0.69693	$C_{38}H_{74}NO_8P$	[M+H]+
705.59044	705.59050	0.08645	$C_{39}H_{81}N_2O_6P$	[M+H]+
706.53773	706.53813	0.56756	$C_{38}H_{76}NO_8P$	[M+H]+
709.47725	709.47788	0.88375	$C_{38}H_{71}O_8P$	[M+Na]+
711.43579	711.43616	0.52570	$C_{37}H_{69}O_8P$	[M+K]+
711.49379	711.49353	-0.36964	$C_{38}H_{73}O_8P$	[M+Na]+
712.43998	712.43954	-0.61760	$C_{34}H_{66}NO_{12}P$	[M+H]+
713.45214	713.45181	-0.45693	$C_{37}H_{71}O_8P$	[M+K]+
714.50390	714.50443	0.73618	$C_{37}H_{74}NO_8P$	[M+Na]+
716.46215	716.46256	0.57365	$C_{39}H_{68}NO_7P$	[M+Na]+
718.53761	718.53813	0.72508	$C_{39}H_{76}NO_8P$	[M+H]+
719.54112	719.54162	0.69906	$C_{19}H_{37}NO_5$	[2M+H]+
719.56023	719.56090	0.93390	$C_{47}H_{74}O_5$	[M+H]+
720.55344	720.55378	0.47464	$C_{39}H_{78}NO_8P$	[M+H]+
721.47727	721.47788	0.84133	$C_{39}H_{71}O_8P$	[M+Na]+
723.49323	723.49353	0.41051	$C_{39}H_{73}O_8P$	[M+Na]+
725.45244	725.45181	-0.86291	$C_{38}H_{71}O_8P$	[M+K]+
725.49600	725.49633	0.44935	$C_{37}H_{73}O_{11}P$	[M+H]+
725.55616	725.55680	0.87657	$C_{39}H_{79}N_2O_6P$	[M+Na]+
727.57233	727.57245	0.15943	$C_{39}H_{81}N_2O_6P$	[M+Na]+
728.51962	728.52008	0.62593	$C_{38}H_{76}NO_8P$	[M+Na]+
730.47847	730.47836	-0.14648	$C_{37}H_{74}NO_8P$	[M+K]+
731.52272	731.52215	-0.78330	$C_{40}H_{75}O_9P$	[M+H]+
732.55330	732.55378	0.65797	$C_{40}H_{78}NO_8P$	[M+H]+
734.56972	734.56943	-0.39207	$C_{40}H_{80}NO_8P$	[M+H]+
737.45166	737.45181	0.20883	$C_{39}H_{71}O_8P$	[M+K]+
737.50875	737.50918	0.57898	$C_{40}H_{75}O_8P$	[M+Na]+
738.45508	738.45519	0.14896	$C_{36}H_{68}NO_{12}P$	[M+H]+
739.46745	739.46746	0.01893	$C_{39}H_{73}O_8P$	[M+K]+
740.51959	740.52008	0.65630	$C_{39}H_{76}NO_8P$	[M+Na]+
742.47868	742.47836	-0.42695	$C_{38}H_{74}NO_8P$	[M+K]+
742.53535	742.53573	0.50637	$C_{39}H_{78}NO_8P$	[M+Na]+
744.49379	744.49386	0.09537	$C_{41}H_{72}NO_7P$	[M+Na]+
746.56902	746.56943	0.55186	$C_{41}H_{80}NO_8P$	[M+H]+
747.49355	747.49353	-0.03077	$C_{41}H_{73}O_8P$	[M+Na]+
747.57244	747.57292	0.64609	$C_{20}H_{39}NO_5$	[2M+H]+
749.50881	749.50918	0.48965	$C_{41}H_{75}O_8P$	[M+Na]+
753.48522	753.48548	0.34904	$C_{47}H_{70}O_5$	[M+K]+
754.53544	754.53573	0.37904	$C_{40}H_{78}NO_8P$	[M+Na]+
756.55193	756.55138	-0.73227	$C_{40}H_{80}NO_8P$	[M+Na]+
758.50981	758.50966	-0.19380	$C_{39}H_{78}NO_8P$	[M+K]+
758.56930	758.56943	0.17401	$C_{42}H_{80}NO_8P$	[M+H]+

760.58491	760.58508	0.22614	$C_{42}H_{82}NO_8P$	[M+H]+
765.48358	765.48311	-0.60877	$C_{41}H_{75}O_8P$	[M+K]+
766.48618	766.48649	0.40444	$C_{38}H_{72}NO_{12}P$	[M+H]+
766.53569	766.53573	0.04696	$C_{41}H_{78}NO_8P$	[M+Na]+
768.55118	768.55138	0.25503	$C_{41}H_{80}NO_8P$	[M+Na]+
770.50946	770.50951	0.06619	$C_{43}H_{74}NO_7P$	[M+Na]+
770.54647	770.54605	-0.54637	$C_{41}H_{82}NO_7P$	[M+K]+
772.58551	772.58508	-0.55398	$C_{43}H_{82}NO_8P$	[M+H]+
774.60049	774.60073	0.31242	$C_{43}H_{84}NO_8P$	[M+H]+
775.60395	775.60422	0.35198	$C_{21}H_{41}NO_5$	[2M+H]+
777.54028	777.54048	0.25336	$C_{43}H_{79}O_8P$	[M+Na]+
778.53627	778.53573	-0.69875	$C_{42}H_{78}NO_8P$	[M+Na]+
780.55148	780.55138	-0.13324	$C_{42}H_{80}NO_8P$	[M+Na]+
782.56715	782.56703	-0.15845	$C_{42}H_{82}NO_8P$	[M+Na]+
784.52557	784.52531	-0.32759	$C_{41}H_{80}NO_8P$	[M+K]+
785.56683	785.56669	-0.17567	$C_{42}H_{83}O_9P$	[M+Na]+
786.60055	786.60073	0.23138	$C_{44}H_{84}NO_8P$	[M+H]+
788.51963	788.52008	0.56562	$C_{43}H_{76}NO_8P$	[M+Na]+
794.56721	794.56703	-0.23157	$C_{43}H_{82}NO_8P$	[M+Na]+
796.52562	796.52531	-0.38542	$C_{42}H_{80}NO_8P$	[M+K]+
796.58273	796.58268	-0.06779	$C_{43}H_{84}NO_8P$	[M+Na]+
798.54125	798.54096	-0.35941	$C_{42}H_{82}NO_8P$	[M+K]+
800.54439	800.54361	-0.97309	$C_{43}H_{78}NO_{10}P$	[M+H]+
800.61597	800.61638	0.51460	$C_{45}H_{86}NO_8P$	[M+H]+
804.55154	804.55138	-0.20384	$C_{44}H_{80}NO_8P$	[M+Na]+
808.58346	808.58268	-0.96960	$C_{44}H_{84}NO_8P$	[M+Na]+
809.65141	809.65070	-0.88186	$C_{45}H_{91}N_2O_6P$	[M+Na]+
810.60050	810.60073	0.28621	$C_{46}H_{84}NO_8P$	[M+H]+
811.66849	811.66875	0.32279	$C_{47}H_{91}N_2O_6P$	[M+H]+
813.56149	813.56161	0.14258	$C_{43}H_{83}O_{10}P$	[M+Na]+
813.68483	813.68440	-0.52600	$C_{47}H_{93}N_2O_6P$	[M+H]+
814.63249	814.63203	-0.56222	$C_{46}H_{88}NO_8P$	[M+H]+
815.70049	815.70005	-0.53696	$C_{47}H_{95}N_2O_6P$	[M+H]+
822.60028	822.60073	0.54948	$C_{47}H_{84}NO_8P$	[M+H]+
824.55704	824.55661	-0.51785	$C_{44}H_{84}NO_8P$	[M+K]+
828.64806	828.64768	-0.45616	$C_{47}H_{90}NO_8P$	[M+H]+
830.56911	830.56943	0.38769	$C_{48}H_{80}NO_8P$	[M+H]+
835.66708	835.66635	-0.87834	$C_{47}H_{93}N_2O_6P$	[M+Na]+
836.61573	836.61638	0.77933	$C_{48}H_{86}NO_8P$	[M+H]+
838.63027	838.62963	-0.76792	$C_{46}H_{90}NO_8P$	[M+Na]+

DHB mass list negative mode

Observed *m/z*	Expected *m/z*	Error (ppm)	Tentative neutral formula	Adduct
153.01930	153.01933	0.20912	$C_7H_6O_4$	[M-H]-
187.04010	187.04007	-0.17109	$C_{11}H_8O_3$	[M-H]-
201.07692	201.07685	-0.36305	$C_9H_{14}O_5$	[M-H]-
214.97518	214.97521	0.15816	$C_9H_6O_4$	[M+K-2H]-
215.03498	215.03498	0.00930	$C_{12}H_8O_4$	[M-H]-
216.04289	216.04308	0.88871	$C_{13}H_9NO$	[M+Na-2H]-
217.05075	217.05063	-0.54365	$C_{12}H_{10}O_4$	[M-H]-
227.03513	227.03498	-0.65188	$C_{13}H_8O_4$	[M-H]-
232.97623	232.97615	-0.35626	$C_7H_6O_7S$	[M-H]-
241.01196	241.01188	-0.34438	$C_6H_{11}O_8P$	[M-H]-
243.03007	243.02990	-0.71185	$C_{13}H_8O_5$	[M-H]-
244.95345	244.95363	0.74708	$C_7H_{12}OS_3$	[M+K-2H]-
245.04560	245.04555	-0.21629	$C_{13}H_{10}O_5$	[M-H]-
259.02487	259.02481	-0.22392	$C_{13}H_8O_6$	[M-H]-
260.03280	260.03295	0.56531	$C_9H_{12}NO_6P$	[M-H]-
261.04066	261.04046	-0.75850	$C_{13}H_{10}O_6$	[M-H]-
273.04061	273.04046	-0.54204	$C_{14}H_{10}O_6$	[M-H]-
281.24862	281.24860	-0.05689	$C_{18}H_{34}O_2$	[M-H]-
288.02778	288.02798	0.68743	$C_{12}H_{13}NO_5$	[M+K-2H]-
289.03557	289.03538	-0.67120	$C_{14}H_{10}O_7$	[M-H]-
299.99526	299.99496	-0.99002	$C_9H_{13}NO_6S$	[M+K-2H]-
305.03050	305.03029	-0.68518	$C_{14}H_{10}O_8$	[M-H]-
321.04066	321.04046	-0.61674	$C_{18}H_{10}O_6$	[M-H]-
323.05634	323.05611	-0.70576	$C_{18}H_{12}O_6$	[M-H]-
327.01230	327.01224	-0.19877	$C_{14}H_{10}O_8$	[M+Na-2H]-
329.01547	329.01562	0.45591	$C_9H_{13}N_2O_8P$	[M+Na-2H]-
329.02790	329.02804	0.41638	$C_{11}H_{16}O_9$	[M+K-2H]-
334.04854	334.04871	0.51789	$C_{17}H_{15}NO_4$	[M+K-2H]-
335.05642	335.05611	-0.91925	$C_{19}H_{12}O_6$	[M-H]-
335.07728	335.07724	-0.11639	$C_{16}H_{16}O_8$	[M-H]-
348.05278	348.05248	-0.86768	$C_{11}H_{21}NO_7S$	[M+K-2H]-
350.04331	350.04363	0.90846	$C_{17}H_{15}NO_5$	[M+K-2H]-
351.05114	351.05103	-0.32474	$C_{19}H_{12}O_7$	[M-H]-
351.07245	351.07216	-0.83743	$C_{16}H_{16}O_9$	[M-H]-
353.06674	353.06668	-0.18127	$C_{19}H_{14}O_7$	[M-H]-
355.17354	355.17382	0.79116	$C_{16}H_{30}O_7$	[M+Na-2H]-
369.06173	369.06159	-0.37663	$C_{19}H_{14}O_8$	[M-H]-
379.04605	379.04594	-0.28756	$C_{10}H_6O_4$	[2M-H]-
381.06168	381.06159	-0.23356	$C_{20}H_{14}O_8$	[M-H]-
382.17352	382.17321	-0.81900	$C_{16}H_{25}N_5O_6$	[M-H]-
395.20498	395.20512	0.35678	$C_{19}H_{34}O_7$	[M+Na-2H]-
397.05674	397.05651	-0.58934	$C_{20}H_{14}O_9$	[M-H]-
397.18446	397.18411	-0.89127	$C_8H_{13}N_3O_3$	[2M-H]-
403.05241	403.05268	0.67733	$C_8H_{10}O_4S$	[2M-H]-
409.18414	409.18439	0.60120	$C_{19}H_{32}O_8$	[M+Na-2H]-
409.22064	409.22077	0.32012	$C_{20}H_{36}O_7$	[M+Na-2H]-
411.19980	411.20004	0.57393	$C_{19}H_{34}O_8$	[M+Na-2H]-
417.24108	417.24115	0.16537	$C_{21}H_{39}O_6P$	[M-H]-
419.25687	419.25692	0.10733	$C_{23}H_{42}O_4$	[M+K-2H]-
423.19981	423.20004	0.53403	$C_{20}H_{34}O_8$	[M+Na-2H]-
425.05132	425.05142	0.23527	$C_{21}H_{14}O_{10}$	[M-H]-
426.05474	426.05475	0.02112	$C_{15}H_{17}N_5O_6S_2$	[M-H]-
435.19998	435.20004	0.12868	$C_{21}H_{34}O_8$	[M+Na-2H]-
438.04375	438.04352	-0.53648	$C_{17}H_{17}N_3O_7S_2$	[M-H]-
439.02586	439.02593	0.15717	$C_{20}H_{18}O_7S$	[M+K-2H]-
447.03348	447.03352	0.08277	$C_{18}H_{18}O_{11}$	[M+K-2H]-
453.21029	453.21060	0.68622	$C_{21}H_{36}O_9$	[M+Na-2H]-

455.00648	455.00621	-0.59779	$C_{13}H_8S_2$	[2M-H]-
465.04429	465.04408	-0.44942	$C_{18}H_{20}O_{12}$	[M+K-2H]-
466.99754	466.99729	-0.52677	$C_{16}H_{12}N_4O_9S_2$	[M-H]-
481.20546	481.20524	-0.46758	$C_{10}H_{15}N_3O_4$	[2M-H]-
483.03373	483.03352	-0.44096	$C_{21}H_{18}O_{11}$	[M+K-2H]-
483.04226	483.04251	0.52169	$C_{10}H_{10}O_5S$	[2M-H]-
500.02260	500.02265	0.09600	$C_{14}H_{18}N_5O_{11}P$	[M+K-2H]-
505.01761	505.01787	0.50889	$C_{23}H_{16}O_{11}$	[M+K-2H]-
519.15246	519.15214	-0.62217	$C_{13}H_{12}N_2O_4$	[2M-H]-
523.26328	523.26295	-0.62875	$C_{11}H_{22}N_2O_3S$	[2M-H]-
523.29952	523.29981	0.54462	$C_{23}H_{40}N_8O_6$	[M-H]-
543.04501	543.04501	0.00737	$C_{21}H_{20}O_{15}S$	[M-H]-
551.01383	551.01371	-0.21052	$C_{22}H_{16}O_{15}S$	[M-H]-
551.25654	551.25692	0.68026	$C_{34}H_{42}O_4$	[M+K-2H]-
553.27866	553.27829	-0.67597	$C_{30}H_{44}O_8$	[M+Na-2H]-
561.03535	561.03554	0.33153	$C_9H_{15}NO_3S_3$	[2M-H]-
571.28916	571.28889	-0.47787	$C_{25}H_{49}O_{12}P$	[M-H]-
577.94956	577.94983	0.46717	$C_{10}H_{18}N_5O_{15}P_3$	[M+K-2H]-
582.31260	582.31311	0.88269	$C_{26}H_{49}NO_{13}$	[M-H]-
595.00151	595.00114	-0.62521	$C_{21}H_{18}O_{17}S$	[M+Na-2H]-
597.30396	597.30454	0.96601	$C_{27}H_{51}O_{12}P$	[M-H]-
599.32004	599.32019	0.24528	$C_{27}H_{53}O_{12}P$	[M-H]-
602.98949	602.98917	-0.53566	$C_4H_6N_4O_{12}$	[2M-H]-
640.96050	640.96114	0.99694	$C_{28}H_{12}O_{16}$	[M+K-2H]-
673.48127	673.48138	0.16185	$C_{37}H_{71}O_8P$	[M-H]-
699.49709	699.49703	-0.08721	$C_{39}H_{73}O_8P$	[M-H]-
790.80237	790.80217	-0.25291	$C_{52}H_{105}NO_3$	[M-H]-
809.51885	809.51855	-0.36688	$C_{41}H_{79}O_{13}P$	[M-H]-
833.51784	833.51855	0.85541	$C_{43}H_{79}O_{13}P$	[M-H]-
835.53341	835.53420	0.94909	$C_{43}H_{81}O_{13}P$	[M-H]-
863.56481	863.56550	0.80249	$C_{45}H_{85}O_{13}P$	[M-H]-

9AA mass list negative mode

Observed *m/z*	Expected *m/z*	Error (ppm)	Tentative neutral formula	Adduct
152.99581	152.99580	-0.08497	$C_8H_4O_2$	[M+Na-2H]-
171.00637	171.00640	0.16374	$C_3H_9O_6P$	[M+Na-2H]-
176.93594	176.93595	0.05087	$H_4O_7P_2$	[M-H]-
188.03532	188.03532	-0.01595	$C_{10}H_7NO_3$	[M-H]-
191.01971	191.01973	0.08376	$C_6H_8O_7$	[M-H]-
194.06114	194.06114	-0.01546	$C_{13}H_9NO$	[M-H]-
195.07749	195.07752	0.13328	$C_9H_{12}N_2O_3$	[M-H]-
195.08241	195.08250	0.48185	$C_9H_{18}OS$	[M+Na-2H]-
196.03799	196.03800	0.03061	$C_{10}H_9NO_2$	[M+Na-2H]-
204.98122	204.98123	0.05854	$C_6H_6O_6S$	[M-H]-
207.04453	207.04450	-0.14007	$C_6H_{12}N_2O_4S$	[M-H]-
210.08834	210.08842	0.35699	$C_9H_{13}N_3O_3$	[M-H]-
211.00131	211.00128	-0.16114	$C_{10}H_6O_4$	[M+Na-2H]-
214.04859	214.04860	0.03270	$C_5H_{14}NO_6P$	[M-H]-
226.08334	226.08333	-0.04865	$C_9H_{13}N_3O_4$	[M-H]-
227.03818	227.03835	0.76199	$C_{10}H_{12}O_4S$	[M-H]-
228.09900	228.09898	-0.08768	$C_9H_{15}N_3O_4$	[M-H]-
235.03945	235.03942	-0.14466	$C_7H_{12}N_2O_5S$	[M-H]-
237.09150	237.09145	-0.20245	$C_8H_{18}N_2O_4S$	[M-H]-
238.89177	238.89172	-0.23023	$H_3O_9P_3$	[M-H]-
241.01193	241.01188	-0.21991	$C_6H_{11}O_8P$	[M-H]-
241.21734	241.21730	-0.14924	$C_{15}H_{30}O_2$	[M-H]-
242.07833	242.07824	-0.35526	$C_9H_{13}N_3O_5$	[M-H]-
249.05512	249.05507	-0.21682	$C_8H_{14}N_2O_5S$	[M-H]-
253.05000	253.04998	-0.07508	$C_7H_{14}N_2O_6S$	[M-H]-
253.21738	253.21730	-0.30014	$C_{16}H_{30}O_2$	[M-H]-
255.23298	255.23295	-0.10187	$C_{16}H_{32}O_2$	[M-H]-
256.90243	256.90228	-0.58388	$H_5O_{10}P_3$	[M-H]-
259.01304	259.01293	-0.43627	$C_6H_{12}O_9S$	[M-H]-
259.02248	259.02244	-0.14671	$C_6H_{13}O_9P$	[M-H]-
260.02346	260.02343	-0.10768	$C_9H_{11}NO_6S$	[M-H]-
260.08878	260.08881	0.11150	$C_9H_{15}N_3O_6$	[M-H]-
260.87358	260.87366	0.30283	$H_3O_9P_3$	[M+Na-2H]-
262.01222	262.01230	0.30533	$C_{10}H_{11}NO_5$	[M+K-2H]-
262.08682	262.08670	-0.45405	$C_9H_{17}N_3O_4S$	[M-H]-
267.23297	267.23295	-0.05987	$C_{17}H_{32}O_2$	[M-H]-
269.24867	269.24860	-0.24513	$C_{17}H_{34}O_2$	[M-H]-
273.09214	273.09210	-0.13549	$C_{19}H_{14}O_2$	[M-H]-
274.10428	274.10446	0.65304	$C_{10}H_{17}N_3O_6$	[M-H]-
275.01747	275.01736	-0.41088	$C_6H_{13}O_{10}P$	[M-H]-
279.23294	279.23295	0.05014	$C_{18}H_{32}O_2$	[M-H]-
281.24866	281.24860	-0.19911	$C_{18}H_{34}O_2$	[M-H]-
283.26430	283.26425	-0.16239	$C_{18}H_{36}O_2$	[M-H]-
295.05882	295.05879	-0.09829	$C_{15}H_{14}O_5$	[M+Na-2H]-
295.22794	295.22787	-0.24388	$C_{18}H_{32}O_3$	[M-H]-
295.26442	295.26425	-0.56221	$C_{19}H_{36}O_2$	[M-H]-
297.03811	297.03806	-0.18179	$C_{14}H_{12}O_6$	[M+Na-2H]-
297.24347	297.24352	0.16148	$C_{18}H_{34}O_3$	[M-H]-
297.27967	297.27990	0.78714	$C_{19}H_{38}O_2$	[M-H]-
300.03960	300.03948	-0.41328	$C_8H_{15}NO_9S$	[M-H]-
300.04905	300.04899	-0.19663	$C_8H_{16}NO_9P$	[M-H]-
303.23300	303.23295	-0.15170	$C_{10}H_{16}O$	[2M-H]-
304.03403	304.03401	-0.06578	$C_9H_{12}N_3O_7P$	[M-H]-
305.01806	305.01803	-0.11475	$C_9H_{11}N_2O_8P$	[M-H]-
305.06414	305.06427	0.42942	$C_{13}H_{16}O_7$	[M+Na-2H]-
306.07658	306.07653	-0.16336	$C_{10}H_{17}N_3O_6S$	[M-H]-
307.07994	307.07992	-0.06187	$C_{13}H_{18}O_7$	[M+Na-2H]-

309.05920	309.05919	-0.04853	$C_{12}H_{16}O_8$	[M+Na-2H]-
309.27997	309.27990	-0.21340	$C_{20}H_{38}O_2$	[M-H]-
311.07463	311.07484	0.65901	$C_{12}H_{18}O_8$	[M+Na-2H]-
315.04864	315.04877	0.42216	$C_{11}H_{18}O_8$	[M+K-2H]-
322.04456	322.04458	0.04658	$C_9H_{14}N_3O_8P$	[M-H]-
323.02866	323.02859	-0.21670	$C_9H_{13}N_2O_9P$	[M-H]-
323.09013	323.09009	-0.12071	$C_{17}H_{18}O_5$	[M+Na-2H]-
325.03873	325.03875	0.05230	$C_{14}H_{14}O_7S$	[M-H]-
327.03068	327.03086	0.55652	$C_{15}H_{14}O_5S$	[M+Na-2H]-
327.23300	327.23295	-0.14057	$C_{22}H_{32}O_2$	[M-H]-
328.04546	328.04524	-0.66149	$C_{10}H_{12}N_5O_6P$	[M-H]-
328.05849	328.05847	-0.04877	$C_{10}H_{17}N_3O_6S$	[M+Na-2H]-
329.04912	329.04902	-0.31910	$C_{11}H_{16}O_{10}$	[M+Na-2H]-
333.05924	333.05922	-0.05404	$C_9H_{19}O_{11}P$	[M-H]-
334.07143	334.07144	0.04191	$C_{11}H_{17}N_3O_7S$	[M-H]-
336.08697	336.08710	0.37193	$C_{11}H_{19}N_3O_7S$	[M-H]-
337.05419	337.05410	-0.26702	$C_{13}H_{16}O_9$	[M+Na-2H]-
338.98882	338.98877	-0.13865	$C_6H_{14}O_{12}P_2$	[M-H]-
340.99451	340.994643	0.184753	$C_{10}H_{13}N_2O_7P$	[M+K-2H]-
342.11124	342.11116	-0.23092	$C_{20}H_{19}NO_3$	[M+Na-2H]-
344.03238	344.03241	0.09011	$C_{10}H_{17}N_3O_6S$	[M+K-2H]-
344.03983	344.04016	0.95338	$C_{10}H_{12}N_5O_7P$	[M-H]-
346.05587	346.05581	-0.17916	$C_{10}H_{14}N_5O_7P$	[M-H]-
350.13733	350.13738	0.13138	$C_{19}H_{23}NO_4$	[M+Na-2H]-
360.97101	360.97072	-0.81170	$C_6H_{14}O_{12}P_2$	[M+Na-2H]-
362.05090	362.05072	-0.48888	$C_{10}H_{14}N_5O_8P$	[M-H]-
363.19403	363.19416	0.36620	$C_{22}H_{30}O_3$	[M+Na-2H]-
364.08208	364.08201	-0.19501	$C_{12}H_{19}N_3O_8S$	[M-H]-
371.05933	371.05958	0.67105	$C_{13}H_{18}O_{11}$	[M+Na-2H]-
371.07486	371.07484	-0.06737	$C_{17}H_{18}O_8$	[M+Na-2H]-
371.13012	371.12985	-0.73290	$C_{19}H_{26}O_4S$	[M+Na-2H]-
372.13332	372.13296	-0.97008	$C_{20}H_{21}N_3O_3$	[M+Na-2H]-
375.01157	375.01136	-0.57332	$C_9H_{15}N_4O_8P$	[M+K-2H]-
376.03101	376.03102	0.02393	$C_{16}H_{11}NO_{10}$	[M-H]-
377.20989	377.20981	-0.20413	$C_{23}H_{32}O_3$	[M+Na-2H]-
387.15269	387.15254	-0.39261	$C_8H_{18}OS_2$	[2M-H]-
388.25259	388.25270	0.29105	$C_{20}H_{39}NO_4S$	[M-H]-
389.20987	389.20997	0.24408	$C_{21}H_{36}O_4$	[M+K-2H]-
391.22556	391.22562	0.14058	$C_{21}H_{38}O_4$	[M+K-2H]-
395.20503	395.20512	0.23026	$C_{19}H_{34}O_7$	[M+Na-2H]-
401.01541	401.01566	0.61344	$C_{10}H_{16}N_2O_{11}P_2$	[M-H]-
401.14058	401.14041	-0.41631	$C_{20}H_{28}O_5S$	[M+Na-2H]-
402.01091	402.01091	-0.01244	$C_9H_{15}N_3O_{11}P_2$	[M-H]-
402.99499	402.99492	-0.17122	$C_9H_{14}N_2O_{12}P_2$	[M-H]-
403.22546	403.22546	0.00744	$C_{25}H_{34}O_3$	[M+Na-2H]-
405.00481	405.00519	0.94814	$C_{16}H_{16}O_8S$	[M+K-2H]-
405.24124	405.24127	0.06169	$C_{22}H_{40}O_4$	[M+K-2H]-
407.22045	407.22041	-0.08840	$C_{19}H_{37}O_7P$	[M-H]-
409.23602	409.23606	0.10752	$C_{19}H_{39}O_7P$	[M-H]-
415.22565	415.22562	-0.08429	$C_{23}H_{38}O_4$	[M+K-2H]-
417.24121	417.24127	0.13182	$C_{23}H_{40}O_4$	[M+K-2H]-
418.95506	418.95510	0.10264	$C_6H_{15}O_{15}P_3$	[M-H]-
419.25685	419.25680	-0.12164	$C_{21}H_{41}O_6P$	[M-H]-
420.26023	420.26029	0.14515	$C_{20}H_{39}NO_8$	[M-H]-
421.06576	421.06575	-0.02375	$C_{12}H_{22}O_{14}S$	[M-H]-
421.23609	421.23606	-0.06172	$C_{20}H_{39}O_7P$	[M-H]-
423.25171	423.25171	0.00945	$C_{20}H_{41}O_7P$	[M-H]-
424.97684	424.97687	0.05883	$C_9H_{14}N_2O_{12}P_2$	[M+Na-2H]-
426.02221	426.02214	-0.16666	$C_{10}H_{15}N_5O_{10}P_2$	[M-H]-

427.02555	427.02593	0.88753	$C_{19}H_{18}O_7S$	[M+K-2H]-
429.05825	429.05819	-0.13984	$C_{11}H_{20}N_4O_{10}P_2$	[M-H]-
431.22062	431.22041	-0.47771	$C_{21}H_{37}O_7P$	[M-H]-
431.25698	431.25676	-0.50318	$C_{27}H_{38}O_3$	[M+Na-2H]-
432.25244	432.25216	-0.63852	$C_{23}H_{41}NO_4$	[M+K-2H]-
433.23617	433.23606	-0.24467	$C_{21}H_{39}O_7P$	[M-H]-
433.27243	433.27241	-0.03924	$C_{27}H_{40}O_3$	[M+Na-2H]-
435.25178	435.25171	-0.15164	$C_{21}H_{41}O_7P$	[M-H]-
437.26746	437.26736	-0.21955	$C_{21}H_{43}O_7P$	[M-H]-
440.95058	440.95080	0.50346	$C_9H_{14}N_2O_{12}P_2$	[M+K-2H]-
441.04120	441.04158	0.85933	$C_{20}H_{20}O_7S$	[M+K-2H]-
442.01713	442.01705	-0.17420	$C_{10}H_{15}N_5O_{11}P_2$	[M-H]-
443.25700	443.25692	-0.19176	$C_{25}H_{42}O_4$	[M+K-2H]-
445.05317	445.05310	-0.14830	$C_{11}H_{20}N_4O_{11}P_2$	[M-H]-
448.00409	448.00408	-0.01562	$C_{10}H_{15}N_5O_{10}P_2$	[M+Na-2H]-
449.23126	449.23094	-0.70788	$C_{26}H_{36}O_5$	[M+Na-2H]-
452.27840	452.27826	-0.30291	$C_{21}H_{44}NO_7P$	[M-H]-
455.05724	455.05723	-0.02417	$C_{21}H_{22}O_7S$	[M+K-2H]-
455.11667	455.11709	0.93163	$C_{18}H_{26}O_{12}$	[M+Na-2H]-
455.12427	455.12421	-0.13623	$C_{18}H_{24}N_4O_8S$	[M-H]-
459.06851	459.068718	0.278825	$C_{17}H_{19}N_4O_8P$	[M+Na-2H]-
460.28325	460.28346	0.46493	$C_{25}H_{45}NO_4$	[M+K-2H]-
462.29898	462.29911	0.28986	$C_{25}H_{47}NO_4$	[M+K-2H]-
463.97817	463.97802	-0.32329	$C_{10}H_{15}N_5O_{10}P_2$	[M+K-2H]-
465.30447	465.30441	-0.13969	$C_{27}H_{46}O_4S$	[M-H]-
466.30785	466.30752	-0.71627	$C_{28}H_{41}N_3O_3$	[M-H]-
473.28257	473.28274	0.35074	$C_{30}H_{44}O_2$	[M+K-2H]-
476.27856	476.27826	-0.62358	$C_{23}H_{44}NO_7P$	[M-H]-
478.29400	478.29391	-0.18190	$C_{23}H_{46}NO_7P$	[M-H]-
479.29295	479.29330	0.73233	$C_{29}H_{46}O_3$	[M+K-2H]-
480.11230	480.11234	0.08956	$C_{19}H_{25}NO_{12}$	[M+Na-2H]-
480.27345	480.27318	-0.56634	$C_{22}H_{44}NO_8P$	[M-H]-
480.30944	480.30956	0.25608	$C_{23}H_{48}NO_7P$	[M-H]-
481.25675	481.25719	0.92051	$C_{22}H_{43}O_9P$	[M-H]-
481.97734	481.97724	-0.21578	$C_9H_{16}N_3O_{14}P_3$	[M-H]-
482.11939	482.11959	0.40861	$C_{19}H_{23}N_7O_6$	[M+K-2H]-
482.96131	482.96125	-0.12216	$C_9H_{15}N_2O_{15}P_3$	[M-H]-
488.27860	488.27823	-0.76391	$C_{29}H_{41}NO_4$	[M+Na-2H]-
491.27825	491.27804	-0.41931	$C_{26}H_{46}O_6$	[M+K-2H]-
501.12973	501.12969	-0.08381	$C_{19}H_{26}N_4O_{10}S$	[M-H]-
505.98854	505.98847	-0.14032	$C_{10}H_{16}N_5O_{13}P_3$	[M-H]-
508.30455	508.30448	-0.14165	$C_{24}H_{48}NO_8P$	[M-H]-
509.28860	509.28849	-0.21010	$C_{24}H_{47}O_9P$	[M-H]-
520.91746	520.91713	-0.62774	$C_9H_{15}N_2O_{15}P_3$	[M+K-2H]-
521.98360	521.98338	-0.41381	$C_{10}H_{16}N_5O_{14}P_3$	[M-H]-
527.11142	527.11137	-0.08917	$C_{28}H_{26}O_8$	[M+K-2H]-
527.97043	527.97041	-0.03220	$C_{10}H_{16}N_5O_{13}P_3$	[M+Na-2H]-
535.03711	535.03718	0.12896	$C_{14}H_{22}N_2O_{16}P_2$	[M-H]-
543.94417	543.94435	0.33275	$C_{10}H_{16}N_5O_{13}P_3$	[M+K-2H]-
551.26284	551.26264	-0.37006	$C_{30}H_{42}O_8$	[M+Na-2H]-
553.27836	553.27829	-0.13375	$C_{30}H_{44}O_8$	[M+Na-2H]-
558.06435	558.06440	0.08422	$C_{15}H_{23}N_5O_{14}P_2$	[M-H]-
561.31995	561.32022	0.48101	$C_{26}H_{55}NO_7P$	[M+K-2H]-
563.06857	563.06848	-0.15984	$C_{16}H_{26}N_2O_{16}P_2$	[M-H]-
565.04772	565.04774	0.04247	$C_{15}H_{24}N_2O_{17}P_2$	[M-H]-
569.27329	569.27324	-0.09310	$C_{25}H_{47}O_{12}P$	[M-H]-
571.28897	571.28889	-0.14529	$C_{25}H_{49}O_{12}P$	[M-H]-
575.19899	575.19901	0.03999	$C_{13}H_{20}O_5S$	[2M-H]-
579.02685	579.02701	0.27460	$C_{15}H_{22}N_2O_{18}P_2$	[M-H]-

579.29404	579.29394	-0.17953	$C_{32}H_{46}O_8$	[M+Na-2H]-
581.30964	581.30959	-0.09289	$C_{32}H_{48}O_8$	[M+Na-2H]-
582.31288	582.31311	0.40185	$C_{26}H_{49}NO_{13}$	[M-H]-
585.95521	585.95480	-0.69971	$C_{10}H_{17}N_5O_{16}P_4$	[M-H]-
597.30440	597.30454	0.22936	$C_{27}H_{51}O_{12}P$	[M-H]-
599.32004	599.32019	0.24528	$C_{27}H_{53}O_{12}P$	[M-H]-
601.02464	601.02436	-0.46421	$C_{16}H_{26}N_2O_{16}P_2$	[M+K-2H]-
606.07412	606.07429	0.28544	$C_{17}H_{27}N_3O_{17}P_2$	[M-H]-
607.36149	607.36166	0.27661	$C_{30}H_{57}O_{10}P$	[M-H]-
611.14454	611.14469	0.23890	$C_{20}H_{32}N_6O_{12}S_2$	[M-H]-
613.13951	613.13999	0.78449	$C_{20}H_{31}N_4O_{16}P$	[M-H]-
616.47111	616.47115	0.06326	$C_{34}H_{68}NO_6P$	[M-H]-
617.41878	617.41878	-0.00162	$C_{33}H_{63}O_8P$	[M-H]-
620.02021	620.02016	-0.07580	$C_{15}H_{22}N_5O_{16}P_3$	[M-H]-
628.05599	628.05624	0.39328	$C_{17}H_{27}N_3O_{17}P_2$	[M+Na]-
631.43499	631.43443	-0.88845	$C_{34}H_{65}O_8P$	[M-H]-
635.10988	635.11012	0.37316	$C_{12}H_{14}O_{10}$	[2M-H]-
642.48686	642.48680	-0.09494	$C_{36}H_{70}NO_6P$	[M-H]-
643.43435	643.43443	0.12278	$C_{35}H_{65}O_8P$	[M-H]-
644.03011	644.03018	0.10093	$C_{17}H_{27}N_3O_{17}P_2$	[M+K-2H]-
645.45015	645.45008	-0.11000	$C_{35}H_{67}O_8P$	[M-H]-
649.10053	649.10057	0.05854	$C_{20}H_{32}N_6O_{12}S_2$	[M+K-2H]-
657.44955	657.45008	0.80462	$C_{36}H_{67}O_8P$	[M-H]-
659.46536	659.46573	0.55954	$C_{36}H_{69}O_8P$	[M-H]-
662.10215	662.10185	-0.46065	$C_{21}H_{27}N_7O_{14}P_2$	[M-H]-
664.11723	664.11750	0.39903	$C_{21}H_{29}N_7O_{14}P_2$	[M-H]-
669.45021	669.450079	-0.19568	$C_{37}H_{67}O_8P$	[M-H]-
671.46565	671.46573	0.11765	$C_{37}H_{69}O_8P$	[M-H]-
673.48154	673.48138	-0.23906	$C_{37}H_{71}O_8P$	[M-H]-
687.49711	687.49703	-0.11782	$C_{38}H_{73}O_8P$	[M-H]-
693.10728	693.10747	0.27269	$C_{28}H_{32}O_{18}$	[M+K-2H]-
699.49689	699.49703	0.19871	$C_{39}H_{73}O_8P$	[M-H]-
701.51280	701.51268	-0.17106	$C_{39}H_{75}O_8P$	[M-H]-
714.50741	714.50793	0.72637	$C_{39}H_{74}NO_8P$	[M-H]-
727.52770	727.52833	0.86595	$C_{41}H_{77}O_8P$	[M-H]-
730.50219	730.50284	0.89391	$C_{39}H_{74}NO_9P$	[M-H]-
742.53889	742.53923	0.45654	$C_{41}H_{78}NO_8P$	[M-H]-
744.51790	744.51849	0.79649	$C_{40}H_{76}NO_9P$	[M-H]-
745.50313	745.50251	-0.83299	$C_{40}H_{75}O_{10}P$	[M-H]-
753.41954	753.41957	0.03584	$C_{36}H_{67}O_{14}P$	[M-H]-
758.53466	758.53414	-0.68158	$C_{41}H_{78}NO_9P$	[M-H]-
788.54460	788.54471	0.13696	$C_{42}H_{80}NO_{10}P$	[M-H]-
807.50231	807.50290	0.73436	$C_{41}H_{77}O_{13}P$	[M-H]-
809.51891	809.518553	-0.44100	$C_{41}H_{79}O_{13}P$	[M-H]-
833.51830	833.51855	0.30353	$C_{43}H_{79}O_{13}P$	[M-H]-
835.53392	835.53420	0.33871	$C_{43}H_{81}O_{13}P$	[M-H]-
863.56507	863.56550	0.50141	$C_{45}H_{85}O_{13}P$	[M-H]-